Metal–Rhodium Bonded Paddlewheel Complexes (Metal = Rhodium or Bismuth):

Consequences of Exchanging Rhodium for Bismuth on their Structure and Reactivity

Related to C–H Functionalization Catalysis

by

Travis Lee Sunderland

A dissertation submitted in partial fulfillment of

the requirements for the degree of

Doctor of Philosophy

(Chemistry)

at the

University of Wisconsin–Madison

2016

Date of final oral examination: Monday, August 15, 2016

The dissertation is approved by the following members of the Final Oral Committee:

    John F. Berry, Professor, Chemistry

    Clark R. Landis, Professor, Chemistry

    Thomas C. Brunold, Professor, Chemistry

    Judith N. Burstyn, Professor, Chemistry

    Jennifer M. Schomaker, Associate Professor, Chemistry

Metal–Rhodium Bonded Paddlewheel Complexes (Metal = Rhodium or Bismuth):

Consequences of Exchanging Rhodium for Bismuth on their Structure and Reactivity

Related to C–H Functionalization Catalysis

Travis Lee Sunderland

Under the supervision of Professor John F. Berry

University of Wisconsin–Madison

Abstract

Homobimetallic metal–metal bonded complexes have a rich history in both coordination chemistry and catalysis. The presence of heterobimetallic metal–metal bonded compounds has been limited, primarily by their synthetic challenge. Within the last decade, a limited set of heterobimetallic BiRh complexes was shown to catalyze metal carbene transfer reactions by the decomposition of donor/acceptor diazo compounds, however, the expansion of this chemistry has been limited by underdeveloped synthetic strategies. *Chapter 3* details equatorial ligand exchange methods that doubled the existing library of BiRh tetracarboxylate compounds, making the synthesis of new families of BiRh complexes possible. *Chapter 4* advances this chemistry to include the heteroatomic (O, N) ligand class of oxypyridinates. The relative oxophilicity of Bi compared to Rh creates a driving force for exclusive formation of the $[4,0]_O$ isomer. *Chapter 5* expands the supporting ligand class to include the more electron rich (N, N) formamidinate ligands. A Hammett series of equatorial ligands allowed for the comparison of both the electrochemical behavior and magnetic anisotropies of related BiRh and Rh_2 compounds. The heterobimetallic compounds have the largest measured magnetic anisotropies of any element–element single bond to date. *Chapter 6* explores the ability of BiRh complexes supported by chiral carboxylate equatorial ligands to catalyze selective C–H functionalization reactions. While the

BiRh compounds perform slower than their Rh_2 analogues, there is a reversal of regioselectivity in C–H insertion reactions, which continues to be explored. In *Chapter 7*, a spectroscopic and computational comparison between BiRh-, Rh_2- and Ir-based C–H functionalization catalysts is made. A strong correlation between the π back-bonding ability of the metal complex and reactivity of the corresponding carbene fragment is proposed.

DEDICATION

This work is dedicated to my parents, Steven Sr. and Nancy Sunderland, for their endless love and support, and instilling in me the value of hard work. To my sister, Nadine, and brother, Steven Jr., for always helping forge the path forward in front of me. To my grandmother, Marilyn Bates, for always supporting and encouraging me. To my loving wife, Julia, who has been by my side throughout this entire journey.

ACKNOWLEDGMENTS

I would like to thank my advisor, Professor John F. Berry, for mentoring me over the last five years, playing a pivotal role in my scientific development, and allowing me the freedom to pursue scientific problems and questions that interested me. He has always driven me by his scientific inquiry, and a lack of projects and experiments to pursue have never been a question. John also provided me the chance to be a member of the National Science Foundation Center for Selective C–H Functionalization, which has always provided both opportunities and challenges that have helped prepare me for my future career in the sciences.

I would like to thank members of the Berry group, past and present, for helping me in many ways, spoken and unspoken. Dr. Kasia Kornecki and Ryan Pakula have always made my time in Madison enjoyable, both in and out of the lab. I would like to specifically acknowledge both Dr. Amanda Corcos and Dr. Wes Brogden. Amanda has always provided constant feedback and guidance throughout my career here, whether it be with presentations, upcoming requirements, or always answering my crystallography questions. She has also been a close friend outside of work and is never too shy to just hang out. Wes has been one of my closest friends throughout my time in Madison. Without our daily interactions and his constant encouragement, I probably would not have completed graduate school. I am thankful for meeting and getting to know you, and I am excited to see our paths continue to cross as we both enter the chemical industry world.

Thank you to my committee members, Thomas Brunold and Clark Landis, for always challenging me and providing support along my path to completion. I was able to participate in the Organometallic Gordon Research Conference while Clark was the vice-chair, where his interactions truly enriched my experience there. I would also like to thank Judith Burstyn and Jennifer Schomaker for sitting on my final oral defense committee. I've had the chance to share several interesting and fun NMR spectra with Jennifer throughout my career, and Judith's service to the department has helped to build one of the premier chemistry graduate schools.

I would like to thank all of the hard working Chemistry Department Staff for their constant effort in helping me and other graduate students reach our goals on a daily basis. I would like to specifically give thanks to Dr. Ilia Guzei, Dr. Charlie Fry, Dr. Martha Vestling, Dr. Arrietta Clauss, and Kristi Heming. Ilia has shown incredible patience in helping me learn everything I know about X-ray crystallography, which has been vital to answering a lot of the questions in my research. Charlie is always interested in the crazy questions and ideas I bring to him in the NMR facility. Martha has always provided encouragement and support when visiting the mass-spec lab. Arrietta was instrumental in helping me throughout my job search. I could not imagine the last five years without the help and support of Kristi. She helped me during my deferment while abroad in Germany, always helps with anything you ask of her, and helps refuel you mentally with quick breaks from science whenever you stop by her office or run into her in the hallway.

I would like to thank my good friends, Dr. Brandon Kilduff and Ambar Rana for their unquestioned friendship throughout graduate school. Our numerous trips to the library and the local frisbee golf courses will never be forgotten. A special thanks to Brandon, who has been my inorganic companion since the very beginning. We have been nearly inseparable during graduate school, and I am excited to continue our careers together in the chemical industry.

Thank you to Dr. Christoph Lambert for taking a chance on me and allowing me to work in his group at the Julius-Maximilians Universität Würzburg. A special thank you to Dr. Johannes Klein for being my mentor and friend while living in Würzburg. You taught me everything I know about column chromatography and every time I run a column, I think about our time together.

Thank you to my undergraduate advisor Dr. Don 'Chopper' Krogstad. You provided me with the opportunity to become involved in research right away during my Freshman year at Concordia College and I have never looked back. I was able to accompany you to the University of Nevada–Reno on an REU to work in Dr. Brian Frost's laboratory to continue exploring the synthesis of water soluble phosphine ligands based on PTA and their metal complexes. That summer also lead to me meeting my wife, Julia, for which I can never forget.

Thank you to my family. My parents, Steve and Nancy, have always supported my hopes and dreams and done everything they could to help me realize them. Their unwavering support for my whole life and especially these last five years has helped me reach this milestone and become the person I am today. Thank you to my siblings, Nadine and Steven. You both helped lay the foundations in front of me my whole life until I finally took on the challenge of earning my Ph.D. Nadine has helped me in so many unspoken ways throughout the years and I can never thank her enough for what she does at home that allows me the freedom and confidence to chase my dreams away from home. Steven has always been my brother and closest friend. He has always been there to discuss every major life decision I've had to ponder. He has afforded me the opportunity and the confidence to travel to so many places and undertake even more adventures, and I look forward to that continuing the rest of our lives.

Thank you to my new family, Christian, Maria and Stefan Wildt. You have all accepted me into your family since the first day I showed up on your doorstep. I am now officially a member of your family, even though I basically already was for the last eight years. You have always offered your encouragement, support and patient understanding to me, especially through this last challenging time in my life.

Above all, words cannot describe how grateful I am for my amazing wife, Julia. I truly believe fate brought us together and you made me believe in love at first site. You have been by my side through every failure and triumph in these following pages, and beyond. No one will ever know how often we've sat together brainstorming ideas, interpreting data, planning our work, coming in early, leaving late, helping each other, laughing, yelling, crying, and just being there for each other through graduate school and beyond. You have always given me the strength and energy to continue pushing forward. You are my everything and I can never thank you enough for what you have done, do, and will do for me. This accomplishment is as much mine as it is yours. Thank you.

Table of Contents

Chapter 1

Wisconsin Initiative for Science Literacy: Introduction for a General Audience

Chapter 2

Introduction: Background, Motivation and Outline

Chapter 3

Expanding the Family of Heterobimetallic Bi–Rh Paddlewheel Carboxylate Complexes via

Equatorial Carboxylate Exchange

Chapter 4

The First Bismuth(II)–Rhodium(II) Oxypyridinate Paddlewheel Complexes:

Synthesis and Structural Characterization

Chapter 5

Metal–Metal Single Bonds with the Magnetic Anisotropy of Quadruple Bonds:

A Systematic Series of Heterobimetallic Bismuth(II)–Rhodium(II) Formamidinate Complexes

Chapter 6

Preliminary Studies on the Synthesis and Application of

Chiral BiRh Tetracarboxylate Complexes in C–H Functionalization Catalysis

Chapter 7

Spectroscopic and Computational Comparison of

Metal Carbene Species that React with C–H Bonds

Appendix 1

Preliminary In Situ Kinetic Data on Rh$_2$(TPA)$_4$ Catalyzed

Donor/Acceptor Carbene C–H Insertion Reactions with 1,4-Cyclohexadiene

Appendix 2

Evidence of an Iridium Donor/Acceptor Carbene Relevant to C–H Functionalization

Appendix 3

Synthesis and Characterization of the Quadruply Bonded

Dirhenium Diazide Complex Re$_2$(DPhF)$_4$(N$_3$)$_2$

List of Figures

List of Schemes

List of Tables

Chapter 1

Wisconsin Initiative for Science Literacy: Introduction for a General Audience

1.1 Chemistry

When people ask me what I do, I say I am a chemist. The next question is almost always, "Do you make new drugs?" Not exactly. Unfortunately, most people think chemistry only involves the making of new drugs. I always tell them that chemistry is all around us. Yes, it includes the synthesis of new pharmaceutical drugs, but it also encompasses the paint we use in our houses and on our cars. It fills our new modern devices, such as computers, cell phones and tablets. It consists of the packaging almost all of our food and drinks come in every day. It is in all those fancy soaps, creams, lotions, and shampoos you use every day at home. It is used to help power our planet, to help provide clean drinking water, help grow our food, provide fuel for our cars and almost anything else you can think of in modern society. I am always amazed that people never think of these things as chemistry, but undoubtedly, they almost always respond with, "I guess you're right, I never thought about it that way", and this always pleases me when people realize what I do for a career has an impact on their daily lives.

1.2 Inorganic Chemistry

When I say that I am an inorganic chemist, people always ask, "What is that?", this question starts to become a little more difficult to give a clear cut answer. The easiest way to start to describe what inorganic chemistry is, is to start with the more familiar concept of organic chemistry. This usually starts to confuse people, because the term 'organic' has become popularized in society today with the craze over organic foods, organic medicines, organic materials, etc. Organic chemistry is the study of molecules that contain carbon–hydrogen bonds. I like to think of inorganic chemistry as the study of all of the elements, which sometimes also

includes carbon–hydrogen bonds. Even though people are usually familiar with elements such as carbon, oxygen, nitrogen, hydrogen, phosphorous, etc., there are in fact many more elements that exist. They are shown in the periodic table in Figure 1.1. Inorganic chemists generally consider this our playground to work with. Very often, inorganic chemists study molecules that contain metals (the majority of the elements), specifically transition metals, shown in yellow in the middle of Figure 1.1. Transition metals carry out important functions in everyday life. People are more familiar with some of them as essential nutrients for bodily functions, such as chromium, manganese, iron (crucial to oxygen transport in hemoglogin), cobalt (required for vitamin B_{12}), nickel, copper, zinc, and molybdenum. There is also a special group of transition metals, the precious metals, made up of rhodium, palladium, silver, iridium, platinum and gold. These are rare elements that are responsible for many important molecular transformations. One widespread use of some of these metals in in the catalytic converter in most cars today. Inside the converter is a combination of rhodium, palladium and platinum that helps transform emissions from our car engines into less toxic gasses before they are released as exhaust. Most of the compounds in this thesis will include the precious metal of rhodium, but first we have to discuss how we make these new molecules.

Figure 1.1. Periodic table of the elements with the transition metals in yellow.[1]

1.3 Synthesis of New Molecules

When people ask me, "How do you make a new molecule?", I often relate it to cooking a new

dish in the kitchen. First, we have to think about what kind of dish we want to make, this is our

molecule. To do this, we could try and imagine something that has never been done before, or

more commonly we base it off of a more common type of dish; are we baking a loaf of bread,

making a dessert, pancakes, lasagna, a salad? Once we know what type of dish we want to make,

we look up recipes to see how other people have made things like this before. As a chemist, our

recipes are the procedures we write that describe how we made the molecule when we write a

new paper for publication. We have to first read through the ingredient list and make sure we have

everything we need to make the recipe work correctly. Once we have everything measured out in

the appropriate quantities, we need to know how to combine them. Do we just need to dump

everything together? Do we need to do it in a specific order so certain things don't mix together

too soon? Do we need to heat it, cool it down? As an inorganic chemist, many of our reactions

have to be heated to a certain temperature for a given amount of time, analogous to cooking or

baking. Once the recipe is complete, in the kitchen it is usually not too hard to tell whether we made ice cream or a pizza, but what about if we couldn't see or touch or smell what we made? This is the world a chemist usually lives in. The final product that comes out of our reaction can be more difficult to analyze. To know what we made, we have to use a variety of characterization methods to help us with what we can't see with our own eyes.

1.4 Characterization Methods

There are numerous techniques to help an inorganic chemist characterize the structure and properties of new molecules they make. One of the most common set of techniques is called spectroscopy, the interaction of matter with electromagnetic radiation. Electromagnetic radiation is a fancy way to say 'light', but there are many different types of 'light', as shown in the electromagnetic spectrum below in Figure 1.2. It turns out that light we can see, visible light, only makes up a very small portion of the types of light. The energy that light possesses depends on the wavelength of the light, with shorter wavelengths possessing higher energy. Molecules and light can interact in different ways, depending largely on the energy of the light. These different interactions give a chemist various tools to help analyze the structure of their molecules, such as infrared (IR), absorption (ultraviolet/visible, UV/Vis), nuclear magnetic resonance (NMR) and electron paramagnetic resonance (EPR) spectroscopy.
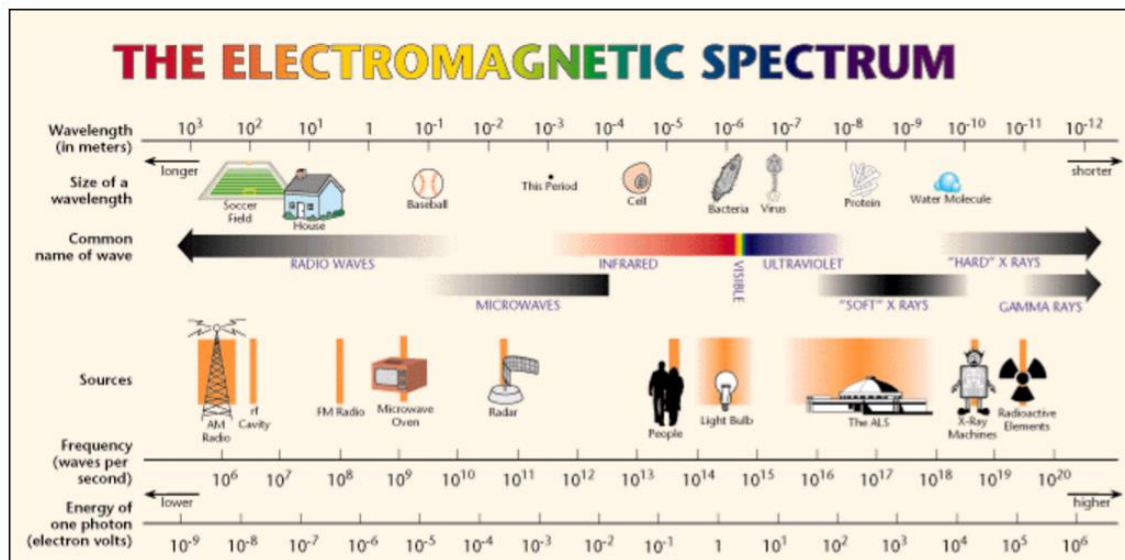
Figure 1.2. The electromagnetic spectrum.[2]

Infrared spectroscopy is based on the idea that atoms within a molecule are bound to each other with a certain amount of energy. If we apply just the right amount of energy to a molecule (infrared light), the bonds between atoms can start to stretch and bend. The energy of these processes can then be displayed in a graph, or spectrum, as different signals. By learning what the different types of shapes and energies of the signals correspond to can help a chemist to decipher which groupings of atoms exist or don't exist within their molecule.

One of the most common and powerful forms of spectroscopy for molecular chemists is NMR spectroscopy. This technique helps to analyze the individual atoms within a molecule. One of the problems is that it only works on certain isotopes of atoms, such as ^{1}H, ^{13}C, ^{19}F, ^{31}P, the good news is that these are some of the more common atoms found in molecules. NMR spectroscopy is predicated on the idea that atomic nuclei can spin around and generate small magnetic fields. When we place these nuclei in a large magnetic field, the spins are forced to align in one of two ways (with or against the external magnetic field). The energy difference between these two states (with or against) is actually quite small, in fact the energy of common radio waves

is enough to cause the states to switch back and forth. When we subject our sample to radio waves inside the magnet, the spins are forced one direction. When the energy is turned off, the spins will slowly go back to their original positions, giving off small amounts of energy during this process, which we can monitor and analyze. These small amounts of energy are different for each atom environment within the molecule, leading to a spectrum with different types of signals seen below in Figure 1.3. A trained chemist can start to use the location and shapes of these signals to learn key information about how the atoms within their molecule are connected to each other. For example, the signal at 7.10 ppm holds two key pieces of information. First, the chemical shift of 7.10 ppm tells us that likely is attributed to a proton attached to an aromatic ring. Second, the shape is a triplet (three peaks), likely meaning that proton has only two other protons next to it in the molecule. Analysis of each signal in this way can start to piece together the molecule we have made in the lab.
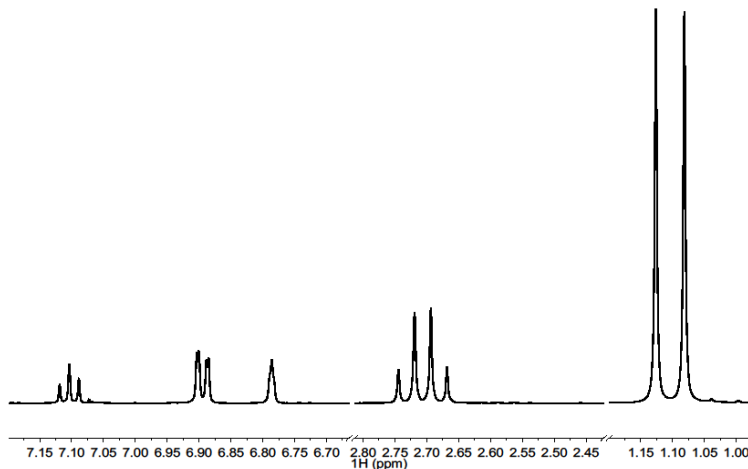
Figure 1.3. Sample ^{1}H NMR spectrum in $CDCl_3$.

Another vital characterization method to most inorganic chemists is X-ray crystallography. This technique is powerful because it can provide a picture of the entire composition and connectivity of a molecule. One hurdle to overcome, is to first obtain a single crystal of the

compound of interest. With some skill and even more luck, single crystals will grow, which you can use for analysis. The crystal is placed on a diffractometer, exposed to high energy X-rays, and hopefully results in a diffraction pattern of spots. Based on the composition of the sample, the location, angle, and intensity of the spots resulting from the X-ray diffraction will be unique. Through a lot of complicated math, these spots can be converted into a picture of your molecule. An example crystal structure is shown in Figure 1.4. A crystal structure was crucial in determining the structure of this molecule because there was no other way to easily determine if the bismuth atom had the four oxygen atoms or the four nitrogen atoms attached to it.
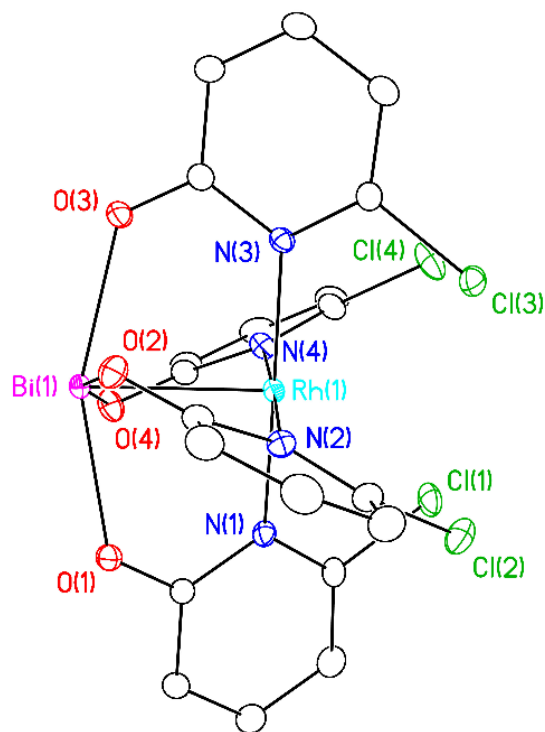
Figure 1.4. X-ray structure of $[4,0]_O$-BiRh(chp)$_4$ (magenta = bismuth, aqua = rhodium, red = oxygen, blue = nitrogen, green = chlorine, black = carbon, hydrogen atoms have been removed for clarity).

1.5 Conclusions and Overview of Thesis Work

In the work presented herein, the synthesis, characterization and application of heterobimetallic BiRh compounds is discussed along with a comparison between three classes of reactive compounds that differ by the metal atoms at their core. *Chapter 2* provides an introduction to the chemistry of metal–metal bonded complexes, including their synthesis and applications specific to C–H functionalization chemistry. *Chapter 3* details synthetic approaches developed in our lab that have now allowed for the expansion to entirely new families of heterobimetallic BiRh compounds, laying the groundwork for the synthesis of most of the compounds in this thesis. *Chapter 4* utilized the techniques from *Chapter 3* to make the first family of BiRh compounds supported by O- and N-atoms (oxypyridinates) rather than only O-atoms (carboxylates). This mixture of atoms makes it possible to make 6 different compounds with slightly different geometries, called isomers. In homobimetallic RhRh compounds, which are closely related to BiRh compounds, predicting which geometry will form in a case like this is difficult and often the isomer formation is driven by whatever makes the atoms not run into each other (sterics). Switching from RhRh to BiRh creates an electronic difference between the metal atoms that doesn't exist when both of them are Rh-atoms. This difference in metal atoms changes the driving force for isomer formation away from sterics towards electronics. This new driving force now allows for predictive and selective formation of a single isomer from the 6 options. *Chapter 5* focuses on making another new family of BiRh compounds, those supported by N-atoms only (formamidinates, (form)), rather than both O- and N-atoms. The compounds that were synthesized are closely related to several other families of this style with other metal atoms at their core instead of Bi- and Rh-atoms. This made it possible to investigate certain properties of the molecules and compare them to other related molecules. The most interesting finding from the $BiRh(form)_4$ compounds was their large difference in electron distribution within the molecule compared to $RhRh(form)_4$ compounds and how this affects one of their magnetic properties. *Chapter 6* goes back to synthesizing new BiRh carboxylate compounds for a particular

application. The goal was to synthesize chiral compounds for use in catalysis. Chiral compounds are special because when they catalyze a reaction, the product formed has a chance to also be chiral. Chiral molecules come in two versions (enantiomers), like our hands, left and right. They are mirror images of each other, but if we try to overlap them, it is impossible. This difference in shape can affect the way molecules interact with each other. Sometimes one enantiomer can be a good drug, while the other does nothing or can even be harmful to our bodies. Being able to synthesize only the good enantiomer is important and difficult. Two new chiral BiRh compounds were synthesized and their ability to perform catalysis were explored. *Chapter 7* looks to compare different metal compounds that are used in the catalysis reactions from *Chapter 6*. The compounds of interest are very reactive, meaning they don't stick around for a long time, making them difficult to analyze by standard methods. We used visible spectroscopy, which is a solution phase technique that is good at detecting these types of short-lived compounds. In addition, we used computational chemistry to compare the three different compounds and draw relationships between their structures and reactivity. Computational chemistry allows us to calculate the molecules with a computer program and learn about their structures, even if they are short-lived and difficult for us to detect and study in real life. When these two techniques are combined, they can help teach us a lot about the chemistry of these molecules.

Overall, the work presented herein focuses on synthetic methods to make interesting new molecules that contain Bi–Rh bonds. Through the use of spectroscopic and computational methods, interesting new insights about these molecules were revealed. One class of the BiRh compounds was applied to catalysis to help change which products are formed in these molecular transformations compared to when the related RhRh compounds are used. The synthetic techniques developed and applied in this thesis have opened up a wide range of new families of BiRh compounds for study. I hope this chapter has helped teach you something about the science I have been working on the last several years, including some of the synthetic and spectroscopic techniques that help chemists synthesize, identify and understand the new molecules we spend

the majority of our time trying to make. I thank you for reading and hope you enjoy learning something new.

1.6 References

(1)   Periodic table of the elements taken from sciencenotes.org/printable-periodic-table/

(2)   Electromagnetic spectrum taken from www2.lbl.gov

Chapter 2

Introduction: Background, Motivation and Outline

2.1 Background and Motivation

2.1.1 Metal–Metal Bonded Rhodium Complexes

Dirhodium compounds have historically played a prominent role in the field of metal–metal bond chemistry,[1] especially in the field of catalysis.[2-7] The stability of Rh_2^{4+} compounds is intrinsically linked to the formation of a Rh–Rh single bond arising from a filled σ orbital made by overlap of the Rh d_z^2 orbitals, illustrated in Figure 2.1 below.[8] The last several decades have resulted in an explosion of published results related to the synthesis and application of Rh_2^{4+} complexes.[9-14] While Rh_2^{4+} compounds have shown a wide diversity in supporting equatorial ligands, a vast majority of the compounds are supported by either (O, O) carboxylate, (N, O) carboxamidate or (N, N) amidinate equatorial ligands.[1]
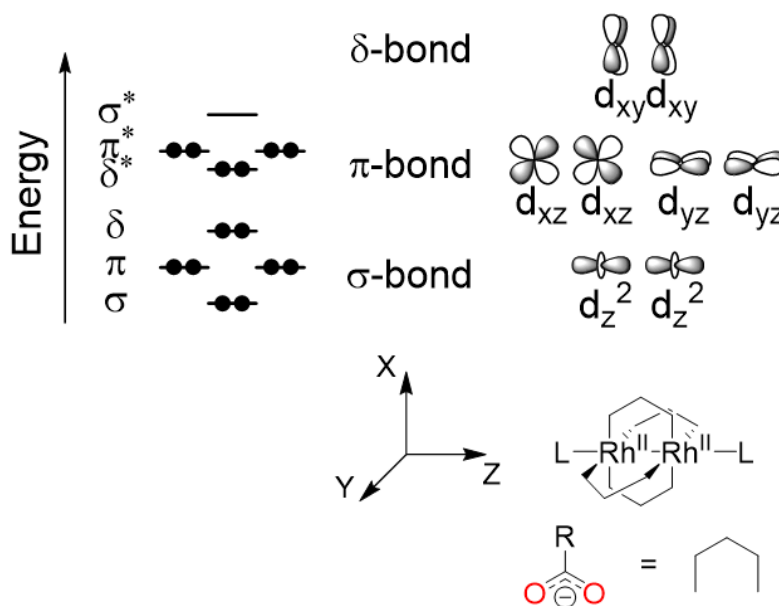
Figure 2.1. General bonding manifold for $Rh_2(O_2CR)_4$ complexes with two axial ligands (L).

Most Rh_2^{4+} tetracarboxylate paddlewheel complexes are synthesized either by heating $RhCl_3 \cdot H_2O$ in an ethanol solution of acetic acid and sodium acetate to form $Rh_2(OAc)_4$ (OAc = acetate), followed by equatorial ligand exchange from $Rh_2(OAc)_4$ to the corresponding carboxylate of choice, or by equatorial ligand exchange directly from $Rh_2(OAc)_4$.[1] A large portion of Rh_2^{4+} paddlewheel complexes are also synthesized by equatorial ligand exchange from $Rh_2(TFA)_4$ (TFA = trifluoroacetate), which tends to react faster than the acetate derivative due to the increased lability of the supporting equatorial ligands. The choice of equatorial ligand can be used to tune both the steric and electronic environment of the complex and its axial coordination sites, on which catalysis can occur. While dirhodium complexes have been shown to catalyze several types of reactions,[9,10,15-18] C–H functionalization by either carbene-[3,19-21] or nitrene-group[21] transfer reactions have been among the most revolutionizing to organic synthesis.[22] Functionalization of C–H bonds has even been considered one of the 'Holy Grails' of modern organic chemistry.[23,24]

Dirhodium paddlewheel complexes were first shown to catalyze organic transformations by the decomposition of diazo compounds by Teyssié and coworkers in 1973.[1,25] The generally accepted mechanism for metal catalyzed C–H insertion of a metal carbene derived from a diazo compound is shown in Scheme 2.1, where coordination of the diazo compound to the metal center is followed by loss of N_2 to form a reactive metal carbene species that can then insert the carbene fragment into a C–H bond to regenerate the catalyst.[26,27]
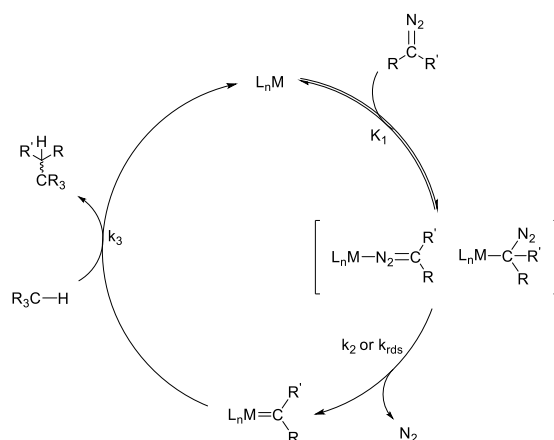
Scheme 2.1. General mechanism for metal catalyzed carbene insertion reaction of diazo compounds into C–H bonds.

One challenge in C–H functionalization is that C–H bonds are both generally inert and abundant within a molecule, making both reactivity and selectivity difficult to achieve.[26] One technique in metal carbene transfer reactions has been tuning the steric and electronic environment of the incoming diazo compound (and consequently metal carbene) by installing either electron withdrawing (EWG) or donating groups (EDG), resulting in three general classes of diazo compounds, acceptor (A), acceptor/acceptor (A/A) and donor/acceptor (D/A) (Figure 2.2) depending on the R-groups flanking the diazo functional group.[28] Installation of at least one EWG is vital to creating a reactive metal carbene fragment,[24] however, when combined with an EDG, the reactivity of the metal carbene fragment is attenuated enough to impart a higher level of intermolecular C–H bond selectivity.[19,20,26,29]

EWG = CO_2R, COR, NO_2, SO_2R, CN, CF_3
EDG = aryl, vinyl, alkynyl
A = Acceptor
D = Donor
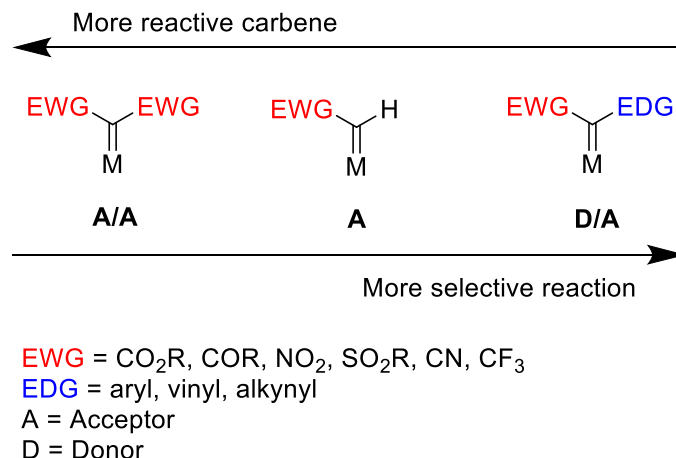
Figure 2.2. Three classes of metal carbenes derived from diazo compounds, acceptor/acceptor (left), acceptor only (middle) and donor/acceptor (right).

While some level of selectivity can be achieved by careful selection of catalyst and carbene fragment, there will still always be an inherent substrate contribution to selectivity, as well. Like most cases in chemistry, C–H bond selectivity is also a delicate balance between sterics and electronics. The general reactivity trends for C–H bonds are shown in Figure 2.3, where 3° C–H bonds are the most electronically activated (from 3°, 2°, and 1°) but sterically least accessible. The opposite is true for 1° C–H bonds, which are sterically the most accessible within molecules, however the most unactivated. This balance often leads to 2° C–H bond functionalization.
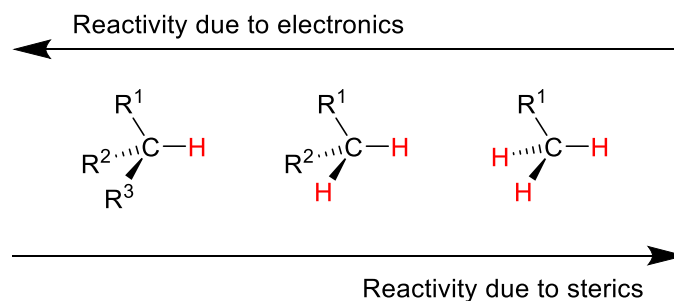
Figure 2.3. General trends of C–H bond selectivity driven by steric and electronic factors for metal carbene insertion reactions.

Approaches to alter the selectivity of Rh_2 complexes have generally been focused on tuning the steric and electronic environment of the axial coordination sites by careful selection of the equatorial ligands, by tuning the steric and electronic nature of the group-transfer fragment or by installing some degree of substrate control within the molecule of interest. One approach that has been underdeveloped is utilization of a heterobimetallic complex including Rh. While several heterobimetallic complexes of Rh have been synthesized, including Mn,[30,31] Fe,[31,32] Co,[33] Zr,[34] Mo,[30] Ru,[30,31] Pd,[35] Os,[36-38] Pt,[35,39,40] Au[41] and Bi,[42-46] only the BiRh complexes have been applied to C–H functionalization catalysis.[43]

2.1.2 Heterobimetallic Bismuth–Rhodium Complexes

The Bi–Rh complexes are of particular interest, because they have been tested in C–H functionalization reactions and compared against their Rh_2 analogues.[43] The replacement of a Rh-atom for a Bi-atom opens up several possibilities and advantages, including that bismuth is ~ 80 times more abundant than rhodium,[47] bismuth is drastically cheaper than rhodium and bismuth has a far lower toxicity level than rhodium. All of these advantages could have a significant impact on making current Rh_2 catalysis more sustainable and applicable, especially to the pharmaceutical industry. Second, it allows for the study of the role the distal metal plays in M_2 catalysis, specifically Rh_2 catalysis. Learning the role the distal metal plays, which has been postulated but never proven, would dramatically impact catalyst design. Third, a BiRh catalyst might have inherently different reactivity or selectivity compared to an Rh_2 catalyst, leading to design and implementation of specific catalysts for specific purposes.

The first example of a heterobimetallic BiRh complex was reported in 2005 by Dikarev and coworkers, with the successful solid-state/gas-phase synthesis of $BiRh(TFA)_4$ (TFA = trifluoroacetate).[46] In this first report, it was shown that the p_z and d_z^2 orbital of the Bi- and Rh-atoms, respectively, are able to sufficiently overlap, resulting in a σ bond between the metal atoms. This solid-state/gas-phase method was further applied to the synthesis of three additional

heteroleptic BiRh tetracarboxylate compounds in 2006,[45] always requiring perfluorinated ligands in their synthesis. In 2009, three BiRh complexes, *cis*-BiRh(TFA)$_2$(piv)$_2$ (piv = pivalate), BiRh(TFA)$_4$ and BiRh(TFA)$_3$(OAc)$_4$ (Figure 2.4) were tested for their ability to decompose diazo compounds and catalyze the carbene transfer reactions of either cyclopropanation or C–H insertion.[43]
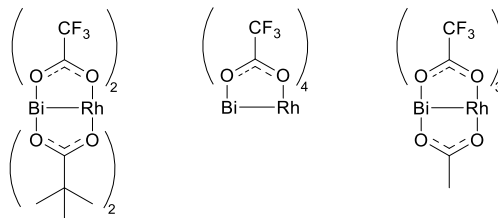
Figure 2.4. Structures of *cis*-BiRh(TFA)$_2$(piv)$_2$ (left), BiRh(TFA)$_4$ (middle) and BiRh(TFA)$_3$(OAc) (right).

It was shown that all three complexes in Figure 2.4 are competent for cyclopropanation and C–H insertion catalysis, however, ReactIR studies showed that BiRh(TFA)$_3$(OAc) decomposes methyl-(phenyl)-diazoacetate 1600 times slower than Rh$_2$(TFA)$_3$(OAc), yet the reactions still progress with reasonable times because usually the diazo compound is slowly added to the reaction mixture.[43] After 2009, appearance of new literature focused on BiRh compounds was lacking, until 2012, when Dikarev and coworkers reported a solution phase method to synthesize the known BiRh(TFA)$_4$ complex along with the perfluorinated ethyl version.[42] The solution route was accomplished by the *in situ* formation of Bi$_2$(TFA)$_4$ from Bi(TFA)$_3$, HTFA and elemental bismuth (reducing agent and Bi source) followed by reaction with Rh$_2$(TFA)$_4$ in a toluene/diphenylether solution. Surprisingly, following the publication of this solution phase synthesis, no further synthetic advances or applications were developed for metal–metal bonded complexes with a BiRh core. A large portion of this thesis is dedicated to advancing the chemistry of BiRh paddlewheel complexes.

2.2 Outline

Chapter 3 describes solution phase equatorial ligand exchange methods applied on the heterobimetallic complex BiRh(TFA)$_4$ to synthesize five novel BiRh tetracarboxylate complexes, doubling the existing library of BiRh compounds at that time. It was shown that standard equatorial ligand exchange methods[1] often applied to Rh$_2$ complexes were also applicable to the heterobimetallic BiRh metal core. It was shown that BiRh complexes are stable across a wide range of electrochemical potentials and form stable Bi–Rh single bonds.

Chapter 4 applies the equatorial ligand exchange methods developed in *Chapter 3* to synthesize the first known heterobimetallic BiRh tetraoxypyridinate complexes supported by (O, N) donor ligands. The use of (O, N) equatorial ligands can result in 4 geometric isomers when coordinated to an Rh$_2$ core, which is increased to 6 isomers upon switching to the BiRh core. While isomer preference in Rh$_2$ tetraoxypyridinate complexes is likely driven by steric repulsion of the equatorial ligands, the electronic differences between the Bi- and Rh-atoms creates a driving force for selective formation of only a single isomer.

Chapter 5 continues to explore the variety of equatorial ligands able to support the BiRh core. Utilization of the (N, N) donor ligand class of formamidinates (form) allowed for the contrast of two key features of Rh$_2$ and BiRh complexes, namely their redox behavior and magnetic anisotropies ($\Delta\chi$), measured in units of 10^{-36} m^3/molecule). A shockingly drastic difference in $\Delta\chi$ between the two families of compounds exists, where BiRh(form)$_4$ compounds have an average $|\Delta\chi|$ value 1.7 times greater than Rh$_2$(form)$_4$ compounds.

Chapter 6 turns its focus back to BiRh tetracarboxylate complexes, but this time utilizing chiral carboxylate ligands to synthesize homochiral BiRh complexes in collaboration with the Davies lab at Emory University. These chiral compounds were applied in C–H functionalization carbene transfer reactions by Dr. Cecilia Tortoreto in the Davies laboratory at Emory University

with the goal of altering the selectivity of the catalysts by exploiting a heterobimetallic BiRh core. The structure of one of the catalysts, along with initial results from catalysis are discussed.

$\quad$ *Chapter 7* conducts a spectroscopic and computational comparative study focusing on metal carbene complexes with three different metal systems used in carbene transfer reactions, Rh_2, Ir and BiRh. It is believed that the π back-bonding ability of the metal core plays a crucial role in the relative stability of the corresponding metal carbene complex.

2.3 References

(1)$\quad$ Cotton, F. A.; Murillo, C. A.; Walton, R. A., *Multiple Bonds Between Metal Atoms*. 3rd ed.; Springer Science and Business Media, Inc.: New York, **2005**.

(2)$\quad$ Doyle, M. P.; Duffy, R.; Ratnikov, M.; Zhou, L. *Chem. Rev.* **2010**, *110*, 704.

(3)$\quad$ Doyle, M. P.; McKervey, M. A.; Ye, T., *Modern Catalytic Methods for Organic Synthesis with Diazo Compounds: From Cyclopropanes to Ylides*. John Wiley & Sons: New York, **1998**.

(4)$\quad$ Doyle, M. P.; Forbes, D. C. *Chem. Rev.* **1998**, *98*, 911.

(5)$\quad$ Doyle, M. P. *Chem. Rev.* **1986**, *86*, 919.

(6)$\quad$ Doyle, M. P. *Acc. Chem. Res.* **1986**, *19*, 348.

(7)$\quad$ Doyle, M. P.; Ren, T. *Prog. Inorg. Chem.* **2001**, *49*, 113.

(8)$\quad$ Kornecki, K. P.; Berry, J. F.; Powers, D. C.; Ritter, T. *Prog. Inorg. Chem.* **2014**, *58*, 225.

(9)$\quad$ Felthouse, T. R. *Prog. Inorg. Chem.* **1982**, 73.

(10)$\quad$ Boyar, E. B.; Robinson, S. D. *Coord. Chem. Rev.* **1983**, *50*, 109.

(11)$\quad$ Ren, T. *Coord. Chem. Rev.* **1998**, *175*, 43.

(12)$\quad$ Housecroft, C. E. *Coord. Chem. Rev.* **1996**, *152*, 107.

(13)$\quad$ Housecroft, C. E. *Coord. Chem. Rev.* **1995**, *146*, 235.

(14)$\quad$ Housecroft, C. E. *Coord. Chem. Rev.* **1992**, *115*, 191.

(15)$\quad$ Doyle, M. P.; Terpstra, J. W.; Winter, C. H.; Griffin, J. H. *J. Mol. Cat.* **1984**, *26*, 259.

(16) Doyle, M. P.; Shanklin, M. S. *Organometallics* **1993**, *12*, 11.

(17) Hui, B. C. Y.; Teo, W. K.; Rempel, G. L. *Inorg. Chem.* **1973**, *12*, 757.

(18) Doyle, M. P.; Phillips, I. M.; Hu, W. *J. Am. Chem. Soc.* **2001**, *123*, 5366.

(19) Davies, H. M. L.; Morton, D. *Chem. Soc. Rev.* **2011**, *40*, 1857.

(20) Davies, H. M. L.; Denton, J. R. *Chem. Soc. Rev.* **2009**, *38*, 3061.

(21) Davies, H. M. L.; Manning, J. R. *Nature* **2008**, *451*, 417.

(22) Davies, H. M. L. *Angew. Chem., Int. Ed.* **2006**, *45*, 6422.

(23) Labinger, J. A.; Bercaw, J. E. *Nature* **2002**, *417*, 507.

(24) Bergman, R. G. *Nature* **2007**, *446*, 391.

(25) Paulissen, R.; Reimlinger, H.; Hayez, E.; Hubert, A. J.; Teyssié, P. *Tetrahedron Lett.* **1973**, *14*, 2233.

(26) Davies, H. M. L.; Beckwith, R. E. J. *Chem. Rev.* **2003**, *103*, 2861.

(27) Pirrung, M. C.; Liu, H.; Morehead, A. T. *J. Am. Chem. Soc.* **2002**, *124*, 1014.

(28) Diaz-Requejo, M. M.; Belderrain, T. R.; Nicasio, M. C.; Perez, P. J. *Dalton Trans.* **2006**, 5559.

(29) Petrukhina, M. A.; Andreini, K. W.; Walji, A. M.; Davies, H. M. L. *Dalton Trans.* **2003**, 4221.

(30) Bosch, H. W.; Wayland, B. B. *J. Organomet. Chem.* **1986**, *317*, C5.

(31) Dahlenburg, L.; Hache, R. *Inorg. Chim. Acta* **2003**, *350*, 77.

(32) Cai, S.; Hou, X.; Chen, Y.; Jin, G. *Dalton Trans.* **2006**, 3736.

(33) Cheng, M.; Mai, C.; Yeh, C.; Lee, G.; Peng, S. *Chem. Commun.* **2013**, *49*, 7938.

(34) Cornelissen, C.; Erker, G.; Kehr, G.; Fröhlich, R. *Organometallics* **2005**, *24*, 214.

(35) Ciriano, M. A.; Perez-Torrente, J. J.; Lahoz, F. J.; Oro, L. A. *Inorg. Chem.* **1992**, *31*, 969.

(36) Hilts, R. W.; Franchuk, R. A.; Cowie, M. *Organometallics* **1991**, *10*, 304.

(37) Trepanier, S. J.; Dennett, J. N. L.; Sterenberg, B. T.; McDonald, R.; Cowie, M. *J. Am. Chem. Soc.* **2004**, *126*, 8046.

(38) Sterenberg, B. T.; McDonald, R.; Cowie, M. *Organometallics* **1997**, *16*, 2297.

(39) Tanabe, M.; Osakada, K. *Inorg. Chim. Acta* **2003**, *350*, 201.

(40) Cook, T. R.; McCarthy, B. D.; Lutterman, D. A.; Nocera, D. G. *Inorg. Chem.* **2012**, *51*, 5152.

(41) Esswein, A. J.; Dempsey, J. L.; Nocera, D. G. *Inorg. Chem.* **2007**, *46*, 2362.

(42) Filatov, A. S.; Napier, M.; Vreshch, V. D.; Sumner, N. J.; Dikarev, E. V.; Petrukhina, M. A. *Inorg. Chem.* **2012**, *51*, 566.

(43) Hansen, J.; Li, B.; Dikarev, E.; Autschbach, J.; Davies, H. M. L. *J. Org. Chem.* **2009**, *74*, 6564.

(44) Dikarev, E. V.; Li, B.; Rogachev, A. Y.; Zhang, H.; Petrukhina, M. A. *Organometallics* **2008**, *27*, 3728.

(45) Dikarev, E. V.; Li, B.; Zhang, H. *J. Am. Chem. Soc.* **2006**, *128*, 2814.

(46) Dikarev, E. V.; Gray, T. G.; Li, B. *Angew. Chem., Int. Ed.* **2005**, *44*, 1721.

(47) Greenwood, N. N.; Earnshaw, A. *Chemistry of the Elements.* 2nd ed., Butterworth-Heinemann: Oxford, **1997**.

Chapter 3

Expanding the Family of Heterobimetallic Bi–Rh Paddlewheel Carboxylate Complexes via Equatorial Carboxylate Exchange

This chapter is adapted from "Expanding the Family of Heterobimetallic Bi–Rh Paddlewheel Carboxylate Complexes via Equatorial Carboxylate Exchange", a published manuscript:

Reprinted with permission. Sunderland, T. L. and Berry, J. F. *Dalton Trans.* **2016**, *45*, 50.

Department of Chemistry, University of Wisconsin–Madison, 1101 University Avenue, Madison, WI 53706, United States

3.1 Abstract

Five novel homoleptic heterobimetallic bismuth(II)-rhodium(II) carboxylate complexes—
BiRh(TPA)₄ (**1**), *BiRh(but)₄* (**2**), *BiRh(piv)₄* (**3**), *BiRh(esp)₂* (**4**), and *BiRh(OAc)₄* (**5**) —were
synthesized in good yields by equatorial ligand substitution starting from *BiRh(TFA)₄* (TPA =
triphenylacetate, but = butyrate, piv = pivalate, esp = α,α,α',α'-tetramethyl-1,3-
benzenedipropionate, OAc = acetate, and TFA = trifluoroacetate). We report here ^{1}H and ^{13}C{^{1}H}
NMR spectra and cyclic voltammograms for complexes **1** - **4**, and IR spectra for all complexes.
Irreversible redox waves appear between −1.4 to −1.5 V for [BiRh]$^{3+/4+}$ couples and 1.3 to 1.5 V
vs Fc/Fc$^+$ for [BiRh]$^{4+/5+}$ couples for complexes **1** - **4** indicating a wide range of stability for the
compounds. The X-ray crystal structure of **1** reveals a Bi–Rh distance of 2.53 Å.

3.2 Introduction

Dinuclear transition metal paddlewheel complexes[1,2] have been of considerable interest
in a wide variety of applications including catalysis.[3-5] Dirhodium tetracarboxylate complexes have
been intensely studied for their ability to promote reactions resulting in the functionalization of
C–H bonds,[6] specifically metal nitrenoid[7] and carbenoid[8-10] transfer chemistry. Catalyst design
has driven many of the major advances in this field, and is a contributing factor why more than
1500 Rh$_2$ complexes have been synthesized.[6] Of these, tetracarboxylate compounds are well-
represented and are readily accessible through a variety of synthetic routes.[1]

In 2005, Dikarev and coworkers reported the first example of a heterobimetallic homoleptic
Bi–Rh tetracarboxylate paddlewheel complex with the solid state synthesis of BiRh(O$_2$CCF$_3$)$_4$.[11]
Further exploration of this solid state technique has afforded three other examples of heteroleptic
heterobimetallic carboxylate complexes.[12] Recently, a synthetic route to heterobimetallic Bi–Rh
complexes was adapted to solution phase chemistry using perfluorinated carboxylates (O$_2$CCF$_3$
and O$_2$CCF$_2$CF$_3$).[13] These Bi–Rh compounds are interesting because they are the first examples
of a heterobimetallic M–M bonded core containing Rh-atoms and their design was driven by the

need to replace expensive and rare precious metals with cheap and earth abundant alternatives while maintaining their functionality. Three of these Bi–Rh complexes have been tested for their ability to perform metal carbenoid transformations, a hallmark of the analogous Rh_2 complexes.[14] The heterobimetallic complexes were successfully able to perform both cyclopropanation and C–H insertion reactions with donor/acceptor diazo compounds with similar or better chemo- and diastereoselectivites compared to their Rh_2 analogues.

Access to novel heterobimetallic Bi–Rh complexes has been limited to the above mentioned solid state methods for volatile compounds or solution phase methods with perfluorinated ligands. Thus, in comparison to the extremely large and versatile family of Rh_2 complexes, Bi–Rh chemistry is severely limited and only five examples are known that contain highly electron-withdrawing carboxylate ligands. In this work, we report efficient carboxylate exchange reactions starting from the well characterized $BiRh(O_2CCF_3)_4$ that can now be expanded to a wide variety of compounds; synthesis of five new Bi–Rh tetracarboxylate complexes reported here now doubles the number of existing Bi–Rh complexes. This is the first report of performing equatorial ligand exchange reactions on a heterobimetallic M–M bonded core containing Rh-atoms. Rapid expansion of the library of heterobimetallic Bi–Rh complexes is now possible and will facilitate further study of their potential uses in catalysis and other important applications.

3.3. Experimental Section

3.3.1 Materials and Methods

All reactions were carried out using oven dried glassware under a dry N_2 atmosphere using Schlenk techniques and glovebox methods. Toluene was purified using a Vacuum Atmospheres solvent purification system. $BiRh(TFA)_4$[13] and H_2esp[15] were prepared according to literature procedures. Dichloromethane (DCM), diethyl ether (Et₂O), ethyl acetate (EtOAc), hexane, methanol (MeOH), chloroform-*d* ($CDCl_3$), butyric acid, pivalic acic, triphenylacetic acid,

acetic acid, and potassium carbonate (K_2CO_3) were purchased from Sigma-Aldrich and used without further purification. Flash column chromatography was performed on Silicycle Siliaflash silica gel (40-63 μm, 230-400 mesh). ^{1}H and ^{13}C{^{1}H} NMR spectra were recorded on a Bruker Avance-500 MHz spectrometer at 500 and 125 MHz, respectively. ^{1}H and ^{13}C{^{1}H} NMR shifts were referenced to residual solvent. [1]H splitting patterns were designated as singlet (s), doublet (d), doublet of doublets (dd), triplet (t), sextet (sex), and AB quartet (ABq). Cyclic voltammetry was performed in 10 mL DCM (dried over calcium hydride and freshly distilled prior to use) solutions containing 0.1 M tetrabutylammonium hexafluorophosphate (TBAH) with 1 mM analyte under an atmosphere of nitrogen. The electrodes consisted of a glassy carbon working electrode, a reference electrode made of a silver wire in a 10 mM $AgNO_3$ solution contained by a Vycor tip, and an auxiliary electrode of platinum wire. All cyclic voltammograms were referenced to the ferrocene/ferrocenium (Fc/Fc[+]) redox couple. Elemental analysis was carried out by Midwest Microlab, LLC, Indianapolis, IN. IR spectra were taken on a Bruker Tensor 27 FTIR spectrometer using an attenuated total reflectance (ATR) adapter. Mass spectra were obtained at the Paul Bender Chemical Instrumentation Center of the Chemistry Department of the University of Wisconsin–Madison using a Thermo Q Exactive™ Plus ESI-MS.

BiRh(TPA)₄ (1). Solid BiRh(TFA)₄ (45.7 mg, 0.0600 mmol) and triphenylacetic acid (138 mg, 0.477 mmol) were combined in a 25 mL Schlenk flask and suspended in 15 mL toluene. The yellow suspension was heated to reflux through a soxhlet extractor (K_2CO_3 in the thimble) at 145 °C using an oil bath for 40 h. After cooling to room temperature, the solvent was removed *in vacuo.* The solids were dissolved in a 20% hexane/DCM solution and passed through a silica plug. The yellow solution was collected and the solvent was removed *in vacuo.* The yellow product was recrystallized from DCM/hexane. Yield: 57.2 mg, 65.6%. X-ray quality crystals of **1**•CH_2Cl_2 were obtained by layering a concentrated DCM solution of **1** with hexane. Anal. Calcd $BiRhC_{80}H_{60}O_8$•(0.5 CH_2Cl_2): C 64.3, H 4.1. Found: C 64.0, H 4.8. ESI-MS (positive ion, CH_3CN): *m/z* 1461 ([M+H][+], 6%). ^{1}H NMR ($CDCl_3$, 500 MHz, ppm): δ 7.10 (t, *J* = 7.31 Hz, 12H), 6.91 (dd,

J = 7.91 Hz, 7.31 Hz, 24H), 6.73 d, *J* = 7.91 Hz, 24H). ^{13}C{^{1}H} NMR (CDCl$_3$, 125 MHz, ppm):

δ 187.4, 143.6, 130.6, 127.5, 126.9, 69.0. IR (ATR, cm^{-1}): 1567 (m), 1492 (w), 1445 (w), 1358 (m),

1339 (w), 1037 (w), 906 (br), 807 (w), 759 (m), 744 (m), 735 (m), 698 (s), 674 (m), 649 (w), 622

(w), 606 (m).

BiRh(but)$_4$•(H$_2$O) (2•H$_2$O). Solid BiRh(TFA)$_4$ (51.6 mg, 0.0676 mmol) and butyric acid (5

mL, 54.5 mmol) were combined in a 10 mL Schlenk flask, resulting in a clear yellow solution. This

solution was heated to reflux at 155 °C using an oil bath for 1 h, after which the acid was distilled

out under reduced pressure and this process was repeated one more time. The remaining yellow

solid was dissolved in a 50% EtOAc/hexane solution and passed through a silica plug. The yellow

solution was collected and the solvent was removed *in vacuo*. The yellow solid was then

recrystallized with hot hexane, filtered, washed with cold hexane and dried *in vacuo*. Yield:

27.8 mg, 60.7%. Anal. Calcd BiRhC$_{16}$H$_{28}$O$_8$: C 29.1, H 4.3. Found: C 29.1, H 4.1. ESI-MS (positive

ion, CH$_3$CN): *m/z* 661 ([M+H]$^+$, 100%). ^{1}H NMR (CDCl$_3$, 500 MHz, ppm): δ 2.32 (t, *J* = 7.3 Hz,

8H), 1.64 (2H, s), 1.56 (sex, *J* = 7.3 Hz, 8H), 0.79 (t, *J* = 7.3 Hz, 12H). ^{13}C{^{1}H} NMR (CDCl$_3$, 125

MHz, ppm): δ 187.9, 37.9, 19.6, 13.6. IR (ATR, cm^{-1}): 2963 (w), 2933 (w), 2874 (w), 1556 (s),

1488 (m), 1460 (m), 1406 (m), 1349 (m), 1313 (m), 1264 (w), 1210 (w), 1102 (w), 897 (w), 870

(w), 803 (w), 736 (w), 668 (m), 648 (w), 634 (w), 613 (w), 608 (w).

BiRh(piv)$_4$•(H$_2$O) (3•H$_2$O). Solid BiRh(TFA)$_4$ (50.9 mg, 0.0666 mmol) and pivalic acid

(1.51 g, 14.8 mmol) were combined in a 10 mL Schlenk flask and sealed under static vacuum.

The mixture was heated to 130 °C using an oil bath, resulting in a yellow solution. After heating

for 1 h, the acid was distilled out under reduced pressure and this process was repeated one

more time. The yellow solid was purified by flash column chromatography on silica using DCM as

the eluent (R$_f$ = 0.40, DCM). The yellow solution was collected and the solvent was removed *in*

vacuo. Yield: 40.0 mg, 81.7%. Anal. Calcd BiRhC$_{20}$H$_{36}$O$_8$•H$_2$O: C 32.7, H 5.2. Found: C 32.7, H

5.1. ESI-MS (positive ion, CH$_3$CN): *m/z* 717 ([M+H]$^+$, 100%). ^{1}H NMR (CDCl$_3$, 500 MHz, ppm):

δ 1.93 (s, 2H), 1.05 (s, 36H). $^{13}C\{^1H\}$ NMR (CDCl$_3$, 125 MHz, ppm): δ 192.1, 40.3, 28.1. IR (ATR, cm^{-1}): 3491 (br), 2962 (w), 1556 (s), 1483 (m), 1411 (s), 1224 (m), 895 (w), 800 (w), 786 (w), 747 (w), 735 (w), 709 (w), 688 (w), 680 (w), 662 (w), 649 (w), 640 (w), 634 (s), 626 (s), 613 (m), 605 (m).

BiRh(esp)$_2$ (*4*). Solid BiRh(TFA)$_4$ (63.6 mg, 0.0833 mmol) and H$_2$esp (278 mg, 0.237 mmol) were combined in a 25 mL Schlenk flask and dissolved in 15 mL toluene. The yellow solution was heated to reflux through a soxhlet extractor (K$_2$CO$_3$ in thimble) at 145 °C using an oil bath for 5 h during which some yellow precipitate formed. After cooling to room temperature, the solvent was removed *in vacuo*. The yellow solid was washed with Et$_2$O and dried *in vacuo*. Yield: 61.6 mg, 85.6%. Anal. Calcd BiRhC$_{32}$H$_{40}$O$_8$: C 44.5, H 4.7. Found: C 44.4, H 4.8. ESI-MS (positive ion, MeOH): *m/z* 865 ([M+H]$^+$, 12%). ^1H NMR (CDCl$_3$, 500 MHz, ppm): δ 7.10 (t, *J* = 7.5 Hz, 2H), 6.89 (dd, *J* = 7.5 Hz, 1.6 Hz, 4H), 6.79 (t, *J* = 1.6 Hz, 2H), 2.73, 2.68 (ABq, *J$_{AB}$* = 12.6 Hz, 8H), 1.13 (s, 12H), 1.08 (s, 12H). $^{13}C\{^1H\}$ NMR (CDCl$_3$, 125 MHz, ppm): δ 189.9, 138.1, 130.7, 128.3, 127.1, 47.7, 45.9, 26.4, 26.0. IR (ATR, cm^{-1}): 2963 (w), 2952 (w), 2919 (w), 1561 (s), 1473 (m), 1454 (w), 1433 (w), 1403 (s), 1375 (m), 1360 (m), 1301 (w), 1262 (m), 1245 (m), 1198 (w), 1166 (w), 1132 (w), 965 (w), 931 (w), 904 (w), 882 (w), 826 (m), 798 (w), 783 (m), 775 (m), 747 (m), 706 (s), 632 (s).

BiRh(OAc)$_4$ (*5*). Solid BiRh(TFA)$_4$ (50.1 mg, 0.0656 mmol) and acetic acid (5 mL, 87.4 mmol) were combined in a 10 mL Schlenk flask, resulting in a clear yellow solution. This solution was heated to reflux at 125 °C using an oil bath for 1 h, after which the acid was distilled out under reduced pressure and this process was repeated one more time, during which a yellow solid precipitated from the reaction mixture. The remaining yellow solid (completely insoluble in all solvents) was washed with H$_2$O, DCM, hexane, MeOH and dried *in vacuo*. Yield: 35.4 mg, 98.4%. Anal. Calcd BiRhC$_8$H$_{12}$O$_8$: C 17.5, H 2.2. Found: C 17.6, H 2.1. IR (ATR, cm^{-1}): 1556 (s),

1485 (w), 1412 (s), 1345 (m), 1043 (w), 689 (s), 625 (m). Further spectral characterization was not possible due to the insolubility of the compound.

3.3.2 Crystallography

Crystallographic data were measured at the Molecular Structure Laboratory of the Chemistry Department of the University of Wisconsin–Madison. Crystals were selected under oil under ambient conditions and attached to the tip of a MiTeGen MicroMount©. Each crystal was mounted in a stream of cold nitrogen at 100(1) K and centered in the X-ray beam using a video camera. The crystal evaluation and data collection were performed on a Bruker Quazar SMART APEX-II diffractometer with Cu Kα (λ= 1.54178 Å) radiation. The data were collected using a routine to survey an entire sphere of reciprocal space and indexed by the SMART program.[16] The structures were solved via direct methods and refined by iterative cycles of least-squares refinement on F^2 followed by difference Fourier synthesis.[17,18] All H-atoms were included in the final structure factor calculation at idealized positions and allowed to ride on the neighboring atoms with relative isotropic displacement coefficients. Single crystals of **1**•CH_2Cl_2 suitable for structural determination were obtained by slow diffusion of hexane into a dichloromethane solution of **1**. The unit cell contains an additional 8 molecules of dichloromethane which have been removed by SQUEEZE.

3.4 Results and Discussion

3.4.1 Synthesis and Characterization

Carboxylate exchange reactions are well-known synthetic methods in the chemistry of metal–metal bonded compounds.[1] While this method has been used successfully on heterobimetallic compounds with strong quadruple bonds[19] (e.g. [MoW]$^{4+}$ compounds), it was not immediately obvious whether the [BiRh]$^{4+}$ core, having a lower metal–metal bond order, would be robust enough to survive these reaction conditions. Nevertheless, we tested reactions of

$BiRh(O_2CCF_3)_4$ with excess carboxylic acids to see (by $^{19}F\{^1H\}$ NMR spectroscopy) whether carboxylate exchange takes place. Gratifyingly, these carboxylate exchange reactions were found to be quite clean and straightforward. Using carboxylate exchange, we have obtained $BiRh(TPA)_4$ (**1**), $BiRh(but)_4$ (**2**), $BiRh(piv)_4$ (**3**), $BiRh(esp)_2$ (**4**), and $BiRh(OAc)_4$ (**5**) in useful yields starting from $BiRh(TFA)_4$[13] (TPA = triphenylacetate, but = butyrate, piv = pivalate, esp = α,α,α',α'-tetramethyl-1,3-benzenedipropionate, OAc = acetete and TFA = trifluoroacetate); (see Table 3.1). Complete equatorial ligand exchange was observed for all compounds by either refluxing a toluene solution of $BiRh(TFA)_4$ and excess ligand through a soxhlet extractor containing K_2CO_3 (**1** and **4**) or by successive heating and distillation of excess acid (**2**, **3** and **5**), as evidenced by silent $^{19}F\{^1H\}$ NMR spectra for **1** - **4**. The resulting yellow compounds **1** - **4** were all characterized by ^1H and $^{13}C\{^1H\}$ NMR and IR spectroscopy along with cyclic voltammetry, ESI-MS, and elemental analysis. Compound **5** was characterized by elemental analysis and IR spectroscopy. A one-pot synthetic route to **1** was attempted by reacting elemental Bi with $Bi(TFA)_3$ and $Rh_2(TFA)_4$ in a suspension of toluene/diphenyl ether/HTFA (conditions typically used to form $BiRh(TFA)_4$)[13] with excess HTPA ligand present. This reaction resulted in a complex mixture of substituted homo- and heterobimetallic complexes that were not easily separable; therefore, equatorial ligand exchange from pre-formed $BiRh(TFA)_4$ is the preferred route to the novel compounds discussed in this work. Attempts to synthesize **1** without the use of the soxhlet method described above resulted in incomplete substitution of all four TFA ligands; instead a trisubstitued complex, $BiRh(TPA)_3(TFA)$, was observed and characterized by ^1H and $^{19}F\{^1H\}$ NMR spectroscopies.[20] The observation of a partially substituted complex suggests that the equatorial ligands are exchanged in a stepwise fashion, similar to the ligand substitution mechanism for Rh_2 complexes.[21, 22]

Table 3.1. General reaction scheme and conditions for synthesis of complexes **1** - **5**.

Complex	Carboxylic Acid	Equivalents	Solvent	Time (h)	Yield (%)
1		8.0	Toluene	40	65.6
2		810	Neat	2	60.7
3		220	Neat	2	81.7
4		2.8	Toluene	5	85.6
5		1300	Neat	2	98.4

The ^{1}H NMR spectrum of **1** in CDCl$_3$ shows well resolved resonances in the aryl region with the *para*-hydrogen atoms at 7.10 ppm (t), *meta*-hydrogen atoms at 6.91 ppm (dd), and *ortho*-hydrogen atoms at 6.73 ppm (d) showing downfield shifts ($\Delta \delta$ = 0.02, 0.05, and 0.11 ppm, respectively) compared to the spectrum of the analogous homobimetallic Rh$_2$(TPA)$_4$. The ^{1}H NMR spectrum of **2** in CDCl$_3$ shows resonances at 2.32 ppm (t), 1.64 ppm (s) for an axially bound water molecule, 1.56 ppm (sex) and 0.79 ppm (t). The ^{1}H NMR spectrum of **3** in CDCl$_3$ shows resonances at 1.93 ppm (s) for an axially bound water molecule and at 1.05 ppm (s) corresponding to the pivalate ligands. The ^{1}H NMR spectrum of **4** in CDCl$_3$ shows aryl resonances at 7.10 ppm (t), 6.89 ppm (dd) and 6.79 ppm (t) along with alkyl resonances at 2.73 and 2.68 ppm (ABq), 1.13 ppm (s) and 1.08 ppm (s). There are two interesting distinctions in the ^{1}H NMR spectrum of **4** compared to that of the analogous homobimetallic Rh$_2$(esp)$_2$. First, both the methyl

and methylene protons are diastereotopic in the heterobimetallic complex where they both appear as singlets in the homobimetallic complex. The heterobimetallic core causes these particular protons to be magnetically inequivalent due to the loss of symmetry along the M–M axis. Second, all of the ^{1}H-atom resonances in the BiRh complex are shifted downfield compared to several $Rh_2(esp)_2$ complexes with various axially ligated molecules[23] with the exception of the aryl hydrogen atom at the 2-position of the ring ($\Delta \delta \sim 0.18$ ppm upfield), which points towards the metal–metal core.

3.4.2 Crystallography

The asymmetric unit of the monoclinic $P2_1/n$ crystal of **1** contains one BiRh complex with one molecule of DCM axially bound to the Rh-atom along with additional disordered solvent in the lattice. The molecular structure of **1**•CH_2Cl_2, determined by single-crystal X-ray crystallography and the summary of crystallographic data are shown in Figure 3.1 and Table 3.2, respectively. The structure has a typical paddlewheel geometry with the Bi-atom in a distorted square pyramidal geometry coordinated by four O-atoms and capped by the Rh-atom. The Rh-atom lies at the center of an octahedron with four O-atoms occupying the equatorial sites, a Bi-atom and Cl-atom from a DCM molecule occupy the axial sites.
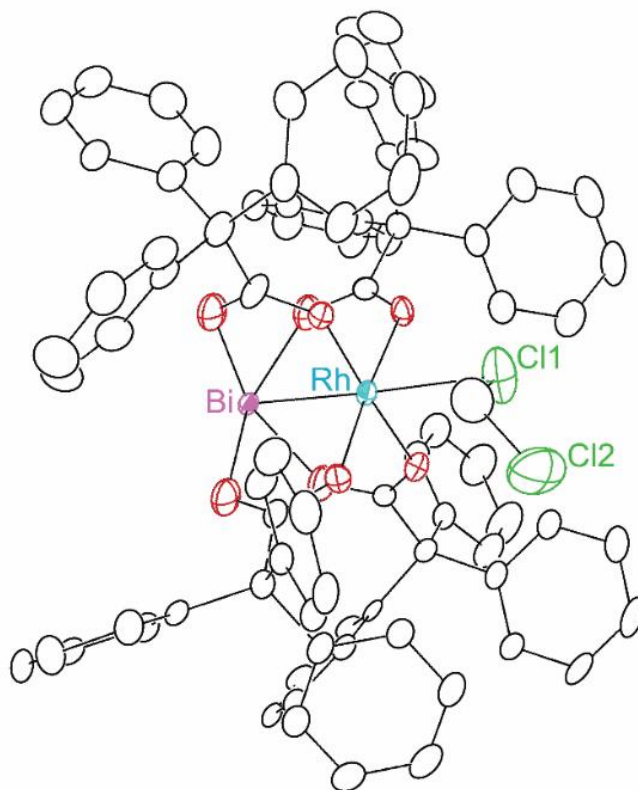
Figure 3.1. X-ray crystal structure of **1**•CH$_2$Cl$_2$, with thermal ellipsoids drawn at the 50% probability level. Hydrogen atoms and two disordered CH$_2$Cl$_2$ molecules have been omitted for clarity.

Table 3.2. Crystallographic data for **1**•CH_2Cl_2 at 100 K.

Identification code	**1**•CH_2Cl_2
Empirical formula	$BiRhC_{83}H_{66}O_8Cl_6$
Formula weight	1715.94
Temperature	100(1) K
Wavelength	1.54178 Å
Crystal system	Monoclinic
Space group	$P2_1/n$
Unit cell dimensions	a = 15.5675(3) Å
	b = 14.3374(3) Å
	c = 35.8081(8) Å
	α = 90°
	β = 100.401(1)°
	γ = 90°
Volume	7860.9(3) Å^3
Z	4
Density (calculated)	1.450 g/cm^3
Crystal size	0.391 x 0.116 x 0.056 mm^3
Data / restraints / parameters	15663/ 0 / 820
Goodness-of-fit on F^2	1.169
Final R[a,b] indices [$I>2\sigma(I)$]	R_1 = 0.0422, wR_2 = 0.0952
R indices (all data)	R_1 = 0.0448, wR_2 = 0.0964

[a]$R_1 = \Sigma||F_0| - |F_c||/\Sigma|F_0|$

[b]w$R_2 = |[\Sigma[w(F_0^2 - F_c^2)^2] / \Sigma[w(F_0^2)^2]]1/2$, w = $1/\sigma^2 (F_0^2) + (aP)^2 + bP$, where P = $[\max(0 \text{ or } F_0^2) + 2(F_c^2)]/3$.

The Bi–Rh bond distance is 2.5326(3) Å. The average M–O bond distances of 2.357[5] and 2.027[4] Å for Bi and Rh, respectively, are expectedly longer for the larger metal. The Rh···Cl distance to the axial CH_2Cl_2 molecule is 2.741(2) Å. The bond distances in the related $Rh_2(TPA)_4$•2 CH_2Cl_2 complex[24] are 2.3708(5), 2.033[3] and 2.651[1] Å for Rh–Rh, Rh–O$_{av}$, and Rh···Cl$_{av}$, respectively (Table 3.3). Although the M–M distance appears longer in **1**•CH_2Cl_2, the

formal shortness ratio (FSR)[1,25] is calculated to be 0.917 for **1**•CH_2Cl_2 compared to 0.948 for the

$Rh_2(TPA)_4$•2 CH_2Cl_2, suggesting a stronger M–M bond in the heterobimetallic complex. This

added bond strength is likely attributed to increased polarization and ionic character of the M–M

bond not present in the homobimetallic complex. The Bi–Rh, Bi–O and Rh–O bond lengths for

1•CH_2Cl_2 lie in the expected regions of 2.53 - 2.57, 2.32 - 2.60 and 2.02 - 2.04 Å, respectively, for

tetrabridged BiRh carboxylate complexes.[11-13]

Table 3.3. Experimental bond distances (Å) for **1**•CH_2Cl_2 and $Rh_2(TPA)_4$•2 CH_2Cl_2[24]

Compound	**1**•CH_2Cl_2	$Rh_2(TPA)_4$•2 CH_2Cl_2
M–Rh	2.5326(3)	2.3708(5)
Rh–O_{av}	2.028[4]	2.033[3]
Bi–O_{av}	2.358[5]	–
Rh⋯Cl	2.741(2)	2.651[1]

3.4.3 Electrochemical Properties

Dirhodium tetracarboxylate complexes show characteristic redox waves for the $[Rh_2]^{4+/5+}$

couple; however, electrochemical properties of BiRh compounds have not previously been

investigated.[6] A high band gap is indicated for the complexes due to their pale yellow color, and

thus redox events are not predicted to be very accessible. The cyclic voltammograms (CVs) of

1 - **4** are shown in Figure 3.2. The CVs were measured in 0.1 M tetrabutylammonium

hexafluorophosphate (TBAH)/CH_2Cl_2. All complexes display an irreversible $[BiRh]^{3+/4+}$ couple at

highly negative potentials, E_{pc} = −1.50 V, −1.45 V, −1.44 V, and −1.43 V *vs* ferrocene/ferrocenium

(Fc/Fc$^+$) for **1** - **4**, respectively. This reduction becomes more reversible upon faster scan rates,

suggesting a fast chemical change following electron transfer for all complexes (see SI Figure

3.7). The complexes also display an irreversible $[BiRh]^{4+/5+}$ couple at positive potentials,

E_{pa} = 1.31 V, 1.30 V, and 1.34 V *vs* Fc/Fc$^+$ for **2** - **4**, respectively. The $[BiRh]^{4+/5+}$ couple of **4** is

shifted by 0.54 V to higher potential *vs* the analogous $Rh_2(esp)_2$ complex, which shows a reversible redox couple at $E_{1/2}$ = 0.80 V *vs* Fc/Fc[+] (Table 3.4).[26] All of the complexes are stable across a wide range of potentials. This redox stability could be advantageous in catalysis requiring harsh oxidative or reductive conditions.
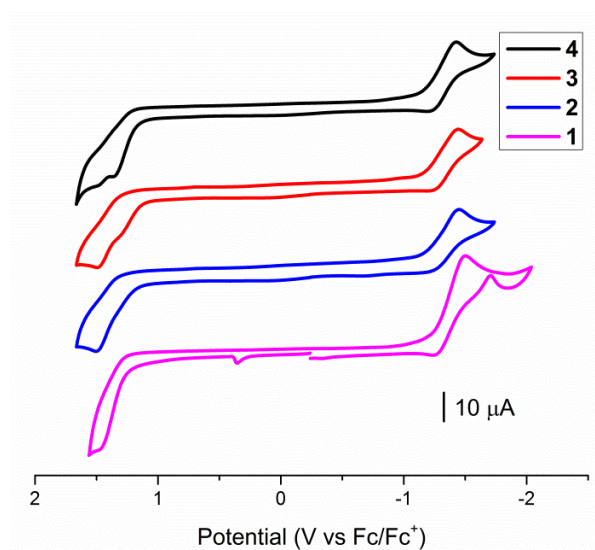
Figure 3.2. Cyclic voltammograms of **1** - **4** in CH_2Cl_2 with scan rate = 100 mv/s (0.1 M TBAH).

Table 3.4. Comparison of electrochemical data for compounds **1** – **4**,[a] $Rh_2(OAc)_4$[27] and $Rh_2(esp)_2$.[26]

Compound	$[MRh]^{3+/4+}$ E_{pc} (V)	$[MRh]^{4+/5+}$ E_{pa} (V)	Reference
1	−1.50	1.46	This work
2	−1.45	1.49	This work
3	−1.44	1.30	This work
4	−1.43	1.34	This work
$Rh_2(OAc)_4$	–	0.77	27
$Rh_2(esp)_2$	–	0.80	26

[a]All potentials are *vs* Fc/Fc[+] in CH_2Cl_2.

3.5 Conclusions

Carboxylate exchange is a viable synthetic method for BiRh tetracarboxylate compounds. Five novel heterobimetallic BiRh compounds, $BiRh(TPA)_4$, $BiRh(but)_4$, $BiRh(piv)_4$, $BiRh(esp)_2$, and $BiRh(OAc)_4$ have now been prepared from the equatorial ligand exchange reaction of $BiRh(TFA)_4$. These complexes have doubled the library of known heterobimetallic BiRh carboxylate complexes and are the first examples that contain no perfluorinated ligands. This is also the first example of solution phase equatorial ligand exchange from $BiRh(TFA)_4$ leading to the synthesis of novel homoleptic BiRh carboxylate complexes. This synthetic advance should enable the rapid derivatization of the BiRh core to include numerous ligands of interest (not just carboxylates) used in applications such as catalysis. Routes to these complexes along with exploration of their catalytic activity are currently underway in our laboratory.

3.6 Acknowledgments

3.7 Supplemental Information
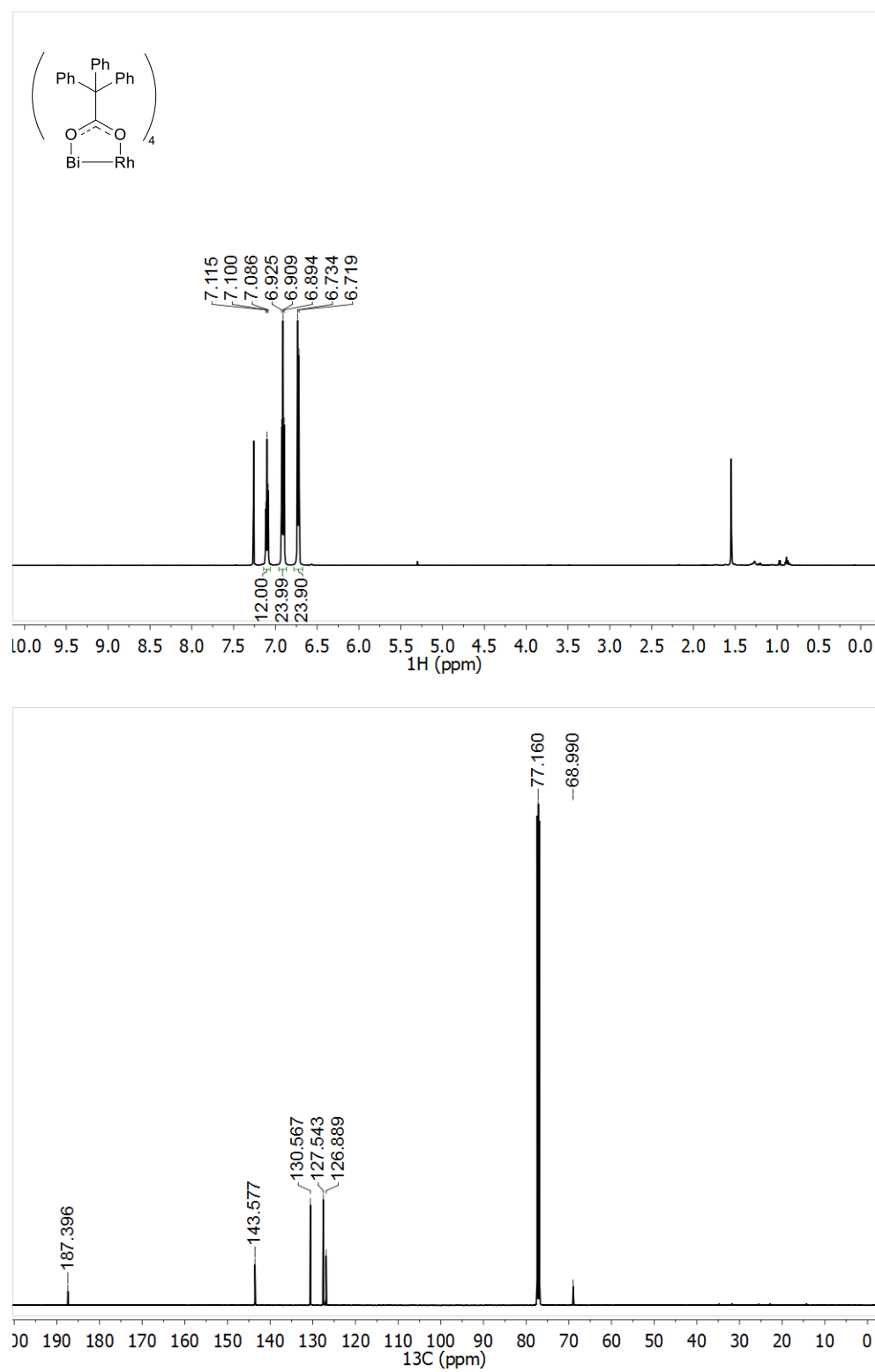
Figure 3.3. NMR spectra of **1** in CDCl₃ at room temperature (¹H (top), ¹³C{¹H} (bottom)).
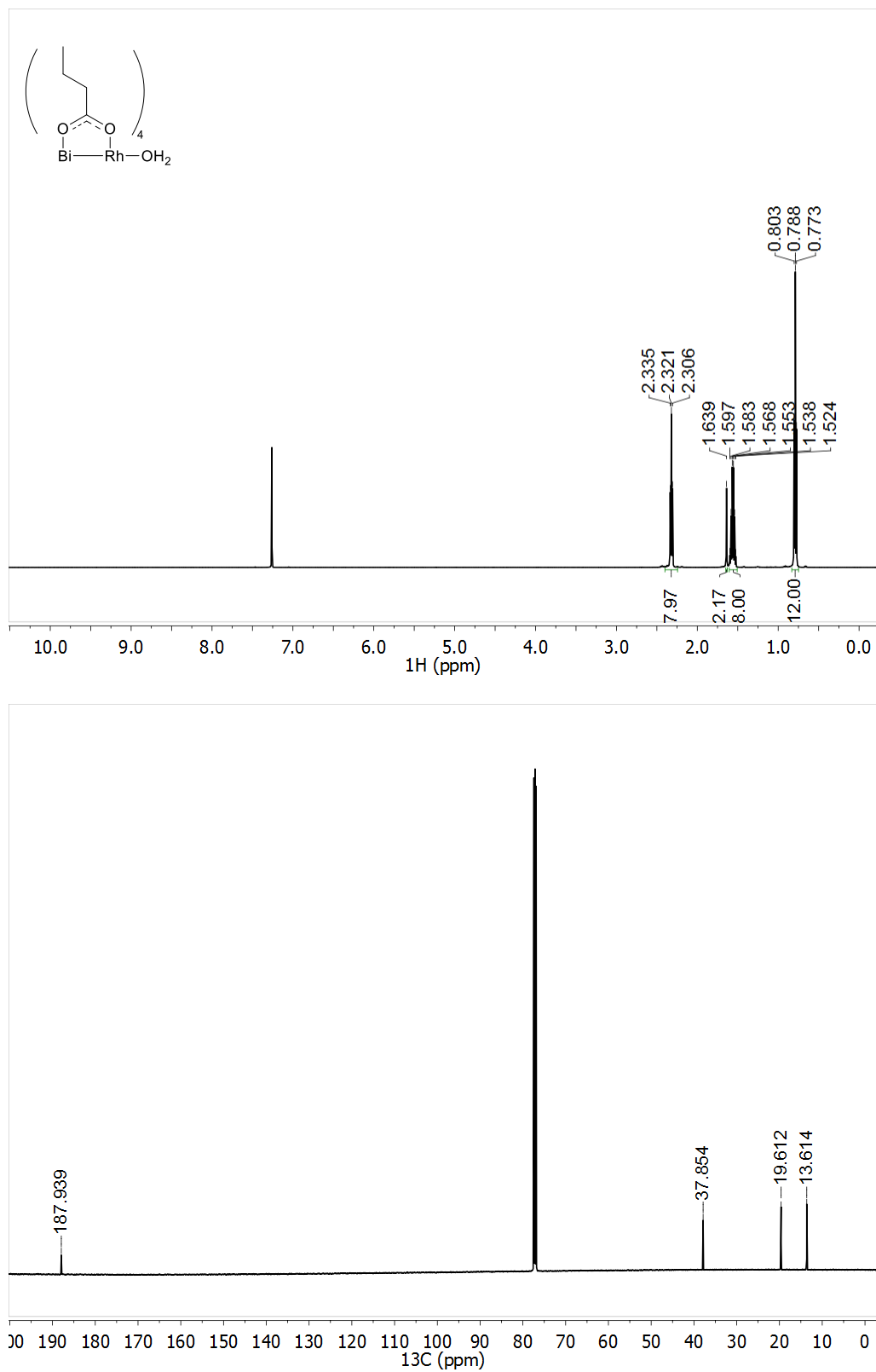
Figure 3.4. NMR spectra of **2** in CDCl₃ at room temperature (¹H (top), ¹³C{¹H} (bottom)).

Figure 3.5. NMR spectra of **3** in CDCl₃ at room temperature (¹H (top), ¹³C{¹H} (bottom)).
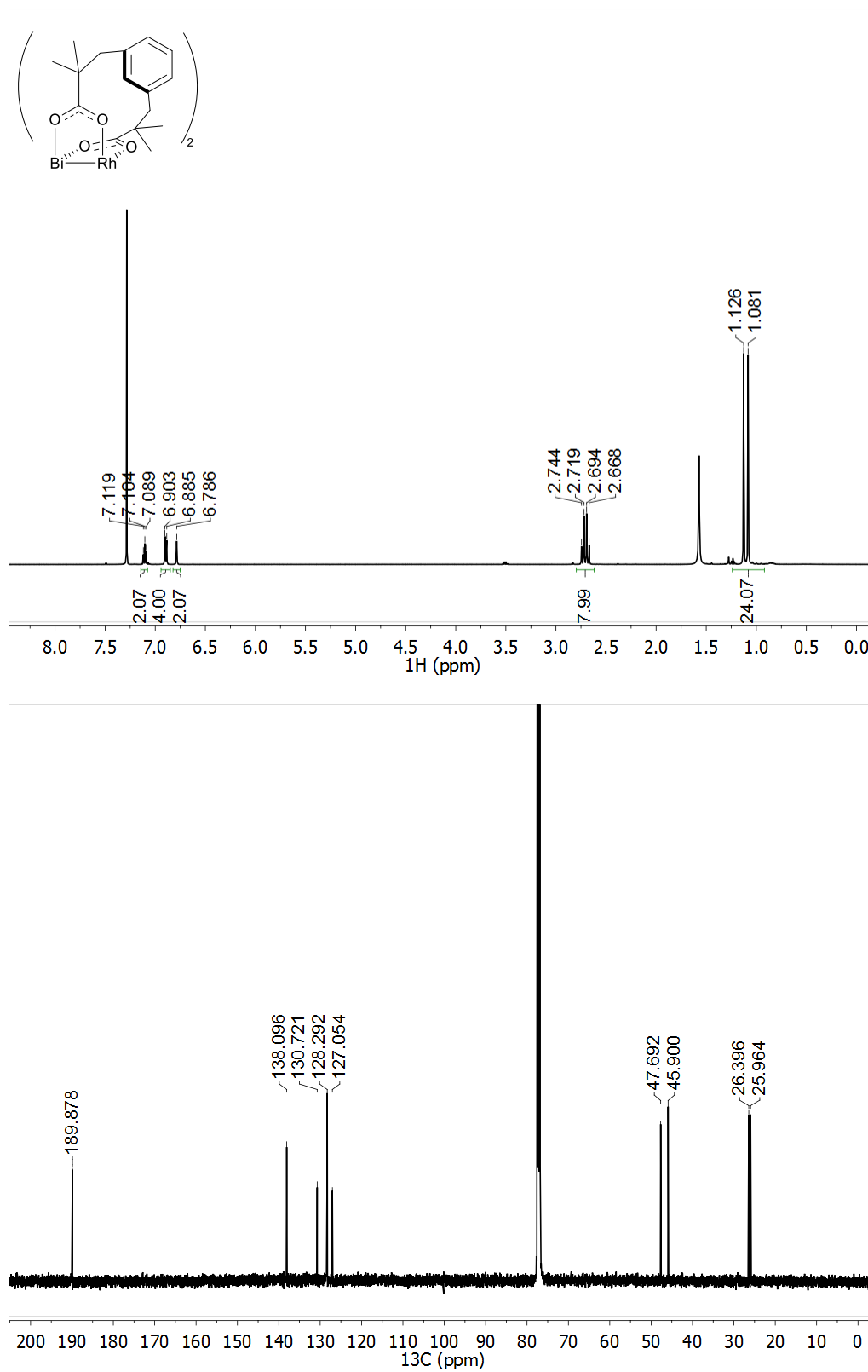
Figure 3.6. NMR spectra of **4** in CDCl$_3$ at room temperature (^{1}H (top), ^{13}C{^{1}H} (bottom)).
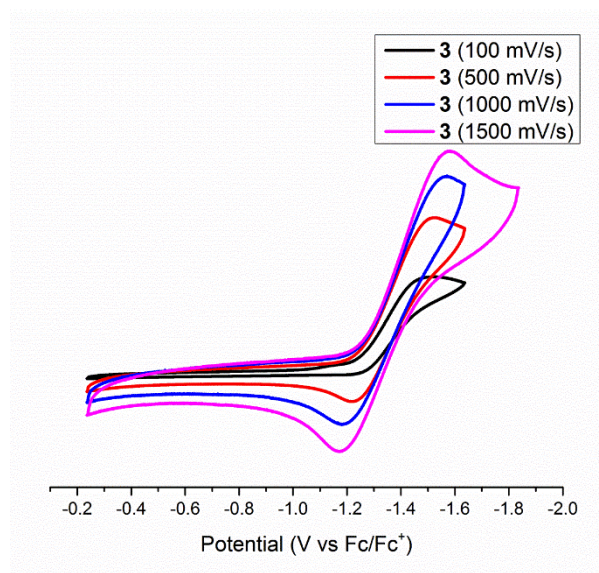
Figure 3.7. Cyclic voltammograms of **3** in CH_2Cl_2 with scan rate = 100, 500, 1000 and 1500 mV/s

(0.1 M TBAH).

Table 3.5. Selected bond distances (Å) and angles (°) for **1**•CH_2Cl_2.

Bi1–Rh1	2.5326(3)	O2–Bi1–Rh1	80.21(9)
Rh1–O1	2.022(3)	O4–Bi1–Rh1	80.39(9)
Rh1–O3	2.029(3)	O6–Bi1–Rh1	79.28(9)
Rh1–O5	2.024(3)	O8–Bi1–Rh1	79.69(9)
Rh1–O7	2.035(3)	O1–Rh1–Bi1	92.16(9)
Bi1–O2	2.365(4)	O3–Rh1–Bi1	91.99(9)
Bi1–O4	2.355(4)	O5–Rh1–Bi1	92.91(9)
Bi1–O6	2.379(4)	O7–Rh1–Bi1	92.33(9)
Bi1–O8	2.332(4)	Bi1–Rh1–Cl1	177.69(5)
Rh1–Cl1	2.741(2)		

3.8 References

(1)   Cotton, F. A.; Murillo, C. A.; Walton, R. A. *Multiple Bonds Between Metal Atoms*; 3rd ed., Springer Science and Business Media, Inc., New York, **2005**, 465-467.

(2)   Chisholm, M. H.; Macintosh, A. M. *Chem. Rev.* **2005**, *105*, 2949.

(3)   Hansen, J.; Davies, H. M. L. *Coord. Chem. Rev.* **2008**, *252*, 545.

(4)   Davies, H. M. L.; Denton, J. R. *Chem. Soc. Rev.* **2009**, *38*, 3061.

(5)   Doyle, M. P.; Duffy, R.; Ratnikov, M.; Zhou, L. *Chem. Rev.* **2010**, *110*, 704.

(6)   Kornecki, K. P.; Berry, J. F.; Powers, D. C.; Ritter, T. *Prog. Inorg. Chem.* **2014**, *58*, 225.

(7)   Che, C. M.; Lo, V. K. Y.; Zhou, Y. C. *Comprehensive Organic Synthesis II*, 2nd ed. Knochel, P. Elsevier, Amsterdam, 2, **2014**, 26.

(8)   Davies, H. M. L.; Beckwith, R. E. J. *Chem. Rev.* **2003**, *103*, 2861.

(9)   Doyle, M. P. *Chem. Rev.* **1986**, *86*, 919.

(10)   Doyle, M. P.; Forbes, D. C. *Chem. Rev.* **1998**, *98*, 911.

(11)   Dikarev, E. V.; Gray, T. G.; Li, B. *Angew. Chem., Int. Ed.* **2005**, *44*, 1721.

(12)   Dikarev, E. V.; Li, B.; Zhang, H. *J. Am. Chem. Soc.* **2006**, *128*, 2814.

(13)   Filatov, A. S.; Napier, M.; Vreshch, V. D.; Sumner, N. J.; Dikarev, E. V.; Petrukhina, M. A. *Inorg. Chem.* **2012**, *51*, 566.

(14)   Hansen, J.; Li, B.; Dikarev, E.; Autschbach, J.; Davies, H. M. L. *J. Org. Chem.* **2009**, *74*, 6564.

(15)   Espino, C.; Fiori, K. W.; Kim, M.; Du Bois, J. *J. Am. Chem. Soc.* **2004**, *126*, 15378.

(16)   Bruker-AXS, *SMART* Program, Madison, Wisconsin, USA, **2009**.

(17)   Sheldrick, G. *Acta Crystallogr. A.* **2008**, *64*, 112.

(18)   Dolomanov, O. V. B.; Bourhis, L. J.; Gildea, R. J.; Howard, J. A. K.; Puschmann, H. *J. Appl. Crystallogr.* **2009**, *42*, 339.

(19)   Garner, C. D.; Senior, R. G. *J. Chem. Soc., Chem. Commun.* **1974**, 580.

(20) ^{1}H NMR (CDCl$_3$, 400 MHz, ppm) δ 7.20 (t, J = 7.2 Hz, 2H), 7.15 (t, J = 7.2 Hz, 1H), 7.11 (t, J = 7.2 Hz, 4H), 7.00 (t, J = 7.2 Hz, 2H), 6.84 (d, J = 7.2 Hz, 6H), ^{19}F{^{1}H} NMR (CDCl$_3$, 376.5 MHz, ppm) δ 72.5 (s).

(21)   Doyle, M. P.; Raab, C. E.; Roos, G. H. P.; Lynch, V.; Simonsen, H. S. *Inorg. Chim. Acta* **1997**, *266*, 13.

(22)   Tu, Q.; Wang, T.; Welch, C. J.; Wang, P.; Jia, X.; Raab, C.; Bu, X.; Bykowski, D.; Hohenstaufen, B.; Doyle, M. P. *Anal. Chem.* **2006**, *78*, 1282.

(23)   Warzecha, E.; Berto, T. C.; Berry, J. F. *Inorg. Chem.* **2015**, *54*, 8817.

(24)   Kornecki, K. P.; Briones, J. F.; Boyarskikh, V.; Fullilove, F.; Autschbach, J.; Schrote, K. E.; Lancaster, K. M.; Davies, H. M. L.; Berry, J. F. *Science* **2013**, *342*, 351.

(25)   Pyykkö, P.; Atsumi, M. *Chem. Eur. J.* **2009**, *15*, 186.

(26)   Kornecki, K. P.; Berry, J. F. *Chem. Eur. J.* **2011**, *17*, 5827.

(27)   Zhu, T. P.; Ahsan, M. Q.; Malinski, T.; Kadish, K. M.; Bear, J. L. *Inorg. Chem.* **1984**, *23*, 2.

Chapter 4

The First Bismuth(II)–Rhodium(II) Oxypyridinate Paddlewheel Complexes:

Synthesis and Structural Characterization

This chapter is adapted from "The First Bismuth(II)–Rhodium(II) Oxypyridinate Paddlewheel Complexes: Synthesis and Structural Characterization", a published manuscript:

Department of Chemistry, University of Wisconsin–Madison, 1101 University Avenue, Madison, WI 53706, United States

4.1 Abstract

The first examples of heterobimetallic Bi–Rh bonded complexes supported by heteroatom ligands have been synthesized and structurally characterized. BiRh(hp)$_4$ (**1**) and BiRh(chp)$_4$ (**2**) each adopt a [4,0]$_O$ polar geometry with Bi–Rh bond distances of 2.5409(4) and 2.5848(1) Å, respectively (hp = 2-hydroxypyridine, chp = 6-chloro-2-hydroxypyridine). The relative oxophilicity of bismuth compared to rhodium clearly influences the selective formation of the [4,0]$_O$ arrangement, especially for the sterically crowded **2**.

4.2 Introduction

Recently, the chemistry of heterometallic coordination compounds containing direct metal–metal bonds has been of significant interest.[1-6] The field of heterobimetallic M–M bonded complexes of rhodium was first established in 2005, with the synthesis of BiRh(O$_2$CCF$_3$)$_4$ by Dikarev and coworkers.[7] Several other BiRh carboxylates have since been synthesized by gas-phase,[8] or solution-phase BiRh-core formation,[9] as well as carboxylate exchange methods on BiRh(O$_2$CCF$_3$)$_4$.[10] We were curious to learn whether a heterobimetallic BiRh complex could be supported by non-carboxylate ligands, such as oxypyridinates. An ideal ligand class to test was the 6-X-oxypyridinates (X = H, Cl), which have been well established in supporting M–M bonded complexes of Rh,[11] Cr, Mo, and W.[12] The 6-methyl-oxypyridinate (mhp) ligand has been used to support a Mo≡W quadruply-bonded compound.[13] Moreover, the 6-Cl-oxypyridinate ligand (chp) has been investigated by us for its ability to support Ru$_2$ complexes relevant to N–atom transfer chemistry.[14-16]

Homoleptic M–M bonded paddlewheel complexes supported by 6-X-oxypyridinates as well as other (N, O) donor groups have considerable structural diversity.[17] The four possible geometric isomers for homobimetallic complexes supported by (N, O) donor groups are designated as [4,0] (where four oxygen atoms bind to one metal center and four nitrogen atoms bind to the other metal center), [3,1], *cis*-[2,2] and *trans*-[2,2] (Scheme 4.1, top). Upon

changing to a heterobimetallic complex, six possible geometric isomers exist, designated as $[4,0]_X$ (where the numbers in brackets have the same meaning as above, but where the subscript X denotes the majority donor atom that binds to the metal center with the highest atomic number), $[3,1]_X$, *cis*-[2,2] and *trans*-[2,2] (Scheme 4.1, bottom).

Homobimetallic:

| [4,0] | [3,1] | *cis*-[2,2] | *trans*-[2,2] |

Heterobimetallic:

| $[4,0]_N$ | $[4,0]_O$ | $[3,1]_N$ | $[3,1]_O$ | *cis*-[2,2] | *trans*-[2,2] |
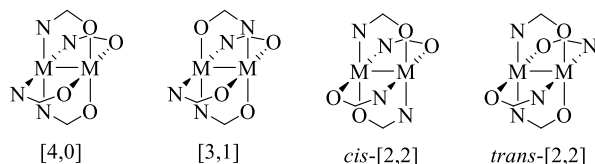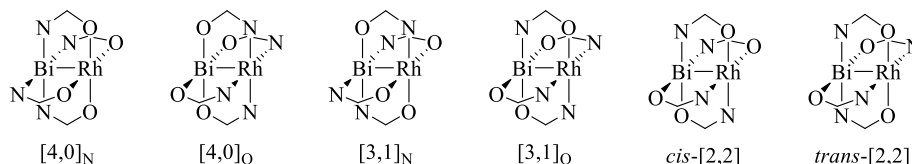
Scheme 4.1. The four possible geometric isomers of a homobimetallic M_2 complex (top), and the six possible geometric isomers of a heterobimetallic M_2 complex (bottom, BiRh shown) supported by an asymmetric bridging ligand ((O, N) shown).

The preferred orientation of the ligands around the M–M core for homobimetallic complexes is generally thought to be driven by the steric profile of the ligands since there is no electronic difference between the metal centers.[18] This consideration nicely explains why the *trans*-[2,2] isomer is most often preferred for 6-X-oxypyridinates.[17] The *trans*-[2,2] isomer is also observed for MoW(mhp)$_4$, the only other prior example of a heterobimetallic oxypyridinate compound, reflecting a steric rather than electronic driving force for the regioselectivity of ligand substitution.[13] We report below the synthesis, characterization and structures of the first Bi–Rh bonded complexes supported by mixed atom donor ligands, in which the steric and electronic discretions must compete to find the preferred geometry.

4.3 Experimental Section

4.3.1 Physical Measurements

All reactions were carried out using oven dried glassware under a dry N_2 atmosphere using Schlenk techniques and glovebox methods. Toluene was purified using a Vacuum Atmospheres solvent purification system. $BiRh(TFA)_4$ (TFA = trifluoroacetate) was prepared according to literature procedures.[9] Dichloromethane (DCM), diethyl ether (Et_2O), hexane, methanol (MeOH), chloroform-*d* ($CDCl_3$), potassium carbonate (K_2CO_3), and 2-hydroxypyridine (hp) were purchased from Sigma-Aldrich and used without further purification. The ligand 6-chloro-2-hydroxypyridine (chp) was purchased from Sigma-Aldrich and recrystallized from hot hexane prior to use. ^{1}H and ^{13}C{^{1}H} NMR spectra were recorded on a Bruker Avance-500 MHz spectrometer at 500 and 125 MHz, respectively. ^{1}H and ^{13}C{^{1}H} NMR shifts were referenced to residual solvent. [1]H splitting patterns were designated as doublet of doublets (dd) and doublet of doublet of doublets (ddd). Elemental analysis was carried out by Midwest Microlab, LLC, Indianapolis, IN. IR spectra were taken on a Bruker Tensor 27 FTIR spectrometer using an attenuated total reflectance (ATR) adapter. Mass spectra were obtained at the Paul Bender Chemical Instrumentation Center of the Chemistry Department of the University of Wisconsin–Madison using a Thermo Q Exactive™ Plus ESI-MS. Cyclic voltammetry was performed in 10 mL DCM solutions containing 0.1 M tetrabutylammonium hexafluorophosphate (TBAH) with 1 mM analyte. The electrodes consisted of a glassy carbon working electrode, a reference electrode made of a silver wire in a 10 mM $AgNO_3$ solution contained by a Vycor tip and an auxiliary electrode of platinum wire. All cyclic voltammograms were referenced to the ferrocene/ferrocenium (Fc/Fc^+) redox couple.

[4,0]$_O$-BiRh(hp)$_4$ (1). Solid $BiRh(TFA)_4$ (42.1 mg, 0.0551 mmol) and 2-hydroxypyridine (41.9 mg, 0.440 mmol) were combined in a 25 mL Schlenk flask and suspended in 15 mL toluene. The yellow suspension was heated to reflux through a soxhlet

extractor (K_2CO_3 in the thimble) at 145 °C using an oil bath for 17 h, during which a yellow precipitate formed. After cooling to room temperature, the solvent was removed *in vacuo*. The yellow solid was washed with H_2O, MeOH, hexane and dried under reduced pressure resulting in a yellow solid. Yield: 34.0 mg, 89.7%. X-ray quality crystals of **1**•0.79 H_2O were obtained by layering a concentrated DCM solution of **1** with hexane. Anal. Calcd $BiRhC_{20}H_{16}O_4N_4$: C 34.9, H 2.3, N 8.1. Found: C 35.1, H 2.3, N 8.1. ESI-MS (positive ion, MeOH): *m/z* 689.01 ([M+H]$^+$). ^{1}H NMR (CDCl$_3$, 500 MHz, ppm): δ 8.35 (dd, *J* = 6.0 Hz, 1.8 Hz, 4H) 7.56 (ddd, *J* = 8.5 Hz, 6.8 Hz, 1.8 Hz, 4H), 6.39 (dd, *J* = 8.5 Hz, 1.3 Hz, 4H), 6.36 (ddd, *J* = 6.8 Hz, 6.0 Hz, 1.3 Hz, 4H). ^{13}C{^{1}H} NMR (CDCl$_3$, 125 MHz, ppm): δ 169.6, 144.0, 138.8, 116.0, 112.6. IR (ATR, cm^{-1}): 1611 (s), 1550 (w), 1486 (s), 1466 (m), 1432 (s), 1343 (s), 1275 (w), 1148 (w), 1115 (w), 1023 (w), 944 (w), 854 (s), 789 (s), 771 (s), 740 (m), 650 (w).

[4,0]$_O$-BiRh(chp)$_4$ (**2**). Solid BiRh(TFA)$_4$ (34.3 mg, 0.0449 mmol) and 6-chloro-2-hydroxypyridine (47.5 mg, 0.0.367 mmol) were combined in a 25 mL Schlenk flask and suspended in 15 mL toluene. The yellow suspension was heated to reflux through a soxhlet extractor (K_2CO_3 in the thimble) at 145 °C using an oil bath for 14 h. After cooling to room temperature, the solvent was removed in vacuo. The yellow solid was washed with Et$_2$O and hexane, extracted into DCM and filtered through a medium porosity glass frit. The solvent was removed in vacuo, resulting in a yellow solid. Yield: 29.4 mg, 79.3%. X-ray quality crystals of **2** were obtained by layering a concentrated DCM solution of **2** with hexane. Anal. Calcd $BiRhC_{20}H_{12}O_4N_4Cl_4$ • 0.5 DCM : C 28.3, H 1.5, N 6.5. Found: C 28.3, H 2.1, N 6.4. ESI-MS (positive ion, MeOH): *m/z* 824.85 ([M+H]$^+$). ^{1}H NMR (CDCl$_3$, 500 MHz, ppm): δ 7.35 (dd, *J* = 8.4 Hz, 7.4 Hz, 4H), 6.53 (dd, *J* = 7.4 Hz, 1.1 Hz, 4H), 6.30 (dd, *J* = 8.4 Hz, 1.1 Hz, 4H). ^{13}C{^{1}H} NMR (CDCl$_3$, 125 MHz, ppm): δ 171.0, 149.1, 139.3, 113.8, 113.0. IR

(ATR, cm^{-1}): 1600 (s), 1532 (m), 1462 (s), 1437 (s), 1389 (m), 1354 (m), 1206 (w), 1170 (m), 1015 (m), 929 (m), 918 (m), 877 (w), 785 (s), 729 (m), 707 (s).

4.3.2 Crystallography

Crystallographic data were measured at the Molecular Structure Laboratory of the Chemistry Department of the University of Wisconsin–Madison. Crystals were selected under oil under ambient conditions and attached to the tip of a MiTeGen MicroMount©. Each crystal was mounted in a stream of cold nitrogen at 100(1) K and centered in the X-ray beam using a video camera. The crystal evaluation and data collection were performed on a Bruker Quazar SMART APEX-II diffractometer with Mo Kα (λ = 0.71073 Å) radiation. The data were collected using a routine to survey an entire sphere of reciprocal space and indexed by the SMART program.[19] The structures were solved *via* direct methods (**1**•0.79 H$_2$O) or charge flipping (**2**) and refined by iterative cycles of least-squares refinement on F^2 followed by difference Fourier synthesis.[20,21] All H-atoms were included in the final structure factor calculation at idealized positions and allowed to ride on the neighboring atoms with relative isotropic displacement coefficients. Single crystals of both **1**•0.79 H$_2$O and **2** suitable for structural determination were obtained by slow diffusion of hexane into a dichloromethane solution of **1** and **2**, respectively.

4.4 Results and Discussion

4.4.1 Synthesis and Characterization

Homobimetallic M–M bonded complexes supported by oxypyridinate ligands can adopt one of four isomers that is expanded to six isomers for heterobimetallic M–M' bonded complexes, as described above. Much to our surprise, the ^{1}H NMR spectra of the crude reaction mixtures of both **1** and **2** were quite clean indicating the formation of a single isomer in each case. Complete ligand exchange was observed for both **1** and **2** by refluxing a

toluene solution of BiRh(TFA)$_4$ with excess ligand through a soxhlet extractor containing K$_2$CO$_3$, as evidenced by silent ^{19}F{^{1}H} NMR spectra.[10] The crude ^{1}H NMR spectrum of **1** contained only the signals for the excess free ligand and one new set of aryl resonances belonging to a mono-substituted pyridine ring. The ^{1}H NMR spectrum of purified **1** in CDCl$_3$ is well resolved with hydrogen atom signals at 8.35 (dd), 7.56 (ddd), 6.39 (dd) and 6.36 ppm (ddd). The observation of only one set of new signals suggested a highly symmetric geometry around the BiRh core, consistent with either the [4,0]$_O$ (where all four O-atoms are bound to the Bi-atom and all four N-atoms are bound to the Rh-atom) or [4,0]$_N$ isomer (where all four N-atoms are bound to the Bi-atom and all four O-atoms are bound to the Rh-atom). Likewise, the crude ^{1}H NMR spectrum from the reaction to form **2** contained only one new set of pyridine aryl resonances, suggesting either the [4,0]$_O$ or [4,0]$_N$ structure. The ^{1}H NMR spectrum of **2** in CDCl$_3$ is well resolved with H-atom signals at 7.35 (dd), 6.53 (dd), and 6.30 ppm (dd). The cyclic voltammogram of **2** (see SI Figure 4.3) is similar to known BiRh carboxylate complexes with irreversible redox couples at E_{pc} = –1.52 V and E_{pa} = 1.12 V *vs* Fc/Fc$^+$ for the [BiRh]$^{3+/4+}$ and [BiRh]$^{4+/5+}$ couples, respectively.[10]

4.4.2 Crystal Structures

The asymmetric unit of the orthorhombic *Pbcn* crystal of **1**•0.79 H$_2$O contains one half molecule of BiRh(hp)$_4$ and a partially occupied water molecule bound axially to the Rh-atom that lies on a two-fold axis within the unit cell. The molecular structure of **1** (Figure 4.1), determined by single-crystal X-ray crystallography, and the summary of crystallographic data are provided in Table 4.1. The structure of **1**•0.79 H$_2$O clearly shows the geometry to be the [4,0]$_O$ isomer with the Rh center in an octahedral environment bound to four N-atoms equatorially and capped by the Bi-atom and O-atom from the water molecule, which is only partially occupied. The Bi center lies in a distorted square pyramidal geometry bound equatorially by four O-atoms and capped by the Rh-atom. The Bi–Rh

distance in **1** is 2.5409(4) Å and the average Bi–O and Rh–N bond distances are 2.343[4] and 2.065[4] Å, respectively (Table 4.2). The axial water molecule in **1** has an Rh–O distance of 2.421(4) Å, which is longer than the axial water molecule distance of 2.352(2) Å in the homobimetallic *cis*-[2,2]-$Rh_2(HNCOCH_3)_4(H_2O)$.[22] The equatorial ligands also experience a considerable twisting about the M–M axis with an average torsion angle of 18.4[4]° for O–Bi–Rh–N.
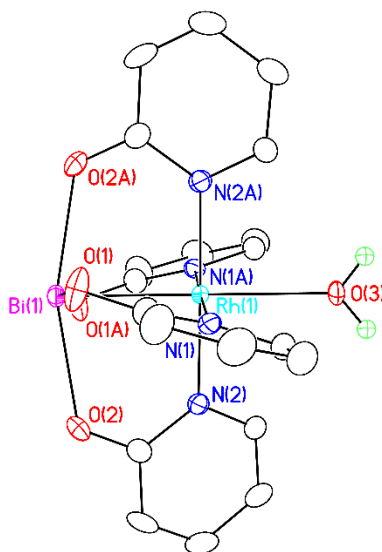
Figure 4.1. X-ray crystal structure of **1**•0.79 H_2O, with thermal ellipsoids drawn at the 50% probability level. All hydrogen atoms except those of the H_2O molecule have been omitted for clarity.

The asymmetric unit of the triclinic $P\bar{1}$ crystal structure of **2** contains two BiRh complexes and one molecule of DCM. The molecular structure of **2** (Figure 4.2), determined by single-crystal X-ray crystallography, and the summary of crystallographic data are provided in Table 4.1.

Table 4.1. Crystallographic data for **1**•0.79 H_2O and **2** at 100 K.

Identification code	**1** • 0.79 H_2O	**2**
Empirical formula	Bi Rh C_{20} $H_{17.58}$ $O_{4.79}$ N_4	Bi_2 Rh_2 C_{41} H_{26} O_8 N_8 Cl_{10}
Formula weight	702.49	1736.98
Temperature	100(1) K	100(1) K
Wavelength	0.71073 Å	0.71073 Å
Crystal system	Orthorhombic	Triclinic
Space group	*Pbcn*	$P\bar{1}$
Unit cell dimensions	a = 8.8897(4) Å	a = 12.6952(3) Å
	b = 12.6012(5) Å	b = 14.1407(3) Å
	c = 18.5811(8) Å	c = 15.7194(3) Å
	α = 90°	α = 87.4813(9)°
	β = 90°	β = 68.0769(8)°
	γ = 90°	γ = 71.1407(9)°
Volume	2081.5(2) $Å^3$	2467.84(9) $Å^3$
Z	4	2
Density (calculated)	2.242 g/cm^3	2.338 g/cm^3
Crystal size	0.205 x 0.100 x 0.057 mm^3	0.236 x 0.212 x 0.122 mm^3
Data / restraints / parameters	1923 / 1 / 151	18240 / 0 / 640
Goodness-of-fit on F^2	1.317	1.032
Final R[a,b] indices [$I>2\sigma(I)$]	R_1 = 0.0146, wR_2 = 0.0335	R_1 = 0.0157, wR_2 = 0.0357
R indices (all data)	R_1 = 0.0178, wR_2 = 0.0347	R_1 = 0.0173, wR_2 = 0.0361

[a]$R_1 = \Sigma||F_0| - |F_c||/\Sigma|F_0|$

[b]$wR_2 = |[\Sigma[w(F_0^2 - F_c^2)^2] / \Sigma[w(F_0^2)^2]]1/2$, w = $1/\sigma^2 (F_0^2) + (aP)^2 + bP$, where P = [max(0 or F_0^2) + $2(F_c^2)$]/3.

The structure of **2** clearly shows the geometry to be the $[4,0]_O$ isomer that has all of the Cl-atoms in the vicinity of the Rh center, effectively blocking the Rh-atom from coordinating any axial ligand. The Bi center is in a distorted square pyramidal geometry coordinated by four O-atoms and capped by the Rh-atom. The Rh center lies in a square

pyramidal geometry coordinated by four N-atoms and capped by the Bi-atom. The Bi–Rh distance in **2** is 2.5848(1) Å, significantly elongated compared to the Rh–Rh distance of 2.379(1) Å in the homobimetallic *trans*-[2,2]-Rh$_2$(chp)$_4$ complex (Table 4.2).[11]

Table 4.2. Selected bond distances (Å) and angles (°) for **1**•0.79 H$_2$O and **2**.

	1•0.79 H$_2$O	**2**
M–M	2.5409(4)	2.5848(1)
Bi–O$_{av}$	2.343[4]	2.307[2]
Rh–N$_{av}$	2.065[4]	2.081[3]
Rh–O$_{ax}$	2.421(4)	—
Torsion Angle$_{av}$	18.4[4]	25.9[3]
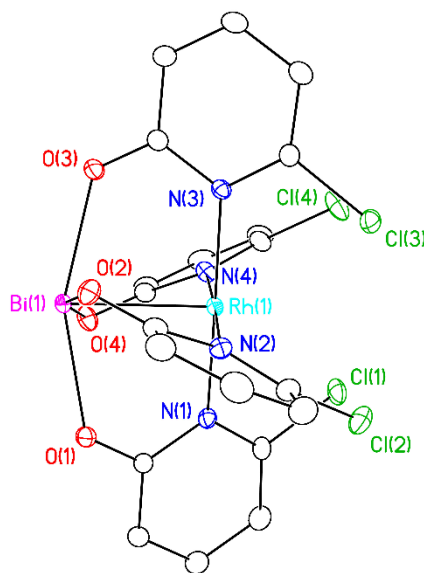
Figure 4.2. X-ray crystal structure of **2**, with thermal ellipsoids drawn at the 50% probability level. Hydrogen atoms and one molecule each of BiRh(chp)$_4$ and CH$_2$Cl$_2$ have been omitted for clarity.

The average Bi–O and Rh–N bond distances are 2.307[2] Å and 2.081[3] Å, respectively. The ligands in **2** also display a twist, having an average torsion angle of 25.9[3]° for O–Bi–Rh–N that is significantly larger than the twist observed in $Rh_2(chp)_4$. Interestingly, complex **2** adopts a $[4,0]_O$ geometry, whereas the homobimetallic complex is found in either the *trans*-[2,2] or the [3,1] geometry, which both alleviate steric repulsion of the Cl-atom attached to the pyridine rings.[11] The formation of the $[4,0]_O$ isomer is clearly driven by the relative oxophilicity of Bi compared to Rh, which is strong enough to overcome the steric crowding experienced by the Cl-atoms. Binding of axial ligands *trans* to a Rh–Rh bond has the effect of slightly elongating the Rh–Rh bond.[23] It is curious to see that, in comparing **1** and **2**, the Bi–Rh bond in **1**, having a partially occupied H_2O axial ligand is ~0.04 Å *shorter* than that in **2**. The Bi–Rh bond contraction in **1** is most likely attributed to the change in equatorial ligand basicity. There is also an ~ 0.02 Å M–M bond contraction in the related homobimetallic complexes *trans*-[2,2]-$Rh_2(mhp)_4$ and *trans*-[2,2]-$Rh_2(chp)_4$ when replacing a chlorine atom with a methyl group.[11]

4.5 Conclusions

The first heterobimetallic Bi–Rh bonded paddlewheel complexes supported by oxypyridinate ligands have been synthesized in good yields. The ligand exchange reactions from $BiRh(TFA)_4$ are remarkably clean, showing a distinct preference to form only one of the six possible geometric isomers. No other products are observed. The choice of the $[4,0]_O$ orientation of the (N, O) ligand here is clearly electronic, different from the related homobimetallic Rh_2 complexes, the geometries of which are driven by steric effects. The relative oxophilicity of Bi compared to Rh allows for the selective formation of the $[4,0]_O$ isomers for BiRh complexes of both 6-X-hydroxypyridine (X = H, Cl). This synthetic methodology should allow for the selective formation of other $[4,0]_O$ BiRh complexes with other heteroatom-donor ligands in the near future.

4.6 Acknowledgments

4.7 Supporting Information

Crystallographic data for the structures reported above have been deposited with the Cambridge Crystallographic Data Center as supplementary publication, 1444847-144848.

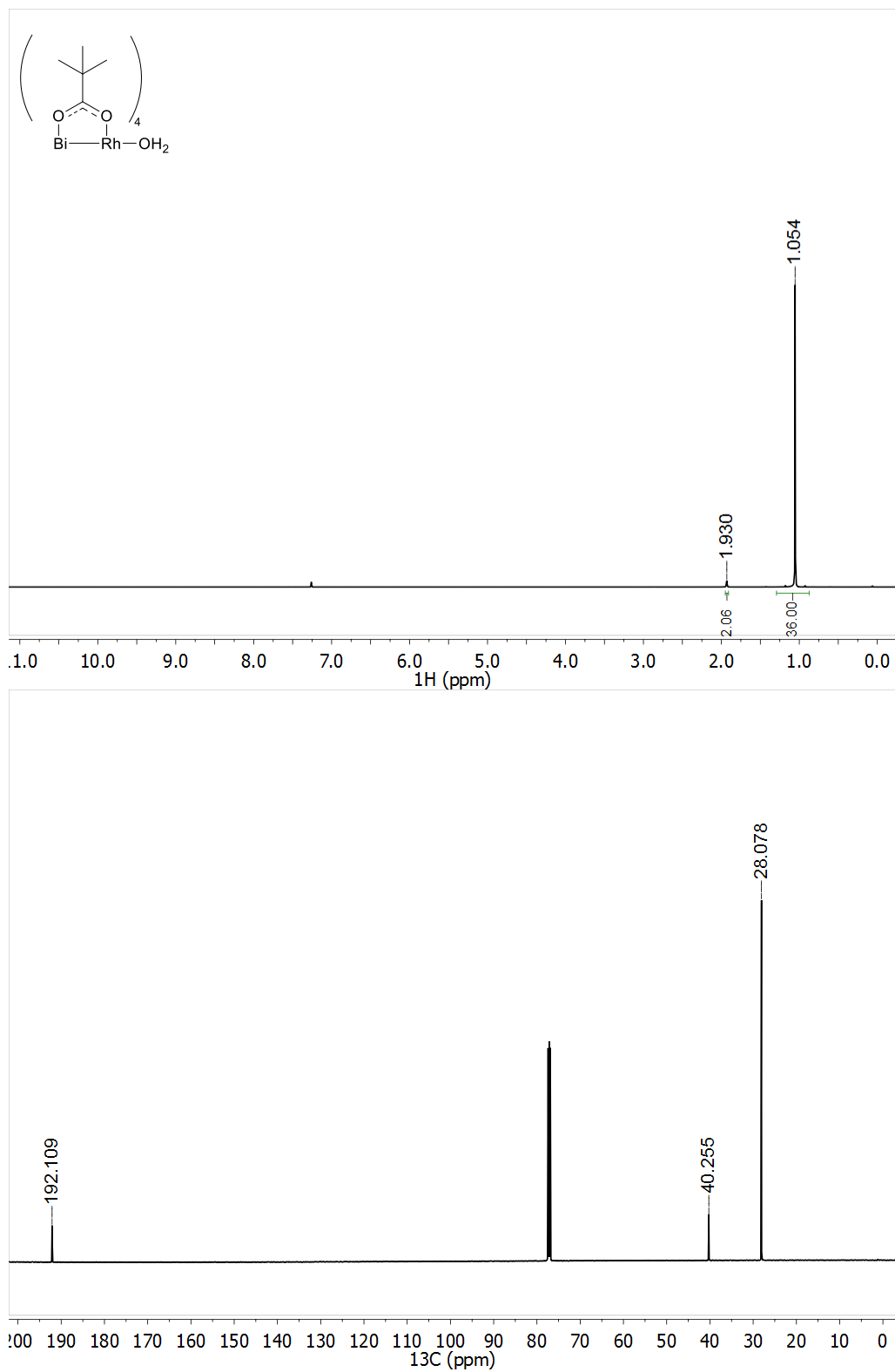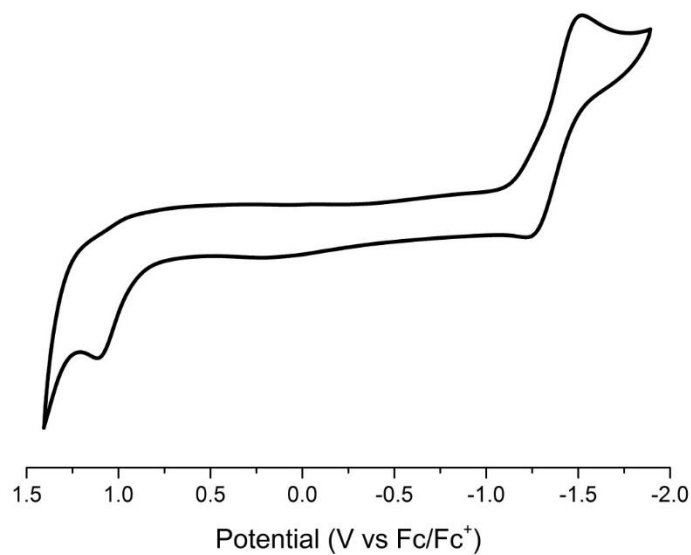**Figure 4.3.** Cyclic voltammogram of **2** in CH_2Cl_2 with scan rate = 100 mV/s (0.1 M TBAH).
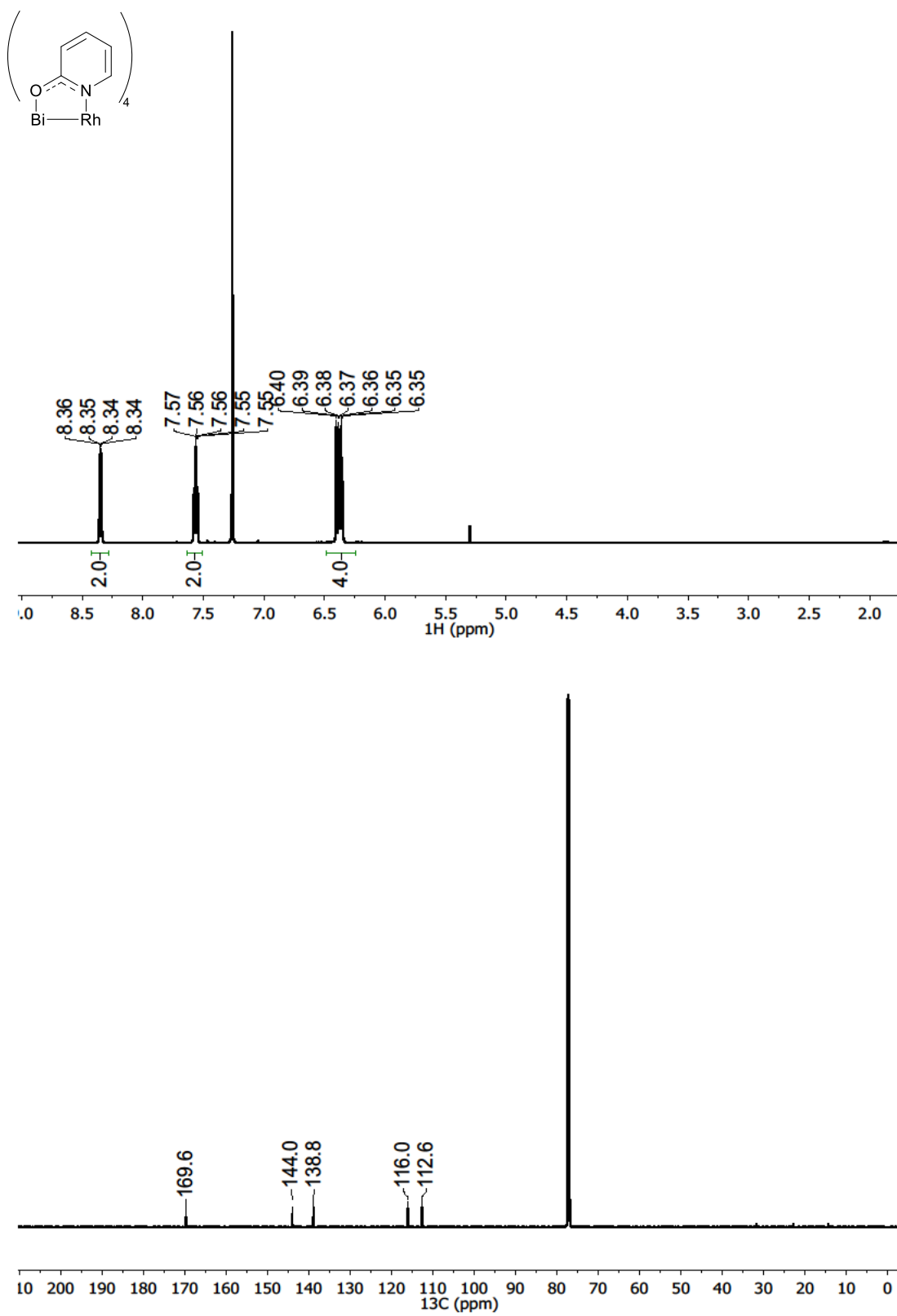
Figure 4.4. NMR spectra of **1** in CDCl₃ at room temperature (¹H (top), ¹³C{¹H} (bottom)).
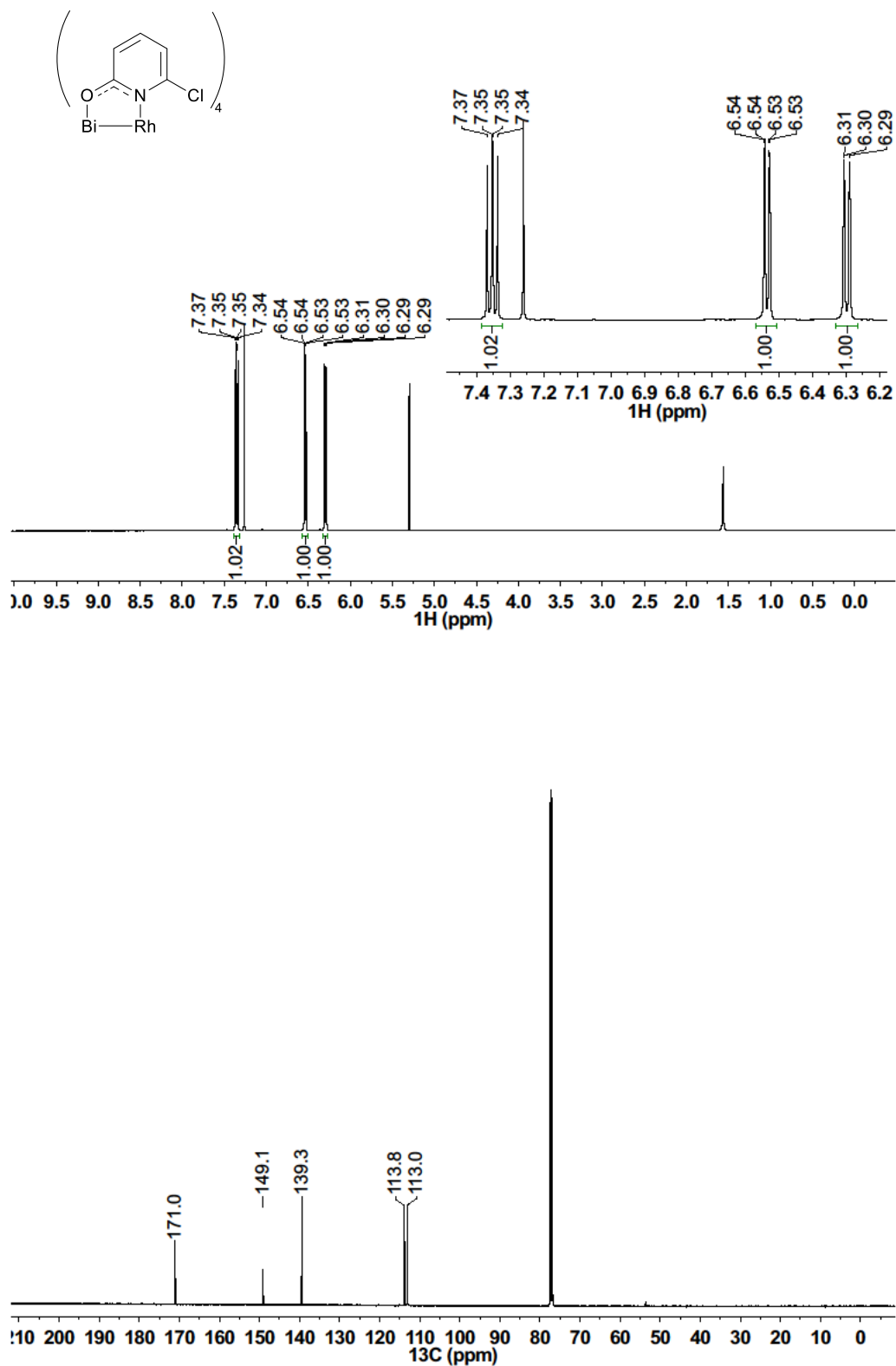
Figure 4.5. NMR spectra of **2** in CDCl₃ at room temperature (^{1}H (top), ^{13}C{^{1}H} (bottom)).

4.8 References

(1)   Berry, J. F. *Structure and Bonding,* Mingos, D. M. P. series ed., Parkin, G. volume ed., **2010**, *136*, 1, Springer, Berlin.

(2)   Buchwalter, P.; Rosé, J.; Braunstein, P. *Chem. Rev.* **2015**, *115*, 28.

(3)   Kuppuswamy, S.; Powers, T. M.; Krogman J. P.; Bezpalko, M. W.; Foxman, B. M.; Thomas. C. M. *Chem. Sci.* **2013**, *4*, 3557.

(4)   Clouston, L. J.; Siedschlag, R. B.; Rudd, P. Planas, N.; Hu, S.; Miller, A. D.; Gagliardi, L.; Lu, C. C. *J. Am. Chem. Soc.* **2013**, *135*, 13142.

(5)   Cooper, B. G.; Napoline, J. W.; Thomas, C. M. *Catal. Rev.* **2012**, *54*, 1.

(6)   Thomas, C. M. *Comments Inorg. Chem.* **2011**, *32*, 14.

(7)   Dikarev, E. V.; Gray, T. G.; Li, B. *Angew. Chem., Int. Ed.* **2005**, *44*, 1721.

(8)   Dikarev, E. V.; Li, B.; Zhang. H. *J. Am. Chem. Soc.* **2006**, *128*, 2814.

(9)   Filatov, A. S.; Napier, M.; Vreshch, V. D.; Sumner, N. J.; Dikarev, E. V.; Petrukhina, M. A. *Inorg. Chem.* **2012**, *51*, 566.

(10)   Sunderland, T. L.; Berry J. F. *Dalton Trans.* **2016**, *45*, 50.

(11)   Cotton, F. A.; Felthouse, T. R. *Inorg. Chem.* **1981**, *20*, 584.

(12)   Cotton, F. A.; Fanwick, P. E.; Niswander, R. H.; Sekutowski, J. C. *J. Am. Chem. Soc.* **1978**, *100*, 4725.

(13)   Cotton, F. A.; Hanson, B. E. *Inorg. Chem.* **1978**, *17*, 3237.

(14)   Corcos, A. R.; Long, A. K. M.; Guzei, I. A.; Berry, J. F. *Eur. J. Inorg. Chem.* **2013**, *2013*, 3808.

(15)   Brown, T. R.; Dolinar, B. S.; Hillard, E. A.; Clérac, R. Berry, J. F. *Inorg. Chem.* **2015**, *54*, 8571.

(16)   Corcos, A. R.; Berry, J. F. *Dalton Trans.* **2016**, *45*, 2386.

(17)   Cotton, F. A.; Murillo, C. A.; Walton, R. A. *Multiple Bonds Between Metal Atoms*, 3rd Ed., Springer Science and Business Media, Inc., New York, **2005**.

(18)   Cotton, F.; Han, S.; Wang, W. *Inorg. Chem.* **1984**, *23,* 4762.

(19)   Bruker-AXS Inc., *SMART* Program, Madison, Wisconsin, USA, **2009**.

(20)   Sheldrick. G. *Acta Crystallogr.* **2008***,* A*64*, 112.

(21)   Dolomanov, O. V.; Bourhis, L. J.; Gildea, R. J.; Howard, J. A. K.; Puschmann, H. *J. Appl. Crystallogr.* **2009**, *42*, 339.

(22)   Ahsan, M. Q.; Bernal, I.; Bear, J. L. *Inorg. Chem.* **1986**, *25*, 260.

(23)   Cotton, F. A.; Hillard, E. A.; Murillo, C. A. *J. Am. Chem. Soc.* **2002**, *124*, 5658.

Chapter 5

Metal–Metal Single Bonds with the Magnetic Anisotropy of Quadruple Bonds:

A Systematic Series of Heterobimetallic Bismuth(II)–Rhodium(II) Formamidinate Complexes

This chapter has recently been submitted for publication in *Chemistry – A European Journal*.

Sunderland, T. L. and Berry, J. F.

Department of Chemistry, University of Wisconsin–Madison, 1101 University Avenue, Madison, WI 53706, United States

5.1 Abstract

The first set of five heterobimetallic MM'(form)$_4$ (form = formamidinate) complexes has been successfully synthesized containing a BiRh core. The Bi–Rh bond distances lie between 2.5196(6) and 2.572[2] Å, consistent with Bi–Rh single bonds. All complexes have rich electrochemistry, with the [BiRh]$^{4+/5+}$ redox couples spanning ~ 700 mV and showing a strong correlation to remote ligand substitution. Visible spectroscopy shows two features for complexes **1** - **5** at ~ 459 and ~ 551 nm, unique to BiRh paddlewheel complexes. The large spin-orbit coupling (SOC) of Bi creates a massive magnetic anisotropy, $\Delta\chi$, ~ –4800 x 10^{-36} m^3/molecule, which is the largest value reported for any single bond to date.

5.2 Introduction

The diamagnetism of bismuth is unmatched among the stable elements. When combined with magnetic elements, the large diamagnetism and spin-orbit coupling of Bi have recently been shown to engender materials with ferromagnetism and large magnetic anisotropies.[1-5] However, discrete coordination complexes in which heterometallic Bi···M interactions can be directly probed remain uncommon.[6-13] In 2005, Dikarev and coworkers reported a synthetic breakthrough allowing access to carboxylate complexes with Bi–Rh single bonds.[14] Further development of solution routes to these complexes has opened up access to a wide variety of BiRh carboxylate and oxypyridinate compounds.[15-17] We now report a systematic series of new BiRh compounds, the first to be supported by (N, N) donor formamidinate ligands, which allows us to contrast two important properties of Rh–Rh and Bi–Rh single bonds, namely, their redox chemistry and their magnetic anisotropy ($\Delta\chi$ (measured in units of 10^{-36} m^3/molecule) where χ is magnetic susceptibility). Typically, large values of $\Delta\chi$ are expected for molecules with an element–element multiple bond. Recent work[18, 19] on the impact of bond polarity on $\Delta\chi$ has prompted us to measure $\Delta\chi$ for the Bi–Rh single bond, and we report here that $\Delta\chi$ is exceptionally large in this case.

5.3 Experimental Section

5.3.1 Materials and Methods

All reactions were carried out using oven dried glassware under a dry N_2 atmosphere using Schlenk techniques and glovebox methods. BiRh(TFA)$_4$[15] (TFA = trifluoroacetate) was prepared according to literature procedures. The HDArF (DArF = di-aryl-formamidinate) ligands were prepared according to known literature procedures.[20] The ligand H(p-OMe-DArF) was purified by sublimation under reduced pressure prior to use. Hexane, ethyl acetate (EtOAc), dichloromethane (DCM), acetonitrile (MeCN), chloroform-d (CDCl$_3$), diethyl ether (Et$_2$O), and tetrahydrofuran (THF) were purchased from Sigma-Aldrich and used without further purification. ^{1}H and^{13}C{^{1}H} NMR spectra were recorded on a Bruker Avance-500 MHz spectrometer at 500 and 125 MHz, respectively. The ^{19}F{^{1}H} NMR spectrum was recorded on a Bruker Avance-400 MHz spectrometer at 376 MHz. ^{1}H and ^{13}C{^{1}H} NMR shifts were referenced to residual proteo solvent, ^{19}F{^{1}H} NMR shifts were referenced from the corresponding ^{1}H NMR frequency. ^{1}H splitting patterns are designated as doublet (d), multiplet (m), singlet (s), doublet of doublets (dd), triplet (t), and quartet (q). Cyclic voltammetry was performed in 10 mL DCM solutions containing 0.1 M tetrabutylammonium hexafluorophosphate (TBAH) with 1 mM analyte. The electrodes consisted of a glassy carbon working electrode, a reference electrode made of a silver wire in a 10 mM AgNO$_3$ solution contained by a Vycor tip and an auxiliary electrode of platinum wire. All cyclic voltammograms were referenced to the ferrocene/ferrocenium (Fc/Fc$^+$) redox couple. Spectroelectrochemistry was performed in a 40 mL DCM solution containing 0.1 M TBAH. The electrodes consisted of a Pt wire working electrode, a counter electrode made of a platinum wire in contact with carbon felt separated from the solution by a glass frit and a silver wire as the reference electrode. UV-Vis spectra were obtained using a StellarNet Miniature BLUE-wave UV-Vis dip probe with a Tungsten-Krypton light source and a 10 mm path length tip. Elemental analysis was carried out by Midwest Microlab, LLC, Indianapolis, IN. IR spectra were taken on a Bruker Tensor 27 FTIR spectrometer using an attenuated total reflectance (ATR) adapter. Mass

spectra were obtained at the Paul Bender Chemical Instrumentation Center of the Chemistry Department of the University of Wisconsin–Madison using a Thermo Q Exactive™ Plus ESI-MS.

5.3.2 Crystallography

Crystallographic data were measured at the Molecular Structure Laboratory of the Chemistry Department of the University of Wisconsin–Madison. Crystals were selected under oil under ambient conditions and attached to the tip of a MiTeGen MicroMount©. Each crystal was mounted in a stream of cold nitrogen at 100(1) K and centered in the X-ray beam using a video camera. The crystal evaluation and data collection were performed on a Bruker Quazar SMART APEX-II diffractometer with Mo Kα (λ = 0.71073 Å) radiation. The data were collected using a routine to survey an entire sphere of reciprocal space and indexed by the SMART program.[21] The structures were solved *via* direct methods and refined by iterative cycles of least-squares refinement on F^2 followed by difference Fourier synthesis.[22,23] All H-atoms were included in the final structure factor calculation at idealized positions and allowed to ride on the neighboring atoms with relative isotropic displacement coefficients. Single crystals of **1**, **2** - **3** and **4** - **5** suitable for structural determination were obtained by slow cooling a DCM/hexane to −20 °C, slow diffusion of hexane into THF, and slow diffusion of hexane into Et$_2$O solutions, respectively. Complex **1** was treated with the SQUEEZE function of the PLATON program to remove solvent molecules from the void space, removing 277 electrons from a void of 1168 Å^3, which is consistent with approximately 6.6 CH$_2$Cl$_2$ molecules.[24] Complex **2** was treated with the SQUEEZE function of the PLATON program to remove solvent molecules from the void space, removing 76 electrons from a void of 263 Å^3, which is consistent with approximately 2 THF molecules.[24]

5.3.3 EPR Spectroscopy

EPR data were acquired with a Bruker ELEXSYS E500 EPR spectrometer with a Varian E102 microwave bridge interfaced with a Linux system. An Oxford Instruments ESR-900 continuous-flow helium flow cryostat and an Oxford Instruments 3120 temperature controller were used to set and maintain the temperature of the sample. A Hewlett-Packard 432A power meter was used for microwave power calibration, with measurement conditions as follows: for [**1**]$^+$ in DCM 9.3826 GHz, 100 MHz modulation frequency, 3.000 G modulation amplitude, 3250 G center field, 3000 G sweep width, 0.5024 mW power, 70 dB gain, 20.48 ms time constant and 10 K. The simulation was performed using EasySpin software.[25] The following parameters were used to model the data for [**1**]$^+$, g_x = 2.105, g_y = 2.000, g_z = 1.960, $A_{x,Rh}$ = 200, $A_{y,Rh}$ = 100, $A_{z,Rh}$ = 150 MHz, HStrain$_x$ = 75, HStrain$_y$ = 150, HStrain$_z$ = 80 MHz and S = ½.

5.3.4 Computational Methods

Initial coordinates of **1** and [**1**]$^+$ were obtained from the crystallographic data for compound **1**. All geometry optimizations were carried out with ORCA version 2.9.1[26] and the BP86 exchange-correlation functional.[27] The TZVP basis set[28] including all electron scalar relativistic effects within the ZORA[29] approximation were used with the TZVP/J auxiliary basis set[30] for Rh and Bi. The SVP basis set[28] and SVP/J auxiliary basis set[30] were used on all remaining atoms. Solvation effects were treated with the COSMO solvation model[31,32] in a DCM solution. Tight optimization and tight self-consistent field convergence criteria were employed along with grid4 for all calculations. Frequency calculations were performed following geometry optimizations to ensure minimum energy structures. Molecular graphics were created with the UCSF Chimera package.[33]

5.3.5 Synthesis and Characterization

BiRh(p-OMe-DArF)₄ (1). Solid BiRh(TFA)₄ (52.3 mg, 0.0685 mmol) and H(*p*-OMe-DArF) (1.20 g, 4.68 mmol) were combined in a 10 mL Schlenk flask, degassed, and heated under static

vacuum to 135 °C using an oil bath for 17 h, during which time the ligand became molten and the mixture turned red/brown. After cooling to room temperature, the solids were purified by column chromatography on SiO_2 using hexane/EtOAc (3:2) as eluent (R_f = 0.56 (hexane/EtOAc (1:1))). The red/brown fraction was collected and dried *in vacuo* to yield a red/brown solid. Yield: 45.6 mg, 49.9%. X-ray quality crystals of **1** were obtained overnight from a DCM/hexane solution of **1** at −20 °C. ESI-MS (positive ion, MeCN): *m/z* [M+H]$^+$ Calcd. 1333.3471. Found: 1333.3471. ^{1}H NMR (CDCl$_3$, 500 MHz, ppm): δ 8.45 (d, $^3J_{H-Rh}$ = 1.5 Hz, 4H), 6.83 - 6.74 (m, 16H), 6.67 - 6.55 (m, 16H), 3.78 (s, 12H), 3.78 (s, 12H). ^{13}C{^{1}H} NMR (CDCl$_3$, 125 MHz, ppm): δ 161.7, 156.7, 155.2, 144.9, 142.1, 127.2, 121.3, 114.8, 114.2, 55.8, 55.7. IR (ATR, cm^{-1}): 2950 (w), 1610 (w), 1563 (w), 1533 (m), 1508 (w), 1467 (s), 1442 (w), 1332 (w), 1316 (m), 1242 (w), 1220 (s), 1218 (m), 1204 (m), 1181 (w), 1168 (w), 1104 (m), 1035 (s), 953 (w), 936 (w), 835 (s), 828 (s), 789 (w), 749 (m), 661 (w), 652 (w), 633 (w). UV-Vis (DCM) λ$_{max}$ (nm) (ε (M^{-1}cm^{-1})): 453 (8775), 544 (934).

BiRh(p-Me-DArF)$_4$ (2). Solid BiRh(TFA)$_4$ (42.3 mg, 0.0553 mmol) and H(*p*-Me-DArF) (1.23 g, 5.48 mmol) were combined in a 10 mL Schlenk flask, degassed, and heated under static vacuum to 145 °C using an oil bath for 17 h, during which time the ligand became molten and the mixture turned red/brown. After cooling to room temperature, the solids were extracted with hexane/Et$_2$O (2:1), filtered, concentrated under reduced pressure and purified by column chromatography on SiO_2 using hexane/Et$_2$O (2:1) as eluent (R_f = 0.46 (hexane/Et$_2$O (1:1))). The red/orange fraction was collected and dried *in vacuo* to yield a red/orange solid. Yield: 26.0 mg, 38.9%. X-ray quality crystals of **2** were obtained by layering a concentrated THF solution of **2** with hexane. ESI-MS (positive ion, MeCN): *m/z* [M+H]$^+$ Calcd. 1205.3873. Found: 1205.3875. ^{1}H NMR (CDCl$_3$, 500 MHz, ppm): δ 8.44 (d, $^3J_{H-Rh}$ = 1.6 Hz, 4H), 6.97 (d, *J* = 8.0 Hz, 8H), 6.87 (d, *J* = 8.0 Hz, 8H), 6.76 (d, *J* = 8.0 Hz, 8H), 6.55 (d, *J* = 8.0 Hz, 8H), 2.25 (s, 24H). ^{13}C{^{1}H} NMR (CDCl$_3$, 125 MHz, ppm): δ 161.7, 149.1, 146.0, 133.6, 131.3, 129.9, 129.4, 126.3, 120.1, 21.0, 20.9. UV-Vis (DCM) λ$_{max}$ (nm) (ε (M^{-1}cm^{-1})): 464 (4047), 558 (373).

BiRh(DPhF)₄ *(3).* Solid BiRh(TFA)$_4$ (50.6 mg, 0.0663 mmol) and H(DPhF) (1.07 g, 5.45 mmol) were combined in a 10 mL Schlenk flask, degassed, and heated under static vacuum to 130 °C using an oil bath for 17 h, during which time the ligand became molten and the mixture turned red/brown. After cooling to room temperature, excess ligand was removed by sublimation at 120 °C under reduced pressure. The remaining brown solids were recrystallized from Et$_2$O/hexane, filtered, washed with small amounts of cold hexane and dried *in vacuo* to yield a red/brown solid. Yield: 43.6 mg, 60.2%. X-ray quality crystals of **3** were obtained by layering a concentrated THF solution of **3** with hexane. ESI-MS (positive ion, MeCN): *m/z* [M+H]$^+$ Calcd. 1093.2621. Found: 1093.2629. ^{1}H NMR (CDCl$_3$, 500 MHz, ppm): δ 8.57 (d, $^3J_{H-Rh}$ = 1.8 Hz, 4H), 7.18 (dd, *J* = 7.8, 7.4 Hz, 8H), 7.10 - 7.05 (m, 12H), 6.96 (t, *J* = 7.5 Hz, 4H), 6.88 (d, *J* = 8.5 Hz, 8H), 6.67 (dd, *J* = 7.8, 2.0 Hz, 8H). ^{13}C{^{1}H} NMR (CDCl$_3$, 125 MHz, ppm): δ 161.9, 151.2, 148.1, 129.4, 128.8, 126.3, 124.2, 122.2, 120.2. IR (ATR, cm^{-1}): 1555 (s), 1527 (s), 1484 (s), 1449 (w), 1334 (s), 1262 (w), 1216 (s), 1178 (w), 1079 (m), 1028 (m), 962 (s), 933 (s), 815 (m), 767 (s), 751 (s), 700 (s), 689 (s), 656 (w). UV-Vis (DCM) λ$_{max}$ (nm) (ε (M^{-1}cm^{-1})): 460 (4736), 551 (402).

BiRh(p-Cl-DArF)₄ *(4).* Solid BiRh(TFA)$_4$ (38.3 mg, 0.0501 mmol) and H(*p*-Cl-DArF) (1.21 g, 4.56 mmol) were combined in a 10 mL Schlenk flask, degassed and heated under static vacuum to 180 °C using an oil bath for 17 h, during which time the ligand became molten and the mixture turned red/brown. After cooling to room temperature, the solids were extracted with hexane/Et$_2$O (2:1), filtered, concentrated under reduced pressure and purified by column chromatography on SiO$_2$ using hexane/Et$_2$O (2:1) as eluent (R$_f$ = 0.42 (hexane/Et$_2$O (1:1))). The red/orange fraction was collected and dried *in vacuo* to yield a red/orange solid. Yield: 35.2 mg, 51.4%. X-ray quality crystals of **4** were obtained by layering a concentrated Et$_2$O solution of **4** with hexane. ESI-MS (positive ion, MeCN): *m/z* [M+H]$^+$ Calcd. 1364.9503. Found: 1364.9506. ^{1}H NMR (CDCl$_3$, 500 MHz, ppm): δ 8.51 (d, $^3J_{H-Rh}$ = 1.6 Hz, 4H), 7.16 (d, *J* = 8.4 Hz, 8H), 7.09 (d, *J* = 8.4 Hz, 8H), 6.72 (d, *J* = 8.4 Hz, 8H), 6.56 (d, *J* = 8.4 Hz, 8H). ^{13}C{^{1}H} NMR (CDCl$_3$, 125 MHz, ppm):

δ 161.9, 149.1, 146.0, 130.7, 129.8, 129.4, 128.4, 127.0, 121.3. UV-Vis (DCM) λ_{max} (nm) (ε ($M^{-1}cm^{-1}$)): 462 (11795), 557 (1429).

BiRh(p-CF$_3$-DArF)$_4$ (**5**). Solid BiRh(TFA)$_4$ (51.9 mg, 0.0680 mmol) and H(*p*-CF$_3$-DArF) (1.50 g, 4.51 mmol) were combined in a 10 mL Schlenk flask, degassed and heated under static vacuum to 165 °C using an oil bath for 17 h, during which time the ligand became molten and the mixture turned red/brown. After cooling to room temperature, the solids were extracted with hexane/DCM (2:1), filtered, concentrated under reduced pressure and purified by column chromatography on SiO$_2$ using hexane/DCM (2:1) as eluent (R_f = 0.42 (hexane/DCM (2:1))). The red/orange fraction was collected and dried *in vacuo* to yield a red/orange solid. Yield: 45.0 mg, 40.4%. X-ray quality crystals of **5** were obtained by layering a concentrated Et$_2$O solution of **5** with hexane. Anal. Calcd BiRhC$_{60}$H$_{36}$N$_8$F$_{24}$: C 44.0, H 2.2, N 6.9. Found: C 43.8, H 2.2, N 6.7. ESI-MS (positive ion, MeCN): *m/z* [M+H]$^+$ Calcd. 1637.1612. Found: 1637.1631. ^{1}H NMR (CDCl$_3$, 500 MHz, ppm): δ 8.74 (d, $^3J_{H-Rh}$ = 1.6 Hz, 4H), 7.47 (d, *J* = 8.3 Hz, 8H), 7.38 (d, *J* = 8.3 Hz, 8H), 6.86 (d, *J* = 8.3 Hz, 8H), 6.79 (d, *J* = 8.3 Hz, 8H). ^{13}C{^{1}H} NMR (CDCl$_3$, 125 MHz, ppm): δ 162.4 (s), 153.1 (s), 149.7 (s), 127.7 (q, $^2J_{C-F}$ = 33 Hz), 127.3 (q, $^3J_{C-F}$ = 4 Hz), 126.8 (q, $^3J_{C-F}$ = 4 Hz), 125.9 (q, $^2J_{C-F}$ = 33 Hz), 125.5 (s), 124.3 (q, $^1J_{C-F}$ = 272 Hz), 124.1 (q, $^1J_{C-F}$ = 272 Hz), 120.0 (s). ^{19}F{^{1}H} NMR (CDCl$_3$, 376 MHz, ppm): δ –62.0, –62.3. IR (ATR, cm^{-1}):1610 (w), 1563 (s), 1538 (m), 1508 (m), 1316 (s), 1218 (m), 1181 (m), 1160 (m), 1105 (s), 1065 (s), 1010 (w), 979 (w), 936 (w), 835 (m), 661 (w), 633 (w). UV-Vis (DCM) λ_{max} (nm) (ε ($M^{-1}cm^{-1}$)): 457 (5965), 553 (812).

5.4 Results and Discussion

5.4.1 Synthesis and Characterization

Complexes **1** - **5** were all synthesized by combining BiRh(TFA)$_4$[15] (TFA = trifluoroacetate) with an excess of H(form) (form = formamidinate) and heating the mixture above the melting point

of the ligand under a static vacuum, which causes a color change from yellow to red/brown upon equatorial ligand exchange (Scheme 5.1).

The ^{1}H NMR spectra of **1** - **5** in chloroform-*d* (CDCl$_3$) are all consistent with C$_{4v}$ symmetry on the NMR time scale, where the four equatorial ligands are symmetry equivalent, but the phenyl rings and associated *para*-substituents from an individual formamidinate ligand are inequivalent due to the heterobimetallic BiRh core. The methine H-atoms appear as doublets due to coupling to the Rh nucleus ($I = \frac{1}{2}$, $^3J_{H-Rh} = \sim 1.7$ Hz) and are significantly deshielded due to the magnetic anisotropy of the Bi–Rh single bond, appearing near 8.5 ppm in CDCl$_3$ (*vide infra*).

Scheme 5.1. General reaction conditions to synthesize **1** - **5**.
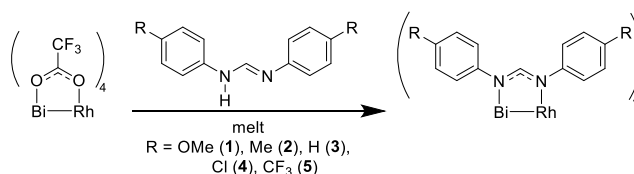
5.4.2 Crystallography

Complexes **1** - **5** have been crystallographically characterized and are all isostructural with the Rh-atom in a square pyramidal geometry with four N-atoms bound equatorially and capped by the Bi-atom. Likewise, the Bi-atom is in a distorted square pyramidal geometry, puckered out of the plane of four N-atoms away from the apical Rh-atom (see Figure 5.1, Table 5.1 and SI Figures 5.11 - 5.14 and Tables 5.5 - 5.10). The Bi–N bonds are all uniformly longer than the Rh–N bonds by 0.4 Å. All complexes have short Bi–Rh bond distances between 2.5196(6) and 2.572[2] Å, consistent with a Bi–Rh single σ bond (see SI Figure S5). As observed for other M$_2$(form)$_4$ compounds,[34] more electron rich ligands lead to slightly shorter M–M bond lengths. The equatorial ligands also display a significant twisting with N–Bi–Rh–N torsion angles between 18.0[5] and 25.9(5)°.

Table 5.1. Experimental bond distances (Å) and angles (°) for **1** – **5**.

Compound	**1**[a]	**2**	**3**	**4**	**5**
Bi–Rh	2.527(1)	2.5196(6)	2.5279(3)	2.5420(3)	2.5407(2)
Bi–N$_{av}$	2.436(7)	2.457(3)	2.451[3]	2.438[2]	2.451[2]
Rh–N$_{av}$	2.040(7)	2.052(3)	2.051[2]	2.056[2]	2.053[2]
Torsion	23.7(1)	25.9(5)	23.2[5]	18.0[5]	18.6[5]

[a]Data are from the non-disordered molecule in the asymmetric unit

Figure 5.1. X-ray crystal structure of **3**, with thermal ellipsoids drawn at the 50% probability level. Hydrogen atoms have been removed for clarity.

5.4.3 Electrochemistry

Metal–metal bonded complexes often show interesting redox features. Specifically, singly-bonded Rh$_2$ paddlewheel complexes supported by either (O, O), (O, N) or (N, N) donor ligands often display reversible [Rh$_2$]$^{4+/5+}$ redox couples with the tetracarboxylate complexes spanning a wide range of potentials from 1.06 to –0.345 V *vs* Fc/Fc$^+$.[35] Heterobimetallic BiRh complexes supported by either carboxylate or oxypyridinate ligands both have *irreversible* [BiRh]$^{4+/5+}$ redox

couples at *higher* potentials than their corresponding Rh_2 complexes.[16] In contrast, **1** - **5**, supported by more basic amidinate ligands, display *reversible* $[BiRh]^{4+/5+}$ redox couples at *lower* potentials than the corresponding Rh_2 complexes, as shown in Figure 5.2 and Table 5.2 (see SI Figure 5.16–5.17 and Table 5.11).
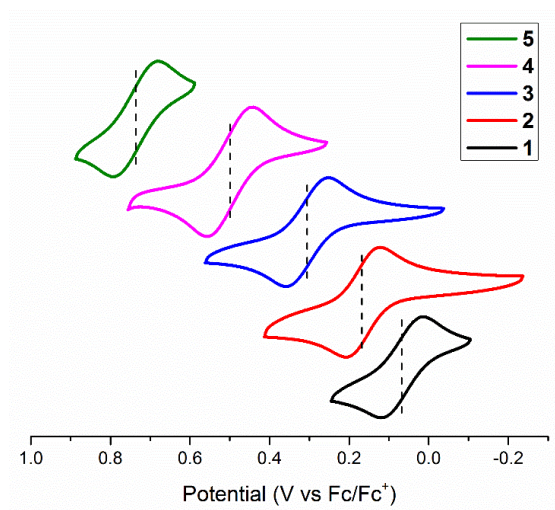
Figure 5.2. Cyclic voltammograms of **1** - **5** in CH_2Cl_2 with scan rate = 100 mV/s (0.1 M tetrabutylammonium hexaflurophosphate (TBAH)).

Table 5.2. Comparison of electrochemical data[a] for compounds **1** - **5** and $Rh_2(form)_4$.

Compound	$[MRh]^{4+/5+}$ $E_{1/2}$ (mV)	Reference
1	70.6	This work
2	168	This work
3	307	This work
4	502	This work
5	736	This work
$Rh_2(p\text{-OMe-DArF})_4$	274	37
$Rh_2(DFM)_4{}^b$	341	37
$Rh_2(DPhF)_4$	471	37
$Rh_2(p\text{-Cl-DArF})_4$	667	37
$Rh_2(p\text{-CF}_3\text{-DArF})_4$	891	37

[a]All potentials are *vs* Fc/Fc+ in CH_2Cl_2. [b]DFM = tolyl-formamidinate

Linear free energy relationships between redox potential and the Hammett parameter (σ) have been established for several homobimetallic[36-42] formamidinate complexes, however, no such analysis has been made on heterobimetallic formamidinate complexes. Using Equation 5.1, a reactivity constant (ρ) can be extracted from the electrochemical data, which quantifies the sensitivity the corresponding redox couple experiences from remote substitution on the equatorial ligand.[41]

$$\Delta E_{(1/2)} = \rho(8\sigma)\ mV \qquad \text{(Eq. 5.1)}$$

Values of ρ for the $[M_2(form)_4]^{4+/5+}$ couple range from 87 - 114 mV and are listed below in Table 5.3. Based on the electronic structure of **1** - **5**, we expect oxidation from $[BiRh]^{4+}$ to $[BiRh]^{5+}$ to be localized on the Rh-atom (see SI Figure 5.15). This analysis suggests that all eight aryl substituents may not contribute equally to ρ and that ρ for BiRh complexes should be smaller than for homobimetallic compounds. Surprisingly, this is not the case: analysis of the electrochemical data for the $[BiRh(form)_4]^{4+/5+}$ couple reveals a ρ value of 102 mV, slightly higher than that for $[Rh_2(form)_4]^{4+/5+}$ (98 mV),[37] as shown in Figure 5.3 and Table 5.3.

Table 5.3. Comparison of ρ values for $[MM(form)_4]^{4+/5+}$ redox couples.

MM(form)$_4$	ρ (mV)	Reference
BiRh	102	This work
Mo$_2$	87	38, 39
Rh$_2$	98	37
Ni$_2$	114	36
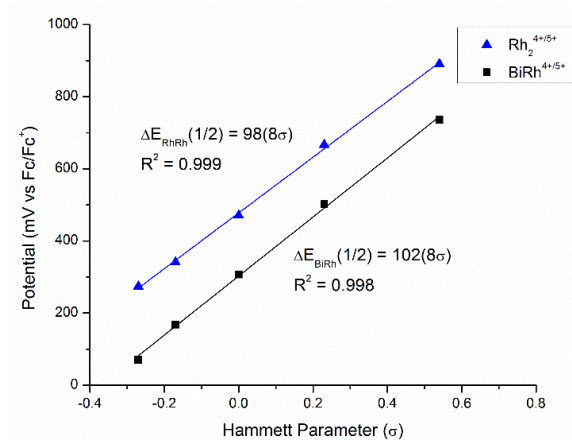
Figure 5.3. Hammett plots of potential *vs* σ for [BiRh(form)$_4$]$^{4+/5+}$ (black squares) and [Rh$_2$(form)$_4$]$^{4+/5+}$ (blue triangles) redox couples[37] with lines of best fit for each.

5.4.4 UV-Vis Spectroscopy

Heterobimetallic BiRh carboxylates and oxypyridinates are featureless in the visible spectrum.[16,17] Consistent with their more accessible redox couples, **1** - **5** also have more accessible electronic transitions and are red/brown in color.[43] The UV-Vis spectra for **1** - **5** are shown in Figure 5.4. All complexes have a strong absorption feature at ~ 459 nm. A second, weaker, feature at ~ 551 nm is also present for all complexes.
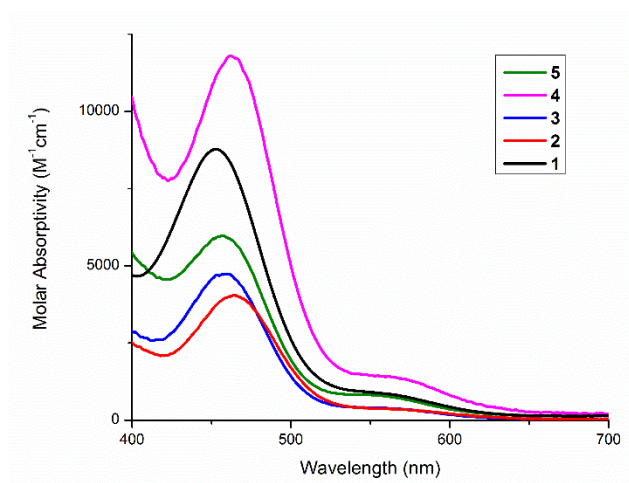
Figure 5.4. Overlay of UV-Vis spectra of **1** - **5** in CH$_2$Cl$_2$.

To gain more insight into the electronic structure of BiRh(form)$_4$ complexes, spectroelectrochemisty was performed at the [BiRh]$^{4+/5+}$ redox couple of **1**, which has the most accessible one electron oxidation from complexes **1** - **5**. The oxidation process was monitored by UV-Vis spectroscopy, as shown in Figure 5.5. During the oxidation, the red/brown solution becomes darker brown. The feature of **1** at λ = 453 appears to lose intensity and shift to lower energy. The feature at 544 nm appears to lose intensity followed by the growth of a new feature at slightly lower energy at ~ 645 nm and an additional broad feature at λ ~ 900 nm. The presence of two isosbestic points at 440 and 505 nm indicate a direct conversion of **1** to [**1**]$^{+}$.
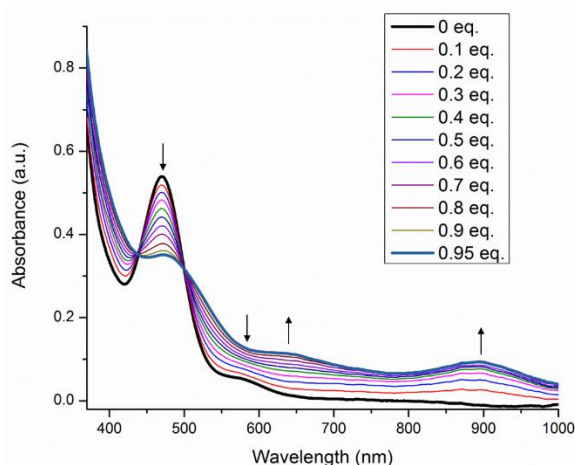
Figure 5.5. UV-Vis spectra from electrochemical oxidation of **1** in DCM.

5.4.5 Density Functional Theory Calculations

The nature of the transitions of both **1** and [**1**]$^{+}$ were investigated with time dependent-density functional theory (TD-DFT). An overlay of the predicted absorption spectra for both complexes, with remarkable agreement to the experimental spectra, is shown in Figure 5.6. For complex **1**, the band at 575 nm can be assigned as a LMCT band with excitations into the Bi–Rh σ^* orbital. The higher energy bands at 453 nm is a combination of LMCT bands and d$\rightarrow$d transitions from orbitals localized on the Rh-atom. The one electron oxidation of **1** removes one electron from the HOMO, which is the Rh$_{xy}$ orbital shown in Figure 5.7.
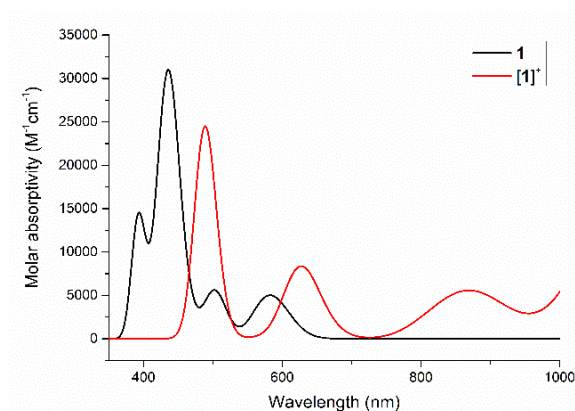
Figure 5.6. TD-DFT predicted absorption spectra for **1** and [**1**]⁺.
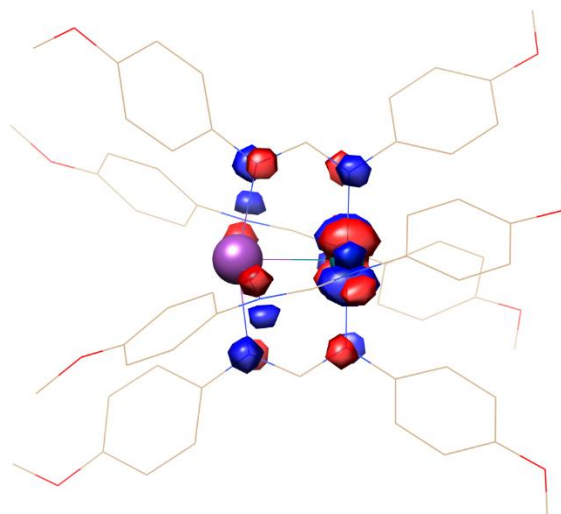
Figure 5.7. DFT calculated highest occupied molecular orbital (HOMO) for **1**.

Removal of one electron from the non-bonding δ type orbital on the Rh-atom allows for new lower-energy electronic absorption features to arise, Figure 5.6, namely, excitations into the singly occupied molecular orbital (SOMO) from orbitals of π symmetry localized on the Rh-atom around 875 nm. The features predicted at ∼ 620 and 490 nm are assigned as mainly LMCT bands into the Bi–Rh σ* orbital. The DFT calculated structures of both **1** and [**1**]⁺ show little structural

changes upon oxidation. The Bi–Rh bond elongates slightly from 2.609 to 2.625 Å. The Bi–N equatorial bonds remain essentially unchanged at 2.463 and 2.466 Å and the Rh–N bonds contract slightly from 2.095 to 2.073 Å. All of these structural changes are consistent with removal of one electron from the non-bonding δ type orbital localized on the Rh-atom, resulting in a stronger coulombic repulsion between the metal atoms and a slight contraction of the Rh–N bonds to stabilize a higher oxidation state on the Rh-atom.

5.4.6 EPR Spectroscopy

To confirm the assignment of Rh centered oxidation, an aliquot of [**1**]$^+$ following electrochemical oxidation was collected and frozen in liquid nitrogen. An EPR spectrum of [**1**]$^+$ was collected at 10 K, shown in Figure 5.8. The spectrum displays a rhombic $S = \frac{1}{2}$ signal with g values of $g_x = 2.105$, $g_y = 2.000$, $g_z = 1.960$ and hyperfine coupling constants of $A_{x,Rh} = 200$, $A_{y,Rh} = 100$ and $A_{z,Rh} = 150$ MHz. These data are in agreement with a one-electron oxidized species where the single unpaired electron is localized on the Rh-atom.
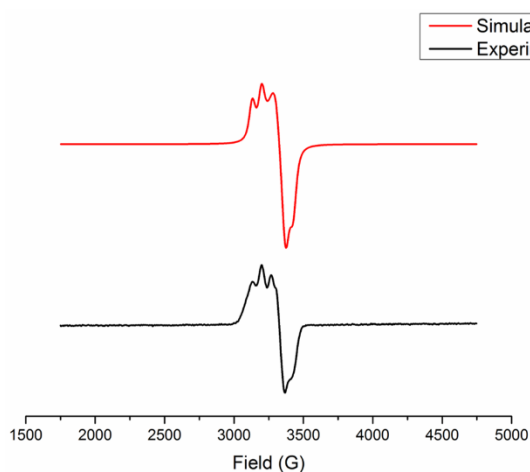
Figure 5.8. EPR experimental (bottom) and simulated (top) spectra for [**1**]$^+$ in DCM at 10 K.

5.4.7 Magnetic Anisotropy

The ^{1}H NMR spectroscopy data for **1** - **5** can be analyzed to determine the magnetic anisotropy of the compounds, $\Delta\chi$, using the model first introduced by McGlinchey.[44] In this model, the NMR chemical shifts are affected by $\Delta\chi$,[45] resulting in two spatial zones, shielding ($-\delta$) and deshielding ($+\delta$), signified by the double cone shown in Figure 5.9 for MM(form)$_4$ complexes. Notably, the methine H-atom of the form ligand resides in the $+\delta$ zone fairly close to the M$_2$ centroid, and has therefore been used as a sensitive probe for $\Delta\chi$ in a broad range of M$_2$(form)$_4$ compounds.[19,37,38,46-52] Representative examples of these are given in Table 5.4.
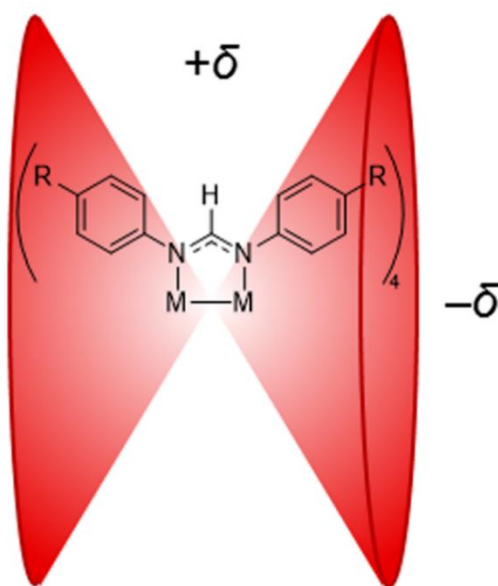
Figure 5.9. Spatial zones of shielding ($-\delta$) and deshielding ($+\delta$) arising from the magnetic anisotropy of the M–M bond.

Table 5.4. Magnetic anisotropy values for **1** - **5**, along with several other M–M bonded complexes and three organic multiple bonds.

Compound	$\Delta\chi$ (10^{-36} m^3/molecule)	Bond Order	Reference
1	−4663	1	This work
2	−4611	1	This work
3	−4729	1	This work
4	−4876	1	This work
5	−4862	1	This work
$Rh_2(DFM)_4$[a]	−2902[b]	1	37, 51
$Rh_2(DPhF)_4$	−2689[b]	1	37, 46
Co_2(p-OMe-DArF)$_4$	−3877[b]	1	47
$Pt_2(DPhF)_4Cl_2$	−3222[b]	1	48
$Cr_2(DFM)_4$	−5230	4	49
$Mo_2(DFM)_4$	−5060	4	38
$W_2(DFM)_4$	−5480	4	49
$Re_2(DFM)_4Cl_2$	−4430	4	50
$Ru_2(DFM)_4$	−3780	2	50
$V_2(DFM)_4$	−7300	3	52
Cr_2L^{-}[c]	−3500	5	19
$MnCrL$[c]	−3900	5	19
$FeCrL^{+}$[c]	−5800	3[d]	19
C≡C	−340	3	54
C=O	420	2	54
N=O	1300	2	54

[a]DFM = tolyl-formamidinate. [b]Calculated from data within the reference. [c]L = (N(o-(NCH$_2$P^{i}Pr$_2$)C$_6$H$_4$)$_3$). [d]Bond order lies between 3 - 5

The $\Delta\chi$ of the complexes in Table 4 is calculated according to Equation 5.2, where $\Delta\delta$ is the difference in ^{1}H NMR chemical shift of an H-atom on the complex of interest and a reference complex without a M–M bond (traditionally, Ni$_2$(form)$_4$ has been used as the reference complex):

r (Å) is the distance from the H-atom to the centroid of the M–M bond, and *θ* is the acute angle made between the H-atom, the centroid of the M–M bond and the M-atom.[53]

$$\Delta\delta = \left(\frac{1}{3r^3}\right)\frac{(\chi_\| - \chi_\perp)[1 - 3\cos^2(\theta)]}{4\pi} \qquad \text{(Eq. 5.2)}$$

The *Δχ* values of **1** - **5** are given in Table 5.4 along with those of a number of reference compounds. It is expected that *Δχ* should depend on the M–M bond order; additionally, Bill, Gagliardi, Lu and coworkers have suggested that the polarity of M–M bonds in heterobimetallic species can affect *Δχ*.[18, 19]

The range of *Δχ* for homobimetallic M–M singly bonded complexes is –(2700 - 3900) for Rh$_2$(form)$_4$,[37,46] Co$_2$(form)$_4$[47] and Pt$_2$(form)$_4$Cl$_2$.[48] Surprisingly, despite a fairly non-polar Bi–Rh bond, the heterobimetallic complexes **1** - **5** display the highest known *Δχ* values for single bonds (–4800), which places the magnetic anisotropy of these complexes in the range more commonly expected of quadruply bonded complexes.[38,49,50] There are a number of unusual features of the data in Table 5.4, which become even more apparent when most of the known *Δχ* values from the literature are plotted as a function of M–M bond order, as in Figure 5.10. In organic compounds, |*Δχ*| increases with bond order (from 140 to 150 to 340 for C–C, C=C and C≡C bonds, respectively, in units of 10^{-36} m^3/molecule),[54] but no such simple relationship exists in M$_2$ compounds of varying bond orders.
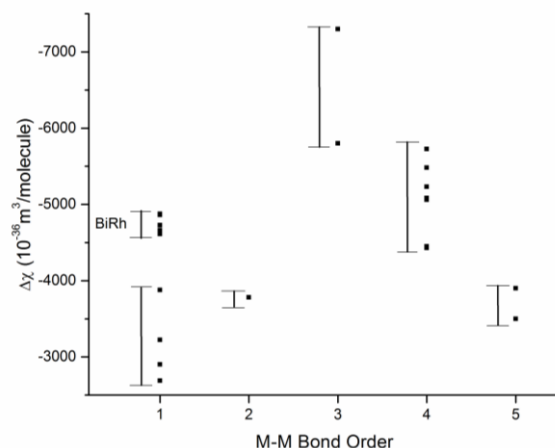
Figure 5.10. Plot of magnetic anisotropy ($\Delta\chi$ (10^{-36} m^3/molecule)) *vs* M–M bond order for several M–M bonded complexes.

To explain the trend seen in Table 5.4 and Figure 5.10, we recall that the magnetic susceptibility, χ, is the sum of diamagnetic (χ_D) and paramagnetic (χ_P) contributions (Equation 5.3).[55]

$$\chi = \chi_D + \chi_P \qquad \text{(Eq. 5.3)}$$

Paired electrons contribute to χ_D, with higher bond orders having a larger χ_D due to the ring currents based on the number of electron pairs of the multiple bond. The $S = 0$ ground state of the multiply bonded compounds yields a vanishing first-order Zeeman contribution to χ_P. However, second-order Zeeman terms of the form $\sum_{n\neq0}\frac{<\psi_o|\hat{H}_z|\psi_n>^2}{E_0-E_n}$ do not vanish (here ψ_o and ψ_n are ground and excited state wavefunctions with E_0 and E_n being their energies; $\hat{H}_z$ is the Zeeman Hamiltonian, $\hat{H}_z = \beta(\hat{L} + g\hat{S}) \cdot H$, with β = the Bohr magneton, $\hat{L}$ and $\hat{S}$ being orbital and spin angular momentum operators, respectively, g = the Landé factor and H = applied magnetic field). These second-order Zeeman terms describe field-induced mixing of the ground state with non-thermally populated excited states, resulting in a non-zero temperature-independent

contribution to χ_P, called temperature-independent paramagnetism or TIP.[56] Like χ_D, χ_P is anisotropic and must be described as a tensor. TIP of diamagnetic compounds should therefore contribute to measured $\Delta\chi$ values. Two important properties of molecules can facilitate excited state mixing and therefore increase the contribution of χ_P: relatively small ΔE values, with $\Delta E = E_o - E_n$ and large spin-orbit coupling (SOC). Let's revisit the data in Table 5.4 and Figure 5.10 with these concepts in mind. For the series of Group 6 $M_2(form)_4$ compounds, the trend in $|\Delta\chi|$ of $Mo_2 < Cr_2 < W_2$ may at first glance appear puzzling. However, it appears that both Cr_2 and W_2 compounds have stronger χ_P contributions to $\Delta\chi$ than does $Mo_2(DFM)_4$. If we only consider SOC, we would expect the trend to be $Cr_2 < Mo_2 < W_2$, which does explain why the W_2 molecule has the largest $|\Delta\chi|$. For the Cr_2 molecule, however, ΔE becomes important, since it is well known that Cr_2 quadruple bonds are weak and have several low-lying excited states.[57] This ΔE analysis likely contributes to the large $\Delta\chi$ values of all first-row metal dimers.

In the case of the present BiRh compounds, the apparently large $\Delta\chi$ for these compounds can be attributed to a paramagnetic SOC contribution to the methine chemical shifts. Thus, unlike in organic molecules with large ΔE and small SOC,[58] the data in Table 5.4 and Figure 5.10 for metal–metal bonded compounds are highly influenced by χ_P contributions to $\Delta\chi$, and no simple trend in bond order exists. However, if we consider only the systematic series of $M_2(DFM)_4$ compounds with second row M-atoms Mo_2, Ru_2, and Rh_2, for which neither ΔE or SOC contributions are dominant, we do see the expected increase of $|\Delta\chi|$ with bond order from 2902 (Rh_2, single bond) to 3780 (Ru_2, double bond) to 5060 (Mo_2, quadruple bond). At this time, it is unfortunately not possible to disentangle χ_D and χ_P contributions to $\Delta\chi$. To reflect this ambiguity, we suggest that this term is best described henceforth as "magnetic anisotropy" rather than the more traditional term "diamagnetic anisotropy".

5.5 Conclusions

Thus, the inclusion of Bi into BiRh(form)$_4$ dimers yields strongly colored compounds with unusually accessible redox properties and creates a massive magnetic anisotropy reflected in chemical shift changes similar to those seen in quadruply bonded metal dimers. The large $\Delta\chi$ values seen for BiRh dimers are attributed to strong paramagnetic second-order Zeeman effects amplified by the large SOC of Bi.

5.6 Acknowledgments

5.7 Supporting Information
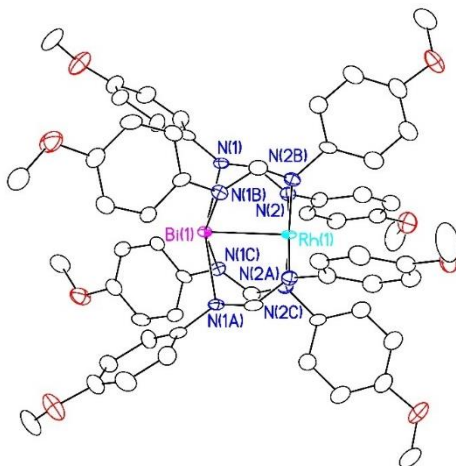
Figure 5.11. X-ray crystal structure of **1**, with thermal ellipsoids drawn at the 50% probability level. Hydrogen atoms, 6.6 disordered molecules of CH_2Cl_2, and 2 quarter molecules of **1** have been removed for clarity.
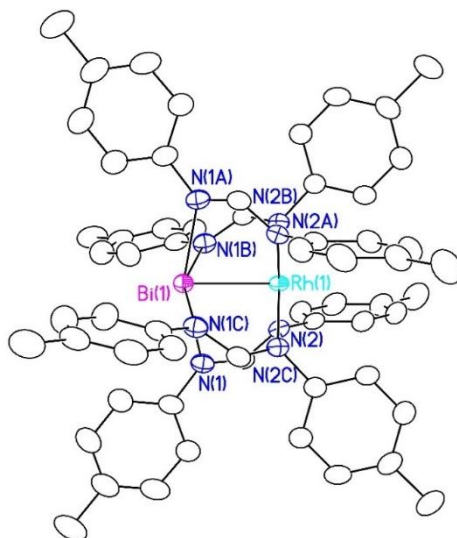
Figure 5.12. X-ray crystal structure of **2**, with thermal ellipsoids drawn at the 50% probability level. Hydrogen atoms, 2 disordered molecules of THF, and 1 minor (4%) disordered position for each metal atom have been removed for clarity.
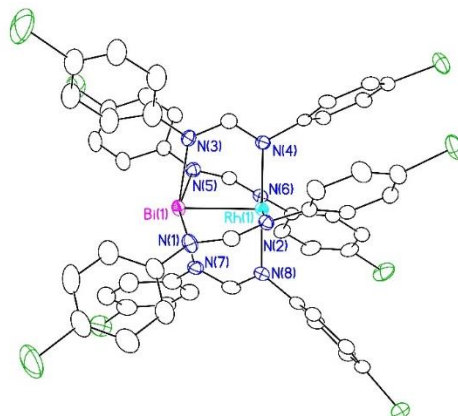
Figure 5.13. X-ray crystal structure of **4**, with thermal ellipsoids drawn at the 50% probability level. Hydrogen atoms and 1 disordered aryl ring have been removed for clarity.

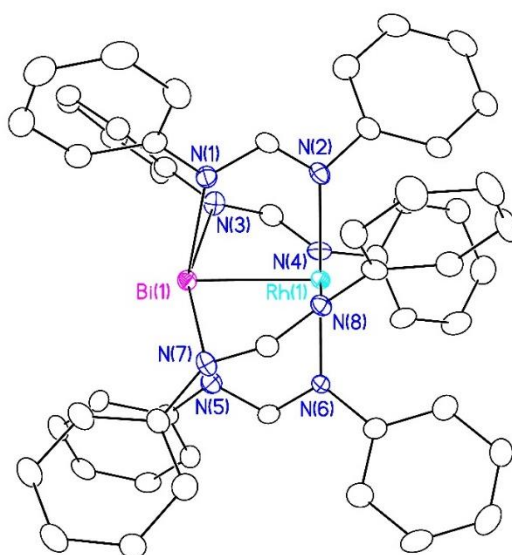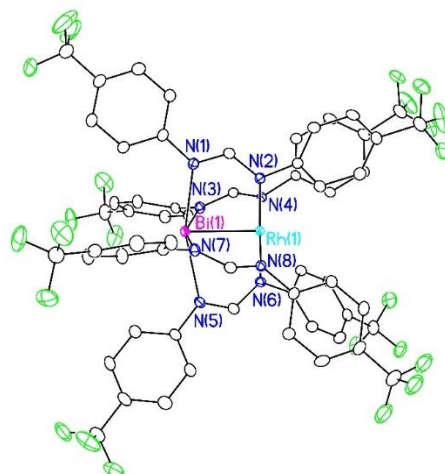**Figure 5.14.** X-ray crystal structure of **5**, with thermal ellipsoids drawn at the 50% probability level. Hydrogen atoms and 1 disordered CF_3 group have been removed for clarity.

Table 5.5. Crystallographic data for **1** - **5** at 100 K.

Identification code	**1**•6.6 CH_2Cl_2	**2**•2 THF	**3**	**4**	**5**
Empirical formula	$Bi_{0.75} Rh_{0.75} C_{51.6} H_{58.2} O_6 N_6 Cl_{13.2}$	$Bi Rh C_{64} H_{68} O N_8$	$Bi Rh C_{52} H_{44} N_8$	$Bi Rh C_{52} H_{36} N_8 Cl_8$	$Bi Rh C_{60} H_{36} N_8 F_{24}$
Formula weight	1560.30	1277.15	1092.84	1368.38	1636.86
Temperature	100(1) K	100(1) K	100(1) K	100(1) K	100(1) K
Wavelength	0.71073 Å	0.71073 Å	0.71073 Å	0.71073 Å	0.71073 Å
Crystal system	Tetragonal	Tetragonal	Monoclinic	Triclinic	Triclinic
Space group	$P4/n$	$P4/n$	$P2_1/n$	$P\bar{1}$	$P\bar{1}$
Unit cell dimensions	a = 14.1081(3) Å	a = 14.3960(2) Å	a = 13.3670(3) Å	a = 10.6383(2) Å	a = 11.3105(3) Å
	b = 14.1081(3) Å	b = 14.3960(2) Å	b = 19.5273(4) Å	b = 11.4542(2) Å	b = 11.8763(3) Å
	c = 45.988(1) Å	c = 13.2639(2) Å	c = 16.9064(3) Å	c = 23.8322(5) Å	c = 24.7296(6) Å
	$\alpha = 90°$	$\alpha = 90°$	$\alpha = 90°$	$\alpha = 101.931(1)°$	$\alpha = 94.996(1)°$
	$\beta = 90°$	$\beta = 90°$	$\beta = 98.620(1)°$	$\beta = 92.640(1)°$	$\beta = 101.950(1)°$
	$\gamma = 90°$	$\gamma = 90°$	$\gamma = 90°$	$\gamma = 113.380(1)°$	$\gamma = 112.022(2)°$
Volume	9153.4(5) Å^3	2748.87(9) Å^3	4363.1(2) Å^3	2581.34(9) Å^3	2962.6(1) Å^3
Z	8	2	4	2	2
Density (calculated)	2.264 g/cm^3	1.543 g/cm^3	1.664 g/cm^3	1.761 g/cm^3	1.835 g/cm^3
Crystal size (mm^3)	0.145 x 0.095 x 0.042	0.09 x 0.069 x 0.04	0.100 x 0.055 x 0.040	0.100 x 0.081 x 0.043	0.146 x 0.122 x 0.043
Data/restraints/parameters	8415/ 122 / 548	2636/ 0 / 167	10871/ 0 / 559	12933/ 0 / 617	20661/ 0 / 845
Goodness-of-fit on F^2	1.205	1.082	1.085	1.048	1.022
Final R[a,b] indices [$I>2\sigma(I)$]	R_1 = 0.0826 wR_2 = 0.2091	R_1 = 0.0270 wR_2 = 0.0600	R_1 = 0.0354 wR_2 = 0.0611	R_1 = 0.0343 wR_2 = 0.0856	R_1 = 0.0279 wR_2 = 0.0603
R indices (all data)	R_1 = 0.0926 wR_2 = 0.2158	R_1 = 0.0321 wR_2 = 0.0619	R_1 = 0.0571 wR_2 = 0.0695	R_1 = 0.0415 wR_2 = 0.0882	R_1 = 0.0353 wR_2 = 0.0621

[a]$R_1 = \Sigma||F_0| - |F_c||/\Sigma|F_0|$

[b]$wR_2 = |[\Sigma[w(F_0^2 - F_c^2)^2] / \Sigma[w(F_0^2)^2]]1/2$, w = $1/\sigma^2 (F_0^2)$ + (aP)^2 + bP, where P = [max(0 or F_0^2) + 2(F_c^2)]/3.

Table 5.6. Selected bond distances (Å) and angles (°) for **1**•6.6 CH_2Cl_2.

Bi1–Rh1	2.527(1)	N1–Bi1–Rh1	80.1(2)
Bi2–Rh2	2.588(3)	N2–Rh1–Bi1	89.9(2)
Bi3–Rh3	2.602(2)	N3–Bi2–Rh2	81.1(3)
Bi1–N1	2.436(7)	N4–Rh2–Bi2	89.7(3)
Bi2–N3	2.38(1)	N5–Bi3–Rh3	81.2(3)
Bi3–N5	2.41(1)	N6–Rh3–Bi3	89.1(3)
Rh1–N2	2.040(7)		
Rh2–N4	2.04(1)		
Rh3–N6	2.05(1)		

Table 5.7. Selected bond distances (Å) and angles (°) for **2**•2 THF.

Bi1–Rh1	2.5196(6)	N1–Bi1–Rh1	79.55(7)
Bi1–N1	2.457(3)	N2–Rh1–Bi1	89.51(8)
Rh1–N2	2.052(3)		

Table 5.8. Selected bond distances (Å) and angles (°) for **3**.

Bi1–Rh1	2.5279(3)	N1–Bi1–Rh1	79.89(8)
Bi1–N1	2.439(3)	N3–Bi1–Rh1	79.01(8)
Bi1–N3	2.442(4)	N5–Bi1–Rh1	80.57(8)
Bi1–N5	2.466(4)	N7–Bi1–Rh1	80.05(8)
Bi1–N7	2.455(3)	N2–Rh1–Bi1	89.6(1)
Rh1–N2	2.048(3)	N4–Rh1–Bi1	90.8(1)
Rh1–N4	2.048(4)	N6–Rh1–Bi1	90.13(9)
Rh1–N6	2.050(3)	N8–Rh1–Bi1	88.93(9)
Rh1–N8	2.057(3)		

Table 5.9. Selected bond distances (Å) and angles (°) for **4**.

Bi1–Rh1	2.5420(3)	N1–Bi1–Rh1	79.99(8)
Bi1–N1	2.478(3)	N3–Bi1–Rh1	82.16(8)
Bi1–N3	2.380(3)	N5–Bi1–Rh1	81.11(8)
Bi1–N5	2.407(3)	N7–Bi1–Rh1	78.51(8)
Bi1–N7	2.486(3)	N2–Rh1–Bi1	92.69(9)
Rh1–N2	2.037(3)	N4–Rh1–Bi1	90.05(9)
Rh1–N4	2.063(3)	N6–Rh1–Bi1	89.79(9)
Rh1–N6	2.049(3)	N8–Rh1–Bi1	90.94(9)
Rh1–N8	2.076(3)		

Table 5.10. Selected bond distances (Å) and angles (°) for **5**.

Bi1–Rh1	2.5407(2)	N1–Bi1–Rh1	81.99(4)
Bi1–N1	2.398(2)	N3–Bi1–Rh1	79.71(4)
Bi1–N3	2.495(2)	N5–Bi1–Rh1	79.11(4)
Bi1–N5	2.476(2)	N7–Bi1–Rh1	80.72(4)
Bi1–N7	2.433(2)	N2–Rh1–Bi1	90.47(5)
Rh1–N2	2.063(2)	N4–Rh1–Bi1	92.71(5)
Rh1–N4	2.033(2)	N6–Rh1–Bi1	90.38(5)
Rh1–N6	2.074(2)	N8–Rh1–Bi1	90.37(5)
Rh1–N8	2.042(2)		
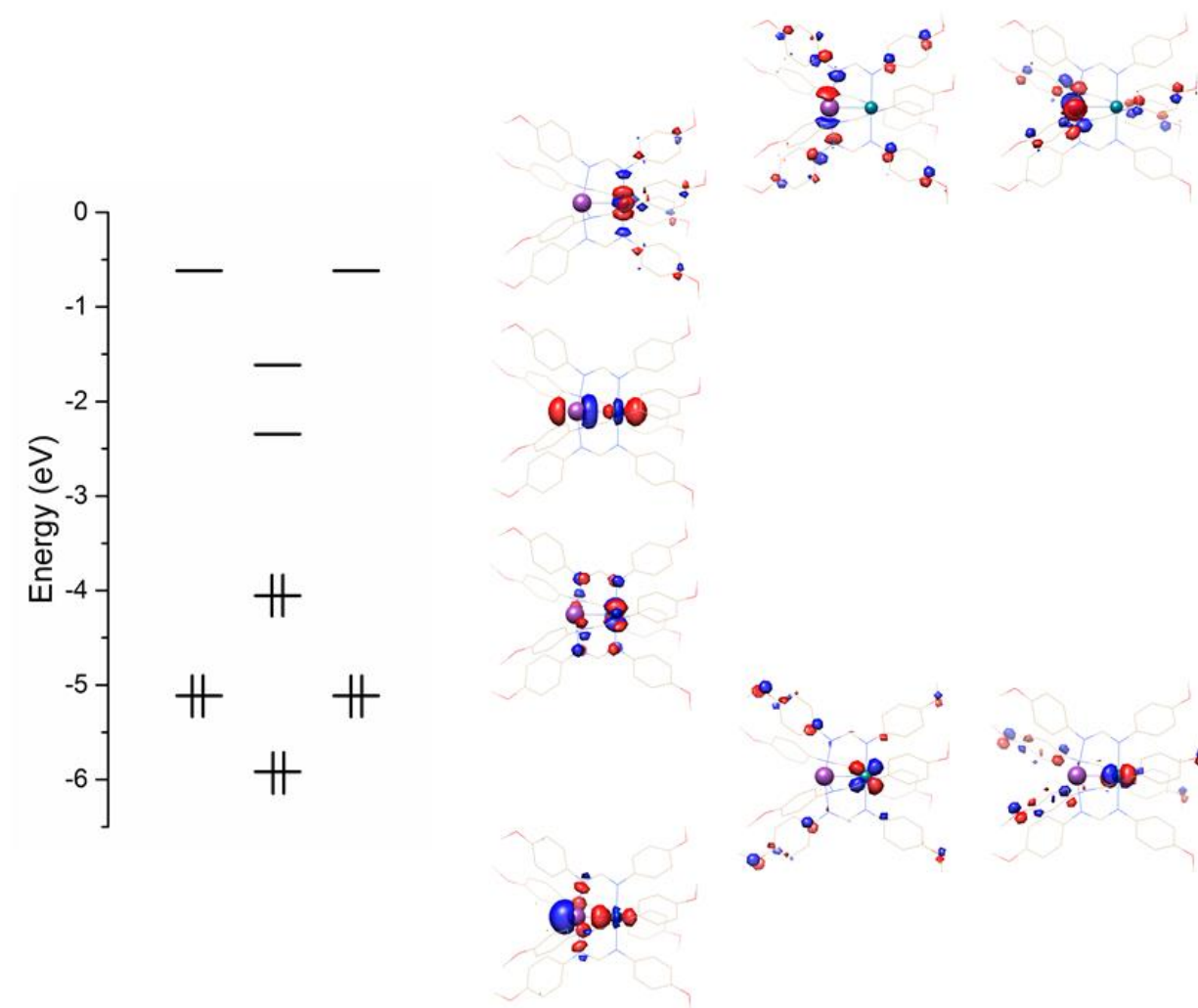
Figure 5.15. Calculated molecular orbital diagram of **1** (left) and metal-based molecular orbitals for **1** (right).
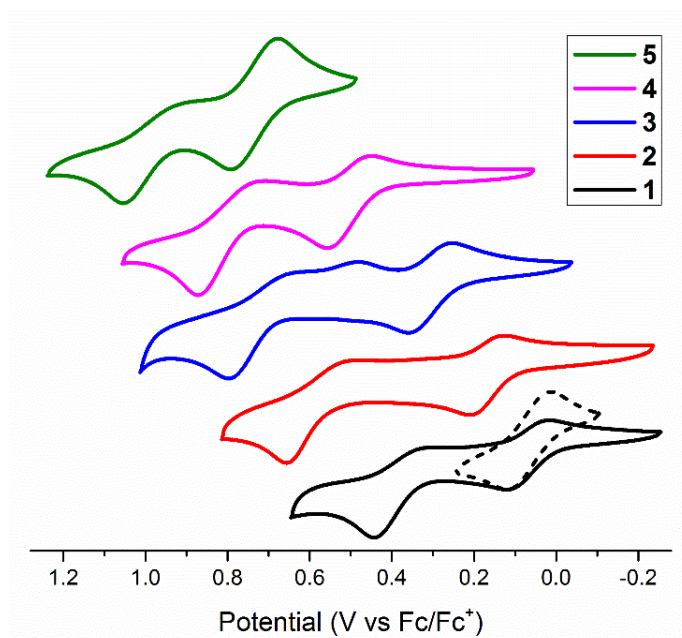
Figure 5.16. Cyclic voltammograms of **1** - **5** in CH_2Cl_2 with scan rate = 100 mV/s (0.1 M TBAH). Black dotted line is the $[BiRh]^{4+/5+}$ redox couple of **1**.
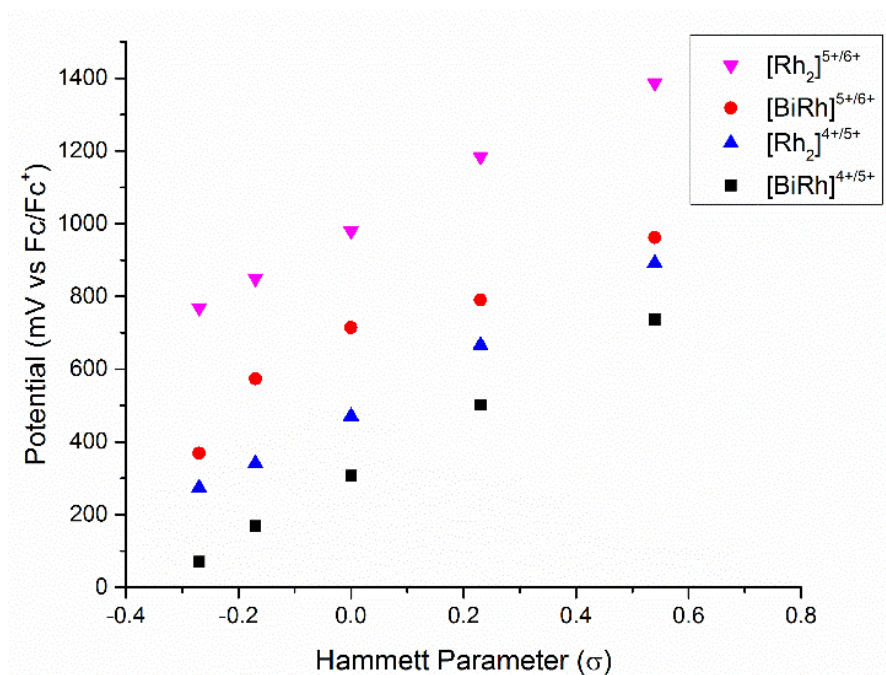
Figure 5.17. Hammett plots of potential *vs σ* for $[BiRh(form)_4]^{4+/5+}$ (black square), $[Rh_2(form)_4]^{4+/5+}$ (blue triangle), $[BiRh(form)_4]^{5+/6+}$ (red circle) and $[Rh_2(form)_4]^{5+/6+}$ (purple triangle) couples.

Table 5.11. Comparison of electrochemical data[a] for compounds **1** - **5** and $Rh_2(form)_4$.

Compound	$[MRh]^{4+/5+}$ $E_{1/2}$ (mV)	$[MRh]^{5+/6+}$ $E_{1/2}$ (mV)	Reference
1	70.6	369	This work
2	168	573	This work
3	307	714	This work
4	502	790	This work
5	736	962	This work
$Rh_2(p\text{-OMe-DArF})_4$	274	769	37
$Rh_2(DFM)_4$	341	850	37
$Rh_2(DPhF)_4$	471	980	37
$Rh_2(p\text{-Cl-DArF})_4$	667	1184	37
$Rh_2(p\text{-CF}_3\text{-DArF})_4$	891	1387	37

[a]All potentials are *vs* Fc/Fc^+ in CH_2Cl_2.

Table 5.12. Optimized XYZ coordinates for **1**.

Bi	-0.00000	-0.00000	2.60920
Rh	0.00000	0.00000	0.00000
O	1.55615	5.68585	6.69017
N	-0.00004	2.09458	-0.01370
C	-0.47654	2.77705	-1.16595
C	-1.56354	3.67683	-1.08426
H	-2.05767	3.83232	-0.11720
C	-2.04629	4.35404	-2.21870
H	-2.89368	5.03935	-2.10913
C	-1.45122	4.12847	-3.47933
C	-0.36796	3.22245	-3.57402
H	0.09363	3.05916	-4.55558
C	0.11173	2.56221	-2.43809
H	0.96380	1.87956	-2.52555
O	-1.84362	4.72521	-4.64125
C	-2.93192	5.64667	-4.59886
H	-2.70960	6.51092	-3.94290
H	-3.86483	5.16072	-4.25205
H	-3.07398	6.00397	-5.63030
N	0.61252	2.35875	2.24717
C	0.44278	5.24812	4.65247
H	-0.08337	6.20023	4.79602
C	2.03866	3.60187	5.46885
H	2.76709	3.25030	6.20746
C	0.85646	3.21127	3.34004
C	0.30127	2.84262	1.04800
H	0.31629	3.93895	0.89368
C	1.37448	4.83703	5.63420
C	2.47861	5.30999	7.70998
H	2.46769	6.12311	8.45207
H	3.50618	5.19787	7.31128
H	2.17980	4.36457	8.20415
C	1.77996	2.81001	4.33556
H	2.32425	1.86547	4.20460
C	0.18035	4.44812	3.53539
H	-0.57397	4.77866	2.81079
O	-1.55078	-5.68047	6.69533
N	-0.00006	-2.09450	-0.01310
C	0.47635	-2.77664	-1.16565
C	1.56375	-3.67596	-1.08434
H	2.05805	-3.83151	-0.11740
C	2.04661	-4.35264	-2.21910

H	2.89440	-5.03746	-2.10987
C	1.45124	-4.12684	-3.47957
C	0.36748	-3.22130	-3.57378
H	-0.09429	-3.05795	-4.55522
C	-0.11222	-2.56169	-2.43751
H	-0.96469	-1.87940	-2.52465
O	1.84384	-4.72297	-4.64175
C	2.93264	-5.64378	-4.59984
H	2.71088	-6.50843	-3.94420
H	3.86528	-5.15747	-4.25296
H	3.07472	-6.00068	-5.63141
N	-0.61165	-2.35832	2.24783
C	-0.43945	-5.24512	4.65593
H	0.08701	-6.19702	4.80017
C	-2.03488	-3.59825	5.47185
H	-2.76275	-3.24590	6.21074
C	-0.85471	-3.20989	3.34156
C	-0.30069	-2.84241	1.04870
H	-0.31532	-3.93885	0.89462
C	-1.37028	-4.83297	5.63810
C	-2.47198	-5.30332	7.71572
H	-2.46002	-6.11546	8.45893
H	-3.49998	-5.19171	7.31821
H	-2.17253	-4.35721	8.20825
C	-1.77745	-2.80766	4.33744
H	-2.32204	-1.86332	4.20580
C	-0.17820	-4.44639	3.53771
H	0.57558	-4.77769	2.81281
O	5.68356	-1.54664	6.69420
N	2.09439	0.00034	-0.01317
C	2.77634	0.47764	-1.16548
C	3.67377	1.56665	-1.08393
H	3.82783	2.06138	-0.11692
C	4.35017	2.05052	-2.21834
H	5.03342	2.89954	-2.10899
C	4.12614	1.45453	-3.47880
C	3.22268	0.36906	-3.57345
H	3.06072	-0.09324	-4.55487
C	2.56325	-0.11165	-2.43735
H	1.88244	-0.96524	-2.52470
O	4.72217	1.84793	-4.64077
C	5.64089	2.93852	-4.59872
H	6.50559	2.71859	-3.94257
H	5.15253	3.87026	-4.25216

H	5.99794	3.08105	-5.63009
N	2.35896	-0.61137	2.24765
C	5.24666	-0.43663	4.65449
H	6.19831	0.09038	4.79805
C	3.60103	-2.03266	5.47185
H	3.24940	-2.76028	6.21125
C	3.21109	-0.85365	3.34112
C	2.84275	-0.30012	1.04852
H	3.93902	-0.31401	0.89428
C	4.83542	-1.36721	5.63726
C	5.30743	-2.46758	7.71526
H	6.11977	-2.45486	8.45803
H	5.19615	-3.49591	7.31836
H	4.36133	-2.16846	8.20798
C	2.80977	-1.77603	4.33758
H	1.86569	-2.32117	4.20663
C	4.44736	-0.17637	3.53651
H	4.77786	0.57725	2.81111
O	-5.68296	1.55938	6.69150
N	-2.09459	0.00025	-0.01353
C	-2.77744	-0.47625	-1.16562
C	-3.67679	-1.56361	-1.08367
H	-3.83157	-2.05790	-0.11658
C	-4.35428	-2.04646	-2.21786
H	-5.03913	-2.89421	-2.10821
C	-4.12954	-1.45093	-3.47850
C	-3.22407	-0.36721	-3.57345
H	-3.06158	0.09464	-4.55493
C	-2.56355	0.11247	-2.43765
H	-1.88133	0.96491	-2.52520
O	-4.72667	-1.84343	-4.64023
C	-5.64760	-2.93211	-4.59768
H	-6.51167	-2.71027	-3.94123
H	-5.16111	-3.86480	-4.25134
H	-6.00544	-3.07393	-5.62891
N	-2.35821	0.61300	2.24735
C	-5.24668	0.44520	4.65391
H	-6.19894	-0.08051	4.79805
C	-3.59929	2.04067	5.46904
H	-3.24711	2.76916	6.20725
C	-3.21027	0.85762	3.34038
C	-2.84238	0.30183	1.04828
H	-3.93878	0.31710	0.89422
C	-4.83467	1.37704	5.63524

C	-5.30617	2.48211	7.71073
H	-6.11898	2.47175	8.45327
H	-5.19372	3.50944	7.31173
H	-4.36064	2.18296	8.20461
C	-2.80809	1.78117	4.33551
H	-1.86340	2.32511	4.20387
C	-4.44725	0.18208	3.53659
H	-4.77849	-0.57230	2.81239

Table 5.13. Optimized XYZ coordinates for [**1**]⁺.

Bi	0.00000	0.00000	2.62530
Rh	0.00000	0.00000	0.00000
O	1.83589	5.59410	6.64713
N	-0.00005	2.07252	-0.01416
C	-0.49218	2.76238	-1.15908
C	-1.57101	3.66831	-1.04625
H	-2.04194	3.82688	-0.06829
C	-2.07539	4.34742	-2.16788
H	-2.91720	5.03560	-2.03896
C	-1.50646	4.12280	-3.44244
C	-0.42760	3.21267	-3.56346
H	0.01452	3.05388	-4.55435
C	0.07081	2.54538	-2.44145
H	0.92010	1.86206	-2.54866
O	-1.91841	4.72232	-4.58935
C	-2.99904	5.65596	-4.52764
H	-2.75331	6.51717	-3.87730
H	-3.92803	5.17659	-4.16360
H	-3.15506	6.01209	-5.55694
N	0.68978	2.33329	2.22193
C	0.68764	5.22622	4.62205
H	0.21831	6.20641	4.76940
C	2.19345	3.48721	5.43437
H	2.90461	3.09637	6.16950
C	0.97900	3.17084	3.31552
C	0.34617	2.82427	1.03852
H	0.37378	3.91746	0.87688
C	1.60174	4.76066	5.59998
C	2.74282	5.17592	7.66972
H	2.77629	5.99548	8.40313
H	3.75912	5.00757	7.26487
H	2.39135	4.25321	8.16983
C	1.88041	2.71175	4.30703

H	2.36905	1.73757	4.17520
C	0.37548	4.44544	3.50781
H	-0.36091	4.82069	2.78707
O	-1.83482	-5.58914	6.65078
N	0.00007	-2.07243	-0.01374
C	0.49255	-2.76213	-1.15862
C	1.57162	-3.66785	-1.04555
H	2.04236	-3.82625	-0.06751
C	2.07640	-4.34679	-2.16702
H	2.91842	-5.03475	-2.03804
C	1.50771	-4.12244	-3.44166
C	0.42864	-3.21252	-3.56294
H	-0.01338	-3.05391	-4.55385
C	-0.07029	-2.54541	-2.44105
H	-0.91962	-1.86219	-2.54834
O	1.92001	-4.72179	-4.58855
C	3.00106	-5.65488	-4.52666
H	2.75554	-6.51626	-3.87640
H	3.92970	-5.17514	-4.16251
H	3.15735	-6.01104	-5.55586
N	-0.68995	-2.33268	2.22217
C	-0.68763	-5.22364	4.62475
H	-0.21843	-6.20378	4.77281
C	-2.19276	-3.48354	5.43603
H	-2.90342	-3.09178	6.17110
C	-0.97902	-3.16955	3.31628
C	-0.34605	-2.82395	1.03898
H	-0.37331	-3.91720	0.87752
C	-1.60109	-4.75683	5.60263
C	-2.74088	-5.16956	7.67358
H	-2.77405	-5.98820	8.40798
H	-3.75737	-5.00131	7.26943
H	-2.38875	-4.24627	8.17238
C	-1.88003	-2.70919	4.30777
H	-2.36856	-1.73504	4.17511
C	-0.37580	-4.44405	3.50959
H	0.36017	-4.82022	2.78883
O	5.59180	-1.82822	6.65074
N	2.07254	0.00025	-0.01394
C	2.76256	0.49329	-1.15848
C	3.66598	1.57414	-1.04505
H	3.82254	2.04565	-0.06697
C	4.34513	2.07971	-2.16610
H	5.03138	2.92313	-2.03681

C	4.12310	1.50987	-3.44067
C	3.21558	0.42889	-3.56230
H	3.05882	-0.01391	-4.55320
C	2.54825	-0.07072	-2.44075
H	1.86673	-0.92142	-2.54833
O	4.72287	1.92282	-4.58713
C	5.65369	3.00579	-4.52489
H	6.51493	2.76239	-3.87372
H	5.17173	3.93364	-4.16172
H	6.01052	3.16227	-5.55390
N	2.33301	-0.68907	2.22231
C	5.22441	-0.68243	4.62428
H	6.20404	-0.21193	4.77187
C	3.48627	-2.18918	5.43674
H	3.09551	-2.89994	6.17211
C	3.17031	-0.97687	3.31648
C	2.82409	-0.34535	1.03890
H	3.91739	-0.37211	0.87763
C	4.75894	-1.59599	5.60269
C	5.17346	-2.73421	7.67419
H	5.99232	-2.76606	8.40842
H	5.00640	-3.75113	7.27058
H	4.24991	-2.38286	8.17301
C	2.71138	-1.87796	4.30850
H	1.73775	-2.36757	4.17622
C	4.44429	-0.37209	3.50913
H	4.81925	0.36409	2.78804
O	-5.59065	1.84228	6.64806
N	-2.07271	0.00014	-0.01366
C	-2.76288	-0.49243	-1.15813
C	-3.66775	-1.57204	-1.04475
H	-3.82528	-2.04316	-0.06663
C	-4.34728	-2.07691	-2.16591
H	-5.03471	-2.91938	-2.03649
C	-4.12421	-1.50775	-3.44043
C	-3.21503	-0.42803	-3.56220
H	-3.05747	0.01427	-4.55311
C	-2.54743	0.07088	-2.44055
H	-1.86477	0.92076	-2.54807
O	-4.72423	-1.92003	-4.58707
C	-5.65671	-3.00161	-4.52472
H	-6.51771	-2.75677	-3.87369
H	-5.17622	-3.93007	-4.16119
H	-6.01357	-3.15781	-5.55371

N	-2.33266	0.69086	2.22229
C	-5.22455	0.69242	4.62372
H	-6.20507	0.22388	4.77172
C	-3.48408	2.19752	5.43416
H	-3.09233	2.90888	6.16849
C	-3.16967	0.98134	3.31592
C	-2.82404	0.34687	1.03910
H	-3.91728	0.37468	0.87766
C	-4.75785	1.60682	5.60071
C	-5.17133	2.74977	7.66981
H	-5.99045	2.78445	8.40358
H	-5.00248	3.76555	7.26412
H	-4.24855	2.39802	8.16969
C	-2.70934	1.88308	4.30660
H	-1.73494	2.37095	4.17399
C	-4.44460	0.37898	3.50927
H	-4.82077	-0.35770	2.78916
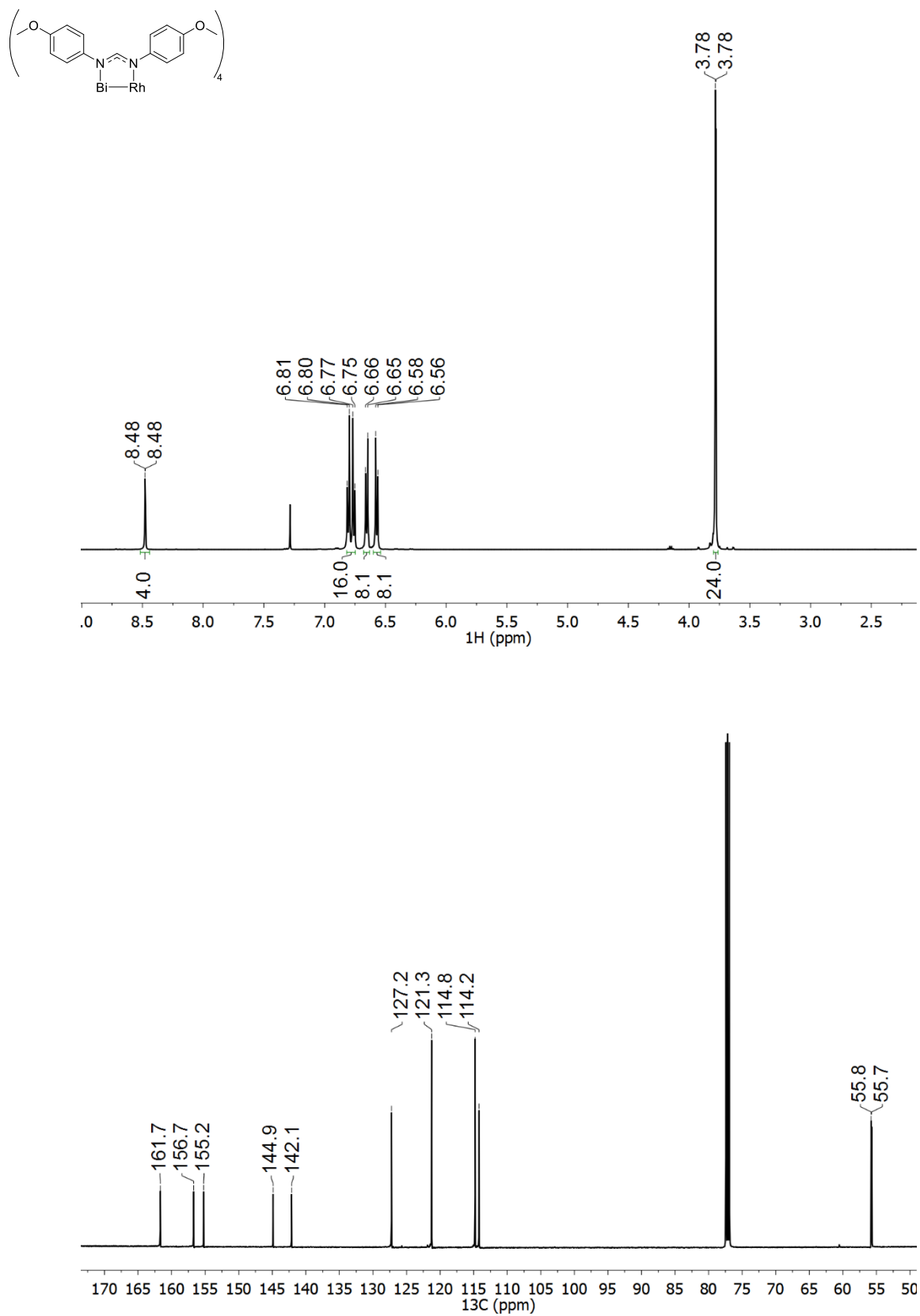
Figure 5.18. NMR spectra of **1** at room temperature in CDCl$_3$ (^{1}H (top), ^{13}C{^{1}H} (bottom)).
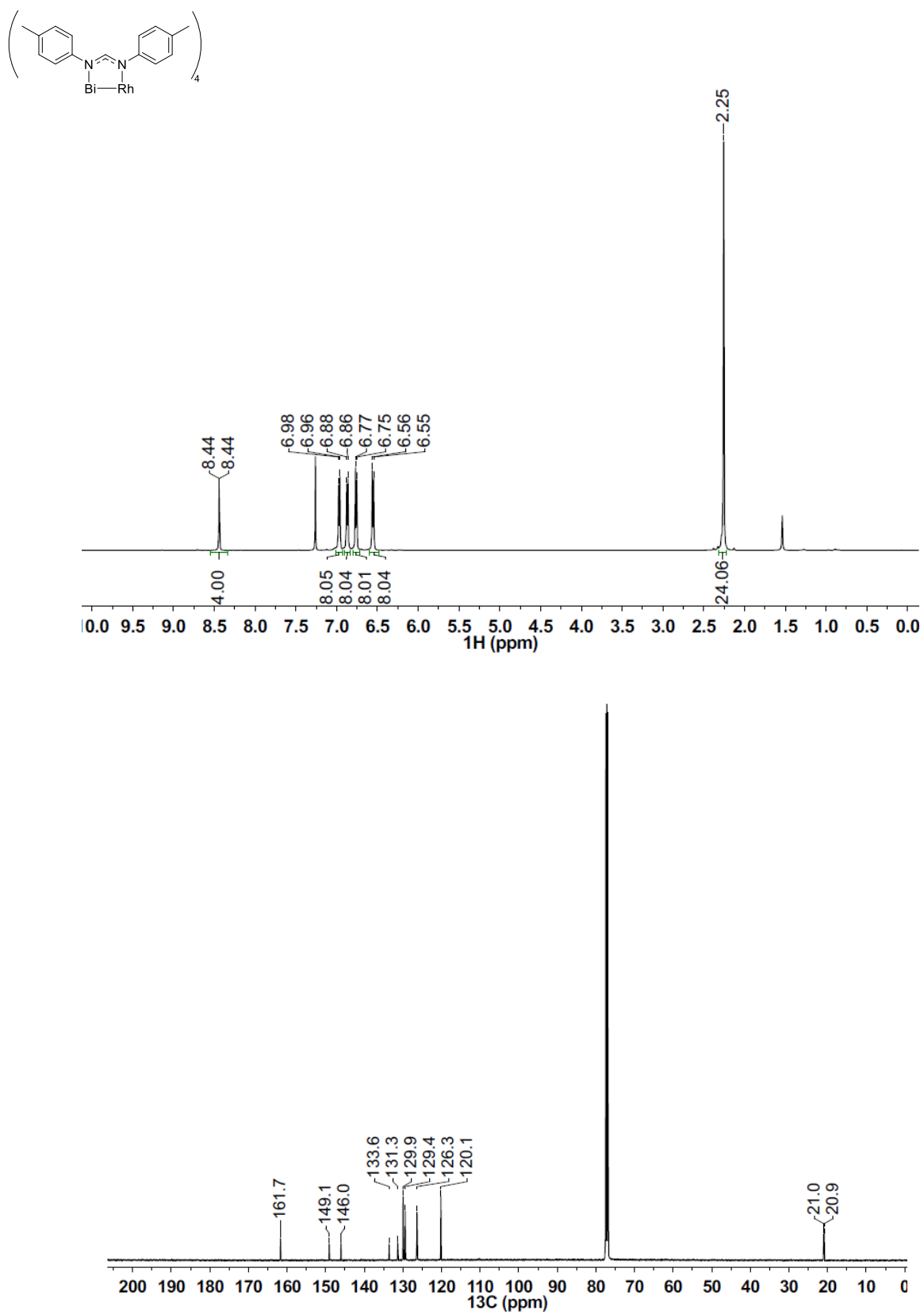
Figure 5.19. NMR spectra of **2** at room temperature in CDCl$_3$ (^{1}H (top), ^{13}C{^{1}H} (bottom)).
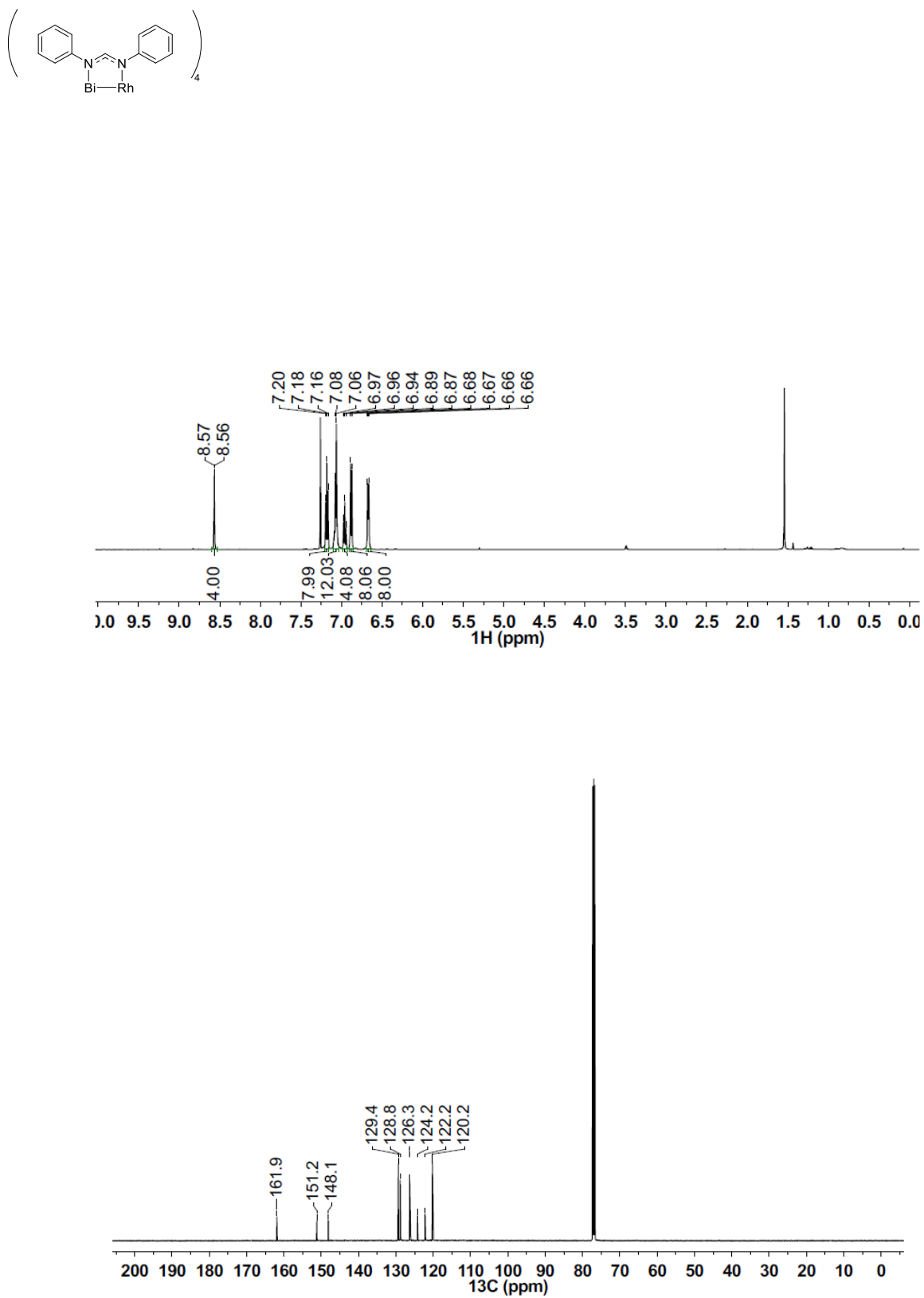
Figure 5.20. NMR spectra of **3** at room temperature in CDCl$_3$ (^{1}H (top), ^{13}C{^{1}H} (bottom)).
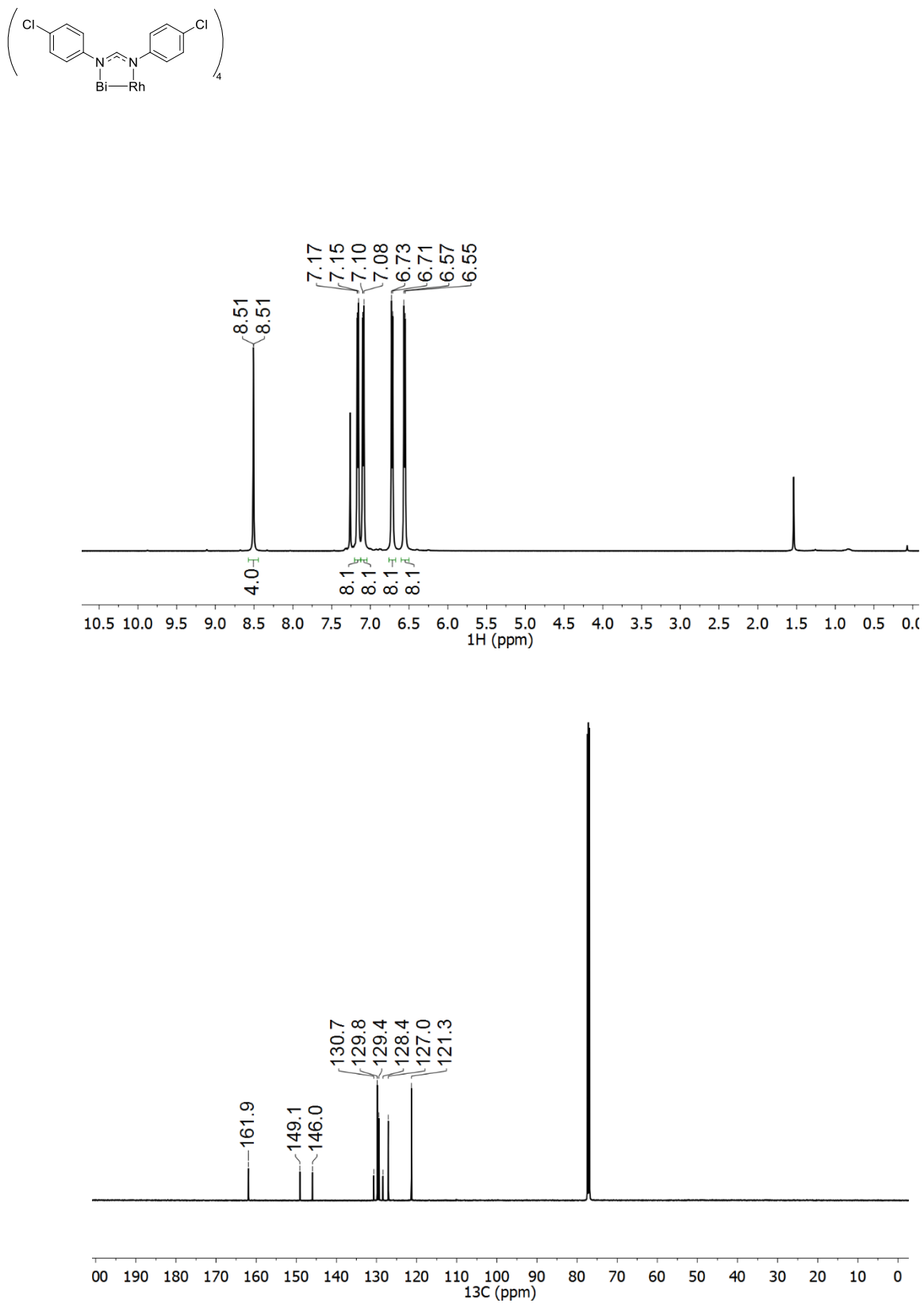
Figure 5.21. NMR spectra of **4** at room temperature in CDCl₃ (¹H (top), ¹³C{¹H} (bottom)).

1H (ppm)

13C (ppm)
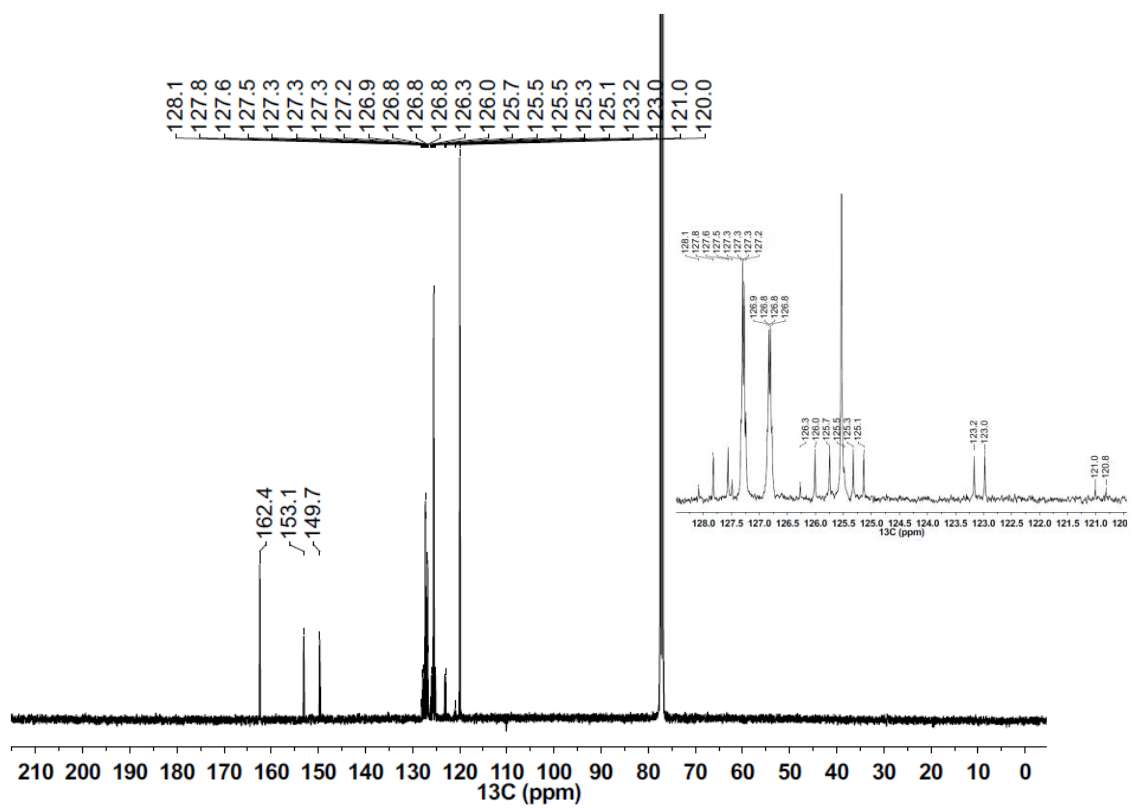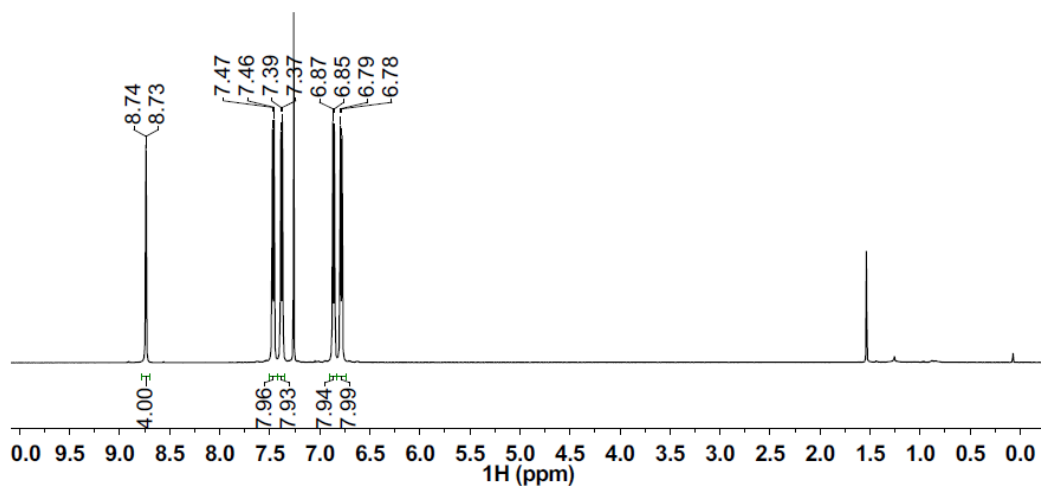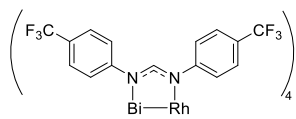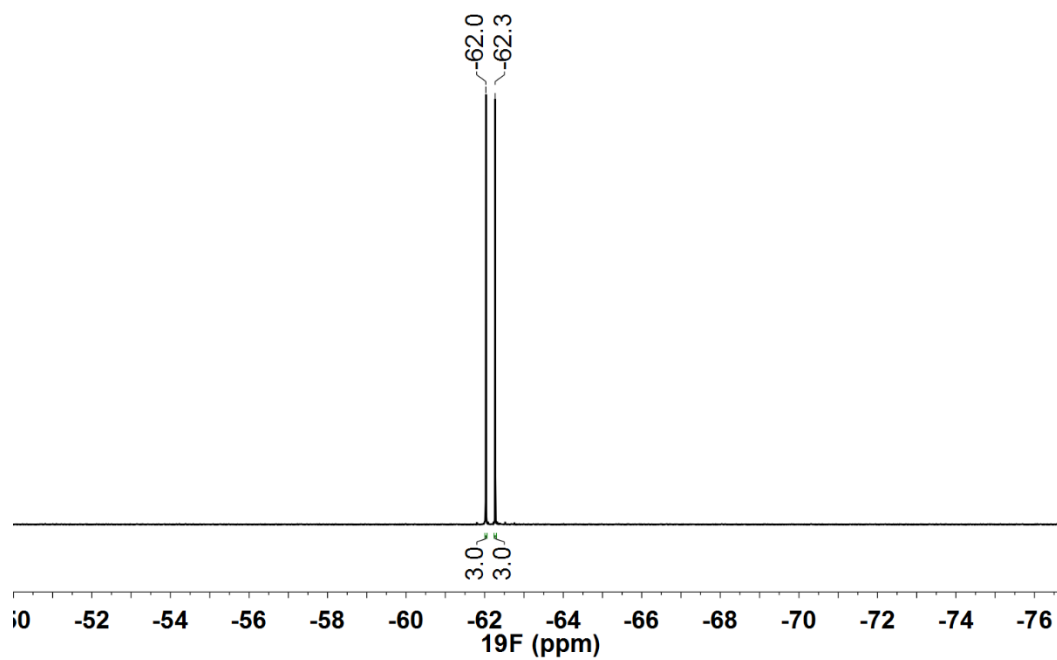
Figure 5.22. NMR spectra of **5** at room temperature in CDCl$_3$ (^{1}H (top), ^{13}C{^{1}H} (middle) and ^{19}F{^{1}H} (bottom)).

5.8 References

(1)   Kulbachinskii, V. A.; Kaminskii, A. Y.; Kindo, K.; Narumi, Y.; Suga, K.; Lostak, P.; Svanda, P. *Physica B: Condensed Matter* **2002**, *311*, 292.

(2)   Chen, Y. L.; Chu, J. H.; Analytis, J. G.; Liu, Z. K.; Igarashi, K.; Kuo, H. H.; Qi, X. L.; Mo, S. K.; Moore, R. G.; Lu, D. H.; Hashimoto, M.; Sasagawa, T.; Zhang, S. C.; Fisher, I. R.; Hussain, Z.; Shen, Z. X. *Science* **2010**, *329*, 659.

(3)   Hor, Y. S.; Roushan, P.; Beidenkopf, H.; Seo, J.; Qu, D.; Checkelsky, J. G.; Wray, L. A.; Hsieh, D.; Xia, Y.; Xu, S. Y.; Qian, D.; Hasan, M. Z.; Ong, N. P.; Yazdani, A.; Cava, R. J. *Phys. Rev. B* **2010**, *81*, 195203.

(4)   Liu, W.; West, D.; He, L.; Xu, Y.; Liu, J.; Wang, K.; Wang, Y.; van der Laan, G.; Zhang, R.; Zhang, S.; Wang, K. L. *ACS Nano* **2015**, *9*, 10237.

(5)   Clarke, S. M.; Freedman, D. E. *Inorg. Chem.* **2015**, *54*, 2765.

(6)   Thurston, J. H.; Whitmire, K. H. *Inorg. Chem.* **2003**, *42*, 2014.

(7)   Thurston, J. H.; Kumar, A.; Hofmann, C.; Whitmire, K. H. *Inorg. Chem.* **2004**, *43*, 8427.

(8)   Thurston, J. H.; Trahan, D.; Ould-Ely, T.; Whitmire, K. H. *Inorg. Chem.* **2004**, *43*, 3299.

(9)   Dikarev, E. V.; Zhang, H.; Li, B. *J. Am. Chem. Soc.* **2005**, *127*, 6156.

(10)   Stavila, V.; Thurston, J. H.; Whitmire, K. H. *Inorg. Chem.* **2009**, *48*, 6945.

(11)   Stamatatos, T. C.; Oliver, K.; Abboud, K. A.; Christou, G. *Inorg. Chem.* **2011**, *50*, 5272.

(12)   Hołyńska, M. *Inorg. Chem. Commun.* **2012**, *20*, 322.

(13)   Bulimestru, I.; Shova, S.; Popa, N.; Roussel, P.; Capet, F.; Vannier, R. N.; Djelal, N.; Burylo, L.; Wignacourt, J. P.; Gulea, A.; Whitmire, K. H. *Chem. Mater.* **2014**, *26*, 6092.

(14)   Dikarev, E. V.; Gray, T. G.; Li, B. *Angew. Chem., Int. Ed.* **2005**, *44*, 1721.

(15)   Filatov, A. S.; Napier, M.; Vreshch, V. D.; Sumner, N. J.; Dikarev, E. V.; Petrukhina, M. A. *Inorg. Chem.* **2012**, *51*, 566.

(16)   Sunderland, T. L.; Berry, J. F. *Dalton Trans.* **2016**, *45*, 50.

(17)   Sunderland, T. L.; Berry, J. F. *J. Coord. Chem.* **2016**, *69*, 1949.

(18)   Clouston, L. J.; Bernales, V.; Cammarota, R. C.; Carlson, R. K.; Bill, E.; Gagliardi, L.; Lu, C. C. *Inorg. Chem.* **2015**, *54*, 11669.

(19)   Eisenhart, R. J.; Rudd, P. A.; Planas, N.; Boyce, D. W.; Carlson, R. K.; Tolman, W. B.; Bill, E.; Gagliardi, L.; Lu, C. C. *Inorg. Chem.* **2015**, *54*, 7579.

(20)   Bradley, W.; Wright, I. *J. Chem. Soc.* **1956**, 640.

(21)   Bruker-AXS, *SMART* Program*,* Madison, Wisconsin, USA, **2009**.

(22)   Sheldrick, G. *Acta Cryst. A* **2008**, *64*, 112.

(23)   Dolomanov, O. V.; Bourhis, L. J.; Gildea, R. J.; Howard, J. A. K.; Puschmann, H. *J. Appl. Crystallogr.* **2009**, *42*, 339.

(24)   Spek, A. *Acta Cryst. D* **2009**, *65*, 148.

(25)   Stoll, S.; Schweiger, A. *J. Mag. Res.* **2006**, *178*, 42.

(26)   Neese, F. *ORCA- an ab initio, Density Functional and Semiempirical program package*, University of Bonn: Bonn, **2006**.

(27)   Becke, A. D. *J. Chem. Phys.* **1993**, *98*, 5648.

(28)   Pantazis, D. A.; Chen, X. Y.; Landis, C. R.; Neese, F. *J. Chem. Theory Comput.* **2008**, *4*, 908.

(29)   Wullen, C. V. *J. Chem. Phys.* **1998**, *109*, 392.

(30)   Eichkorn, K.; Treutler, O.; Öhm, H.; Häser, M.; Ahlrichs, R. *Chem. Phys. Lett.* **1995**, *240*, 283.

(31)   Sinnecker, S.; Rajendran, A.; Klamt, A.; Diedenhofen, M.; Neese, F. *J. Phys. Chem. A* **2006**, *110*, 2235.

(32)   Klamt, A.; Schuurmann, G. *J. Chem. Soc., Perkin Trans. 2* **1993**, 799.

(33)   Pettersen, E. F.; Goddard, T. D.; Huang, C. C.; Couch, G. S.; Greenblatt, D. M.; Meng, E. C.; Ferrin, T. E. *J. Comput. Chem.* **2004**, *25*, 1605.

(34)   Berry, J. F.; Bill, E.; Bothe, E.; Cotton, F. A.; Dalal, N. S.; Ibragimov, S. A.; Kaur, N.; Liu, C. Y.; Murillo, C. A.; Nellutla, S.; North, J. M.; Villagrán, D. *J. Am. Chem. Soc.* **2007**, *129*, 1393.

(35)   Cotton, F. A.; Murillo, C. A.; Walton, R. A. *Multiple Bonds Between Metal Atoms*. 3rd ed.; Springer Science and Business Media, Inc.: New York, **2005**.

(36)   Lin, C.; Protasiewicz, J. D.; Ren, T. *Inorg. Chem.* **1996**, *35*, 7455.

(37)   Ren, T.; Lin, C.; Valente, E. J.; Zubkowski, J. D. *Inorg. Chim. Acta* **2000**, *297*, 283.

(38)   Lin, C.; Protasiewicz, J., D.; Smith, E. T.; Ren, T. *J. Chem. Soc., Chem. Commun.* **1995**, 2257.

(39)   Lin, C.; Protasiewicz, J. D.; Smith, E. T.; Ren, T. *Inorg. Chem.* **1996**, *35*, 6422.

(40)   Lin, C.; Ren, T.; Valente, E. J.; Zubkowski, J. D.; Smith, E. T. *Chem. Lett.* **1997**, *26*, 753.

(41)   Ren, T. *Coord. Chem. Rev.* **1998**, *175*, 43.

(42)   Lin, C.; Ren, T.; Valente, E. J.; Zubkowski, J. D. *J. Organomet. Chem.* **1999**, *579*, 114.

(43)   Pearson, R. G. *J. Am. Chem. Soc.* **1988**, *110*, 2092.

(44)   McGlinchey, M. J. *Inorg. Chem.* **1980**, *19*, 1392.

(45)   San Filippo, J. *Inorg. Chem.* **1972**, *11*, 3140.

(46)   Bear, J. L.; Yao, C. L.; Lifsey, R. S.; Korp, J. D.; Kadish, K. M. *Inorg. Chem.* **1991**, *30*, 336.

(47)   Cotton, F. A.; Li, Z.; Murillo, C. A.; Poplaukhin, P. V.; Reibenspies, J. H. *J. Clust. Sci.* **2008**, *19*, 89.

(48)   Cotton, F. A.; Matonic, J. H.; Murillo, C. *Inorg. Chim. Acta* **1997**, *264*, 61.

(49)   Cotton, F. A.; Ren, T. *J. Am. Chem. Soc.* **1992**, *114*, 2237.

(50)   Cotton, F. A.; Ren, T. *J. Am. Chem. Soc.* **1992**, *114*, 2495.

(51)   Piraino, P.; Bruno, G.; Lo Schiavo, S.; Laschi, F.; Zanello, P. *Inorg. Chem.* **1987**, *26*, 2205.

(52)   Cotton, F. A.; Daniels, L. M.; Murillo, C. A. *Angew. Chem., Int. Ed. Engl.* **1992**, *31*, 737.

(53)   McConnell, H. M. *J. Chem. Phys.* **1957**, *27*, 226.

(54)   Harris, R. K. *Nuclear Magnetic Resonance Spectroscopy: A Physiocochemical View*. Longman: London, **1986**.

(55)   Bain, G. A.; Berry, J. F. *J. Chem. Ed.* **2008**, *85*, 532.

(56)   Kahn, O. *Molecular Magnetism*. Wiley-VCH: New York, **1993**.

(57)   Li, G.; Dzubak, A. L.; Mulla, A.; Brogden, D. W.; Berry, J. F.; Gagliardi, L. *Chem. Eur. J.* **2012**, *18*, 1737.

(58)   Though small similar effects do exist in organic compounds. For example, the relatively low-energy n→π* excitation in pyridine contributes to the *o*-H-atoms appearing ~ 1 ppm downfield of the *m*- and *p*-H-atoms. Protonation of pyridine (i.e., elimination of the n→ π* excitation) raises the chemical shifts of the *m*- and *p*-H-atoms uniformly by 0.6 - 0.7 ppm, but only raises the *o*-H-atom chemical shifts by 0.3 ppm.[59]

(59)   Gowland, J. A.; McClelland, R. A. *Can. J. Chem.* **1979**, *57*, 2140.

Chapter 6

Preliminary Studies on the Synthesis and Application of

Chiral BiRh Tetracarboxylate Complexes in C–H Functionalization Catalysis

Sunderland, T. L.;[a] Tortoreto, C.;[b] Davies, H. M. L.;[b] Berry, J. F.[a]

[a]Department of Chemistry, University of Wisconsin–Madison, 1101 University Avenue, Madison, WI 53706, United States

[b]Department of Chemistry, Emory University, 1515 Dickey Drive, Atlanta, GA 30322, United States

Contributions: Tortoreto, C. performed all of the catalysis experiments. All other work was done by Sunderland, T. L.

6.1 Abstract

The first two examples of homochiral heterobimetallic complexes containing rhodium, BiRh(*S*-TBSP)$_4$ (**1**) and BiRh(*S*-BTPCP)$_4$ (**2**), were synthesized (TBSP = *N*-(*p*-tertbutylphenylsulfonyl)-prolinate, BTPCP = 1-(4-bromophenyl)-2,2-diphenylcyclopropanecarboxylate). The solid state structure of **1**•1.12 THF shows that the complex adopts a C$_4$-symmetric geometry with the aryl rings of the equatorial ligands pointing away from the Bi–Rh single bond; all equatorial ligands are canted towards the Rh-axial site due to an ~ 0.4 Å difference in metal–O bond distances. Complex **1** activates donor/acceptor diazo compounds and shows modest yields in cyclopropanation reactions but enhances the enantioselectivity from 78% to 86% (enantiomeric excess) for cyclopropanation of styrene compared to the analogous homobimetallic complex Rh$_2$(*S*-TBSP)$_4$ (**5**). Both complexes **1** and **2** are able to catalyze carbene insertion reactions into C–H bonds with a select number of substrates. Complex **1** provides enhanced regioselectivity for 1° C–H bonds compared to **5** and in three examples actually *reverses* the regioselectivity from either 3° or 2° to 1° for activated C–H bonds.

6.2 Introduction

Dirhodium(II,II) tetraacetate was first employed as a catalyst in 1973 by Teyssié and coworkers for the decomposition of diazo compounds.[1] Equatorial ligand exchange of carboxylates ((O, O) donors) for other mono-anionic ligands such as carboxamidates ((O, N) donors) and amidinates ((N, N) donors) allows for fine tuning of both the electronic structure of the bimetallic unit and the steric environment surrounding the metal-axial sites, where catalysis generally occurs. This strategy led to the preparation of chiral dirhodium(II,II) complexes in the 1990's by Brunner,[2] McKervey,[3] Ikegami[4] and Hashimoto.[4] These complexes generally possess chiral carboxylate ligands by exploiting the chirality of amino acids, or more generally, α-substituted carboxylic acids. Since then, dirhodium tetracarboxylate complexes have been the

most widely used catalysts for metal carbene reactions, and are very active catalysts, capable of efficient site selective and stereoselective transformations. Modification of the electronic and/or steric properties of the equatorial ligands have allowed for careful control of both reactivity and selectivity. In particular, the proline derivative $Rh_2(DOSP)_4$ (DOSP = *N*-(*p*-dodecylphenylsulfonyl)-prolinate), developed in the Davies group, has represented a breakthrough in site-selective and stereoselective metal carbene reactions, and is proven to be versatile and effective in both cyclopropanation and C–H insertion reactions.[5] Recently, a new class of sterically hindered cyclopropane-carboxylate ligands has been introduced that has allowed for control of the selectivity at both activated[6,7] and unactivated[8] C–H bonds.

While steric and electronic control by careful choice of equatorial ligands has been a widespread strategy in catalysis, alternative strategies have been underexplored. Three alternative catalyst design strategies recently described in the literature have been either the use of mixed valent dirhodium(II,III) species,[9,10] use of complexes with axially coordinated N-heterocyclic carbenes[11,12] and catalysts with mixed ligand systems.[13,14] A more challenging strategy is to break away from the oft-utilized dirhodium system and explore the use of heterobimetallic systems that include rhodium.

In 2005 and 2006, Dikarev and coworkers reported the first examples of heterobimetallic complexes of Rh, namely BiRh tetracarboxylate complexes.[15,16] One of the driving forces for studying these heterobimetallic complexes of Rh was the desire to replace a rare and expensive metal with one that is both more abundant and cheaper. Another benefit of replacing Rh for Bi is the significant difference in toxicity, which is important because of the impact dirhodium catalysis could have on the pharmaceutical industry. In addition, use of heterobimetallic complexes of Rh for catalysis offers two key pieces of information for investigation: 1) the role and importance of the distal Rh-atom in dirhodium catalysis and 2) the possibility of tuning the bimetallic core for alternative reactivity. In 2009, the catalytic activity of a few BiRh tetracarboxylate complexes was evaluated for metal carbene chemistry.[17] The BiRh complexes were found to efficiently catalyze

both cyclopropanation and C–H insertion reactions with selectivities similar to those obtained with the analogous dirhodium complexes. However, the heterobimetallic complexes reacted slower; the $BiRh(O_2CCF_3)_3(O_2CCH_3)$ complex specifically was found to be 1600 times less reactive than its Rh_2 analogue.

Further advances in heterobimetallic BiRh catalysis had been hindered by the lack of synthetic procedures to access a wide variety of BiRh complexes, until recently where Sunderland and Berry have demonstrated procedures to synthesize families of BiRh complexes supported by either carboxylate,[18] oxypyridinate[19] or amidinate[20] equatorial ligands. This increased accessibility of BiRh complexes has encouraged a more extensive and comprehensive study with the aim of understanding steric and electronic comparisons between Rh_2 and BiRh complexes for use in metal carbene catalysis.

6.3 Experimental Section

6.3.1 Materials and Methods

All reactions were carried out using oven dried glassware under a dry N_2 or Ar atmosphere using Schlenk techniques and glovebox methods. Toluene was purified using a Vacuum Atmospheres solvent purification system. $BiRh(TFA)_4$[21] (TFA = trifluoroacetate) was prepared according to literature procedures. Potassium carbonate (K_2CO_3), diethyl ether (Et_2O), hexane, methanol (MeOH), chloroform-*d* ($CDCl_3$), dichloromethane (DCM), cyclohexane (CY) and tetrahydrofuran (THF) were purchased from Sigma-Aldrich and used without further purification. ^1H and $^{13}C\{^1H\}$ NMR spectra were recorded on a Bruker Avance-500 MHz spectrometer at 500 and 125 MHz, respectively. ^1H and $^{13}C\{^1H\}$ NMR chemical shifts were referenced to residual solvent. ^1H splitting patterns were designated as doublet (d), multiplet (m) and singlet (s). Elemental analysis was carried out by Midwest Microlab, LLC, Indianapolis, IN. IR spectra were taken on a Bruker Tensor 27 FTIR spectrometer using an attenuated total reflectance (ATR) adapter. Mass spectra were obtained at the Paul Bender Chemical Instrumentation Center of the

Chemistry Department of the University of Wisconsin–Madison using a Thermo Q Exactive™ Plus ESI-MS.

BiRh(S-TBSP)₄ (1). Solid BiRh(TFA)₄ (68.6 mg, 0.0897 mmol) and H(*S*-TBSP) (141 mg, 0.453 mmol) were combined in a 25 mL Schlenk flask and suspended in 15 mL of toluene. The yellow suspension was heated to reflux through a soxhlet extractor (K_2CO_3 in the thimble) at 145 °C using an oil bath for 18 h. After cooling to room temperature, the solvent was removed *in vacuo*. The yellow solid was purified by flash column chromatography using a gradient eluent of Et_2O/hex (1:1), 2:1 Et_2O/hex (2:1) and Et_2O (R_f = 0.55 (Et_2O/hex (2:1))). The yellow fraction was collected, concentrated *in vacuo*, washed with hexane and dried *in vacuo*. Yield: 102.0 mg, 73.2%. Anal. Calcd $BiRhC_{60}H_{80}O_{16}N_4S_4$: C 46.4, H 5.2, N 3.6. Found: C 46.2, H 5.2, N 3.6. ESI-MS (positive ion, MeOH): *m/z* 1553.3385 ([M+H]⁺). ¹H NMR ($CDCl_3$, 500 MHz, ppm): δ 7.73 (d, *J* = 8.3 Hz, 8H), 7.48 (d, *J* = 8.3 Hz, 8H), 4.62 - 4.46p (m, 4H), 3.45 - 3.37 (m, 4H), 3.12 - 3.04 (m, 4H), 2.10 - 2.02 (m, 4H), 2.01 - 1.82 (m, 8H), 1.60 - 1.51 (m, 4H), 1.29 (s, 36H). ¹³C{¹H} NMR ($CDCl_3$, 125 MHz, ppm): δ 186.9, 156.3, 135.5, 127.6, 126.1, 62.3, 48.6, 35.2, 31.6, 31.2, 25.1. IR (ATR, cm⁻¹): 2958 (w), 2927 (w), 2871 (w), 2857 (w), 1723 (w), 1594 (m), 1462 (w), 1403 (m), 1365 (w), 1339 (s), 1308 (m), 1295 (w), 1269 (w), 1200 (m), 1161 (s), 1115 (m), 1090 (m), 1072 (w), 1024 (w), 1011 (w), 962 (w), 932 (w), 921 (w), 855 (w), 843 (w), 735 (m), 702 (w), 637 (s).

BiRh(S-BTPCP)₄ (2). Solid BiRh(TFA)₄ (67.4 mg, 0.0882 mmol) and H(*S*-BTPCP) (174 mg, 0.442 mmol) were combined in a 25 mL Schlenk flask and suspended in 15 mL of toluene. The yellow suspension was heated to reflux through a soxhlet extractor (K_2CO_3 in the thimble) at 145 °C using an oil bath for 18 h. After cooling to room temperature, the solvent was removed *in vacuo*. The yellow solid was purified by flash column chromatography using an eluent of DCM/CY (3:1) (R_f = 0.63 (DCM/CY (3:1))). The yellow fraction was collected and dried *in vacuo*. Yield: 80.6 mg, 48.6%. Anal. Calcd $BiRhC_{88}H_{64}O_8Br_4 \cdot H_2O$: C 55.7, H 3.5. Found: C 55.0, H 3.4. ESI-MS (positive ion, CH_3CN): *m/z* 1881.0245 ([M+H]⁺). ¹H NMR ($CDCl_3$, 500 MHz, ppm):

δ 7.23 - 7.16 (m, 4H), 7.14 - 7.10 (m, 1H), 7.08 - 7.01 (m, 2H), 6.92 - 6.78 (m, 7H), 2.51 (d, J = 4.3 Hz, 1H), 2.27 (d, J = 4.3 Hz, 1H). $^{13}C\{^1H\}$ NMR (CDCl$_3$, 125 MHz, ppm): δ 184.1, 142.6, 140.2, 136.1, 133.2, 130.6, 129.5, 129.0, 128.4, 127.9, 126.5. 126.4, 120.9, 47.4, 42.7, 24.7. IR (ATR, cm^{-1}): 1565 (m), 1491 (m), 1449 (w), 1376 (s), 1200 (w), 1077 (m), 1012 (m), 964 (m), 939 (m), 775 (m), 759 (m), 718 (m), 703 (s), 648 (w).

6.3.2 Crystallography

Crystallographic data were measured at the Molecular Structure Laboratory of the Chemistry Department of the University of Wisconsin–Madison. The crystal was selected under oil under ambient conditions and attached to the tip of a MiTeGen MicroMount©. The crystal was mounted in a stream of cold nitrogen at 200(1) K and centered in the X-ray beam using a video camera. The crystal evaluation and data collection were performed on a Bruker Quazar SMART APEX-II diffractometer with Mo Kα (λ = 0.71073 Å) radiation. The data were collected using a routine to survey an entire sphere of reciprocal space and indexed by the SMART program.[22] The structure was solved via direct methods and refined by iterative cycles of least-squares refinement on F^2 followed by difference Fourier synthesis.[23, 24] All H-atoms were included in the final structure factor calculation at idealized positions and allowed to ride on the neighboring atoms with relative isotropic displacement coefficients. The final absolute configuration of the ligand was determined to be (*S*) by examination of a Flack parameter of –0.021(3). Single crystals of **1** suitable for structural determination were obtained by slow cooling of a concentrated THF solution of **1** to –20 °C.

6.4 Results and Discussion

6.4.1 Synthesis and Characterization

Dirhodium paddlewheel complexes supported by homochiral equatorial ligands have widespread use in the field of C–H functionalization.[25, 26] While the use of chiral dirhodium complexes in catalysis is quite advanced, this approach is yet to be expanded to heterobimetallic complexes of rhodium. Until recently, the library of heterobimetallic rhodium complexes was quite limited,[15-17,21,27] however, general synthetic strategies leading to novel BiRh complexes supported by either carboxylate,[18] oxypyridinate[19] or amidinate[20] equatorial ligands have now been developed by Sunderland *et al.*, provoking the thought of applying these synthetic advances towards the design and subsequent application of chiral BiRh complexes in asymmetric catalysis. Complexes **1** and **2** were synthesized by equatorial ligand exchange by refluxing a toluene solution of BiRh(TFA)$_4$[21] and a slight excess of ligand through a soxhlet extractor containing K$_2$CO$_3$. The resulting yellow compounds are bench stable and were purified by column chromatography. Both compounds were fully characterized by ^{1}H and ^{13}C{^{1}H} NMR and IR spectroscopy along with ESI-MS and elemental analysis. The only well resolved protons in the ^{1}H NMR spectrum of **1** in CDCl$_3$ are the doublets of the *para*-substituted aryl ring (J = 8.3 Hz) and the methyl protons of the ^{t}butyl group at 7.73, 7.48 and 1.29 ppm, respectively. The observation of only one set of aryl resonances suggests the equatorial ligands lie in a highly symmetric environment on the NMR timescale. The only well resolved protons in the ^{1}H NMR spectrum of **2** in CDCl$_3$ are the diastereotopic methylene protons of the cyclopropane ring. These appear as doublets (J = 4.3 Hz) at 2.51 and 2.27 ppm with a typical coupling constant for geminal protons of a substituted cyclopropane ring. The observation of only one set of methylene protons suggests the equatorial ligands lie in a highly symmetric environment on the NMR timescale.

6.4.2 Crystallography

The asymmetric unit of the tetragonal *I*4 crystal of **1**•1.12 THF contains one quarter molecule of BiRh(*S*-TBSP)$_4$, residing on a crystallographic four-fold axis of symmetry with a partially occupied molecule of THF coordinated to the Rh-atom at a distance of 2.291(7) Å, disordered over the four-fold symmetry axis. There are also two solvent accessible voids on opposite sides of the aryl ring of the equatorial ligand, which are both partially occupied by THF molecules. The molecular structure of **1**•1.12 THF determined by single-crystal X-ray crystallography and summaries of crystallographic data and selected bond distances are shown in Figure 6.1, Table 6.1 and Table 6.2, respectively.
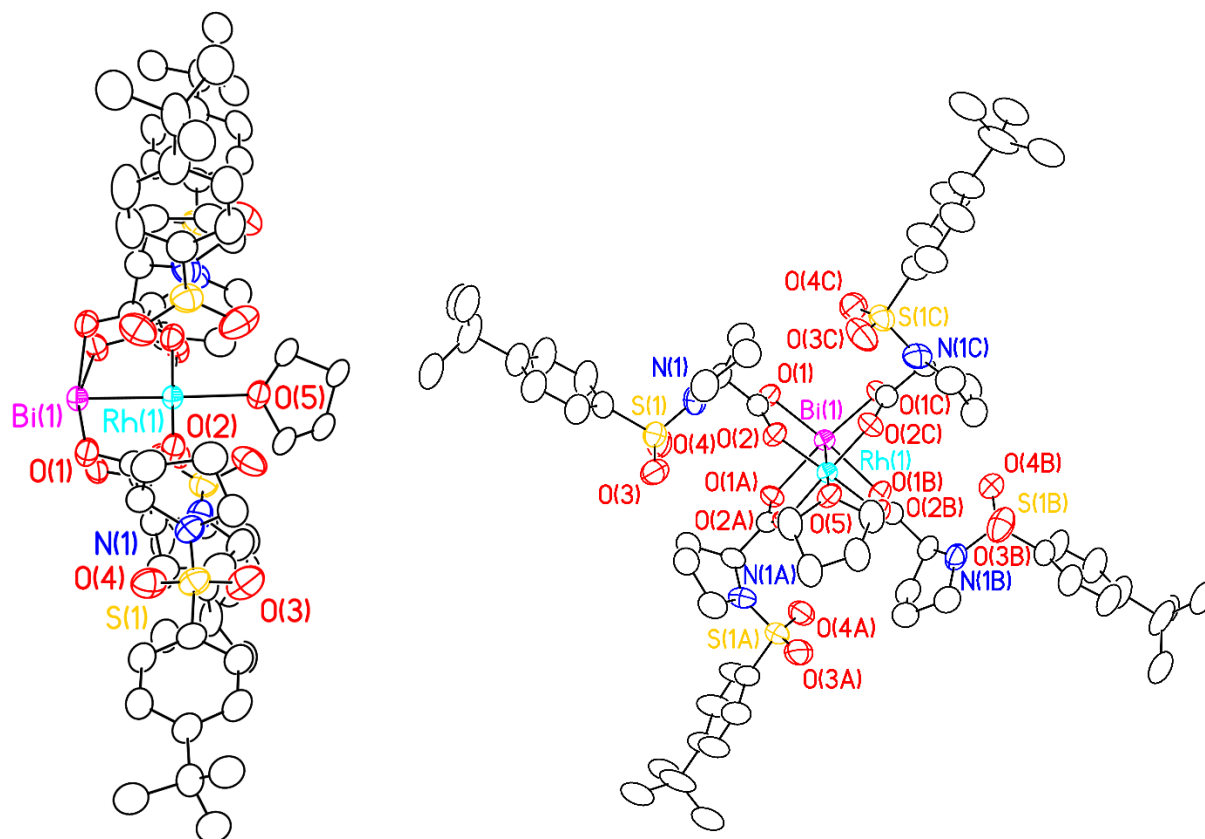
Figure 6.1. X-ray crystal structure of **1**•1.12 THF side view (left) and end-on view (right), with thermal ellipsoids drawn at the 50% probability level. Hydrogen atoms, eight partially occupied THF molecules, and the minor component of the disordered ^{t}butyl group have been removed for clarity.

The Bi–Rh bond distance is 2.5084(7) Å, consistent with a Bi–Rh single bond.[18] The M–O$_{eq}$ bond distances are 2.406(4) and 2.023(5) Å for Bi and Rh, respectively, having an ~ 0.4 Å longer M–O$_{eq}$ bond distance for Bi compared to Rh, consistent with all other BiRh crystal structures.[18-20]

Table 6.1. Crystallographic data for **1**•1.12 THF at 200 K.

Identification code	**1**•1.12 THF
Empirical formula	Bi Rh $C_{67.84}$ $H_{95.68}$ $O_{17.96}$ N_4 S_4
Formula weight	1694.73
Temperature	200(1) K
Wavelength	0.71073 Å
Crystal system	Tetragonal
Space group	*I*4
Unit cell dimensions	a = 22.2169(5) Å
	b = 22.2169(5) Å
	c = 10.9063(3) Å
	α = 90°
	β = 90°
	γ = 90°
Volume	5383.2(3) $Å^3$
Z	2
Density (calculated)	1.046 g/cm^3
Crystal size	0.174 x 0.127 x 0.107 mm^3
Data / restraints / parameters	660/ 347 / 275
Goodness-of-fit on F^2	1.070
Final $R^{a,b}$ indices [I>2σ(I)]	R_1 = 0.0361, wR_2 = 0.0913
R indices (all data)	R_1 = 0.0444, wR_2 = 0.0956

[a]R_1 = $\Sigma||F_0| - |F_c||/\Sigma|F_0|$

[b]wR_2 = $|[\Sigma[w(F_0^2 - F_c^2)^2] / \Sigma[w(F_0^2)^2]]1/2$, w = $1/\sigma^2 (F_0^2) + (aP)^2 + bP$, where P = $[max(0$ or $F_0^2) + 2(F_c^2)]/3$.

Table 6.2. Experimental bond distances (Å) for **1**•1.12 THF.

Compound	**1**•1.12 THF
Bi–Rh	2.5084(7)
Bi–O	2.406(4)
Rh–O_{eq}	2.023(5)
Rh–O_{ax}	2.291(7)

The Bi–ligand bond elongation present in all heterobimetallic BiRh complexes causes a tilting of the equatorial ligand towards the Rh-axial site, effectively providing a more sterically congested active site for Rh catalysis. The relative volume of the Rh-axial site of BiRh complexes compared to Rh_2 complexes could have two beneficial consequences; 1) the more sterically congested site could alter the regioselectivity of BiRh(*S*-TBSP)$_4$ carbene complexes compared to Rh_2(*S*-TBSP)$_4$ to prefer the more sterically accessible sites within a substrate and 2) there could be an enhancement of both diastereo- and enantioselectivity due to the more sterically crowded chiral pocket. Another vital piece of information obtained from the X-ray crystal structure of **1** is the conformation of the equatorial ligands. Complex **1** is closely related to the very active and highly stereoselective C–H functionalization catalyst Rh_2(*S*-DOSP)$_4$. The source of the stereoselectivity has been hypothesized to be closely related to the conformation of the equatorial ligands of the catalyst. Rh_2(*S*-DOSP)$_4$ is hypothesized to lie in a D_2-symmetric conformation with the aryl groups adopting an α–β–α–β arrangement as shown in Figure 6.2.[5] Other common arrangements relevant to chiral Rh_2 catalysts are C_4-symmetric (α–α–α–α) and C_2-symmetric (α–α–β–β).
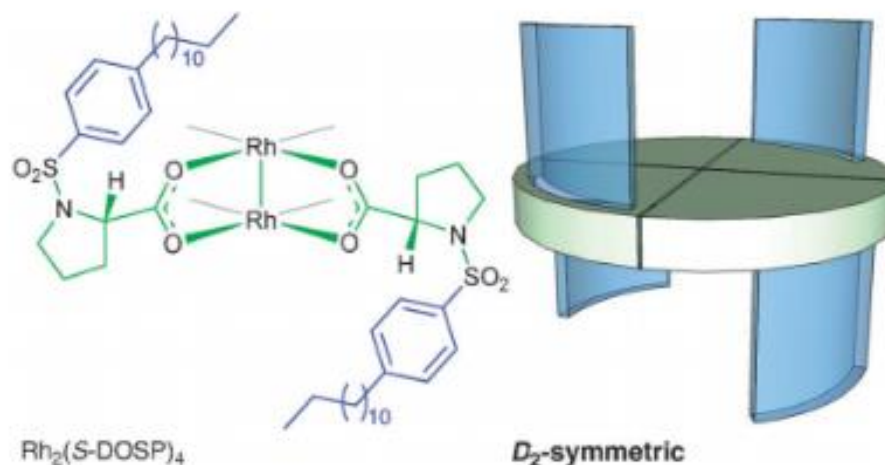
Figure 6.2. Hypothesized conformation of D_2-symmetric $Rh_2(S\text{-DOSP})_4$.[5]

The number of conformations increases when one Rh-atom is replaced by a Bi-atom (i.e. two α–α–α–α conformers exist, etc.). The X-ray crystal structure of **1** confirms the solid state structure to be C_4-symmetric, but with the aryl groups all pointing towards the periphery of the Bi–Rh bond, rather than directed towards one metal-axial site or the other.

6.4.3 Cyclopropanation Reactions

We have initially studied the cyclopropanation of styrene (Scheme 6.1). 2,2,2-trichloroethyl (*p*-bromophenyl)diazoacetate **3** was chosen as a benchmark diazo substrate because recently, the trichloroethyl esters have been shown to be more robust, giving cleaner metal-catalyzed intermolecular reactions than the traditional methyl esters.[7] The experiments were performed by treatment of a pentane solution of styrene and 2,2,2-trichloroethyl (*p*-bromophenyl)diazoacetate **3** with either BiRh complex **1** or Rh_2 complex **5**. At 23 °C, complete consumption of **3** was achieved in 12 h. Analysis of the very clean reaction mixture indicated the formation of the cyclopropane **4** as a single diastereomer. After column chromatography, **4** could be isolated in 67% yield and 86% *ee*, the yield being lower than expected probably because of the very small reaction scale.

For comparison, the reaction catalyzed by Rh$_2$(S-TBSP)$_4$ (**5**) was performed following the same procedure. The diazo was in this case instantaneously consumed, even though the catalyst was not completely soluble in pentane. Cyclopropane adduct **4** was isolated in 89% yield and 78% *ee*.

Rh$_2$(S-TBSP)$_4$ (**5**)   1 min, 89% yield, 78% *ee*

BiRh(S-TBSP)$_4$ (**1**)   12 h, 67% yield, 86% *ee*

Scheme 6.1. Cyclopropanation reaction of styrene catalyzed by either **1** or **5**.

The cyclopropanation reaction of methyl-2-furoate was also achieved with diazo compound **3** (Scheme 6.2). When catalyzed by **1** in isopropyl acetate as solvent, compound **6** was obtained in 28% yield with 49% *ee* after 15 h, the overall yield was increased to 48% when the solvent was switched to triflurotoluene. In comparison, the reaction with catalyst **5** was complete within 1 min, with a yield of 31%, the %*ee* was not measured.

Rh$_2$(S-TBSP)$_4$ (**5**)   1 min, 31% yield

BiRh(S-TBSP)$_4$ (**1**)   15 h, 28% yield, 49% *ee*
                                                          48% yield (trifluorotoluene)

Scheme 6.2. Cyclopropanation reaction of methyl-2-furoate catalyzed by either **1** or **5**.

6.4.4 C–H Insertion Reactions

The activated substrate 1,4-cyclohexadiene was used to evaluate **1** for C–H insertion reactions (Scheme 6.3). Compound **7** was obtained as the single product and was isolated in high yield (up to 85% when trifluorotoluene was used as solvent). It was not possible to separate the two enantiomers of compound **7** by HPLC, therefore product **7** will need to be hydrogenated to obtain information about the enantioselectivity from this reaction.

catalyst	
Rh$_2$(S-TBSP)$_4$ (**5**)	1 min, 52% yield
BiRh(S-TBSP)$_4$ (**1**)	15 h, 61% yield
	85% yield (trifluorotoluene)
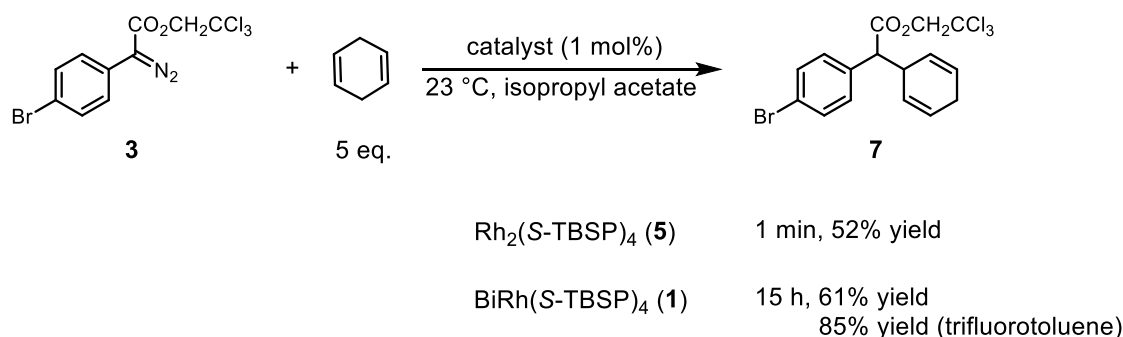
Scheme 6.3. C–H insertion reaction of 1,4-cyclohexadiene catalyzed by either **1** or **5**.

Cyclohexane proved to be a viable substrate for C–H insertion reactions for both **1** and **5** (Scheme 6.4). Compound **8** was the only product of a clean reaction and was isolated in 79% yield. A method to separate the two enantiomers by HPLC was not achieved, so no information about the enantioselectivity is known at this time.

catalyst	
Rh$_2$(S-TBSP)$_4$ (**5**)	5 min, 96% yield
BiRh(S-TBSP)$_4$ (**1**)	15 h, 79% yield
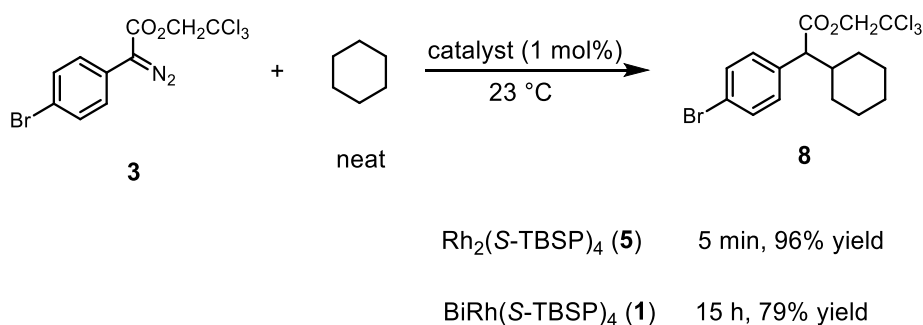
Scheme 6.4. C–H insertion reaction of cyclohexane catalyzed by either **1** or **5**.

The C–H insertion reaction with pentane was tested (Scheme 6.5). Complete consumption of **3** was achieved after 15 h at room temperature with catalyst **5**. The ratio of C2 : C3 insertion was observed to be 24 : 1 from the crude ^{1}H NMR spectrum. Both catalysts **1** and **2** were tested at 40 °C. After 2 days, only traces of **9** were observed, rather compound **11** was the major product, likely derived from the hydrolysis of **3** with subsequent O–H insertion by the metal carbene (even in the presence of molecular sieves). Product **11** was independently confirmed by the reaction of **3** and 2,2,2-trichloroethanol catalyzed by Rh$_2$(OAc)$_4$, obtained as a racemic mixture of enantiomers.

Rh$_2$(*S*-TBSP)$_4$ (**5**)	23 °C 15 h **9 : 10** = 24 : 1 **11** n.o.
BiRh(*S*-TBSP)$_4$ (**1**)	40 °C 2 d traces of **9** **11** mainly obtained
BiRh(*S*-BTPCP)$_4$ (**2**)	40 °C 2 d traces of **9** **11** 23% yield (26% with molecular sieves)
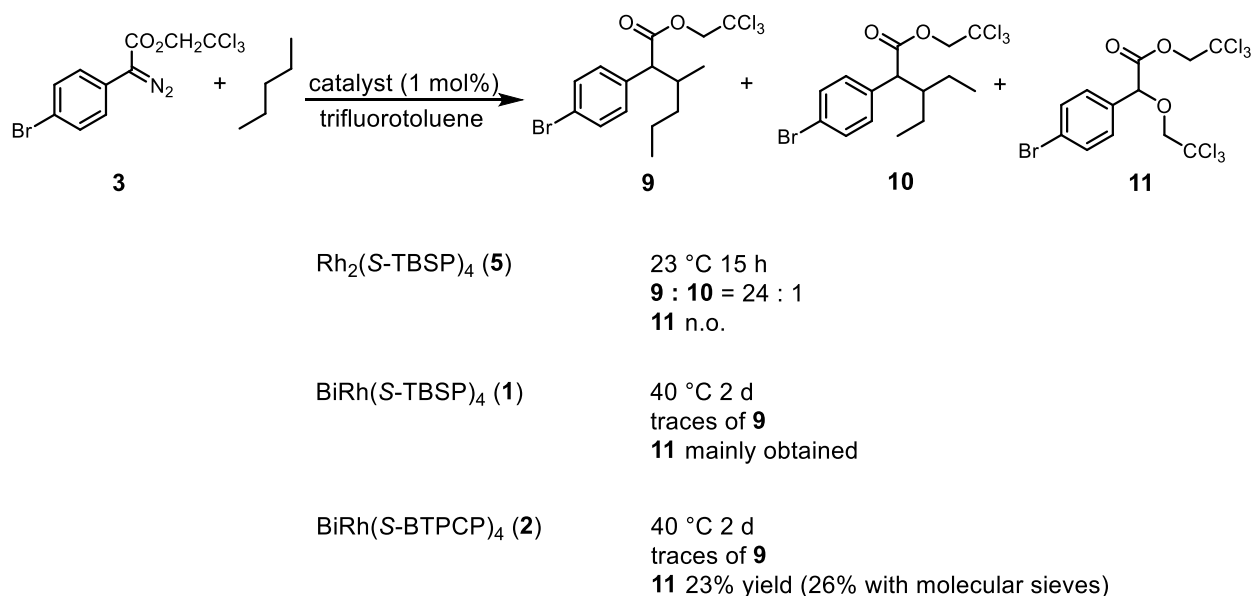
Scheme 6.5. C–H insertion reaction of pentane catalyzed by either **1**, **2** or **5**.

When butyl methyl ether was tested as a substrate for the C–H insertion reaction with catalyst **2**, no reaction was observed (Scheme 6.6). After 5 d heating at 40 °C in CH_2Cl_2, starting diazo **3** was recovered in near quantitative yield. It appears the presence of heteroatoms, able to coordinate to the active Rh-site, lead to catalyst deactivation.

Scheme 6.6. C–H insertion reaction of butyl methyl ether catalyzed by **2**.

When *trans*-4-methyl-2-pentene was tested as a substrate for C–H insertion with diazo **3** (Scheme 6.7), the reaction catalyzed by **5** was complete after 24 h and resulted in the insertion product ratio **14** : **15** of 4 : 1 in favor of the more activated C–H bond. In contrast, the reaction catalyzed by **1** gave a product ratio **14** : **15** of 1 : 2, demonstrating a reversal of selectivity with the more sterically accessible C–H bond being favored for insertion. Unfortunately, product **11** (hydrolysis and O–H insertion) was the major product of the reaction.

Scheme 6.7. C–H insertion reaction of *trans*-4-methyl-2-pentene catalyzed by either **1** or **5**.

When *trans*-2-hexene was used as the substrate for C–H insertion with catalyst **5** (Scheme 6.8), the ratio of products **16** : **17** was 3.6 : 1, having a preference for the electronically more activated C–H bonds. When catalyst **1** was used, the ratio of **16** : **17** was changed to 1 : 1.1, showing a switch in preference for the sterically more accessible C–H bonds, with a significant amount of product **11** formed. Catalyst **2** gave **11** as the major product, even when the reaction was conducted at 40 °C in CH$_2$Cl$_2$.
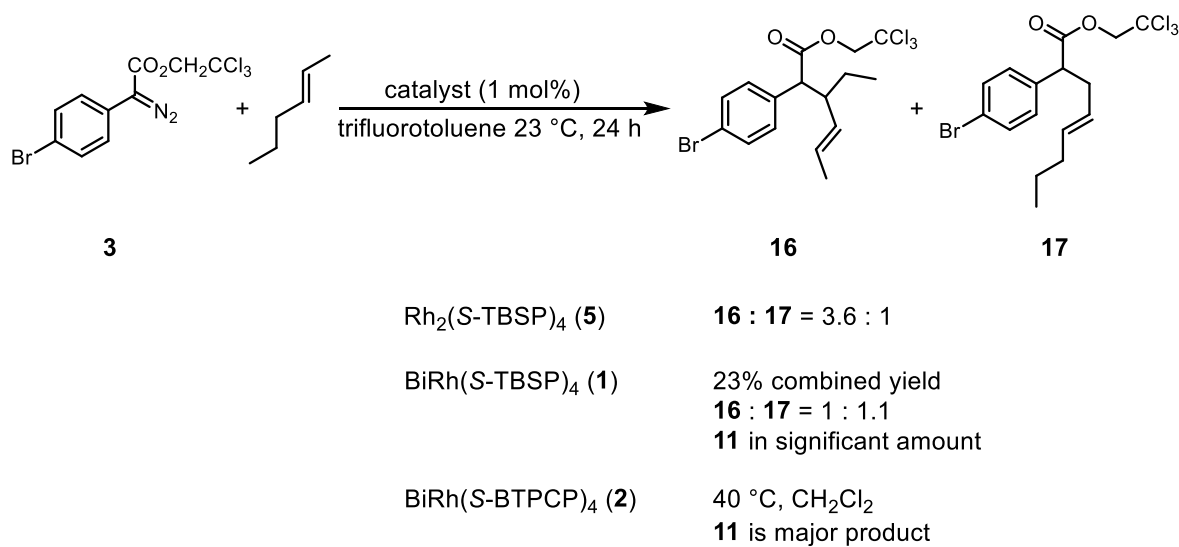
Scheme 6.8. C–H insertion reaction of *trans*-2-hexene catalyzed by either **1**, **2** or **5**.

The substrate 4-ethyltoluene offered the chance to create a competition between 1° and 2° benzylic C–H bonds (Scheme 6.9). The dirhodium catalysts **5** and **20** each prefer the 2° benzylic C–H bonds, with **5** showing no formation of the product of 1° benzylic C–H bond insertion. When switching from **5** to **1**, the selectivity is reversed, preferring the 1° benzylic C–H bonds over 2° with a 2 : 1 ratio. Product **18** was formed with a *dr* of 2.5 : 1 and product **19** was formed with a 92% *ee*, with trace amounts of **11** observed. Catalyst **2**, with the triarlycyclopropyl carboxylate equatorial ligands, required an increased reaction temperature of 40 °C and gave the products **18** : **19** in a ratio of 1 : 1.4, also displaying reversed selectivity compared to the dirhodium analogue. Compound **18** was formed with a *dr* of 3 : 1. Unfortunately, **11** was formed in a significant amount.

Catalyst	
Rh$_2$(*S*-TBSP)$_4$ (**5**)	**18 : 19** = 1 : 0
BiRh(*S*-TBSP)$_4$ (**1**)	**18 : 19** = 1 : 2 **18**, *dr* = 2.5 :1 **19**, 92% *ee* **11** trace amount
Rh$_2$(*S*-BTPCP)$_4$ (**20**)	40 °C, CH$_2$Cl$_2$, 5 eq. 4-ethyl toluene **18 : 19** = 1.8 : 1
BiRh(*S*-BTPCP)$_4$ (**2**)	40 °C, CH$_2$Cl$_2$, 5 eq. 4-ethyl toluene **18 : 19** = 1 : 1.4 **18**, *dr* = 3 :1 **11** in significant amount
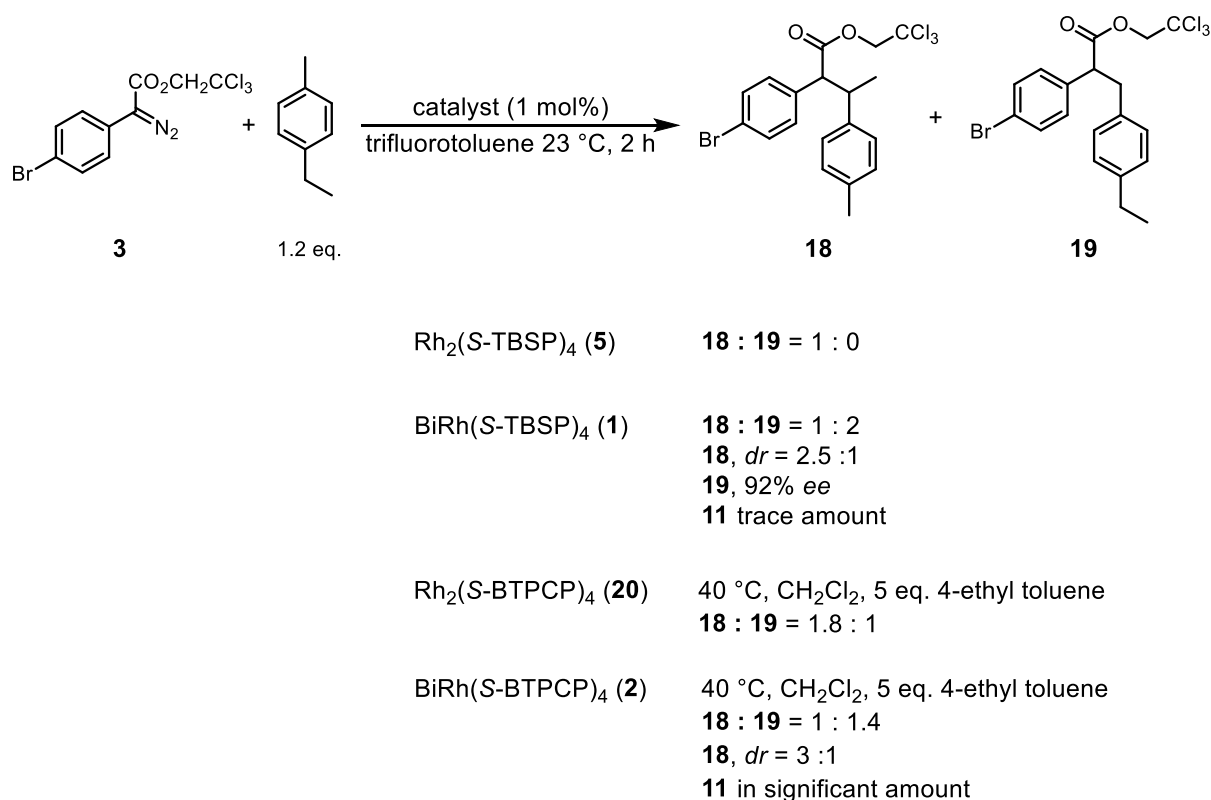
Scheme 6.9. C–H insertion reaction of 4-ethyltoluene catalyzed by either **1**, **2**, **5** or **20**.

Lastly, the selectivity of *p*-cymene as a substrate for C–H insertion was tested (Scheme 6.10). The dirhodium catalyst **5** gave a ratio between 3° and 1° C–H bond insertion of 1 : 1.4. Switching to the heterobimetallic catalyst **1** with the same equatorial ligands gave exclusively **22** as the product of C–H insertion, along with product **11**. Catalyst **2** was tested, again at elevated reaction temperatures, giving exclusively **22** as the product of C–H insertion, but forming **11** as the major product.

Catalyst	Ratio
$Rh_2(S\text{-TBSP})_4$ (**5**)	**21 : 22** = 1 : 1.4
$BiRh(S\text{-TBSP})_4$ (**1**)	**21 : 22** = 0 : 1
	22 : 11 = 4 : 1
$BiRh(S\text{-BTPCP})_4$ (**2**)	40 °C in CH_2Cl_2
	21 : 22 = 0 : 1
	11 is major product
	22 isolated in 4% yield
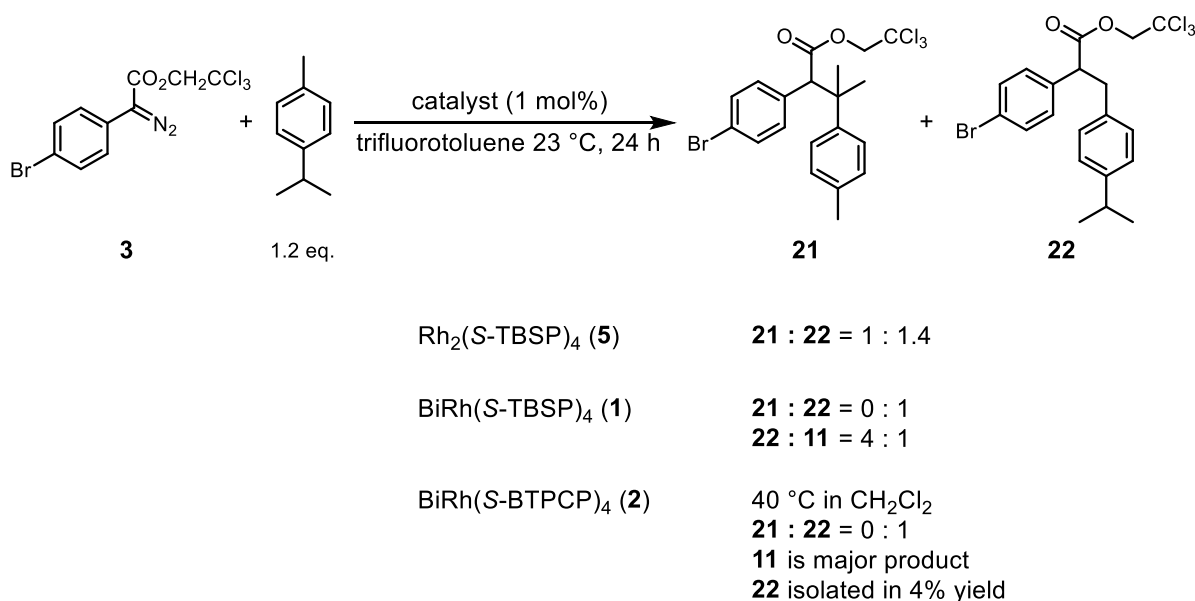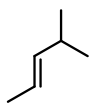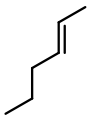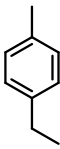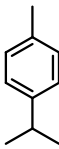
Scheme 6.10. C–H insertion reaction of *p*-cymene catalyzed by either **1**, **2** or **5**.

The initial results of catalysis utilizing either catalyst **1** or **2** are promising. Complex **1** demonstrated the ability to effectively perform cyclopropanation, albeit slower, with modest yields and an enhanced enantioselectivity compared to its Rh_2 analogue with styrene as the substrate. A broader scope of C–H insertion substrates was tested, leading to three central observations. First, catalysis with the heterobimetallic catalysts **1** and **2** is slower compared to the Rh_2 analogues, which has previously been established and is likely due to an increased reaction barrier to loss of dinitrogen to form the corresponding carbene complex.[17] The second observation is that complexes **1** and **2** seem to suffer from an unwanted side reaction (product **11**), which

seems to be the result of O–H insertion of the metal carbene into trichloroethanol, possibly the result of hydrolysis of **3**. Efforts to identify the source of this product and to avoid its formation are currently underway. The third, and most exciting, observation is the change in regioselectivity demonstrated by **1** compared to **5**, a summary of the key substrates is shown in Table 6.3. In all four cases, catalyst **1** results in the enhancement of regioselectivity for the more sterically accessible activated C–H bond. More astonishing, is that in three of the examples, the regioselectivity is actually *reversed*, changing from either tertiary or secondary allylic/benzylic C–H bonds preferred to always primary allylic/benzylic C–H bonds preferred.

Table 6.3. Summary of regioselectivity for C–H insertion reactions catalyzed by **1** or **5**.

	(3° : 1° allylic)	(2° : 1° allylic)	(2° : 1° benzylic)	(3° : 1° benzylic)
Rh$_2$(S-TBSP)$_4$ (**5**)	4 : 1	3.6 : 1	1 : 0	1 : 1.4
BiRh(S-TBSP)$_4$ (**1**)	1 : 2	1 : 1.1	1 : 2	0 : 1

The source of the preference for 1° C–H bond selectivity is not yet fully understood. The hypothesis was that if the heterobimetallic complex **1** adopts a similar conformation as its Rh$_2$ analogue, then the increased Bi-ligand bond lengths would push the equatorial ligands more towards the Rh-axial site, thus created a tighter chiral pocket for catalysis to occur. While the X-ray structure of **1** does show a leaning of the equatorial ligands towards the Rh-axial site, a rigid α–β–α–β arrangement of the aryl rings of the equatorial ligands around the Rh-axial site was not observed. While the solid state structure of **1** does not rule out the presence of other conformations in solution or provide information about the structure of the BiRh carbene species, it suggests further investigation is necessitated to propose a model for the basis of both regio- and stereoselectivity of **1**. Computational analysis is currently underway in the group of Dr. Jamal Musaev at Emory University to gain further insight into the relevant structures during catalysis

and to learn how the reaction pathways compare to the Rh_2 analogues. Hopefully, this will lead to a better understanding of the similarities and differences between BiRh and Rh_2 catalysts and lead to further development of catalyst design principles.

6.5 Conclusions

The first homochiral heterobimetallic complexes containing rhodium have been successfully synthesized and characterized. The solid state structure of **1** is C_4-symmetric about the Bi–Rh axis. Complex **1** has been applied in cyclopropanation catalysis and both **1** and **2** have been applied to C–H functionalization reactions. Both catalysts prove to be competent, however, further exploration is needed to fully optimize these reactions. The most promising result is that catalysis with **1** always results in enhanced regioselectivity for activated 1° C–H bonds compared to its Rh_2 analogue, and in fact was shown to *reverse* the selectivity from either 3° or 2° to 1° C–H bonds in three examples. Further exploration of the capabilities of both **1** and **2** for C–H functionalization reactions are currently underway in the Davies lab at Emory University along with rigorous computational analysis in the Musaev group to gain insights into the nature of the regioselectivity enhancement.

6.6 Acknowledgments

6.7 Supporting Information

General Catalysis Procedures

General procedure for cyclopropanation reactions with styrene

In a 4 mL screw-cap vial equipped with a magnetic stir bar, BiRh or Rh$_2$ complex (0.001 mol, 1 mol%) was dissolved in pentane (2 mL). Styrene (0.5 mmol, 5 eq.) was added to the solution, followed by 2,2,2-trichloroethyl (*p*-bromophenyl)diazoacetate **3** (0.1 mmol, 1 eq.). The vial was flushed with argon and capped. The resulting solution was stirred at 23 °C for the time indicated in the table and until complete conversion of the diazo compound (IR check). The solvent was evaporated and the mixture purified by column chromatography over silica gel (pentane:Et$_2$O (9:1)). The experimental data for compound **4** correspond to previously reported material.[28] Pure compound was analysed by HPLC to calculate the enantioselectivity of the reactions (Method: SS-WHELK column, 1% *^{i}*PrOH in hexane, 1 mL/min, 30 min).

General procedure for cyclopropanation reactions with methyl-2-furoate

In a 4 mL screw-cap vial equipped with a magnetic stirr bar, BiRh or Rh$_2$ complex (0.001 mol, 1 mol%) was dissolved in isopropyl acetate or trifluorotoluene (2 mL). Methyl-2-furoate (0.5 mmol, 5 eq.) was added to the solution, followed by 2,2,2-trichloroethyl (*p*-bromophenyl)diazoacetate **3** (0.1 mmol, 1 eq.). The vial was flushed with argon and capped. The resulting solution was stirred at 23 °C for the time indicated in the table and until complete conversion of the diazo compound (IR check). The solvent was evaporated and the mixture purified by column chromatography over silica gel (hexane:ethyl acetate (50:1) then (25:1) then (9:1)). The experimental data for compound **6** correspond to previously reported material. Pure compound was analysed by HPLC to calculate the enantioselectivity of the reactions (Method: ADH column, 5% *^{i}*PrOH in hexane, 1 mL/min, 30 min; for the racemic sample see MDC_01_151 reaction by Matt Chuba).

General procedure for C–H insertion reactions with 1,4-cyclohexadiene

In a 4 mL screw-cap vial equipped with a magnetic stir bar, BiRh or Rh_2 complex (0.001 mol, 1 mol%) was dissolved in isopropyl acetate or trifluorotoluene (2 mL). 1,4-cyclohexadiene (0.5 mmol, 47 µL, 5 eq.) was added to the solution, followed by 2,2,2-trichloroethyl (*p*-bromophenyl)diazoacetate **3** (0.1 mmol, 1 eq.). The vial was flushed with argon and capped. The resulting solution was stirred at 23 °C for the time indicated in the table and until complete conversion of the diazo compound (IR check). The solvent was evaporated and the mixture purified by column chromatography over silica gel (pentane:Et_2O (9:1)). It was not possible to find a good HPLC method for the separation of the two enantiomers. Compound **7** needs to be hydrogenated.

General procedure for C–H insertion reactions with cyclohexane
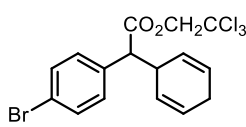
In a 4 mL screw-cap vial equipped with a magnetic stir bar, BiRh or Rh_2 complex (0.001 mol, 1 mol%) was dissolved in cyclohexane (2 mL). 2,2,2-trichloroethyl (*p*-bromophenyl)diazoacetate **3** (0.1 mmol, 1 eq.) was added in one portion. The vial was flushed with argon and capped. The resulting solution was stirred at 23 °C for the time indicated in the table and until complete conversion of the diazo compound (IR check). The solvent was evaporated and the mixture purified by column chromatography over silica gel (pentane:Et_2O (9:1)). It was not possible to find a good HPLC method for the separation of the two enantiomers.

General procedure for C–H insertion reactions with all other substrates
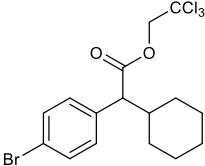
In a 4 mL screw-cap vial equipped with a magnetic stir bar, BiRh or Rh_2 complex (0.001 mol, 1 mol%) was dissolved in isopropyl acetate or trifluorotoluene (2 mL). The desired substrate (0.5 mmol, 47 µL, 5 eq.) was added to the solution, followed by 2,2,2-trichloroethyl (*p*-bromophenyl)diazoacetate **3** (0.1 mmol, 1 eq.). The vial was flushed with argon and capped. The resulting solution was stirred at 23 °C for the time indicated in the table and until complete conversion of the diazo compound (IR check). The solvent was evaporated and the mixture purified by column chromatography over silica gel (pentane:Et_2O (9:1)).

Analysis Data for Products of C–H Insertion Reactions
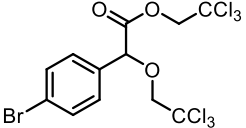
2,2,2-Trichloroethyl 2-(4-bromophenyl)-2-(cyclohexa-2,5-dien-1-yl)acetate (7)

^{1}H NMR (400 MHz, CDCl$_3$, ppm): δ 7.46 (d, J = 8.6 Hz, 2H), 7.25 (d, J = 8.5 Hz, 2H), 5.87 - 5.80 (m, 1H), 5.80 - 5.66 (m, 2H), 5.35 - 5.23 (m, 1H), 4.79 (d, J = 11.9 Hz, 1H), 4.69 (d, J = 11.9 Hz, 1H), 3.60 - 3.49 (m, 2H) and 2.70 - 2.52 (m, 2H);

^{13}C{^{1}H} NMR (100 MHz, CDCl$_3$, ppm): δ 170.93, 134.87, 131.79, 130.67, 127.09, 126.90, 125.92, 125.03, 121.90, 94.82, 74.28, 57.62, 38.38, 26.47; **HR-MS (EI)** m/z calculated for C$_{16}$H$_{14}$Cl$_3$O$_2$BrK$^+$ 260.8880, observed 260.1342.

2,2,2-trichloroethyl 2-cyclohexyl-2-phenylacetate (8)

R$_f$ = 0.75 (SiO$_2$, pentane:Et$_2$O, (9:1)); **^{1}H NMR (400 MHz, CDCl$_3$, ppm):** δ 7.45 (d, J = 8.4 Hz, 2H), 7.24 (d, J = 8.5 Hz, 2H), 4.76 (d, J = 12.0 Hz, 1H), 4.63 (d, J = 12.0 Hz, 1H), 3.34 (d, J = 10.7 Hz, 1H), 2.12 - 1.99 (m, 1H), 1.90 - 1.81 (m, 1H), 1.80 - 1.69 (m, 1H), 1.68 - 1.59 (m, 2H), 1.39 - 1.04 (m, 5H) and 0.89 - 0.70 (m, 1H);

^{13}C{^{1}H} NMR (100 MHz, CDCl$_3$, ppm): δ 171.86, 136.04, 131.80, 130.54, 121.65, 94.89, 74.25, 58.23, 40.96, 31.98, 30.37, 26.26, 25.98 and 25.94; **IR (neat, cm^{-1}):** 2927, 1748, 1488, 1173 and 1122; **HR-MS (EI)** m/z calculated for C$_{16}$H$_{18}$NBrCl$_3$O$_2$$^+$ 439.9581 observed 439.9584.

2,2,2-trichloroethyl 2-(4-bromophenyl)-2-(2,2,2-trichloroethoxy)acetate (11)

^{1}H NMR (400 MHz, CDCl$_3$, ppm): δ 7.55 (d, J = 8.5 Hz, 2H), 7.43 (d, J = 8.4 Hz, 2H), 5.38 (s, 1H), 4.84 (d, J = 11.9 Hz, 1H), 4.73 (d, J = 11.9 Hz, 1H), 4.35 (d, J = 11.5 Hz, 1H) and 4.11 (d, J = 11.5 Hz, 1H).

HPLC Method: SS-WHELK column, 2% ^{i}PrOH in hexane, 1 mL/min, 40 min (ret time: 5.52 and 6.52 min).

Figure 6.3. NMR spectra of **1** at room temperature in CDCl$_3$ (^{1}H (top), ^{13}C{^{1}H} (bottom)).

Figure 6.4. NMR spectra of **2** at room temperature in CDCl$_3$ (^{1}H (top), ^{13}C{^{1}H} (bottom)).

Figure 6.5. NMR spectra of **7** at room temperature in CDCl$_3$ (^{1}H (top), ^{13}C{^{1}H} (bottom)).

Figure 6.6. NMR spectra of **8** at room temperature in CDCl$_3$ (^{1}H (top), ^{13}C{^{1}H} (bottom)).

Figure 6.7. ^{1}H NMR spectrum of **11** at room temperature in CDCl$_3$.

6.8 References

(1)   Paulissen, R.; Reimlinger, H.; Hayez, E.; Hubert, A. J.; Teyssié, P. *Tetrahedron Lett.* **1973**, *14*, 2233.

(2)   Brunner, H.; Kluschanzoff, H.; Wutz, K. *B. Soc. Chim. Belg.* **1989**, *98*, 63.

(3)   Kennedy, M.; McKervey, M. A.; Maguire, A. R.; Roos, G. H. P. *J. Chem. Soc., Chem. Commun.* **1990**, 361.

(4)   Hashimoto, S.; Watanabe, N.; Ikegami, S. *Tetrahedron Lett.* **1990**, *31*, 5173.

(5)   Davies, H. M. L.; Morton, D. *Chem. Soc. Rev.* **2011**, *40*, 1857.

(6)   Qin, C.; Davies, H. M. L. *J. Am. Chem. Soc.* **2014**, *136*, 9792.

(7)   Guptill, D. M.; Davies, H. M. L. *J. Am. Chem. Soc.* **2014**, *136*, 17718.

(8)   Liao, K.; Negretti, S.; Musaev, D. G.; Bacsa, J.; Davies, H. M. L. *Nature* **2016**, *533*, 230.

(9)   Catino, A. J.; Nichols, J. M.; Choi, H.; Gottipamula, S.; Doyle, M. P. *Org. Lett.* **2005**, *7*, 5167.

(10)   Catino, A. J.; Nichols, J. M.; Forslund, R. E.; Doyle, M. P. *Org. Lett.* **2005**, *7*, 2787.

(11)   Trindade, A. F.; Gois, P. M. P.; Veiros, L. F.; André, V.; Duarte, M. T.; Afonso, C. A. M.; Caddick, S.; Cloke, F. G. N. *J. Org. Chem.* **2008**, *73*, 4076.

(12)   Gois, P. M. P.; Trindade, A. F.; Veiros, L. F.; André, V.; Duarte, M. T.; Afonso, C. A. M.; Caddick, S.; Cloke, F. G. N. *Angew. Chem., Int. Ed.* **2007**, *46*, 5750.

(13)   Lou, Y.; Remarchuk, T. P.; Corey, E. J. *J. Am. Chem. Soc.* **2005**, *127*, 14223.

(14)   Lou, Y.; Horikawa, M.; Kloster, R. A.; Hawryluk, N. A.; Corey, E. J. *J. Am. Chem. Soc.* **2004**, *126*, 8916.

(15)   Dikarev, E. V.; Li, B.; Zhang, H. *J. Am. Chem. Soc.* **2006**, *128*, 2814.

(16)   Dikarev, E. V.; Gray, T. G.; Li, B. *Angew. Chem., Int. Ed.* **2005**, *44*, 1721.

(17)   Hansen, J.; Li, B.; Dikarev, E.; Autschbach, J.; Davies, H. M. L. *J. Org. Chem.* **2009**, *74*, 6564.

(18)   Sunderland, T. L.; Berry, J. F. *Dalton Trans.* **2016**, *45*, 50.

(19)   Sunderland, T. L.; Berry, J. F. *J. Coord. Chem.* **2016**, *69*, 1949.

(20)   Sunderland, T. L.; Berry, J. F., *Chem. - Eur. J.* **2016,** *Submitted*.

(21)   Filatov, A. S.; Napier, M.; Vreshch, V. D.; Sumner, N. J.; Dikarev, E. V.; Petrukhina, M. A. *Inorg. Chem.* **2012**, *51*, 566-571.

(22)   Bruker-AXS Inc., *SMART* Program, Madison, Wisconsin, USA, **2009**.

(23)   Sheldrick, G. *Acta Cryst. A* **2008**, *64*, 112.

(24)   Dolomanov, O. V. Bourhis, L. J.; Gildea, R. J.; Howard, J. A. K.; Puschmann, H. *J. Appl. Crystallogr.* **2009**, *42*, 339.

(25)   Davies, H. M. L.; Beckwith, R. E. J. *Chem. Rev.* **2003**, *103*, 2861.

(26)   Cotton, F. A.; Murillo, C. A.; Walton, R. A., *Multiple Bonds Between Metal Atoms*. 3rd ed. Springer Science and Business Media, Inc., New York, **2005**.

(27)   Dikarev, E. V.; Li, B.; Rogachev, A. Y.; Zhang, H.; Petrukhina, M. A. *Organometallics* **2008**, *27*, 3728.

(28)   Negretti, S.; Cohen, C. M.; Chang, J. J.; Guptill, D. M.; Davies, H. M. L. *Tetrahedron* **2015**, *71*, 7415.

Chapter 7

Spectroscopic and Computational Comparison of

Metal Carbene Species that React with C–H Bonds

Sunderland, T. L. and Berry, J. F.

Department of Chemistry, University of Wisconsin–Madison, 1101 University Avenue, Madison, WI 53706, United States

7.1 Abstract

A systematic series of Rh_2 and Ir donor/acceptor carbene complexes has been observed by visible spectroscopy as intermediates in the insertion of the carbene fragments into C–H bonds. All complexes have a M–C $\pi \rightarrow \pi^*$ transition near 700 nm. This electronic transition is sensitive to the electron donating or withdrawing nature of *para*-substituents on the aryl ring of the carbene fragment, showing a tunability over a >2000 cm^{-1} range. This transition is indicative of the relative M–C π bond strength of the metal carbene complexes and those with stronger M–C π bonds tend to have attenuated reactivity. Computational analysis on three classes of catalysts (Ir, Rh_2 and BiRh) indicate weaker M–C bonding as you traverse the series along with increased Molecular Orbital Polarization (MOP) of the lowest unnocuppied molecular orbital (LUMO) towards the C-atom of the carbene fragment, resulting in more reactive metal carbene complexes.

7.2 Introduction

Reactive metal carbene species, particularly those containing Rh_2 units, are critical intermediates in C–H functionalization catalysis,[1-3] however, only recently have such compounds based on an Rh_2 metal core been observed.[4,5] In the absence of spectroscopic information, chemists have instead relied heavily upon computational analysis to develop guiding principles in this field, however, direct links between electronic structure and catalysis have not been rigorously developed. Here we utilize a signature spectroscopic feature, that of the Rh–C $\pi \rightarrow \pi^*$ transition previously observed by Kornecki and Berry,[4] to investigate the role that substitution at the *para*-position of the aryl ring of metal (aryl-ester)-carbene complexes plays, in addition to applying this technique to non-dirhodium complexes in an attempt to establish comparative principles across catalyst classes. The three classes for computational comparison are BiRh, Rh_2 and Ir complexes that have all shown the ability to catalyze C–H functionalization reactions,

BiRh(TPA)$_4$-methyl-(phenyl)-acetate-carbene (TPA = triphenylacetate) (**1**), Rh$_2$(OAc)$_4$-methyl-(phenyl)-acetate-carbene (**2**) and *cis*-Ir(*t*Bu-Phebox-*i*Pr)Cl$_2$-methyl-(4-OMe-aryl)-acetate-carbene (Phebox = (oxazolinyl)phenyl) (**3**). Additionally, the Rh$_2$(*R*-BTPCP)$_4$ (BTPCP = 1-(4-bromophenyl)-2,2-diphenylcyclopropanecarboxylate) was used for the UV-Vis comparative study.

7.3 Experimental Section

7.3.1 Materials and Methods

All reactions were carried out using oven dried glassware under a dry N$_2$ atmosphere using Schlenk techniques. Dichloromethane (DCM) was dried over CaH$_2$ and distilled prior to use. Ethanol, pivalic acid, hexane and chloroform-*d* (CDCl$_3$) were purchased from Sigma-Aldrich and used without further purification. Triphenylphosphine (PPh$_3$) was purchased from Sigma-Aldrich and recrystallized from ethanol prior to use. Rh$_2$(TPA)$_4$,[6] Rh$_2$(*R*-BTPCP)$_4$,[7] Ir(*t*Bu-Phebox-*i*Pr)Cl$_2$(H$_2$O),[8] BiRh(piv)$_4$ (piv = pivalate),[9] Rh$_2$(piv)$_4$[10] and methyl-(4-X-aryl)-diazoacetate (X = OMe, Me, H, Cl, Br, and CF$_3$)[11] were prepared according to literature procedures. ^{1}H and ^{31}P{^{1}H} NMR spectra were recorded on a Bruker Avance-400 MHz spectrometer at 400 and 162 MHz, respectively, and referenced from residual proteo solvent and the corresponding ^{1}H NMR frequency, respectively. ^{1}H NMR spectroscopy splitting patterns were designated as multiplet (m), singlet (s) and doublet of doublets (dd). UV-Vis spectra were obtained using a StellarNet Miniature BLUE-wave UV-Vis dip probe with a Tungsten-Krypton light source and a 10 mm path length tip.

7.3.2 General Procedure for Metal Carbene Observation by UV-Vis Spectroscopy

A Schlenk flask was loaded with a magnetic stir bar and the corresponding metal complex, which was dried under reduced pressure and subsequently dissolved in dry DCM with insertion of the UV-Vis dip probe. To this solution was added the corresponding diazo compound in dry

DCM, followed by data collection. General procedures for each catalyst can be found in the Supporting Information section.

7.3.3 Crystallography

Crystallographic data were measured at the Molecular Structure Laboratory of the Chemistry Department of the University of Wisconsin–Madison. Crystals were selected under oil under ambient conditions and attached to the tip of a MiTeGen MicroMount©. The crystal of **4** was mounted in a stream of cold nitrogen at 100(1) K and centered in the X-ray beam using a video camera. The crystal evaluation and data collection were performed on a Bruker Quazar SMART APEX-II diffractometer with Mo Kα (λ = 0.71073 Å) radiation. The data were collected using a routine to survey an entire sphere of reciprocal space and indexed by the *SMART* program.[12] The structure was solved *via* direct methods and refined by iterative cycles of least-squares refinement on F^2 followed by difference Fourier synthesis.[13, 14] All H-atoms were included in the final structure factor calculation at idealized positions and allowed to ride on the neighboring atoms with relative isotropic displacement coefficients. Single crystals of **4** suitable for structural determination were obtained by cooling a hexane solution of **4** to −20 °C. Complex **4** has one disordered ^{t}Bu group, which was modeled over two positons.

7.3.4 Computational Methods

Initial coordinates for **1** were adapted from crystallographic data for BiRh(TPA)$_4$.[9] Initial coordinates of **2** were adapted from published calculations.[4] Initial coordinates of **3** were adapted from the computed structure of the related Ir(^{t}Bu-Phebox-Bn)Cl$_2$ carbene complex.[8] All geometry optimizations were carried out with ORCA version 2.9.1[15] and the B3LYP[16-19] functional for compounds **1**, **2** and **3** and with the BP86 exchange-correlation functional[18] for all other molecules. The TZVP basis set[20] including all electron scalar relativistic effects within the ZORA[21] approximation were used with the TZVP/J auxiliary basis set[22] for Rh, Bi and Ir. The SVP basis

set[20] and SVP/J auxiliary basis set[22] were used on all remaining atoms. Solvation effects were treated with the COSMO solvation model[23, 24] in a DCM solution. Tight optimization and tight self-consistent field convergence criteria were employed along with grid4 for all calculations. Frequency calculations were performed following geometry optimizations to ensure minimum energy structures. Molecular graphics were created with the UCSF Chimera package.[25]

7.3.5 Synthesis and Characterization

BiRh(piv)$_4$PPh$_3$ (4). Solid BiRh(piv)$_4$ (33.8 mg, 0.0472 mmol), PPh$_3$ (26.0 mg, 0.0990 mmol) and pivalic acid (2.25 g, 22.0 mmol) were combined in a 10 mL Schlenk flask, degassed and heated to 175 °C using an oil bath for 4.5 h, during which time the reaction mixture changed from yellow to orange. After cooling to room temperature, the pivalic acid was distilled out under reduced pressure, the orange oil was dissolved in Et$_2$O and passed through a short SiO$_2$ plug (to remove OPPh$_3$). The Et$_2$O was removed under reduced pressure and the remaining solid was dissolved in a small amount of hexane and cooled to –20 °C, resulting in X-ray quality single crystals of **4**. ^{1}H NMR (CDCl$_3$, 400 MHz, ppm): δ 7.67 (t, *J* = 8.3 Hz, 6H), 7.40 - 7.30 (m, 9H), 0.86 (s, 36H). ^{31}P{^{1}H} NMR (CDCl$_3$, 162 MHz, ppm): δ 170.4 (d, $^1J_{P-Rh}$ = 82.3 Hz).

Rh$_2$(piv)$_4$PPh$_3$ (5). Solid Rh$_2$(piv)$_4$ (34.9 mg, 0.0572 mmol) and PPh$_3$ (15.0 mg, 0.0572 mmol) were combined in a 10 mL Schlenk flask, degassed, dissolved in 4 mL dry DCM and stirred for 2 h under N$_2$, resulting in a brown/purple solution. The DCM was removed under reduced pressure and the solid was dried. ^{1}H NMR (CDCl$_3$, 400 MHz, ppm): δ 7.77 (dd, *J* = 9.8, 7.6 Hz, 6H), 7.45 (dd, *J* = 9.7, 7.6 Hz, 3H), 7.36 (dd, *J* = 9.8, 9.7, 6H), 0.82 (s, 36H). ^{31}P{^{1}H} NMR (CDCl$_3$, 162 MHz, ppm): δ –38.4 (dd, $^1J_{P-Rh}$ = 97.0, $^2J_{P-Rh}$ = 34.4 Hz).

7.4 Results and Discussion

7.4.1 UV-Vis Spectroscopy

Absorption spectroscopy was a key tool in the observation of the first spectroscopically characterized Rh_2 donor/acceptor carbene complex, which displays a short lived absorption feature in the visible region.[4] Analysis of a Hammett type series by visible spectroscopy of metal aryl-ester-carbene complexes helps to inform on the effect that aryl ring electron density has on the electronic structure of these key catalytic intermediates, as well as the role different catalysts can have. The catalyst $Rh_2(TPA)_4$ was found in previous work to yield metastable carbene species.[4] When a DCM solution of $Rh_2(TPA)_4$ is flooded with an excess of diazo compound, a characteristic feature around 740 nm (13500 cm^{-1}) quickly grows in, corresponding to the Rh–C $\pi{\rightarrow}\pi^*$ transition of the Rh_2 carbene complex. A systematic Hammett type series of *para*-substituted aryl-ester carbene complexes of $Rh_2(TPA)_4$ can be observed, as shown in Figure 7.1. A gradual shifting of the Rh–C $\pi{\rightarrow}\pi^*$ transition towards lower energy is observed as the electron withdrawing nature of the *para*-substituent is increased from a methoxy to a trifluoromethyl group (this trend was reproduced computationally, see SI Figure 7.8). Since this electronic transition is localized on the π-system of the Rh–C bond, it can inform on the relative π-bond energy. As the electronic transition shifts to lower energy, the π-bond strength decreases, resulting in more reactive Rh_2 carbene complexes. Surprisingly, the energy of the Rh–C $\pi{\rightarrow}\pi^*$ transition spans an energy of >2000 cm^{-1}, displaying a high level of tunability. While TD-DFT calculations on **2** only predict one absorption feature near 740 nm, the appearance of two features cannot be overlooked. TD-DFT calculations of a $Rh_2(OAc)_4$ *bis*-carbene species do predict a different absorption feature at higher energy (see SI Figure 7.9), while there is no precedence for this type of species being active in catalysis, under the excess diazo addition conditions of this UV-Vis experiment, the possibility of forming a *bis*-carbene complex cannnot be overlooked.

Figure 7.1. Overlay of Rh$_2$(TPA)$_4$ (4-X-aryl)-ester carbene complexes (X = OMe, Me, H, Cl, Br, CF$_3$) in DCM at 0 °C.

Using similar methods, we can now compare the electronic structure of various Rh$_2$ carbene complexes. The complex Rh$_2$(*R*-BTPCP)$_4$ was chosen for comparison. When a DCM solution of Rh$_2$(*R*-BTPCP)$_4$ is flooded with an excess of diazo compound, an analogous feature in the visible region is observed (see SI Figure 7.10). When these visible features are overlaid against those from the Rh$_2$(TPA)$_4$ complex, a similar Hammett correlation is observed (Figure 7.2). Interestingly, the band from all of the Rh$_2$(*R*-BTPCP)$_4$ carbene complexes is red-shifted compared to those from Rh$_2$(TPA)$_4$. This indicates that the Rh$_2$(*R*-BTPCP)$_4$ carbene complexes should be more reactive than those of Rh$_2$(TPA)$_4$. With this new comparative technique in hand, we sought to expand it to see if it could be applied to an entirely different class of catalyst.

Figure 7.2. Overlay of $Rh_2(TPA)_4$ (solid line), $Rh_2(R\text{-}BTPCP)_4$ (dashed line) (4-X-aryl)-ester carbene complexes (X = OMe, Me, H, Cl, Br, CF_3) in DCM at 0 °C.

The catalyst $Ir(^tBu\text{-}Phebox\text{-}^iPr)Cl_2(H_2O)$ was chosen, because it had recently been shown to catalyze C–H insertion reactions with diazo compounds.[8] Based on the observation that this Ir catalyst was slower than Rh_2 catalysts at diazo decomposition, and that third-row transition metals should form more stable M–C bonds, we attempted to observe the Ir carbene complexes by near quantitative addition of diazo compound (1.5 eq) to a DCM solution of $Ir(^tBu\text{-}Phebox\text{-}^iPr)Cl_2(H_2O)$ at room temperature. The initial orange solution slowly changes to green upon mixing, followed by slow growth of a similar feature to the Rh_2 carbene complexes in the visible region at ~ 690 nm (14500 cm^{-1}) (see Figure 7.3), which persists for several hours before decaying. This new feature was also assigned as a charge transfer band with excitation into the M–C π^* orbital by TD-DFT (see Appendix 2, addition evidence of an Ir carbene complex can be seen by the >290 ppm $^{13}C\{^1H\}$ NMR chemical shift), similar to the case of the Rh_2 complexes. When the visible feature of the Ir carbene complexes is overlaid against those of both sets of Rh_2 described above (Figure 7.4), a trend starts to appear. The Ir complexes are all significantly blue-shifted compared

to both sets of Rh_2 complexes. This shift to higher energy of the transition into the M–C π^* orbital is indicative of stronger M–C π-bonding in the Ir complexes compared to those of Rh_2, resulting in more stable metal carbene complexes, evidenced by their longer lifetimes. This analytical technique has potential for broad application across classes of metal carbenes to help elucidate information about the electronic structure of these reactive intermediates that are difficult to observe by other spectroscopic techniques.

Figure 7.3. Overlay of Ir(^{t}Bu-Phebox-^{i}Pr)Cl$_2$ (4-X-aryl)-ester carbene complexes (X = OMe, Me, H, Br) in DCM at room temperature.

Figure 7.4. Overlay of Rh$_2$(TPA)$_4$ (solid line), Rh$_2$(R-BTPCP)$_4$ (dashed line) and Ir(^{t}Bu-Phebox-^{i}Pr)Cl$_2$ (dotted line) carbene complexes in DCM.

7.4.2 Density Functional Theory Calculations

To gain insights into the electronic structure and nature of the M–C bonds in metal carbene complexes, a computational analysis with DFT methods was undertaken. Attempts to observe a BiRh(TPA)$_4$ carbene intermediate were to this point unsuccessful, however, these complexes have also been computationally analyzed and are included here. The focus of the computational analysis was to compare three classes of reactive M carbenes (M = BiRh (**1**), Rh$_2$ (**2**) and Ir (**3**)), with a specific focus on the lowest unoccupied molecular orbital (LUMO) that is responsible for C–H functionalization reactions. The three complexes chosen for analysis are shown in Scheme 7.1.

Scheme 7.1. Complexes **1**, **2** and **3** chosen for computational analysis.

The three key metrics chosen for comparison were the M–C bond length, M–C Mayer bond order (MBO) and molecular orbital polarization (MOP) (Table 7.1). MOP is a way to describe the polarization of a molecular orbital along a bond and is calculated according to Equation 7.1. Here, x is the *p*-orbital contribution of the C-atom to the LUMO and y is the orbital contribution from the M-atom and its *trans*-ligand (either Bi, Rh or Cl in these examples) having π-symmetry. MOP calculations could be applied to any molecular orbital to determine the relative polarization of that orbital towards a particular atom.

Table 7.1. Key metrics to compare metal carbenes **1**, **2** and **3**.

	M–C (Å)	M–C (MBO)	MOP (LUMO)
1	2.174	0.3921	0.767
2	2.023	0.7950	0.508
3	1.963	1.2195	0.336

$$\text{MOP} = \frac{\sum x - \sum y}{\sum x + \sum y} \qquad \text{(Eq 7.1)}$$
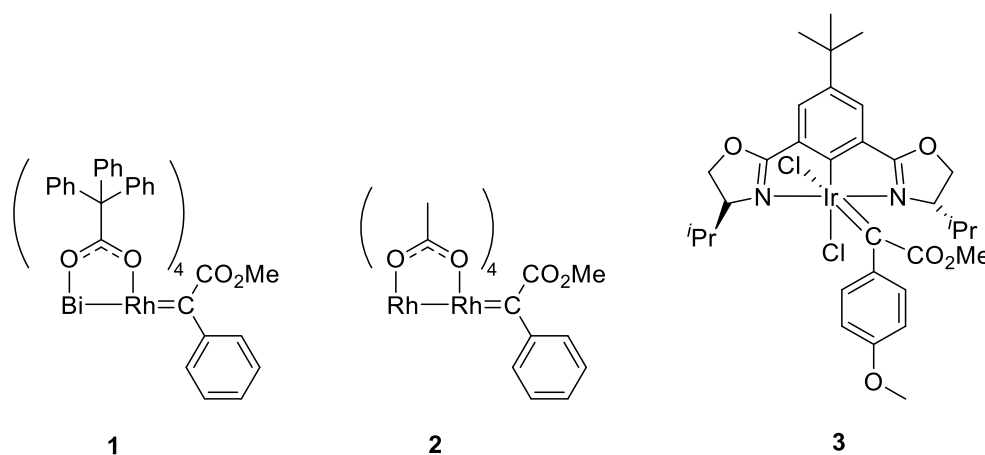
The calculated M–C bond lengths for complexes **1**, **2** and **3** steadily decrease from 2.174 to 2.023 to 1.963 Å, indicating a steady increase in M–C bond strength. This increase in bonding is also reflected in the calculated Mayer bond orders of 0.3921, 0.7950 and 1.2195, respectively. These trends seem to fit well with both the spectroscopic analysis performed above, showing increased π-bond strength for the Ir carbene complexes compared to Rh_2 and the qualitative observation that the Ir carbene complex lifetimes are longer compared to those of Rh_2. When comparing the MOP for complexes **1**, **2** and **3**, the trend in reactivity seems to hold. The MOP for complexes **1**, **2** and **3** are 0.767, 0.508 and 0.336, respectively, decreasing across the series. This can be interpreted as the empty *p*-orbital on the C-atom of the carbene fragment steadily becoming more polarized, and hence more electrophilic and reactive, by moving from an Ir to an Rh_2 to a BiRh metal core, which can be seen visually in Figure 7.5. The calculated energy barrier for carbene transfer in the cyclopropanation of styrene, calculated by Hansen *et al.* was 0.9 kcal/mol *lower* for $BiRh(O_2CH)_4$ than for $Rh_2(O_2CH)_4$ with the same carbene fragment, also indicating a more reactive carbene fragment for the BiRh complex.[26]

| **1** | **2** | **3** |
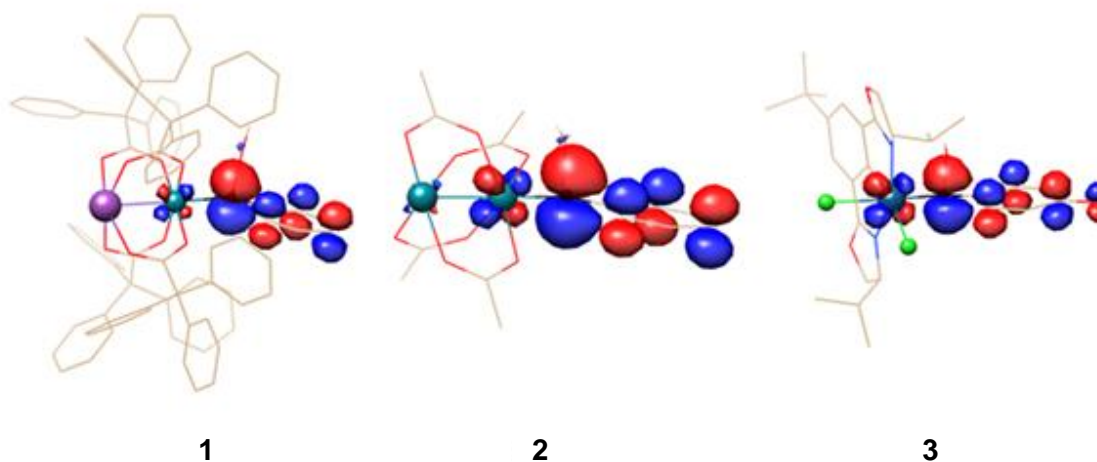
Figure 7.5. Calculated lowest unoccupied molecular orbital (LUMO) for **1**, **2**, and **3**.

7.4.3 M–Rh Phosphine Complexes (M = Bi, Rh)

To acquire another handle on the relative π back-bonding ability between BiRh and Rh_2 complexes, we have prepared PPh_3 adducts of each and compared the ^{31}P NMR chemical shifts of the phosphorous atom. Complex **4** was synthesized by heating $BiRh(piv)_4$ and 2 eq. of PPh_3 in pivalic acid. To confirm the structure, single crystals of **4** were grown by slow cooling a hexane solution of **4** to –20 °C. The molecular structure and crystallographic data are shown in Figure 7.6 and SI Tables 7.2 and 7.3. Complex **4** is indeed an Rh–PPh_3 adduct with a Bi–Rh bond distance of 2.5646(4) Å and an Rh–P bond distance of 2.511(1) Å (Rh–P bond distances of 2.494(2)[27] and 2.4771(5)[28] were found for $Rh_2(TFA)_4(PPh_3)_2$ and $Rh_2(OAc)_4(PPh_3)_2$, respectively).
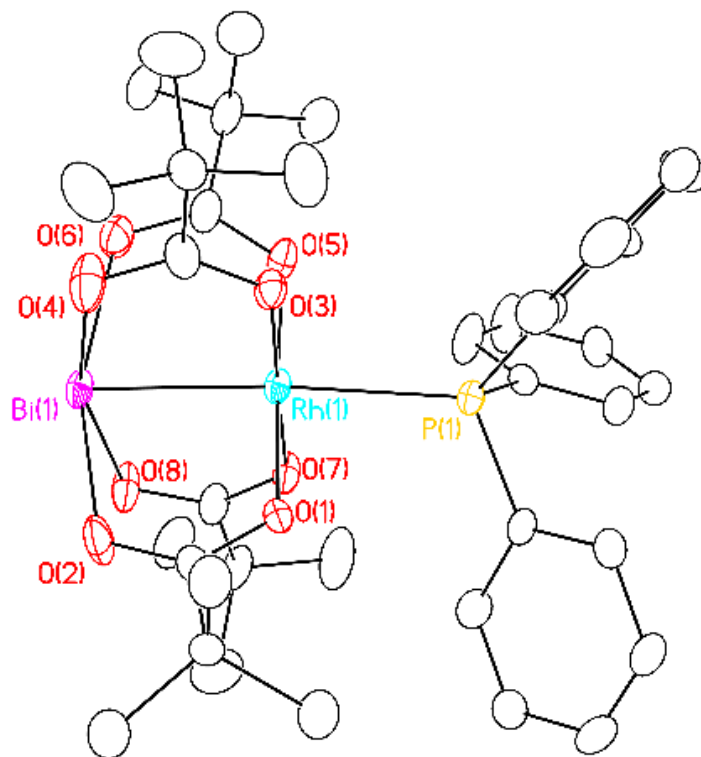
Figure 7.6. X-ray crystal structure of **4**, with thermal ellipsoids drawn at the 50% probability level. Hydrogen atoms and one disordered ^tBu group have been removed for clarity.

The resulting ^{31}P{^{1}H} NMR spectrum of **4** reveals two pieces of information: the phosphorous signal with a ^{31}P chemical shift of 170.4 ppm, which is displayed as a doublet with a coupling constant of 82.3 Hz, indicative of an Rh–PPh$_3$ adduct (Figure 7.7, bottom). To compare the ^{31}P chemical shift, the analogous Rh$_2$(piv)$_4$PPh$_3$ complex **5** was synthesized by stirring a DCM solution of Rh$_2$(piv)$_4$ and 1 eq. of PPh$_3$ together at room temperature. The ^{31}P{^{1}H} NMR spectrum of **5** reveals a ^{31}P chemical shift of –38.4 ppm (dd, $^1J_{\text{P–Rh}}$ = 97.0, $^2J_{\text{P–Rh}}$ = 34.4 Hz) (Figure 7.7 (top). That is a >200 ppm downfield shift in the ^{31}P chemical shift simply by replacing the distal Rh-atom for a Bi-atom! This downfield shift suggests the phosphorous atom in **4** is much more electron poor compared to **5**. The cause of this shift is likely attributed to the reduced π back-bonding ability of BiRh complexes compared to their Rh$_2$ counterparts.
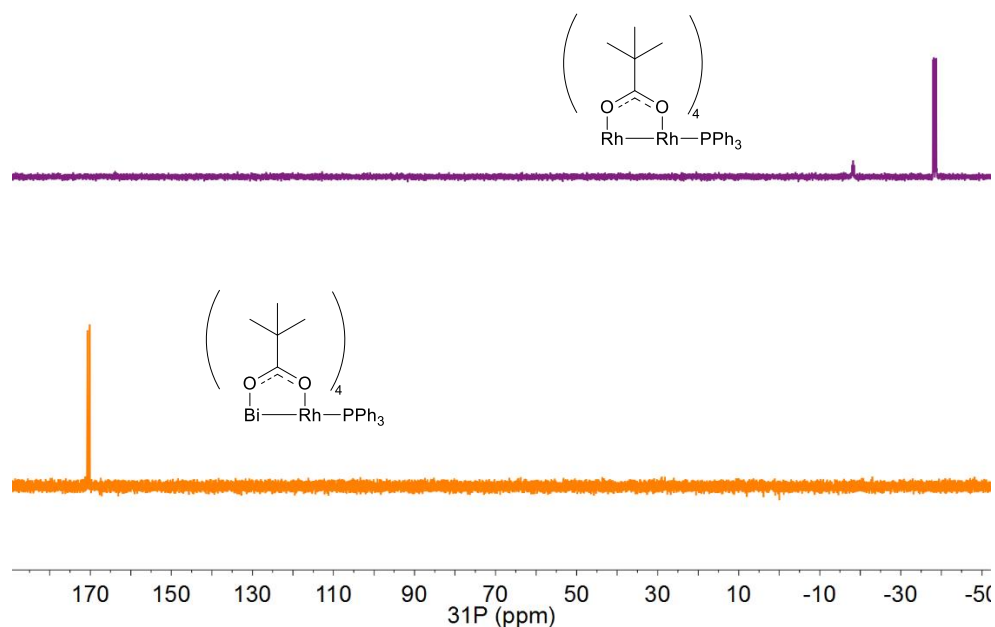
Figure 7.7. ^{31}P{^{1}H} NMR spectra of **4** (bottom, orange) and **5** (top, purple) in CDCl$_3$.

7.5 Conclusions

A systematic series of metal carbene intermediates across three C–H functionalization catalysts was observed. The electronic absorption features in the visible region reveal stronger M–C π-bonding energy in the Ir complexes compared to the Rh_2 complexes. This can be explained by the stronger π back-bonding ability of the third *vs* second row transition metals. Computational analysis on compounds **1**, **2** and **3** reveal a consistent trend of stronger M–C interactions and less reactive metal carbenes across the series from BiRh to Rh_2 to Ir. Complex **4** shows a weaker π back-bonding ability compared to **5**, evidenced by the >200 ppm downfield shift of the ^{31}P-nucleus in the $^{31}P\{^1H\}$ NMR spectra of their PPh_3 adducts.

7.6 Acknowledgments

7.7 Supporting Information

General Procedure for $Rh_2(TPA)_4$ Carbene Observation by UV-Vis Spectroscopy

A 10 mL Schlenk flask was loaded with a magnetic stir bar and $Rh_2(TPA)_4$ (0.002 mmol), which was dried under reduced pressure. Once the solid was yellow, it was dissolved in 5 mL dry DCM and cooled to 0 °C in an ice-water bath with insertion of the UV-Vis dip probe. To this solution was added the corresponding diazo compound (250 eq.) in 5 mL dry DCM at 0 °C, followed by data collection.

General Procedure for Rh₂(*R*-BTPCP)₄ Carbene Observation by UV-Vis Spectroscopy

A 10 mL Schlenk flask was loaded with a magnetic stir bar and Rh₂(*R*-BTPCP)₄ (0.001 mmol), dried under reduced pressure, subsequently dissolved in 5 mL dry DCM and cooled to 0 °C in an ice-water bath with insertion of the UV-Vis dip probe. To this solution was added the corresponding diazo compound (250 eq.) in 5 mL dry DCM at 0 °C, followed by data collection.

General Procedure for Ir(*ᵗ*Bu-Phebox-*ⁱ*Pr)Cl₂ Carbene Observation by UV-Vis Spectroscopy

A 25 mL Schlenk flask was loaded with a magnetic stir bar and Ir(*ᵗ*Bu-Phebox-*ⁱ*Pr)Cl₂(H₂O) (0.003 mmol), which dried under reduced pressure and subsequently dissolved in 7.5 mL dry DCM with insertion of the UV-Vis dip probe. To this solution was added the corresponding diazo compound (1.5 eq.) in 7.5 mL dry DCM, followed by data collection. After the diazo compound addition, the solution changes from orange to green, indicative of the Ir carbene formation.
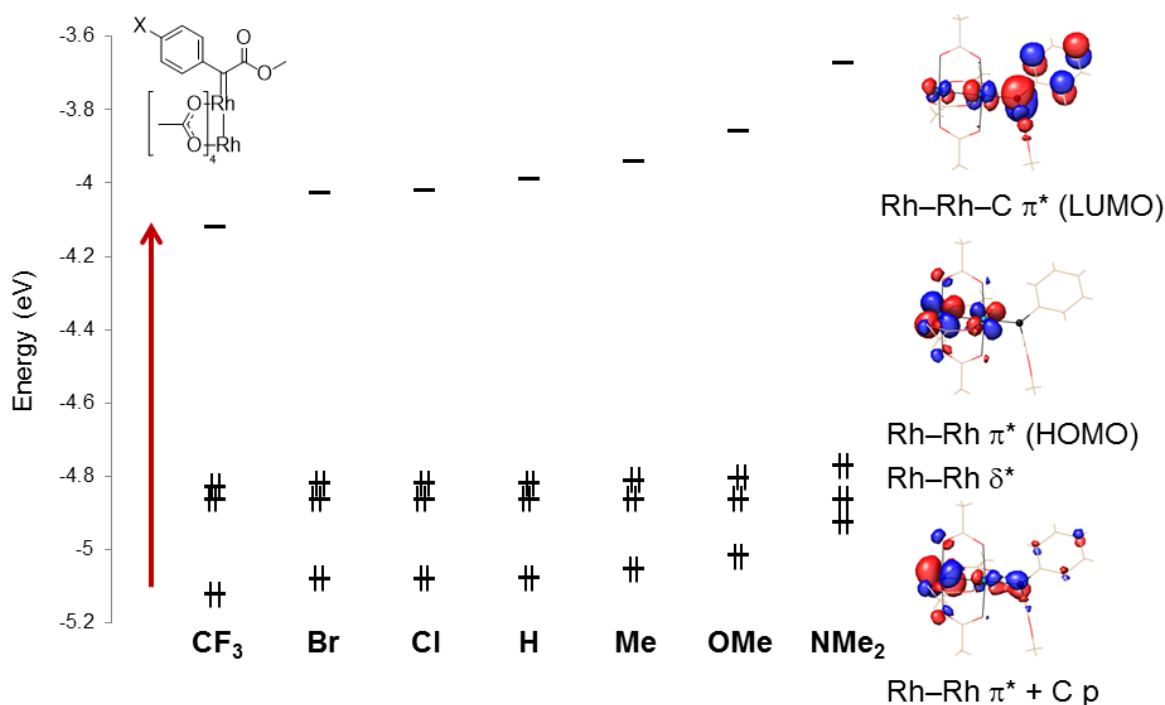
Figure 7.8. Calculated frontier orbitals for Rh₂(OAc)₄ carbene complexes generated from methyl-(4-X-aryl)-diazoacetate (X = CF₃, Br, Cl, H, Me, OMe, NMe₂).
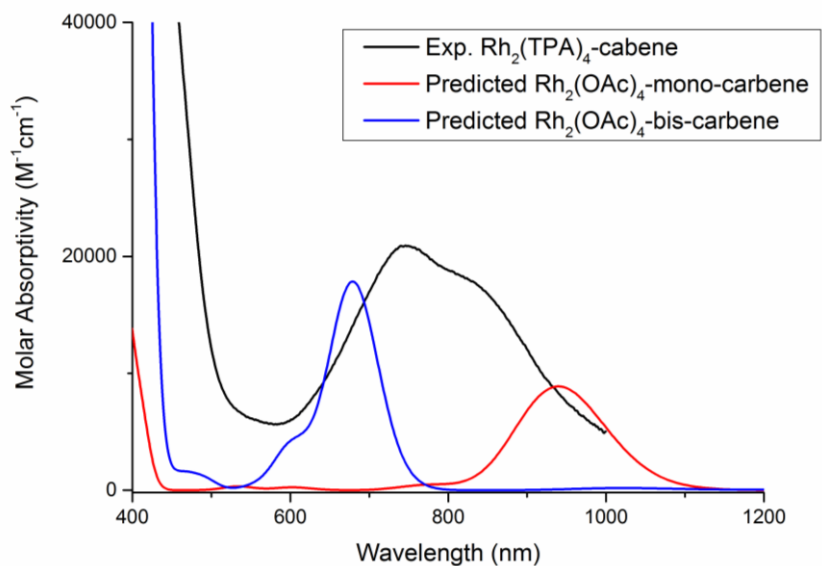
Figure 7.9. Overlay of experimental Rh$_2$(TPA)$_4$ carbene complexes (black), TD-DFT predicted Rh$_2$(OAc)$_4$ carbene complexes (*mono* in red and *bis* in blue).
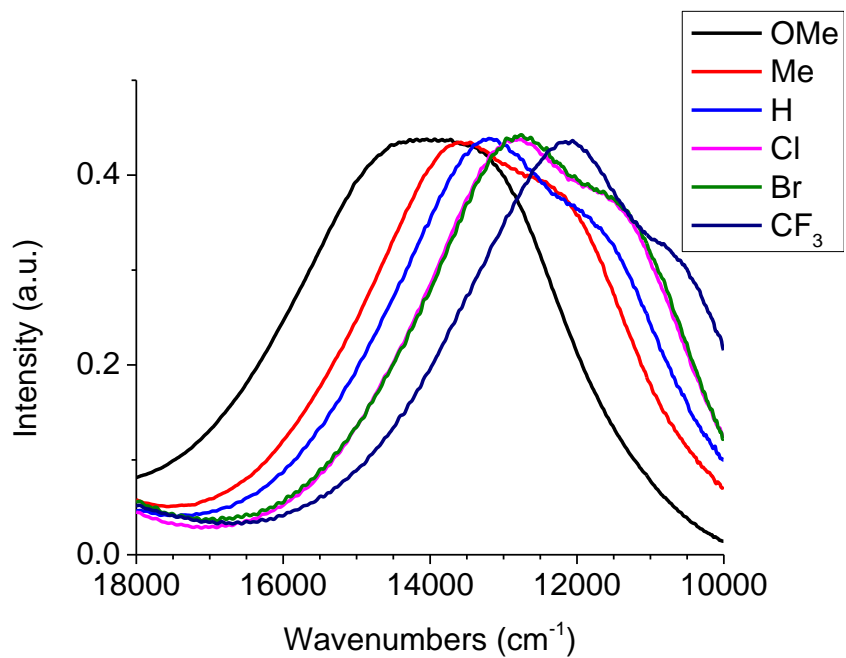
Figure 7.10. Overlay of Rh$_2$(*R*-BTPCP)$_4$ carbene complexes in DCM at 0 °C.

Table 7.2. Crystallographic data for **4** at 100 K.

Identification code	**4**
Empirical formula	Bi Rh C_{38} H_{51} O_8 P
Formula weight	978.64
Temperature	100(1) K
Wavelength	0.71073 Å
Crystal system	Triclinic
Space group	$P\bar{1}$
Unit cell dimensions	a = 10.4797(4) Å
	b = 13.5923(5) Å
	c = 13.9879(8) Å
	α = 91.294(2)°
	β = 92.227(3)°
	γ = 91.361(2)°
Volume	1989.9(1) Å^3
Z	2
Density (calculated)	1.633 g/cm^3
Crystal size	0.030 x 0.011 x 0.011 mm^3
Data / restraints / parameters	9875 / 1 / 458
Goodness-of-fit on F^2	1.020
Final $R^{a,b}$ indices [$I>2\sigma(I)$]	R_1 = 0.0408, wR_2 = 0.0879
R indices (all data)	R_1 = 0.0614, wR_2 = 0.0959

[a]$R_1 = \Sigma||F_0| - |F_c||/\Sigma|F_0|$

[b]w$R_2 = |[\Sigma[w(F_0^2 - F_c^2)^2] / \Sigma[w(F_0^2)^2]]1/2$, w = $1/\sigma^2 (F_0^2) + (aP)^2 + bP$, where P = [max(0 or F_0^2) + $2(F_c^2)]/3$.

Table 7.3. Selected bond distances (Å) and angles (°) for **4**.

Bi1–Rh1	2.5646(4)		Rh1–O1	2.026(3)
Rh1–P1	2.511(1)		Rh1–O3	2.047(3)
Bi1–O2	2.385(3)		Rh1–O5	2.035(3)
Bi1–O4	2.355(4)		Rh1–O7	2.040(3)
Bi1–O6	2.386(4)		Bi1–Rh1–P1	175.31(3)
Bi1–O8	2.401(4)			

Table 7.4. Optimized XYZ coordinates for **1**.

Bi	0.00000	0.00000	0.00000
Rh	0.00000	0.00000	2.65920
O	0.00489	2.09476	2.63605
O	-0.03245	2.35665	0.41710
O	2.09298	-0.00520	2.58976
O	2.35241	-0.00356	0.37022
O	0.02719	-2.09797	2.61321
O	0.08574	-2.36560	0.39480
O	-2.09573	-0.02383	2.61865
O	-2.36951	-0.05191	0.39887
C	-0.01761	2.80930	1.58720
C	-0.06004	4.37408	1.77876
C	0.30490	5.04670	0.42829
C	1.44219	5.85345	0.27866
H	2.10310	6.02544	1.12283
C	1.75297	6.45099	-0.95150
H	2.64317	7.07452	-1.03219
C	0.93011	6.25457	-2.06007
H	1.16967	6.71868	-3.01635
C	-0.21162	5.45426	-1.92666
H	-0.86736	5.28887	-2.78115
C	-0.51719	4.86094	-0.70187
H	-1.40678	4.24141	-0.62446
C	-1.50354	4.76058	2.22917
C	-2.14015	5.91091	1.72920
H	-1.65565	6.51005	0.96327
C	-3.39072	6.31537	2.21135
H	-3.85430	7.21420	1.80505

C	-4.03780	5.57750	3.20526
H	-5.01393	5.88817	3.57648
C	-3.41480	4.43511	3.71632
H	-3.90444	3.83951	4.48568
C	-2.16202	4.03537	3.23986
H	-1.69291	3.15447	3.66732
C	0.93677	4.81167	2.88052
C	2.14203	4.12431	3.09610
H	2.36534	3.21709	2.54230
C	3.08108	4.58306	4.02530
H	4.00029	4.01931	4.17207
C	2.84010	5.75042	4.75509
H	3.57194	6.10914	5.47831
C	1.64843	6.45164	4.54580
H	1.44426	7.36576	5.10304
C	0.70825	5.98410	3.62176
H	-0.21192	6.54501	3.47706
C	2.80627	-0.00757	1.54575
C	4.37626	0.01995	1.68313
C	4.82967	1.49347	1.43633
C	5.87130	2.06377	2.18931
H	6.33454	1.49586	2.99084
C	6.33842	3.35545	1.91951
H	7.15075	3.76518	2.51966
C	5.77175	4.11324	0.89237
H	6.13133	5.12089	0.68604
C	4.73797	3.55931	0.13163
H	4.27985	4.13228	-0.67357
C	4.27833	2.26567	0.39575
H	3.49266	1.84813	-0.22677
C	4.93062	-0.90933	0.57199
C	5.92854	-0.50910	-0.32549
H	6.32410	0.50235	-0.28426
C	6.43229	-1.39727	-1.28617
H	7.20701	-1.05825	-1.97350
C	5.94778	-2.70344	-1.36440
H	6.33844	-3.39316	-2.11202
C	4.95641	-3.11912	-0.46659
H	4.57366	-4.13852	-0.50253
C	4.45833	-2.23210	0.48842
H	3.70405	-2.58334	1.19099
C	4.86703	-0.45398	3.07561
C	4.33066	0.08867	4.25953
H	3.51646	0.80282	4.22310

C	4.82437	-0.28294	5.51242
H	4.37285	0.15335	6.40277
C	5.88389	-1.19067	5.62118
H	6.27319	-1.47394	6.59903
C	6.44272	-1.71893	4.45577
H	7.27705	-2.41786	4.51364
C	5.93828	-1.35519	3.20058
H	6.39792	-1.78081	2.31337
C	0.10998	-2.81232	1.56491
C	0.26000	-4.36744	1.77675
C	1.66984	-4.66828	2.37209
C	2.35235	-5.84480	2.00922
H	1.92334	-6.51293	1.26735
C	3.57790	-6.18266	2.59290
H	4.07864	-7.10199	2.28963
C	4.15684	-5.34872	3.55288
H	5.11696	-5.60358	4.00020
C	3.48966	-4.18009	3.92839
H	3.92894	-3.50977	4.66542
C	2.25866	-3.84837	3.35207
H	1.75902	-2.93949	3.66942
C	0.09946	-5.08293	0.40821
C	-0.88534	-6.05296	0.17338
H	-1.58709	-6.32079	0.95779
C	-0.98602	-6.70113	-1.06655
H	-1.76257	-7.45117	-1.21537
C	-0.09997	-6.39316	-2.09792
H	-0.17743	-6.89477	-3.06211
C	0.89561	-5.43290	-1.87608
H	1.59975	-5.18044	-2.66846
C	0.99378	-4.79168	-0.64170
H	1.77642	-4.05226	-0.49412
C	-0.83892	-4.83934	2.76000
C	-2.14953	-4.34465	2.63854
H	-2.38045	-3.58349	1.89580
C	-3.18833	-4.83432	3.43523
H	-4.19274	-4.43475	3.30502
C	-2.93823	-5.84252	4.37426
H	-3.74812	-6.23644	4.98785
C	-1.63966	-6.34046	4.50998
H	-1.42678	-7.12574	5.23520
C	-0.60106	-5.84002	3.71444
H	0.39998	-6.24550	3.83612
C	-2.81313	-0.04487	1.57580

C	-4.38166	-0.07037	1.73582
C	-4.80197	0.29380	3.18096
C	-4.32981	-0.46826	4.26773
H	-3.64489	-1.29124	4.08791
C	-4.72939	-0.19315	5.57553
H	-4.33884	-0.79819	6.39338
C	-5.62765	0.84913	5.83669
H	-5.94337	1.06302	6.85746
C	-6.11945	1.60217	4.77045
H	-6.83022	2.40863	4.94968
C	-5.71018	1.32640	3.45781
H	-6.11444	1.92624	2.64778
C	-4.94946	0.95207	0.71630
C	-6.04343	0.66183	-0.11049
H	-6.50401	-0.32206	-0.08030
C	-6.55924	1.62480	-0.98804
H	-7.40848	1.37036	-1.62179
C	-5.99045	2.89769	-1.05442
H	-6.38969	3.64550	-1.73903
C	-4.90171	3.20309	-0.22899
H	-4.44923	4.19344	-0.25585
C	-4.39153	2.24089	0.64421
H	-3.55609	2.50944	1.28799
C	-4.88923	-1.50248	1.38113
C	-4.35264	-2.23327	0.30414
H	-3.52987	-1.81810	-0.26943
C	-4.87500	-3.47923	-0.05779
H	-4.42766	-4.02222	-0.88965
C	-5.96119	-4.02218	0.63448
H	-6.37072	-4.99061	0.34921
C	-6.51764	-3.30103	1.69401
H	-7.37309	-3.69923	2.23955
C	-5.98605	-2.05995	2.06348
H	-6.44387	-1.51816	2.88641
C	0.03859	0.09126	4.83079
C	-0.26322	-0.90136	5.82163
C	-0.96926	-2.82626	7.75800
C	0.09695	-0.73428	7.19573
C	-0.97715	-2.07683	5.45954
C	-1.34155	-3.01543	6.42196
C	-0.23941	-1.68874	8.14351
H	0.67119	0.13974	7.49580
H	-1.23467	-2.22909	4.41794
H	-1.89628	-3.90211	6.12374

H	0.05533	-1.55541	9.18337
H	-1.24220	-3.57034	8.50617
C	0.52297	1.37076	5.39111
O	1.70376	1.60189	5.54848
O	-0.46866	2.19743	5.72785
C	-0.09805	3.46018	6.30590
H	0.62688	3.97900	5.67506
H	0.33198	3.30699	7.30321
H	-1.02204	4.03724	6.37732

Table 7.5. Optimized XYZ coordinates for **2**.

Rh	-0.00000	-0.00000	2.46852
Rh	0.00000	0.00000	0.00000
O	-2.06630	0.00601	0.08104
C	-2.65220	0.02455	1.19981
O	-2.07104	0.02344	2.33500
C	-4.16064	0.08111	1.21513
O	-0.01135	-2.06658	0.08545
C	-0.00244	-2.65190	1.20484
O	0.00127	-2.07003	2.33959
C	0.03681	-4.16092	1.21996
O	2.06350	-0.00164	0.08223
C	2.64567	-0.01045	1.20534
O	2.06337	-0.01248	2.33705
C	4.15479	-0.05062	1.22502
O	0.01403	2.06388	0.08399
C	0.03562	2.64681	1.20622
O	0.02025	2.06697	2.33936
C	0.11720	4.15457	1.21822
C	-0.00439	0.00796	4.49138
C	0.96516	0.95960	5.09266
O	2.11150	0.64106	5.33032
O	0.44967	2.16823	5.30269
C	1.35095	3.19634	5.75234
H	1.81126	2.91693	6.70623
H	2.13492	3.36484	5.00631
H	0.74328	4.09498	5.87377
C	-0.76846	-0.81148	5.38089
C	-0.60942	-0.70676	6.79781
C	-1.35737	-1.49550	7.66067
C	-2.29082	-2.40678	7.13955
C	-2.47109	-2.52934	5.75391
C	-1.72071	-1.74882	4.88129

H	-1.85558	-1.83940	3.81011
H	-3.19836	-3.23829	5.36148
H	-2.87935	-3.02336	7.81822
H	-1.22196	-1.40747	8.73735
H	0.11426	-0.00715	7.21122
H	1.07021	-4.48426	1.40348
H	-0.29274	-4.56232	0.25776
H	-0.58589	-4.54922	2.03230
H	-4.56579	-0.22109	0.24574
H	-4.47203	1.11313	1.42528
H	-4.55597	-0.55703	2.01226
H	4.55954	0.27367	0.26241
H	4.47736	-1.08291	1.41620
H	4.53844	0.57668	2.03596
H	-0.30050	4.56624	0.29500
H	1.17395	4.44723	1.28311
H	-0.40345	4.55937	2.09116

Table 7.6. Optimized XYZ coordinates for **3**.

Ir	0.003028	-0.002961	-0.013389
C	-1.211787	2.630639	-0.367207
C	-0.004229	1.951545	-0.182622
C	1.216482	2.629337	-0.308812
C	1.221017	4.009046	-0.549640
C	0.008180	4.723080	-0.689978
C	-1.208919	4.010578	-0.617545
H	2.174177	4.526106	-0.652317
H	-2.155695	4.519543	-0.778725
C	-2.298151	1.662270	-0.447683
O	-3.511817	1.970869	-0.889624
N	-2.063789	0.393250	-0.230001
C	2.311408	1.673667	-0.213425
O	3.598057	1.995447	-0.194293
N	2.030523	0.402546	-0.104819
C	0.059407	6.243416	-0.958982
C	-4.240633	0.725187	-1.056176
H	-5.097029	0.747199	-0.372817
H	-4.604918	0.689250	-2.087275
C	4.328936	0.776753	0.123863
H	5.156076	0.689307	-0.586365
H	4.725118	0.892296	1.138478
C	3.280289	-0.366441	0.015849
C	-3.210801	-0.389651	-0.722907

Cl	-0.076798	0.060026	-2.468518
C	0.010782	0.001567	1.949978
C	0.724540	1.185468	2.547100
C	-0.510255	-0.896379	2.964313
O	1.922589	1.235619	2.715955
O	-0.109571	2.191003	2.860028
C	-1.042237	-2.178916	2.669428
C	-0.480360	-0.526327	4.347190
C	0.490647	3.395097	3.352716
C	-1.500561	-3.035068	3.664005
H	-1.026165	-2.518952	1.636740
C	-0.947564	-1.362060	5.341235
H	-0.094544	0.445698	4.642125
H	-0.336297	4.070451	3.583653
H	1.084644	3.194825	4.252037
H	1.140133	3.838345	2.589967
C	-1.463808	-2.635791	5.013280
H	-1.876831	-4.015090	3.381735
H	-0.925753	-1.068163	6.388829
Cl	0.117432	-2.487058	-0.283104
C	0.816664	6.508601	-2.282954
C	0.797351	6.949315	0.204273
C	-1.346463	6.863251	-1.078843
H	-1.935658	6.724802	-0.162957
H	-1.912284	6.438914	-1.917951
H	-1.260575	7.943142	-1.254911
H	0.314740	6.018531	-3.126988
H	1.847585	6.135985	-2.247753
H	0.860398	7.586431	-2.491117
H	1.825366	6.584355	0.319176
H	0.275687	6.787672	1.156905
H	0.848642	8.032171	0.026410
H	-2.867482	-0.882762	-1.644115
C	-3.705261	-1.483220	0.243780
C	-4.171366	-0.940315	1.600753
C	-4.788279	-2.339213	-0.430835
H	-2.829821	-2.125294	0.405705
H	-5.104245	-0.364253	1.518330
H	-3.412682	-0.295508	2.059371
H	-4.366037	-1.766753	2.295697
H	-4.430135	-2.765571	-1.376982
H	-5.697604	-1.757400	-0.643715
H	-5.083918	-3.172960	0.218894
H	3.235248	-0.927302	0.958397

C	3.503445	-1.376546	-1.134350
C	3.591073	-0.720935	-2.518457
C	4.731181	-2.248941	-0.830520
H	2.614806	-2.022316	-1.122386
H	4.449105	-0.037206	-2.606053
H	2.671657	-0.173450	-2.755950
H	3.717120	-1.493222	-3.288450
H	4.638900	-2.752887	0.141403
H	5.663856	-1.664327	-0.820139
H	4.847240	-3.026058	-1.596484
O	-1.886644	-3.384328	6.044013
C	-2.407823	-4.682548	5.812452
H	-1.660462	-5.339011	5.344732
H	-3.306017	-4.649032	5.179388
H	-2.675328	-5.084962	6.793201

Table 7.7. Optimized XYZ coordinates for $Rh_2(OAc)_4$ NMe_2-carbene.

Rh	0.00000	0.00000	0.00000
Rh	0.00000	0.00000	2.46816
O	2.02143	-0.40089	2.41093
C	2.60433	-0.50050	1.27778
O	2.04211	-0.39713	0.12658
C	4.09541	-0.73305	1.27758
O	-0.40517	-2.02084	2.40989
C	-0.53892	-2.59633	1.27666
O	-0.42332	-2.03567	0.12588
C	-0.89337	-4.06322	1.27604
O	-2.01729	0.40979	2.41190
C	-2.59389	0.51911	1.27427
O	-2.03185	0.40645	0.12647
C	-4.08072	0.77769	1.26861
O	0.39715	2.01944	2.41408
C	0.50407	2.59802	1.27755
O	0.41019	2.03463	0.12868
C	0.73855	4.08915	1.27663
C	-0.00075	-0.00883	-2.03197
C	-0.79847	1.08599	-2.63238
O	-1.99728	0.98851	-2.88139
O	-0.07777	2.21489	-2.84163
C	-0.83212	3.36447	-3.31753
H	-1.29091	3.14911	-4.29126
H	-1.61197	3.63215	-2.59365
H	-0.09758	4.16991	-3.40910

C	0.58691	-0.94713	-2.90482
C	0.47470	-0.82676	-4.33318
C	1.03689	-1.73581	-5.19554
C	1.77280	-2.85998	-4.69737
C	1.90340	-2.98988	-3.27721
C	1.33279	-2.07452	-2.42534
H	1.44591	-2.19862	-1.35140
H	2.46028	-3.82597	-2.85773
N	2.32431	-3.76632	-5.54162
H	0.91491	-1.59411	-6.26792
H	-0.08179	0.01216	-4.75527
H	-1.98444	-4.16391	1.17114
H	-0.58950	-4.53088	2.21936
H	-0.42362	-4.57288	0.42636
H	4.41392	-1.17852	2.22673
H	4.60486	0.23508	1.15627
H	4.38486	-1.37477	0.43674
H	-4.39182	1.24305	2.21079
H	-4.60797	-0.18255	1.16157
H	-4.35535	1.41167	0.41727
H	1.21340	4.40219	2.21352
H	-0.23227	4.60040	1.19006
H	1.35453	4.38095	0.41799
C	2.18217	-3.62155	-6.99394
C	3.07264	-4.91498	-5.02141
H	2.43640	-5.54753	-4.38417
H	3.94635	-4.58839	-4.43741
H	3.42445	-5.51554	-5.86477
H	2.63336	-2.68151	-7.34574
H	1.12336	-3.64107	-7.29321
H	2.69491	-4.45539	-7.48131

Table 7.8. Optimized XYZ coordinates for $Rh_2(OAc)_4$ OMe-carbene.

Rh	0.00000	0.00000	0.00000
Rh	0.00000	0.00000	2.46300
O	-0.77957	1.90731	2.40819
C	-1.01290	2.45186	1.27596
O	-0.79859	1.91983	0.12531
C	-1.59392	3.84405	1.28568
O	1.90891	0.77493	2.40675
C	2.45918	0.99284	1.27426
O	1.92816	0.77438	0.12385
C	3.85857	1.55612	1.28324

O	0.77064	-1.90772	2.40895
C	0.99276	-2.45253	1.27253
O	0.78321	-1.91780	0.12486
C	1.55579	-3.85215	1.27724
O	-1.90305	-0.78113	2.41246
C	-2.44771	-1.00818	1.27733
O	-1.92138	-0.78560	0.12811
C	-3.84004	-1.58970	1.28755
C	0.00822	0.00159	-2.01772
C	-0.43230	-1.27603	-2.62810
O	0.34842	-2.18755	-2.88717
O	-1.76704	-1.34114	-2.83258
C	-2.26671	-2.61576	-3.33088
H	-1.82075	-2.84870	-4.30622
H	-2.03626	-3.41673	-2.61758
H	-3.34785	-2.48024	-3.42490
C	0.45248	1.02759	-2.89598
C	0.40538	0.86107	-4.31623
C	0.82760	1.84886	-5.18750
C	1.32053	3.06683	-4.66670
C	1.37704	3.26637	-3.26717
C	0.95760	2.27485	-2.40693
H	1.00563	2.43341	-1.33327
H	1.76049	4.21546	-2.89013
O	1.75901	4.09462	-5.42289
H	0.77677	1.67832	-6.26172
H	0.03086	-0.07418	-4.73543
H	4.52352	0.87018	1.82649
H	3.86179	2.51594	1.81858
H	4.23021	1.69983	0.26358
H	-0.91258	4.52000	1.82108
H	-2.54918	3.83593	1.82903
H	-1.75273	4.20986	0.26612
H	0.86744	-4.52005	1.81379
H	2.51351	-3.85797	1.81632
H	1.70365	-4.21615	0.25549
H	-4.51442	-0.91214	1.82962
H	-3.83025	-2.54908	1.82354
H	-4.20835	-1.73983	0.26776
C	1.73672	3.95955	-6.86454
H	0.70844	3.81578	-7.22500
H	2.37533	3.12472	-7.18576
H	2.13696	4.90337	-7.24604

Table 7.9. Optimized XYZ coordinates for $Rh_2(OAc)_4$ Me-carbene.

Rh	0.00000	0.00000	0.00000
Rh	-0.00000	-0.00000	2.46099
O	-0.69721	1.93781	2.40713
C	-0.90657	2.49262	1.27524
O	-0.71683	1.95068	0.12472
C	-1.42377	3.90924	1.28463
O	1.93892	0.69265	2.40692
C	2.49851	0.88783	1.27487
O	1.95771	0.69344	0.12450
C	3.92080	1.38912	1.28320
O	0.68907	-1.93750	2.40858
C	0.88759	-2.49231	1.27276
O	0.70157	-1.94841	0.12501
C	1.38858	-3.91479	1.27702
O	-1.93298	-0.70030	2.41325
C	-2.48804	-0.90331	1.27871
O	-1.95244	-0.70336	0.12937
C	-3.90426	-1.42264	1.28894
C	0.00162	-0.00118	-2.00995
C	-0.47880	-1.26349	-2.62318
O	0.28309	-2.18826	-2.89100
O	-1.81371	-1.29661	-2.81925
C	-2.34648	-2.55450	-3.32798
H	-1.91027	-2.78745	-4.30759
H	-2.13207	-3.36737	-2.62336
H	-3.42426	-2.39145	-3.41547
C	0.47333	1.01667	-2.89584
C	0.39012	0.85961	-4.31559
C	0.83357	1.84930	-5.17494
C	1.38505	3.05140	-4.67750
C	1.47192	3.21782	-3.28163
C	1.03203	2.23315	-2.40793
H	1.11003	2.38066	-1.33444
H	1.89636	4.14102	-2.88120
C	1.86342	4.11696	-5.62069
H	0.75742	1.70017	-6.25431
H	-0.02812	-0.05779	-4.73320
H	4.55496	0.67386	1.82543
H	3.96640	2.34726	1.81958
H	4.29756	1.51718	0.26337
H	-0.71153	4.55349	1.81892
H	-2.37755	3.94459	1.82944

H	-1.56704	4.28124	0.26506
H	0.67075	-4.55184	1.81245
H	2.34436	-3.96275	1.81737
H	1.52149	-4.28423	0.25521
H	-4.54774	-0.71480	1.82988
H	-3.93698	-2.38058	1.82654
H	-4.27849	-1.55754	0.26922
H	1.04343	4.45866	-6.27200
H	2.65045	3.72574	-6.28470
H	2.26378	4.98525	-5.08247

Table 7.10. Optimized XYZ coordinates for Rh$_2$(OAc)$_4$ H-carbene.

Rh	0.00000	0.00000	0.00000
Rh	0.00000	0.00000	2.45939
O	2.04916	-0.19648	2.40878
C	2.64152	-0.24022	1.27734
O	2.07041	-0.17995	0.12675
C	4.14358	-0.37191	1.28722
O	-0.20068	-2.04854	2.40587
C	-0.26152	-2.63870	1.27427
O	-0.20735	-2.06597	0.12396
C	-0.41129	-4.13894	1.28258
O	-2.04597	0.20493	2.40579
C	-2.63290	0.26180	1.27035
O	-2.06106	0.19706	0.12262
C	-4.13294	0.41500	1.27434
O	0.19357	2.04606	2.41407
C	0.24506	2.63557	1.27987
O	0.19578	2.06559	0.13061
C	0.37824	4.13780	1.28987
C	-0.00587	-0.00136	-2.00565
C	-0.97235	0.94286	-2.61795
O	-2.11982	0.60295	-2.89217
O	-0.48042	2.18460	-2.80218
C	-1.42666	3.17044	-3.31113
H	-1.80667	2.86481	-4.29410
H	-2.26182	3.28788	-2.60979
H	-0.85376	4.09838	-3.39105
C	0.73493	-0.84768	-2.89596
C	0.63789	-0.68446	-4.31242
C	1.36696	-1.48908	-5.17746
C	2.21411	-2.48336	-4.66372
C	2.32658	-2.66693	-3.27818

C	1.60177	-1.86570	-2.40335
H	1.68592	-2.00856	-1.32988
H	2.98484	-3.44291	-2.88431
H	2.78565	-3.11564	-5.34557
H	1.28020	-1.34825	-6.25589
H	-0.01873	0.08363	-4.72400
H	-1.32827	-4.40942	1.82452
H	0.43691	-4.58629	1.81945
H	-0.45467	-4.53453	0.26279
H	4.42502	-1.29107	1.81985
H	4.57898	0.47614	1.83402
H	4.54173	-0.39756	0.26782
H	-4.40323	1.33600	1.80954
H	-4.58330	-0.42920	1.81499
H	-4.52363	0.45168	0.25247
H	1.29331	4.41853	1.82979
H	-0.47415	4.57487	1.82851
H	0.41417	4.53374	0.27006

Table 7.11. Optimized XYZ coordinates for Rh$_2$(OAc)$_4$ Cl-carbene.

Rh	0.00000	0.00000	0.00000
Rh	0.00000	0.00000	2.45823
O	-0.92306	1.84011	2.40629
C	-1.19699	2.36746	1.27529
O	-0.94306	1.85189	0.12453
C	-1.87949	3.71166	1.28465
O	1.84218	0.91819	2.40512
C	2.37409	1.18194	1.27384
O	1.85931	0.92513	0.12329
C	3.72482	1.85133	1.28222
O	0.91452	-1.84086	2.40741
C	1.17845	-2.36865	1.27210
O	0.92844	-1.85034	0.12441
C	1.84617	-3.72033	1.27612
O	-1.83533	-0.92484	2.41165
C	-2.36197	-1.19476	1.27755
O	-1.85311	-0.93288	0.12826
C	-3.70499	-1.88047	1.28742
C	0.00336	-0.00410	-2.00638
C	-0.32036	-1.31335	-2.62391
O	0.55092	-2.13523	-2.89319
O	-1.63976	-1.50784	-2.82254
C	-2.01514	-2.81894	-3.33944

H	-1.55126	-2.99149	-4.31874
H	-1.70530	-3.60304	-2.63785
H	-3.10441	-2.78683	-3.42928
C	0.35619	1.06524	-2.89202
C	0.30303	0.89645	-4.30955
C	0.62730	1.92838	-5.17641
C	1.01518	3.16370	-4.63929
C	1.08234	3.37865	-3.25715
C	0.75794	2.33931	-2.39658
H	0.80861	2.49556	-1.32289
H	1.38764	4.34910	-2.86644
Cl	1.42580	4.47726	-5.73186
H	0.58288	1.78494	-6.25571
H	0.00431	-0.06375	-4.73220
H	4.44088	1.21694	1.82308
H	3.65421	2.80705	1.82016
H	4.08268	2.02545	0.26243
H	-1.24955	4.43603	1.81962
H	-2.83093	3.63209	1.82884
H	-2.06570	4.06406	0.26509
H	1.20982	-4.43870	1.81160
H	2.80082	-3.65286	1.81637
H	2.02234	-4.07086	0.25422
H	-4.42905	-1.25454	1.82743
H	-3.62217	-2.83492	1.82578
H	-4.05945	-2.06008	0.26755

Table 7.12. Optimized XYZ coordinates for $Rh_2(OAc)_4$ Br-carbene.

Rh	0.00000	0.00000	0.00000
Rh	0.00000	0.00000	2.45812
O	-0.95322	1.82486	2.40626
C	-1.23794	2.34643	1.27522
O	-0.97696	1.83418	0.12460
C	-1.94292	3.67893	1.28430
O	1.82702	0.94811	2.40474
C	2.35366	1.22231	1.27348
O	1.84207	0.95885	0.12300
C	3.69318	1.91369	1.28159
O	0.94445	-1.82589	2.40644
C	1.21717	-2.34921	1.27117
O	0.96008	-1.83423	0.12346
C	1.90528	-3.69055	1.27519
O	-1.82013	-0.95412	2.41244

C	-2.34212	-1.23320	1.27832
O	-1.83669	-0.96455	0.12915
C	-3.67441	-1.93937	1.28817
C	0.00490	-0.00401	-2.00674
C	-0.27510	-1.32307	-2.62470
O	0.62475	-2.11125	-2.90098
O	-1.58748	-1.56724	-2.81402
C	-1.91683	-2.89110	-3.32966
H	-1.45263	-3.04599	-4.31174
H	-1.57397	-3.66342	-2.63035
H	-3.00706	-2.89950	-3.41302
C	0.32217	1.07753	-2.89138
C	0.25518	0.91464	-4.30888
C	0.53868	1.96044	-5.17473
C	0.89988	3.20262	-4.63530
C	0.98323	3.41150	-3.25337
C	0.69805	2.35861	-2.39426
H	0.76168	2.51032	-1.32055
H	1.26889	4.38548	-2.85693
Br	1.28779	4.65165	-5.82078
H	0.48123	1.81751	-6.25337
H	-0.02372	-0.05086	-4.73331
H	4.41991	1.29007	1.82072
H	3.60733	2.86753	1.82060
H	4.04690	2.09473	0.26156
H	-1.32417	4.41426	1.81735
H	-2.89224	3.58390	1.82966
H	-2.13625	4.02678	0.26449
H	1.27937	-4.41848	1.81006
H	2.85865	-3.60866	1.81565
H	2.08692	-4.03787	0.25315
H	-4.40807	-1.32403	1.82737
H	-3.57698	-2.89221	1.82691
H	-4.02536	-2.12483	0.26812

Table 7.13. Optimized XYZ coordinates for $Rh_2(OAc)_4$ CF_3-carbene.

Rh	0.00000	0.00000	0.00000
Rh	-0.00000	0.00000	2.45522
O	1.44911	-1.45991	2.40779
C	1.87472	-1.87694	1.27755
O	1.47242	-1.46584	0.12694
C	2.94172	-2.94118	1.28692
O	-1.46259	-1.44721	2.40301

C	-1.88689	-1.86362	1.27218
O	-1.47938	-1.45584	0.12200
C	-2.95825	-2.92343	1.27933
O	-1.44274	1.46274	2.40427
C	-1.85889	1.88213	1.26943
O	-1.45723	1.46825	0.12207
C	-2.91814	2.95413	1.27237
O	1.45559	1.44972	2.40834
C	1.87088	1.87247	1.27474
O	1.46846	1.46419	0.12565
C	2.92948	2.94559	1.28419
C	-0.00181	0.00614	-1.99963
C	-0.08783	1.35006	-2.62139
O	-1.16958	1.86799	-2.88277
O	1.10932	1.92913	-2.83328
C	1.07170	3.28962	-3.35976
H	0.56776	3.30827	-4.33414
H	0.54923	3.95016	-2.65714
H	2.12014	3.58243	-3.46195
C	-0.01489	-1.12630	-2.88691
C	-0.02450	-0.94896	-4.30307
C	-0.01447	-2.03586	-5.16264
C	0.00842	-3.33858	-4.63516
C	0.01427	-3.54657	-3.25019
C	0.00184	-2.45675	-2.38719
H	0.00841	-2.61815	-1.31360
H	0.03061	-4.55849	-2.84678
C	0.01592	-4.50476	-5.59216
H	-0.01968	-1.87643	-6.24155
H	-0.04203	0.05603	-4.72601
H	-3.83565	-2.54901	1.82483
H	-2.58828	-3.81062	1.81207
H	-3.24616	-3.19685	0.25920
H	2.56800	-3.82629	1.82041
H	3.82012	-2.56947	1.83274
H	3.22962	-3.21680	0.26738
H	-2.54653	3.83147	1.81979
H	-3.80785	2.58330	1.80038
H	-3.18618	3.23971	0.25025
H	3.80785	2.58547	1.83757
H	2.54392	3.83067	1.80936
H	3.21946	3.21750	0.26442
F	1.03525	-4.40462	-6.49913
F	-1.14220	-4.57058	-6.31957

F   0.15668   -5.70288   -4.96575

Table 7.14. Optimized XYZ coordinates for $Rh_2(OAc)_4$ *bis*-(H-carbene).

Rh	0.00000	0.00000	0.00000
Rh	-0.00000	-0.00000	2.54533
O	0.03886	-2.07169	2.44146
C	0.03542	-2.65637	1.30270
O	-0.00072	-2.07846	0.16203
C	0.11126	-4.16360	1.30501
O	-2.07825	-0.01319	2.38050
C	-2.65663	0.01680	1.24003
O	-2.07135	0.02748	0.10177
C	-4.16462	0.07441	1.23840
O	-0.00226	2.07078	2.41839
C	0.02205	2.64554	1.27558
O	0.00859	2.06437	0.13639
C	0.09494	4.15348	1.26910
O	2.06488	0.01409	2.41042
C	2.64595	0.02205	1.27025
O	2.07001	-0.00427	0.12906
C	4.15394	0.09225	1.27598
C	0.03027	-0.04317	-2.09010
C	1.00534	0.86495	-2.70259
O	0.70821	2.02894	-2.98251
O	2.23985	0.33667	-2.86878
C	3.26846	1.26467	-3.31685
H	3.01861	1.67001	-4.30566
H	3.37840	2.08535	-2.59700
H	4.18543	0.67047	-3.36719
C	-0.80192	-0.80591	-2.97711
C	-0.70548	-0.67785	-4.39667
C	-1.51707	-1.42468	-5.24027
C	-2.43680	-2.33725	-4.69905
C	-2.54564	-2.49247	-3.30977
C	-1.74951	-1.73463	-2.45764
H	-1.82822	-1.84638	-1.37923
H	-3.26082	-3.20600	-2.89710
H	-3.06865	-2.92912	-5.36390
H	-1.43556	-1.30827	-6.32206
H	0.00815	0.02829	-4.82475
H	-4.47637	1.12702	1.31781
H	-4.56922	-0.46717	2.10143
H	-4.56535	-0.33567	0.30461

H	-0.32077	-4.56982	2.22654
H	1.16973	-4.46191	1.25833
H	-0.39916	-4.57480	0.42643
H	1.15289	4.45622	1.28390
H	-0.39369	4.56390	2.16020
H	-0.36488	4.55439	0.35865
H	4.55552	-0.39061	2.17431
H	4.45817	1.14986	1.28847
H	4.56228	-0.37426	0.37237
C	-0.05511	0.03506	4.63402
C	0.76122	1.08944	5.24468
O	1.95411	0.91651	5.50571
O	0.10509	2.25827	5.43366
C	0.92283	3.37781	5.87854
C	-0.74917	-0.85392	5.52186
C	-0.56805	-0.79747	6.93783
C	-1.23986	-1.67244	7.78111
C	-2.13482	-2.61247	7.24525
C	-2.34682	-2.67794	5.86077
C	-1.65755	-1.82343	5.00691
H	0.12432	-0.06804	7.36178
H	-1.07953	-1.62385	8.85931
H	-2.66973	-3.29281	7.91064
H	-3.04898	-3.40664	5.45250
H	-1.81314	-1.86864	3.93201
H	0.23267	4.22334	5.95074
H	1.71295	3.58502	5.14599
H	1.37106	3.16330	6.85708
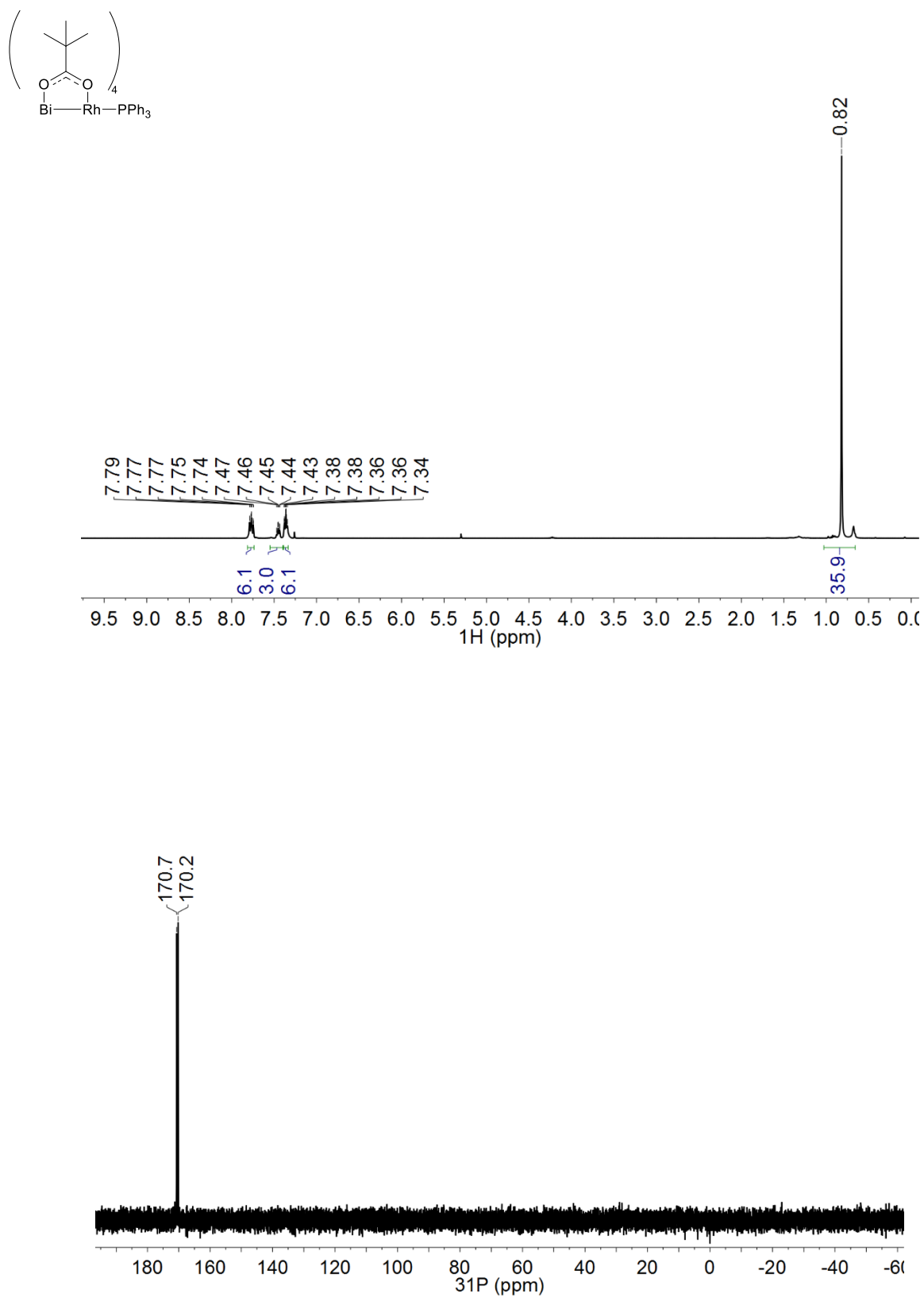
Figure 7.11. NMR spectra of **4** at room temperature in CDCl$_3$ (^{1}H (top), ^{31}P{^{1}H} (bottom)).

Figure 7.12. NMR spectra of **5** at room temperature in CDCl₃ (¹H (top), ³¹P{¹H} (bottom)).

7.8 References

(1)   Davies, H. M. L.; Morton, D. *Chem. Soc. Rev.* **2011**, *40*, 1857.

(2)   Davies, H. M. L.; Beckwith, R. E. J. *Chem. Rev.* **2003**, *103*, 2861.

(3)   Davies, H. M. L. *Angew. Chem., Int. Ed.* **2006**, *45*, 6422.

(4)   Kornecki, K. P.; Briones, J. F.; Boyarskikh, V.; Fullilove, F.; Autschbach, J.; Schrote, K. E.; Lancaster, K. M.; Davies, H. M. L.; Berry, J. F. *Science* **2013**, *342*, 351.

(5)   Werlé, C.; Goddard, R.; Philipps, P.; Farès, C.; Fürstner, A. *J. Am. Chem. Soc.* **2016**, *138*, 3797.

(6)   Hashimoto, S.; Watanabe, N.; Ikegami, S. *Tetrahedron Lett.* **1992**, *33*, 2709.

(7)   Qin, C.; Davies, H. M. L. *J. Am. Chem. Soc.* **2014**, *136*, 9792.

(8)   Owens, C. P.; Varela-Alvarez, A.; Boyarskikh, V.; Musaev, D. G.; Davies, H. M. L.; Blakey, S. B. *Chem. Sci.* **2013**, *4*, 2590.

(9)   Sunderland, T. L.; Berry, J. F. *Dalton Trans.* **2016**, *45*, 50.

(10)   Cotton, F. A.; Murillo, C. A.; Walton, R. A. *Multiple Bonds Between Metal Atoms.* 3rd ed.; Springer Science and Business Media, Inc.: New York, **2005**.

(11)   Chan, W.; Yeung, S.; Zhou, Z.; Chan, A. S. C.; Yu, W. *Org. Lett.* **2010**, *12*, 604.

(12)   Bruker-AXS *SMART* Program*,* Madison, Wisconsin, USA, **2009**.

(13)   Sheldrick, G. *Acta Cryst. A* **2008**, *64*, 112.

(14)   Dolomanov, O. V.; Bourhis, L. J.; Gildea, R. J.; Howard, J. A. K.; Puschmann, H. *J. Appl. Crystallogr.* **2009**, *42*, 339.

(15)   Neese, F. *ORCA- an ab initio, Density Functional and Semiempirical program package*, Univeristy of Bonn: Bonn, **2006**.

(16)   Vosko, S. H.; Wilk, L.; Nusair, M. *Can. J. Phys.* **1980**, *58*, 1200.

(17)   Lee, C.; Yang, W.; Parr, R. G. *Phys. Rev. B* **1988**, *37*, 785.

(18)   Becke, A. D. *J. Chem. Phys.* **1993**, *98*, 5648.

(19)   Stephens, P. J.; Devlin, F. J.; Chabalowski, C. F.; Frisch, M. J. *J. Phys. Chem.* **1994**, *98*, 11623.

(20)   Pantazis, D. A.; Chen, X.; Landis, C. R.; Neese, F. *J. Chem. Theory Comput.* **2008**, *4*, 908.

(21)   Wullen, C. V. *J. Chem. Phys.* **1998**, *109*, 392.

(22)   Eichkorn, K.; Treutler, O.; Öhm, H.; Häser, M.; Ahlrichs, R. *Chem. Phys. Lett.* **1995**, *240*, 283.

(23)   Sinnecker, S.; Rajendran, A.; Klamt, A.; Diedenhofen, M.; Neese, F. *J. Phys. Chem. A* **2006**, *110*, 2235.

(24)   Klamt, A.; Schuurmann, G. *J. Chem. Soc., Perkin Trans. 2* **1993**, 799.

(25)   Pettersen, E. F.; Goddard, T. D.; Huang, C. C.; Couch, G. S.; Greenblatt, D. M.; Meng, E. C.; Ferrin, T. E. *J. Comput. Chem.* **2004**, *25*, 1605.

(26)   Hansen, J.; Li, B.; Dikarev, E.; Autschbach, J.; Davies, H. M. L. *J. Org. Chem.* **2009**, *74*, 6564.

(27)   Bursten, B. E.; Cotton, F. A. *Inorg. Chem.* **1981**, *20*, 3042.

(28)   Christoph, G. G.; Halpern, J.; Khare, G. P.; Koh, Y. B.; Romanowski, C. *Inorg. Chem.* **1981**, *20*, 3029.

Appendix 1

Preliminary In Situ Kinetic Data on Rh$_2$(TPA)$_4$ Catalyzed

Donor/Acceptor Carbene C–H Insertion Reactions of 1,4-Cyclohexadiene

Sunderland, T. L. and Berry, J. F.

Department of Chemistry, University of Wisconsin–Madison, 1101 University Avenue, Madison, WI 53706, United States

A1.1 Abstract

Initial reaction profiles for reaction progress kinetic analysis (RPKA) on the $Rh_2(TPA)_4$ catalyzed insertion of methyl-(aryl)-diazoacetates into 1,4-cyclohexadiene have been collected. The reaction orders of both diazo and catalyst concentrations are estimated at 0.82 and 0.80, respectively. Significant catalyst inhibition by 1,4-cyclohexadiene is seen with an estimated –0.85 reaction order. The same excess experiment with methyl-(4-methyl-aryl)-diazoacetate shows no sign of either catalyst deactivation or product inhibition.

A1.2 Introduction

The generally accepted mechanism for metal catalyzed diazo insertion into O–H, S–H and N–H bonds (see Scheme A1.1) was first proposed by Yates in 1952[1] and the acceptance of this model now generally applies to metal carbene C–H functionalization,[2,3] as well, however, there are still many unanswered questions about the intricacies of the catalytic cycle.[3-6] The productive catalytic pathway includes coordination of the diazo compound to the metal complex to form a metal diazo adduct. Following coordination, loss of N_2 to form a highly reactive metal carbene species is considered to be the rate determining step, however, the rate limiting step can change in the presence of difficult to activate substrates such as cyclopentane, where carbene insertion becomes rate limiting.[7]
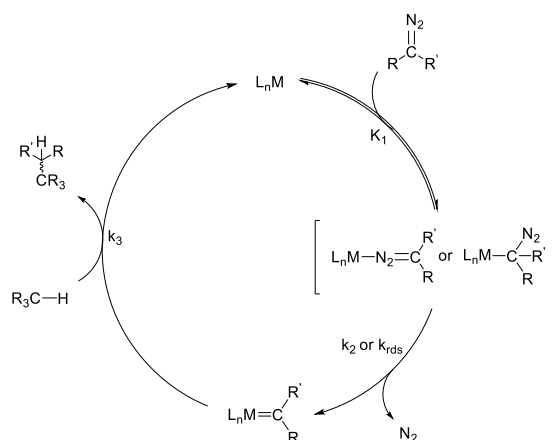
Scheme A1.1. General mechanism for metal catalyzed carbene insertion reaction of diazo compounds into C–H bonds.

Some of the initial catalytic results to support this proposed pathway were published in 1980,[8] and more recently, Wang and coworkers have conducted a Hammett correlation study on Rh_2 complexes that showed methyl-(aryl)-diazoesters bearing electron donating groups on the aryl ring provide more activated diazo compounds but alternatively less reactive Rh_2 carbenes.[9] To provide a more global kinetic picture of Rh_2 catalyzed C–H insertion reactions, a recently developed technique, reaction progress kinetic analysis (RPKA), could be applied.[10,11] This powerful technique allows for kinetic analysis of reactions under catalytically relevant conditions. This technique is predicated on two major categories of experiments, different excess and same excess experiments, which can provide information about the relative reaction orders of each key component, as well as reveal whether catalyst decomposition/product inhibition are factors, respectively. Substrate and/or product inhibition could play a major role in catalysis since Rh_2 compounds are known to coordinate both aromatic rings and Lewis bases.[12,13] While the full RPKA for the reactions herein have not yet been completed, several reaction progress profiles have been collected and are discussed below.

A1.3 Experimental Section

A1.3.1 Materials and Methods

All reactions were carried out using oven dried glassware under a dry N_2 atmosphere using Schlenk techniques. Dichloromethane (DCM) was dried over CaH_2 and distilled prior to use. $Rh_2(TPA)_4$ (TPA = triphenylacetate)[14] and methyl-(4-X-aryl)-diazoacetate (X = OMe, Me, H, Cl and Br)[15] were prepared according to literature procedures. 1,4-Cyclohexadiene was purchased from Sigma-Aldrich and used without further purification. Reaction progress was monitored by *in situ* IR spectroscopy collected using a Mettler Toledo ReactIR ic10 with an AgX probe.

A1.3.2 General Procedure for Collection of ReactIR Data

A 10 mL Schlenk flask was loaded with a magnetic stir bar and the corresponding diazo compound, which was subsequently dissolved in DCM. To this solution was added 1,4-cyclohexadiene and the ReactIR probe inserted. The data collection was started and a DCM solution of $Rh_2(TPA)_4$ was injected at room temperature. The total volume of each reaction was 5 mL.

A1.4 Results and Discussion

A1.4.1 Kinetic Analysis

In order to investigate the overall mechanism of the C–H insertion reactions, a trapping agent that results in clean C–H bond insertion is necessary. 1,4-cyclohexadiene contains some of the most activated C–H bonds for carbene insertion reactions, therefore it is an ideal substrate to adequately trap the reactive Rh_2 carbene and return the catalyst back into the active cycle. To probe the mechanism by reaction progress kinetic analysis (RPKA), two categories of experiments are necessary; different excess experiments to probe the reaction dependency of each component of the reaction, and same excess experiments to investigate whether catalyst deactivation or product inhibition is occurring throughout the duration of the reaction. For the

reaction of interest, shown below in Scheme A1.2, different excess experiments were used to probe the reaction order of the trap, the diazo compound and the catalyst. A representative table for the reaction condition setup is shown in Table A1.1.

X = OMe, Me, H, Cl, Br
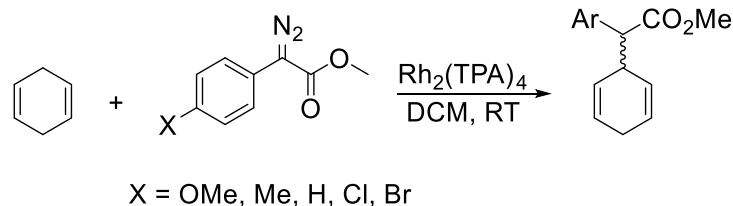
Scheme A1.2. General C–H insertion reaction of diazoesters catalyzed by $Rh_2(TPA)_4$.

Table A1.1. Table of reaction conditions for different and same excess experiments.

Reaction Type	[Trap] (M)	[Diazo] (M)	[Rh₂(TPA)₄] (M)	Excess (M)
Standard	0.18	0.06	3.0×10^{-6}	0.12
Trap Dependency	0.36	0.6	3.0×10^{-6}	0.30
Diazo Dependency	0.18	0.12	3.0×10^{-6}	0.06
Catalyst Dependency	0.18	0.06	6.0×10^{-6}	0.12
Same Excess	0.24	0.12	3.0×10^{-6}	0.12

The progress of each reaction can be adequately monitored by ReactIR due to the distinct and intense IR stretching frequency of the diazo compounds at ~ 2090 cm^{-1}. In order to convert the absorbance of the diazo stretching frequency into concentration, Beer's Law (Equation A1.1) where A =absorbance (a.u.), ε = molar absorptivity (M^{-1}cm^{-1}), b = path length (cm), and c = concentration, can be utilized. To use Beer's law, calibration curves were first made for each diazo compound. The calibration curve for methyl-(4-OMe-aryl)-diazoacetate is shown in Figure A1.1 (all others can be found in the Supporting Information section).

$$A = \varepsilon \, b \, c \qquad\qquad \text{(Eq A1.1)}$$
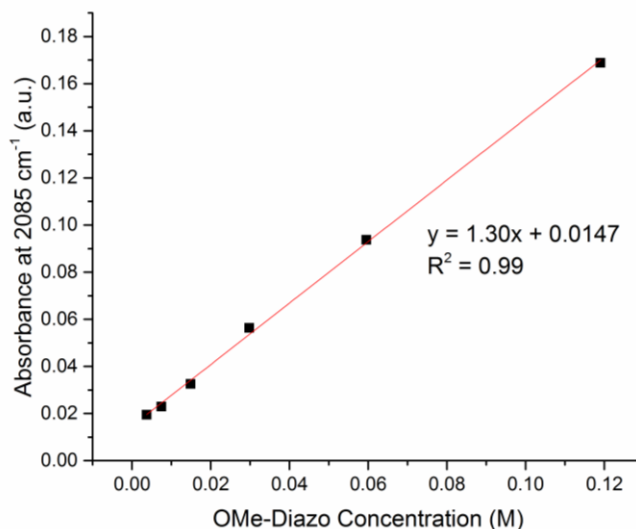
Figure A1.1. Calibration curve for methyl-(4-OMe-aryl)-diazoacetate in DCM.

The currently accepted mechanism for Rh_2 catalyzed diazo decomposition and subsequent C–H insertion is shown in Scheme A1.3. Although mechanistic studies have been performed on Rh_2 catalyzed reactions, unanswered questions still exist. The generally accepted mechanism starts with the formation of an Rh_2 diazo adduct (either N-bound (left) or C-bound (right)), which has not been observed, which is in equilibrium with the unbound species (K_1). Following diazo adduct formation, rate limiting extrusion of N_2 occurs to form an Rh_2 carbene species (k_2 or k_{rds}). The first evidence for this long-proposed reactive intermediate has recently been published.[16,17] Once the Rh_2 carbene is formed, it can then undergo fast (for activated substrates such as 1,4-cyclohexadiene) C–H bond insertion to regenerate the active catalyst (k_3).
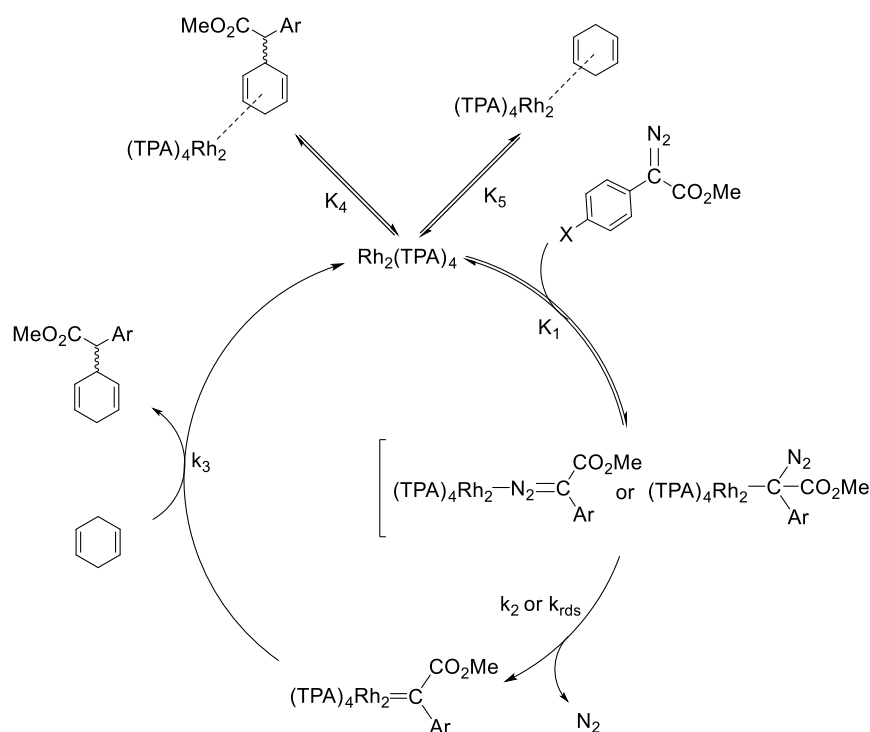
Scheme A1.3. Proposed mechanism for the Rh_2 catalyzed C–H insertion reaction of diazoesters into 1,4-cyclohexadiene.

Additional off-cycle species can also exist, leading to either a slowing or complete shutting down of catalysis, such as coordination of the product to the Rh_2 center (K_4) or coordination of the trapping agent (K_5). Little is currently known about the role that off-cycle species play in slowing down catalysis, or what leads to catalyst decomposition. The goal of this project was to develop a more complete understanding of the overall mechanism of Rh_2 catalyzed C–H insertion reactions, including the role of off-cycle species. While this goal has not yet been achieved, progress has been made to support the mechanism shown in Scheme A1.3.

First, the dependency on incoming diazo concentration was investigated. Different excess experiments were conducted to compare the reaction progress of standard conditions (0.06 M diazo, 0.18 M trap, 3 x 10^{-6} M $Rh_2(TPA)_4$) to different excess of diazo compound (0.12 M diazo, 0.18 M trap and 3 x 10^{-6} M $Rh_2(TPA)_4$). A representative example of the entire reaction progress

with methyl-(4-Cl-aryl)-diazoacetate is shown below in Figure A1.2. To have a clearer comparison and the same starting concentration, [diazo] has been converted into [trap]. This conversion into [trap] means that the diazo compound will be totally consumed once [trap] = 0.12 M, likewise, the 0.12 M [diazo] will result in a final [trap] = 0.06 M. Both the standard (black) and the diazo dependency (red) conditions go to completion (Figure A1.2, left). If we compare the slopes of the initial rates of the reaction, the standard conditions reaction has a slope of –0.0013 compared to –0.0023 for the diazo dependency conditions. Since [diazo] was doubled for this different excess experiment, a doubling of the initial rate would suggest a 1st order dependence on [diazo]. The increase in initial rate appears to be 1.8 times faster, suggesting a diazo reaction order of 0.88.
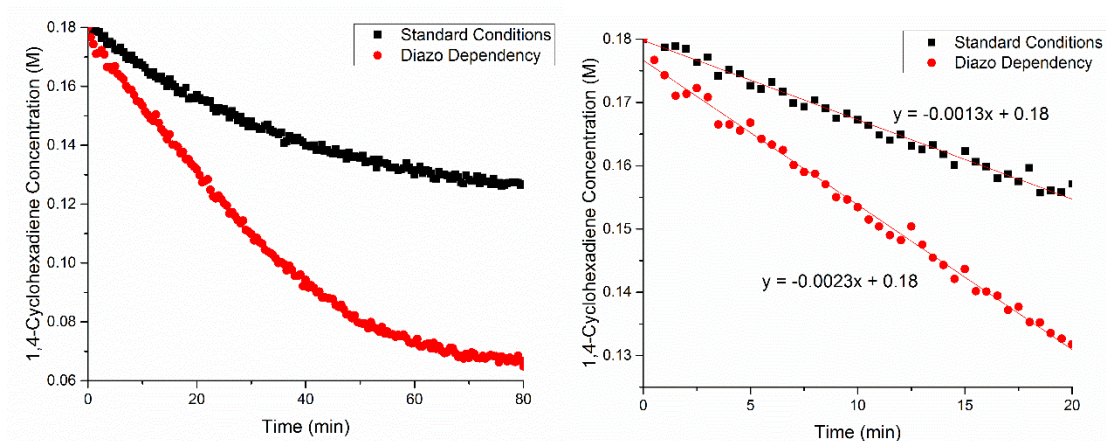
Figure A1.2. Reaction progress of methyl-(4-Cl-aryl)-diazoacetate monitored by ReactIR to probe diazo dependence, full reaction (left) and initial reaction segment (right).

When the diazo dependence is investigated using methyl-(4-Br-aryl)-diazoacetate, similar results are found. The full reaction profile is shown below in Figure A1.3 (left) and the initial reaction segment (right). The [diazo] has again been converted into [trap] for ease of comparison. The doubling of [diazo] resulted in a reaction with a 1.5 times faster initial rate, which suggests a diazo reaction order of 0.75. For both the Cl- and Br-diazo compounds, the diazo order appears to be 0.82, slightly less than 1st order.
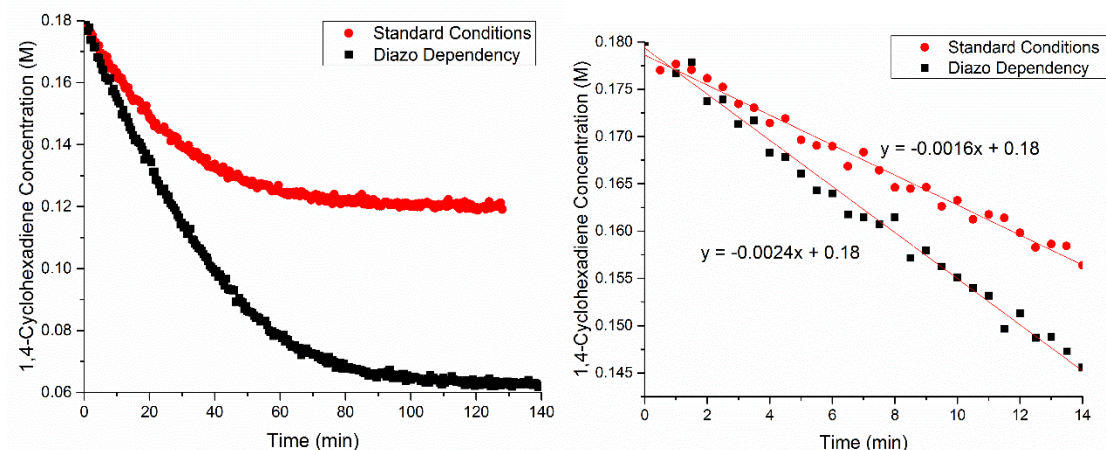
Figure A1.3. Reaction progress of methyl-(4-Br-aryl)-diazoacetate monitored by ReactIR to probe diazo dependence, full reaction (left) and initial reaction segment (right).

Next, the reaction dependence on [catalyst] was investigated. The standard conditions remained the same (0.06 M diazo, 0.18 M trap and 3 x 10^{-6} M catalyst), but the different excess conditions for the catalyst consisted of doubling the [catalyst] (6 x 10^{-6} M). First, the reaction with methyl-(4-Br-aryl)-diazoacetate was explored, the full reaction progress (left) and the initial reaction segment (right) are shown in Figure A1.4. Both the standard and excess catalyst reactions show complete consumption of the diazo compound. The doubling of the catalyst concentration results in a 1.67 times faster initial rate of diazo consumption, which suggests a catalyst dependency of 0.83.
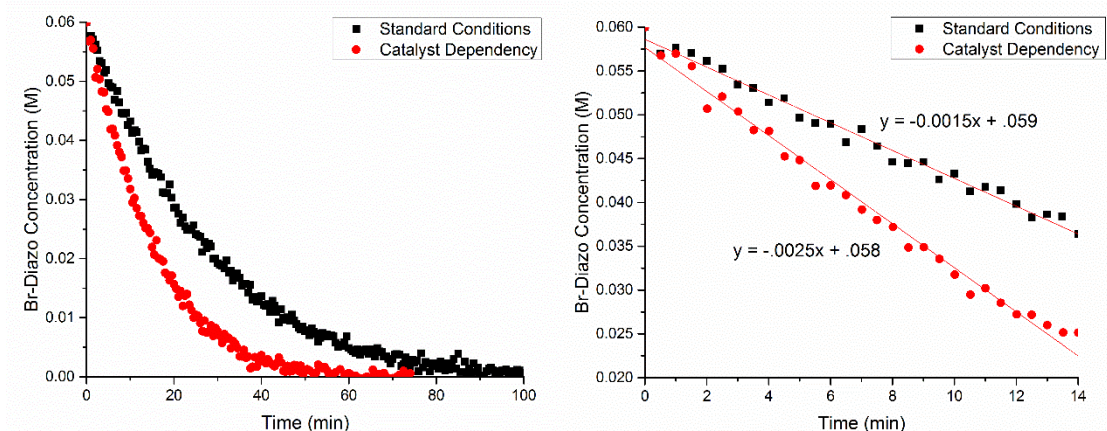
Figure A1.4. Reaction progress of methyl-(4-Br-aryl)-diazoacetate monitored by ReactIR to probe catalyst dependence, full reaction (left) and initial reaction segment (right).

To further corroborate the reaction dependency on [catalyst], a second diazo compound (methyl-4-(Me-aryl)-diazoacetate) was tested under different excess [catalyst] conditions. The initial reaction segment is shown in Figure A1.5. A doubling of [catalyst] results in an increased initial reaction rate of 1.28 and a catalyst order of 0.64. A similar analysis with methyl-(4-OMe-aryl)-diazoacetate and methyl-(phenyl)-diazoacetate (see SI Figures A1.11 and A1.12, respectively) resulted in catalyst reaction orders of 0.88 and 0.85, respectively. Comparing the dependency on [catalyst] between four diazo compounds, an average reaction order of 0.80, slightly less than 1st order, was calculated.
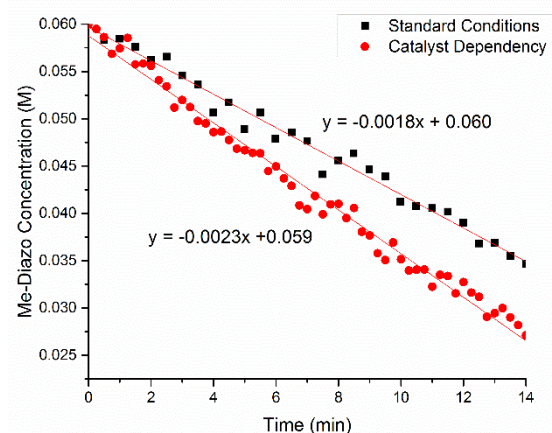
Figure A1.5. Reaction progress of methyl-(4-Me-aryl)-diazoacetate monitored by ReactIR to probe catalyst dependence.

The third dependency to be investigated with different excess experiments was [trap]. These experiments were conducted utilizing both the methyl-(4-OMe-aryl)-diazoacetate and methyl-(phenyl)-diazoacetate compounds under standard conditions and with [trap] = 0.36 M instead of 0.18 M. The initial reaction progress is shown in SI Figures A1.11 and A1.12 for the OMe-aryl- and phenyl-diazoacetate compounds, respectively. After analysis of the initial rates, the methyl-(4-OMe-aryl)-diazoacetate reactions show an initial rate 1.48 and 1.92 times slower when the [trap] is doubled, respectively, which suggests reaction orders of –0.74 and –0.96. The negative reaction order indicates that catalysis is inhibited by excess trapping agent. This inhibition can lead to challenging reaction design, since an excess of trapping agent is often preferred to ensure higher selectivity for C–H insertion over counter-productive side reactions leading to azine and alkene formation.

Following the different excess experiments to determine the reaction orders for the individual components of the mechanism, a same excess experiment was conducted to investigate if alterations in the reaction rate exist as the reaction progresses. The same excess experiment reaction setup entails starting the reaction with the same excess between the two reagents, but at different starting concentrations (0.12 M diazo, 0.24 M 1,4-cyclohexadiene and

3 x 10^{-6} M $Rh_2(TPA)_4$). For this particular reaction setup, once half of the diazo compound is consumed, the remaining reaction progress should be identical to the standard reaction conditions (0.6 M diazo, 0.18 M 1,4-cyclohexadiene and 3 x 10^{-6} M $Rh_2(TPA)_4$). To better compare the standard and same excess experiments to each other, the standard condition plot can be time shifted to the point when the same excess reaction has the same [diazo] as the initial [diazo] from the standard reaction setup. The reaction progress of the same excess experiment (red), the standard reaction (black) and the time shifted standard reaction (blue) monitored with the methyl-(4-Me-aryl)-diazoacetate is shown in Figure A1.6. The reaction progress curves of both the same excess (red) and the time shifted (blue) overlay nearly perfectly. This indicates that under these reaction conditions, neither catalyst deactivation nor product inhibition play a significant role in slowing down the reaction as it progresses. To more firmly test whether coordination of the product is a significant off-cycle species, additional product-inhibition studies should still be conducted.
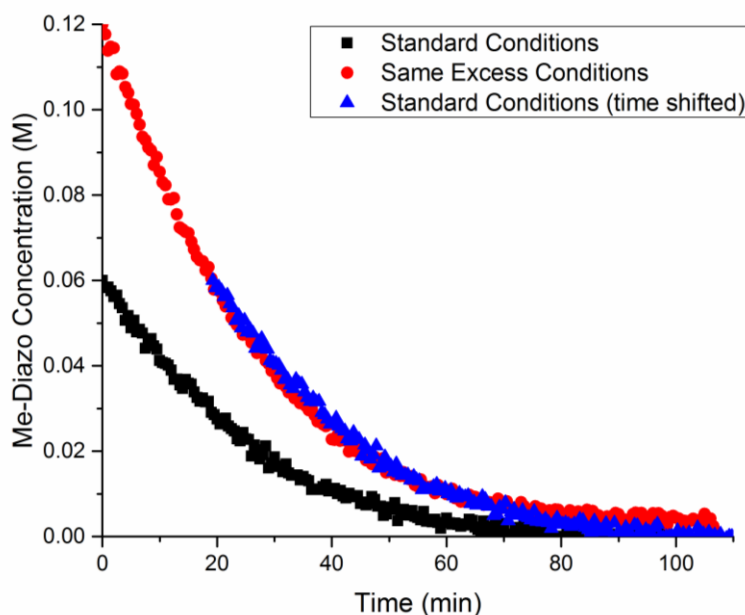
Figure A1.6. Reaction progress of methyl-(4-Me-aryl)-diazoacetate monitored by ReactIR to compare standard conditions (black), same excess conditions (red) and time shifted standard conditions (blue).

A1.5 Conclusions

The full RPKA for the reactions discussed above have not yet been completed, however, initial observations of the C–H insertion reaction into 1,4-cyclohexadiene catalyzed by $Rh_2(TPA)_4$ support the proposed mechanism shown in Scheme A1.3. The reaction has a positive 0.82 order in [diazo] and 0.80 in [catalyst]. Since the proposed rate limiting step is N_2 extrusion rather than diazo adduct formation, reaction orders of 0 for [diazo] and [catalyst] are expected, however, the equilibrium between free diazo and Rh_2 bound diazo will be pushed towards the diazo adduct with increased concentrations of the two free species. The apparent reaction orders of 0.81 in each species supports this hypothesis. Catalyst inhibition by trap coordination is also supported. A reaction order of –0.85 was found for 1,4-cyclohexadiene. This trap inhibition creates a delicate balance between low [trap] that allows the reaction to progress under reasonable reaction times and high [trap] that promote clean reactivity. Finally, the roles of catalyst deactivation and/or product inhibition were investigated by a same excess experiment. Neither of these pathways proved to be significant factors under the reaction conditions chosen. While the goal of a rigorous kinetic analysis of the C–H insertion mechanism has not yet been fully accomplished, the results within this chapter do support the proposed mechanism and provide valuable data towards a more in-depth understanding of Rh_2 catalyzed C–H functionalization catalysis.

A1.6 Acknowledgments

A1.7 Supporting Information

General Reaction for Standard Conditions

A 10 mL Schlenk flask was loaded with a magnetic stir bar and the corresponding diazo compound (0.300 mmol), which was then dissolved in 4.86 mL dry DCM. To this solution was added 85.2 µL 1,4-cyclohexadiene *via* syringe and the ReactIR probe was inserted. The data collection was started and once stable, 50.0 µL of 3.00 x 10^{-4} M $Rh_2(TPA)_4$ in DCM was injected at room temperature in one swift motion. The initial concentration of each component at the start of the reaction were 0.06 M, 0.18 M and 3.0 x 10^{-6} M for diazo, trap and catalyst, respectively.

General Reaction for Diazo Dependency

A 10 mL Schlenk flask was loaded with a magnetic stir bar and the corresponding diazo compound (0.600 mmol), which was then dissolved in 4.86 mL dry DCM. To this solution was added 85.2 µL 1,4-cyclohexadiene *via* syringe and the ReactIR probe was inserted. The data collection was started and once stable, 50.0 µL of 3.00 x 10^{-4} M $Rh_2(TPA)_4$ in DCM was injected at room temperature in one swift motion. The initial concentration of each component at the start of the reaction were 0.12 M, 0.18 M and 3.0 x 10^{-6} M for diazo, trap and catalyst, respectively.

General Reaction for Catalyst Dependency

A 10 mL Schlenk flask was loaded with a magnetic stir bar and the corresponding diazo compound (0.300 mmol), which was then dissolved in 4.81 mL dry DCM. To this solution was added 85.2 µL 1,4-cyclohexadiene *via* syringe and the ReactIR probe was inserted. The data collection was started and once stable, 100.0 µL of 3.00 x 10^{-4} M $Rh_2(TPA)_4$ in DCM was injected at room temperature in one swift motion. The initial concentration of each component at the start of the reaction were 0.06 M, 0.18 M and 6.0 x 10^{-6} M for diazo, trap and catalyst, respectively.

General Reaction for Trap Dependency

A 10 mL Schlenk flask was loaded with a magnetic stir bar and the corresponding diazo compound (0.300 mmol), which was then dissolved in 4.78 mL dry DCM. To this solution was added 170.3 μL 1,4-cyclohexadiene *via* syringe and the ReactIR probe was inserted. The data collection was started and once stable, 50.0 μL of 3.00×10^{-4} M $Rh_2(TPA)_4$ in DCM was injected at room temperature in one swift motion. The initial concentration of each component at the start of the reaction were 0.06 M, 0.36 M and 3.0×10^{-6} M for diazo, trap and catalyst, respectively.

General Reaction for Same Excess Conditions

A 10 mL Schlenk flask was loaded with a magnetic stir bar and the corresponding diazo compound (0.600 mmol), which was then dissolved in 4.84 mL dry DCM. To this solution was added 113.5 μL 1,4-cyclohexadiene *via* syringe and the ReactIR probe was inserted. The data collection was started and once stable, 50.0 μL of 3.00×10^{-4} M $Rh_2(TPA)_4$ in DCM was injected at room temperature in one swift motion. The initial concentration of each component at the start of the reaction were 0.12 M, 0.24 M and 3.0×10^{-6} M for diazo, trap and catalyst, respectively.
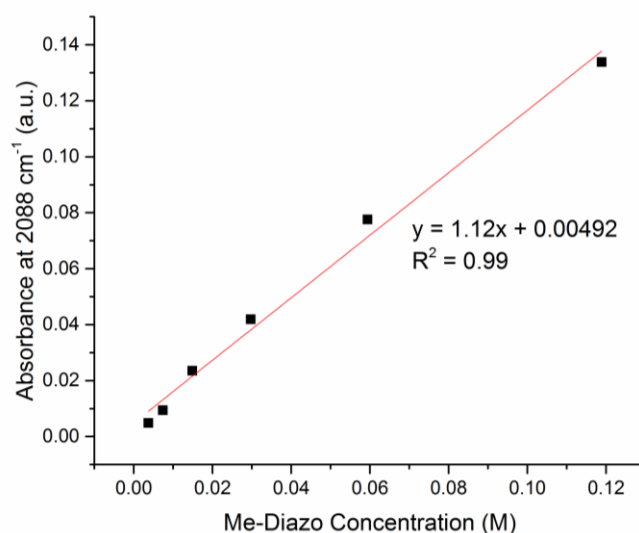
Figure A1.7. Calibration curve for methyl-(4-Me-aryl)-diazoacetate in DCM.
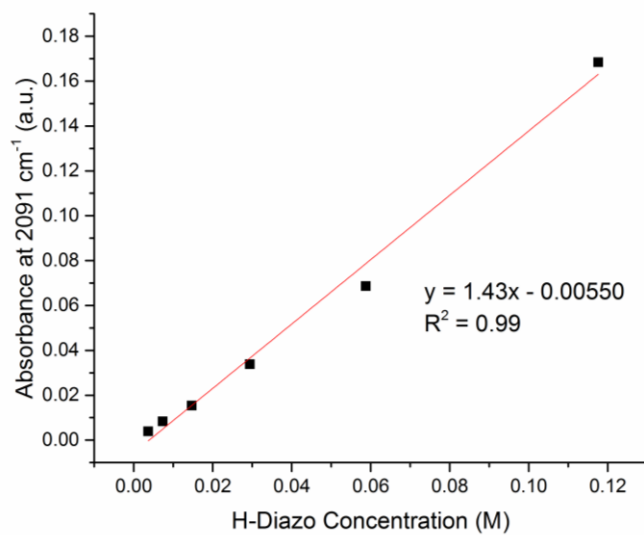
Figure A1.8. Calibration curve for methyl-(phenyl)-diazoacetate in DCM.
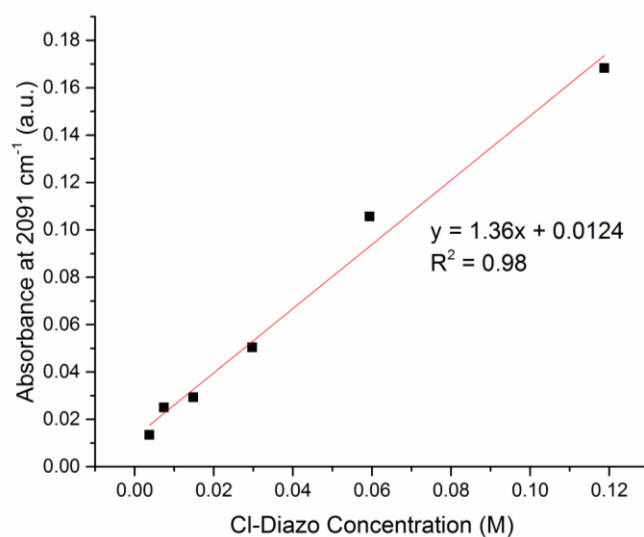
Figure A1.9. Calibration curve for methyl-(4-Cl-aryl)-diazoacetate in DCM.
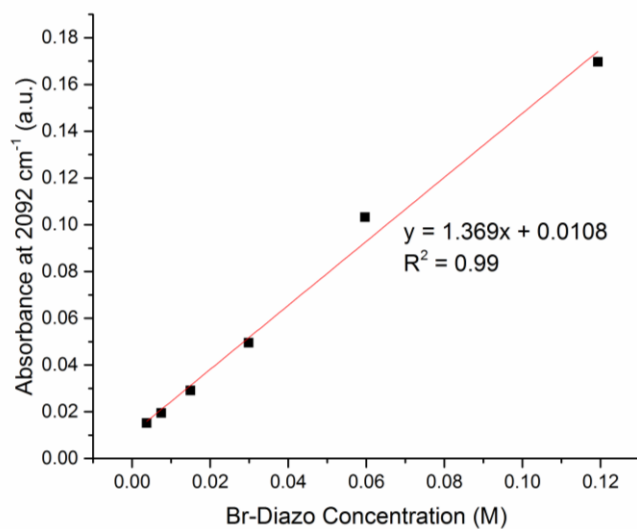
Figure A1.10. Calibration curve for methyl-(4-Br-aryl)-diazoacetate in DCM.
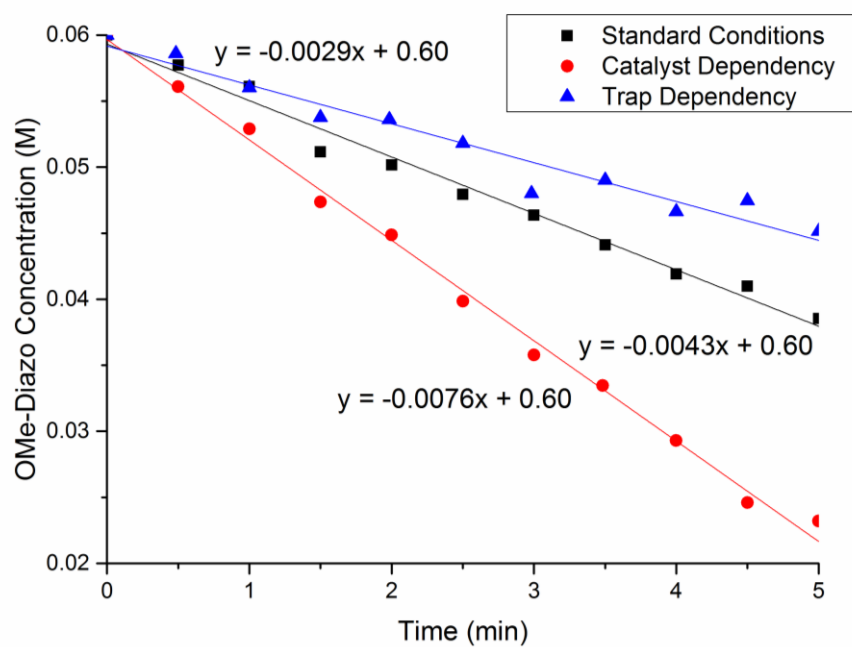
Figure A1.11. Reaction progress of methyl-(4-OMe-aryl)-diazoacetate monitored by ReactIR to probe catalyst dependency (red) and trap dependency (blue).
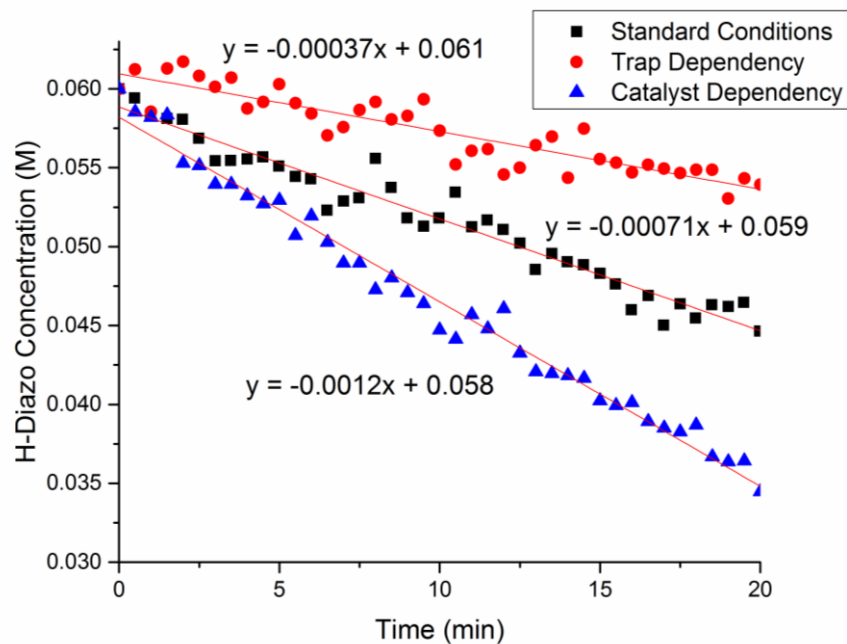
Figure A1.12. Reaction progress of methyl-(phenyl)-diazoacetate monitored by ReactIR to probe catalyst dependency (blue) and trap dependency (red).

A1.8 References

(1)   Yates, P. *J. Am. Chem. Soc.* **1952**, *74*, 5376.

(2)   Davies, H. M. L.; Beckwith, R. E. J. *Chem. Rev.* **2003**, *103*, 2861.

(3)   Pirrung, M. C.; Liu, H.; Morehead, A. T. *J. Am. Chem. Soc.* **2002**, *124*, 1014.

(4)   Doyle, M. P.; McKervey, M. A.; Ye, T. *Modern Catalytic Methods for Organic Synthesis with Diazo Compounds: From Cyclopropanes to Ylides*. John Wiley & Sons: New York, **1998**.

(5)   Nakamura, E.; Yoshikai, N.; Yamanaka, M. *J. Am. Chem. Soc.* **2002**, *124*, 7181.

(6)   Wong, F. M.; Wang, J.; Hengge, A. C.; Wu, W. *Org. Lett.* **2007**, *9*, 1663.

(7)   Hansen, J.; Autschbach, J.; Davies, H. M. L. *J. Org. Chem.* **2009**, *74*, 6555.

(8)   Anciaux, A. J.; Hubert, A. J.; Noels, A. F.; Petiniot, N.; Teyssié, P. *J. Org. Chem.* **1980**, *45*, 695.

(9)   Qu, Z.; Shi, W.; Wang, J. *J. Org. Chem.* **2001**, *66*, 8139.

(10)   Blackmond, D. G. *Angew. Chem., Int. Ed.* **2005**, *44*, 4302.

(11)   Mathew, J. S.; Klussmann, M.; Iwamura, H.; Valera, F.; Futran, A.; Emanuelsson, E. A. C.; Blackmond, D. G. *J. Org. Chem.* **2006**, *71*, 4711.

(12)   Drago, R. S.; Tanner, S. P.; Richman, R. M.; Long, J. R. *J. Am. Chem. Soc.* **1979**, *101*, 2897.

(13)   Drago, R. S.; Long, J. R.; Cosmano, R. *Inorg. Chem.* **1981**, *20*, 2920.

(14)   Hashimoto, S.; Watanabe, N.; Ikegami, S. *Tetrahedron Lett.* **1992**, *33*, 2709.

(15)   Chan, W.; Yeung, S.; Zhou, Z.; Chan, A. S. C.; Yu, W. *Org. Lett.* **2010**, *12*, 604.

(16)   Kornecki, K. P.; Briones, J. F.; Boyarskikh, V.; Fullilove, F.; Autschbach, J.; Schrote, K. E.; Lancaster, K. M.; Davies, H. M. L.; Berry, J. F. *Science* **2013**, *342*, 351.

(17)   Werlé, C.; Goddard, R.; Philipps, P.; Farès, C.; Fürstner, A. *J. Am. Chem. Soc.* **2016**, *138*, 3797.

Appendix 2

Evidence of an Iridium Donor/Acceptor Carbene Relevant to C–H Functionalization

Sunderland, T. L. and Berry, J. F.

Department of Chemistry, University of Wisconsin–Madison, 1101 University Avenue, Madison, WI 53706, United States

A2.1 Abstract

The ability of Ir-Phebox (Phebox = bis(oxazolinyl)phenyl) complexes to catalytically decompose diazo compounds and perform C–H insertion reactions has recently been shown.[1] The insertion reactions are proposed to proceed *via* an Ir carbene intermediate. In order to further investigate the mechanism of this reaction, stoichiometric formation and subsequent characterization of the Ir carbene species has been undertaken. Under stoichiometric conditions, formation of two Ir carbene species are observed by $^{13}C\{^1H\}$ NMR spectroscopy, showing two extremely deshielded signals with chemical shifts of 293.6 and 292.5 ppm in a 19 : 81 ratio. The transient species have additionally been observed by UV-Vis spectroscopy. Density functional theory (DFT) and time dependent-DFT (TD-DFT) calculations have also been carried out to aid in the characterization of the two generated intermediates.

A2.2 Introduction

Traditional synthesis of complex molecules often requires multiple steps, various protecting groups and numerous functional group transformations to achieve the desired product. One way to avoid this intensive process is through C–H functionalization, which has been and continues to be a 'Holy Grail' in synthetic chemistry.[2,3] One difficulty is that C–H bonds are generally both inert and abundant, requiring reactive, yet selective and controllable conditions for functionalization.[4] Direct functionalization of C–H bonds could revolutionize modern synthesis of pharmaceutical drugs, natural products, organic materials and other industrially relevant molecules by requiring fewer steps, resulting in better overall yields, greater atom economy and greener synthetic conditions.[4-6] Traditional organometallic C–H activation entails oxidative addition of a C–H bond to a transition metal center, resulting in stable M–C and M–H bonds that are difficult to turn over in a catalytic process.[4,7] An alternative option has recently been developed, involving metal carbene (MC) chemistry, which offers several advantages over traditional organometallic C–H activation; such as higher catalytic turnover numbers, a broader

substrate scope and higher regio- and stereoselectivity.[5,8] One general approach for generating a MC species is release of N_2 from diazo compounds (Figure A2.1).[9]

Figure A2.1. Traditional organometallic C–H activation (bottom) proceeds *via* oxidative addition of the C–H bond to a metal species in a ligand environment, followed by reaction with an incoming group (X) to regenerate the catalyst. Metal carbene C–H functionalization (top), rather, can undergo extrusion of N_2 from a diazo compound to form the transient MC, which can directly undergo C–H insertion to complete the catalytic cycle.[5]

Transition metal complexes possessing metal–carbon multiple bonds are proposed intermediates in carbene C–H functionalization. The electronic structures of the MCs, which form transiently in catalytic reactions, have proven difficult to study.[10] The first stable MC was synthesized by Fischer in 1964[11] and followed up with the first catalytic example using a diazo compound as the carbene source for C–H insertion 10 years later by Scott.[12] In recent years, there have been several reviews on M–C multiple bonds.[13,14]

In 1981, Teyssié and coworkers demonstrated differential reactivity between metal-bound and free carbenes.[15] Since that time, three categories of diazo-derived carbenes have emerged: acceptor only (A), acceptor-acceptor (A/A) and donor-acceptor (D/A) (Figure A2.2).[4,16] It has been shown that at least one electron withdrawing group (EWG) is needed to make the carbene

sufficiently electrophilic to functionalize C–H bonds.[6] If the carbene becomes too electrophilic, unwanted side reactions can occur, such as reaction of the MC with a diazo compound to form an azine, homo-coupling of MC to form alkenes or loss of selectivity toward C–H insertions.[17] Dimerization can be discouraged by adding bulky protecting groups.[16]
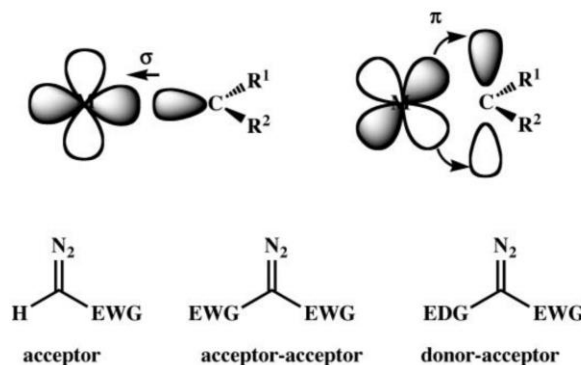
Figure A2.2. Orbital overlap between M- and C-atoms to form σ and π bonds (top). Three categories of diazo-derived carbenes (bottom, EWG = electron withdrawing group, EDG = electron donating group).[16]

Not only can the reactivity of the carbene be sterically and electronically tuned by the nature of the attached organic substituents, but the metal center and ligand environment of the catalyst also have an important influence. Teyssié and coworkers first demonstrated the ability of Rh_2 tetracarboxylates ($Rh_2(O_2CR)_4$) to decompose diazo compounds to form a MC and perform C–H insertion reactions.[18] Since that time, Rh_2 species have been the most investigated metal systems for this chemistry. Another advancement came when Davies was able to achieve good enantiomeric excess (*ee*) with excellent regioselectivity by utilizing a chiral catalyst (Rh_2(*S*-DOSP)$_4$) in conjunction with D/A diazo compounds.[5,6,19,20] Although a MC is the proposed intermediate for these C–H functionalization reactions, only in two cases has such an intermediate been observed.[21,22] There has been an in-depth computational study into the mechanism using Rh_2 catalysts, however, direct evidence to confirm the mechanism is still lacking.[23] This absence of knowledge surrounding the mechanism and intermediates of carbene formation and insertion

into C–H bonds necessitates its further investigation. Development of this field is vital, as it will lead to better catalyst design with the goals of achieving higher turnover numbers combined with greater selectivity. Although Rh_2 catalysts are the most commonly used, it has been found that other metal systems, such as Ir, are also able to decompose diazo compounds and undergo C–H insertion reactions that offer complementary reactivity to the Rh_2 systems.[1,24]

A useful set of tunable chiral ligands, and corresponding metal complexes for asymmetric catalysis, has recently been synthesized by the Nishiyama group.[25-27] The Blakey group at Emory University (in collaboration with Davies and Musaev) was able to supplement this work by adding the analogous Ir-(oxazolinyl)phenyl (Phebox) complexes for use as asymmetric catalysts for C–H insertion reactions utilizing diazo compounds. From an initial screen with methy-phenyldiazoacetate as the diazo source, 1-4-cyclohexadiene as the substrate, and (^{t}Bu-Phebox-^{i}Pr)IrCl$_2$(OH$_2$) as catalyst, they found that these conditions gave excellent yield (97%) and *ee* (94%) of the insertion product (Scheme A2.1).[1]
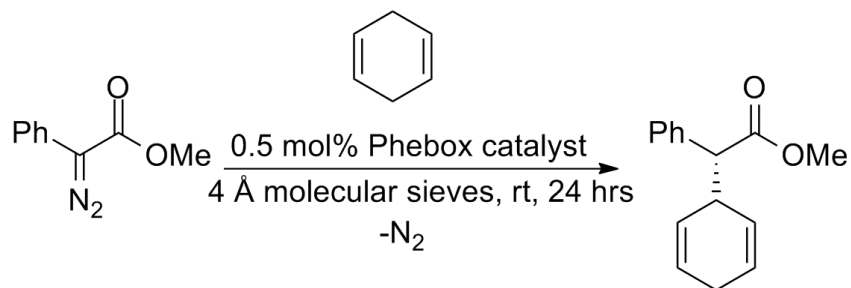
Scheme A2.1. C–H insertion test reaction with the (^{t}Bu-Phebox-^{i}Pr)IrCl$_2$(OH$_2$) catalyst.

Furthermore, the proposed reaction pathway to form the Ir carbene was calculated using the (^{t}Bu-Phebox-Bn)IrCl$_2$(OH$_2$) catalyst. Two potential isomers (*cis* and *trans*) were found that differ by 77.8 kJ/mol favoring the *cis*-isomer. In order to form the *cis*-isomer, the complex must first lose H_2O to solution, then undergo a Cl$^-$ rearrangement before forming the diazo adduct and finally lose N_2 to give the Ir carbene (Scheme A2.2).[1]
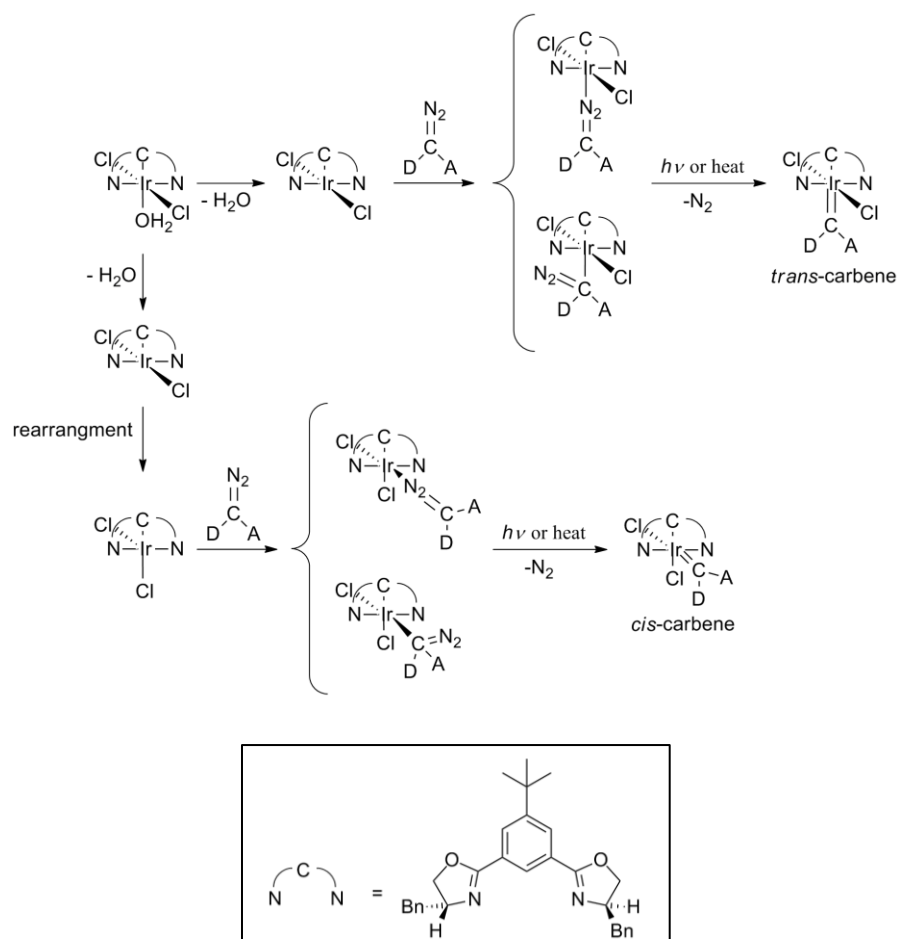
Scheme A2.2. Pathways to form *cis-* and *trans*-carbene: D = 4-methoxyphenyl, A = COOMe.

We have entered into a collaboration with the Blakey group through the NSF Center for Selective C–H Functionalization to further investigate the mechanism of this reaction and validate the computations. Our goal is to isolate and characterize the proposed Ir carbene intermediates, which will provide a great deal of information not only to support the mechanism, but also elucidate factors leading to regio- and enantioselectivity of catalysts proceeding through MC transient species.

A2.3 Experimental Section

A2.3.1 Materials and Methods

All reagents were obtained commercially unless otherwise noted. All reactions were performed using oven dried glassware under an atmosphere of N_2, either in a Vacuum Atmospheres glove box or using Schlenk techniques. Air and moisture sensitive liquids and solutions were transferred by syringe or stainless steel cannula. Organic solutions were concentrated under reduced pressure either by rotary evaporation or vacuum pump on a Schlenk line. Dichloromethane (DCM) and pentane were dried over CaH_2 and distilled under N_2 before use. Ethanol (EtOH) was dried over magnesium/magnesium oxide (Mg/MgO) and distilled under N_2 before use. Hexane was obtained from a Vacuum Atmospheres Solvent System and freeze-pump-thawed or purged with N_2 before use. Chloroform ($CHCl_3$ or $CDCl_3$) was neutralized and dried with K_2CO_3 prior to use and freeze-pump-thawed or purged with N_2 for NMR spectroscopic experiments. ^1H and $^{13}C\{^1H\}$ NMR spectra were collected on either a Bruker-Avance 400 or 500 MHz spectrometer at room temperature unless otherwise noted at 400 or 500 (^1H) or 100 or 125 ($^{13}C\{^1H\}$) MHz. Chemical shifts are reported in parts per million (ppm). The spectra were referenced to solvent residual proteo peaks or TMS at 0 ppm. UV-Vis spectra were obtained in real-time using a Miniature BLUE-Wave UV-Vis dip probe with Tungsten-Krypton lightsource, 10 mm path length tip. The Ir carbene formation reaction is shown in Scheme A2.3.
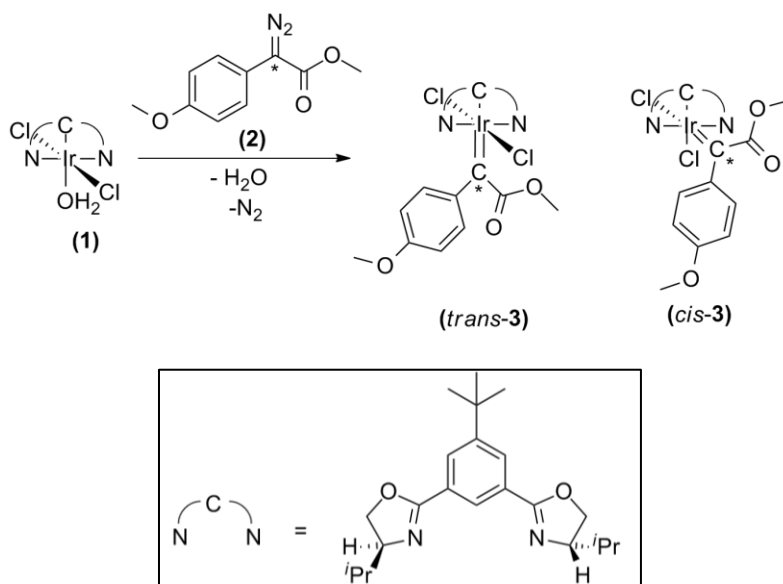
Scheme A2.3. Reaction between (^{t}Bu-Phebox-^{i}Pr)IrCl$_2$(OH$_2$) (**1**) and methyl-(4-methoxyphenyl)-diazoacetate (**2**) to form two possible Ir carbene isomers, (*trans*-**3**) and (*cis*-**3**). Site of ^{13}C labeling is denoted with a star (*).

A2.3.2 UV-Vis Studies

A 25 mL Schlenk flask was charged with (^{t}Bu-Phebox-^{i}Pr)IrCl$_2$(OH$_2$)[1] (2.31 mg, 0.00363 mmol) (**1**) and degassed. To a separate 25 mL Schlenk flask methyl-(4-methoxyphenyl)-diazoacetate[20] (0.77 mg, 0.0037 mmol) (**2**) was added and degassed. Both compounds were dissolved in 7.5 mL freshly distilled DCM, resulting in orange solutions. UV-Vis spectra of both starting compounds were collected, followed by monitoring of solution **1** upon syringe addition of **2**, which resulted in an instant color change from orange to green with evolution of small bubbles.

A2.3.3 Computational Methods

Coordinates for *cis*- and *trans*-**3** were adapted from the initial coordinates reported in reference 1 by changing R_1 = H, R_2 = Bn to R_1 = ^{i}Pr, R_2 = H. All geometry optimizations were carried out with ORCA version 2.8.0[28] and the B3LYP hybrid functional.[29-32] The TZVP basis set[33,34] including all electron scalar relativistic effects within the ZORA approximation[35] was used with the TZVP/J auxiliary basis set for Ir. The SVP basis set and SVP/J auxiliary basis sets[36,37] were used for all remaining atoms. Tight optimization and tight self-consistent field convergence criteria were employed along with grid4 for all calculations. Frequency calculations were performed following geometry optimizations to ensure minimum energy structures.

A2.3.4 ^{13}C{^{1}H} NMR Spectroscopy Studies

Exp. 1 (constant temperature)

An NMR tube was filled with **1** (4.89 mg, 0.00768 mmol) and ^{13}C labeled **2**[38] (1.68 mg, 0.00815 mmol). The orange solids were dissolved in approximately 0.5 mL CDCl$_3$ immediately before the NMR tube was placed into the NMR spectrometer, pre-cooled to 14.5 °C. Upon solvent addition, the solution immediately turned green with the evolution of small gas bubbles.

Exp. 2 (variable temperature)

A J-Young NMR tube was charged with **1** (4.66 mg, 0.00732 mmol) and ^{13}C labeled **2** (1.51 mg, 0.00732 mmol), degassed and cooled in a dry-ice/acetone bath to –78 °C. To a 25 mL Schlenk flask, CDCl$_3$ was added and cooled in a dry-ice/acetone bath to –78 °C. Approximately 1.0 mL of cold CDCl$_3$ was cannula transferred to the J-Young NMR tube resulting in an orange solution. The head space of the J-Young tube was evacuated and the tube was sealed. The NMR spectrometer was cooled to –55 °C and ^{13}C{^{1}H} NMR spectra were collected between –55 °C and 24 °C.

A2.4 Results and Discussion

A2.4.1 UV-Vis Studies

The results of the UV-Vis studies show that under inert conditions a meta-stable species (**3**) is formed with a lifetime on the order of days at room temperature. The formation and decay of this intermediate species can be monitored by the band centered at 652 nm (Figure A2.3). The lifetime of this transient species is prolonged compared to most Rh_2 carbene species, which should allow for its further study. The rates of both formation and decay of this transient species can be further controlled by temperature changes. When solutions of **1** and **2** are pre-cooled to $-78\ °C$ in a dry-ice/acetone bath, there is no color change or growth of the band at 652 nm, indicating no formation of **3** occurs at this temperature. Upon warming to room temperature, the solution color changes from orange to green along with a slow growth of the 652 nm band. When the solution is again cooled to $-78\ °C$, no further changes of the UV-Vis spectrum are observed for weeks.
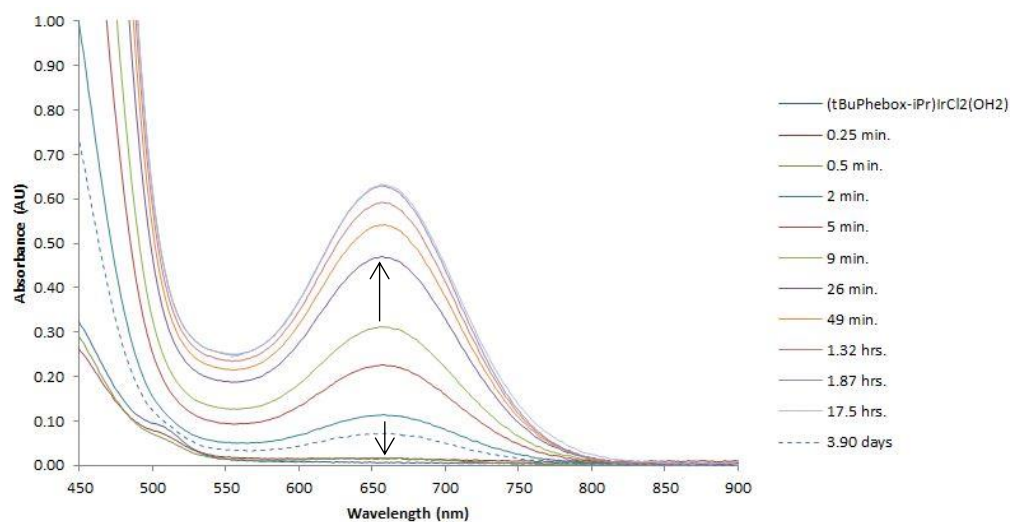
Figure A2.3. UV-Vis spectrum of formation and decay of **3** (652 nm) in DCM under N_2 at room temperature.

A2.4.2 ^{13}C{^{1}H} NMR Spectroscopy

The ^{13}C{^{1}H} NMR spectrum of **3** reveals that two types of Ir carbene species are present in solution by the two highly deshielded signals with chemical shifts of 293.6 and 292.5 ppm in a 19 : 81 ratio, respectively (Figure A2.4). The assignment of these as MC signals is supported by several examples with Ir,[39] Os,[40,41] Ru,[42] Cu[43] and others.[10] Our current hypothesis for the observation of two signals is either: 1) two isomers (*cis* and *trans*) are formed, or 2) two rotational conformers are observed. Assignment of the individual resonances has not yet been confirmed. Additional supporting evidence for an Ir carbene was provided by an HMBC experiment. This correlation experiment showed weak coupling between the C$_{carbene}$-atom and protons on the oxazoline ring of the NCN pincer ligand. This coupling could only result from a bound MC species.
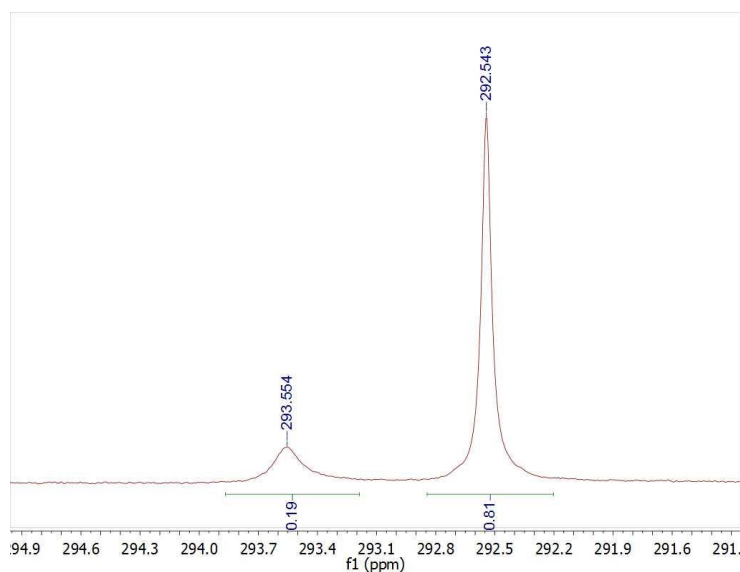
Figure A2.4. ^{13}C{^{1}H} NMR spectrum of **3** in CDCl$_3$ at 14.5 °C.

To distinguish whether these two signals arise from rotomers rather than isomers, a VT-NMR experiment was utilized. This experiment resulted in the monitoring of decomposition of **2** (62.2 ppm), growth of **3** (~292 ppm) and decay of **3** by carbene insertion into the O–H bond of H$_2$O, resulting in the corresponding alcohol **4** (72.5 ppm)[44] (Figure A2.5). Decomposition of the carbene by reaction with water is a well-known decomposition pathway for MCs. Formation of **3**

is first observed after approximately 86 min, with almost complete loss of the starting diazoacetate signal. Observation of **4** can be seen after 301 min under the conditions of this experiment. The fact that the ratio of Ir carbene signals is unchanged during the experiment is more consistent with isomers rather than conformers. The resonances identified for **3** are consistent with reported resonances for the related $Rh_2(TPA)_4$ carbene,[21] which support our identification of this proposed intermediate as an Ir carbene complex.
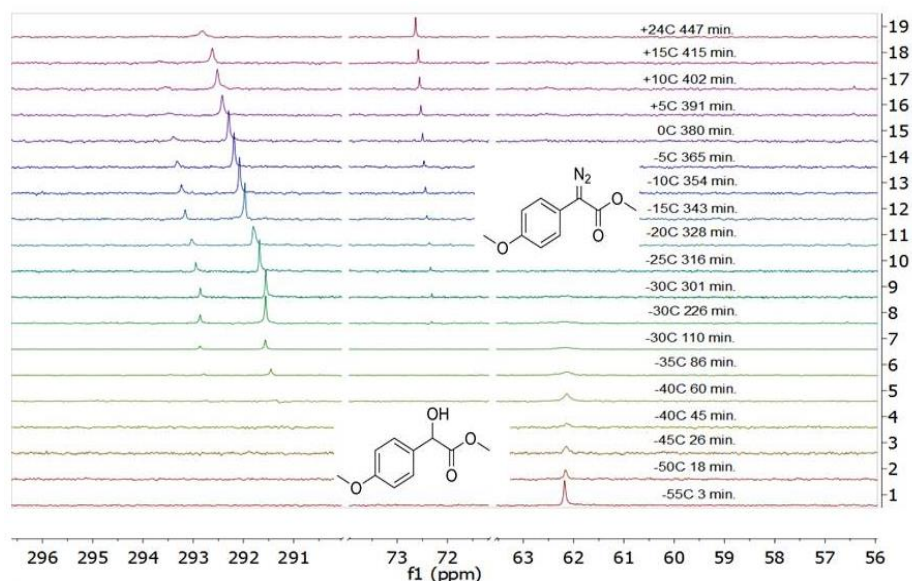
Figure A2.5. $^{13}C\{^1H\}$ NMR spectra of decay of **2**, formation and decay of **3** and formation of **4** in CDCl₃.

A2.4.3 Density Functional Theory Results

In order to analyze the bonding in the calculated isomers, one must be familiar with the main bonding motifs in MC complexes. Two general classes of MC exist, Fischer carbenes and Schrock carbene/alkylidenes, which differ both in their electronic structures and reactivities.[45] Fischer carbenes are composed of a singlet carbene, which can donate a lone pair to the metal center and accept electrons into the empty *p*-orbital on the carbon atom, forming the σ and π bonds, respectively (Figure A2.6). Fischer carbenes result in an electrophilic carbon center.

Conversely, Schrock carbenes have a triplet ground state and form the MC by radical recombination of two triplet fragments, resulting in nucleophilic carbon centers.

Fischer carbene   Schrock carbene/alkylidene

Figure A2.6. Bonding contributions for Fischer and Schrock carbenes to form the M–C bonds.[45]

To investigate the electronic structure of **3**, DFT calculations were carried out on the two possible isomers. The optimized geometries of the two isomers are illustrated below in Figure A2.7, with *cis-* and *trans-***3** Ir–C$_{carbene}$ bond lengths of 1.927 and 2.037 Å, respectively. The calculated Ir–C$_{carbene}$ bond lengths are consistent with other calculated MC species, including those of Ir[46] and Os.[40] The Ir–C$_{carbene}$ bond elongation in *trans-***3** can be explained by the fact that the phenyl group has a larger *trans-*influence compared to the Cl⁻ anion.

*cis-***3**   *trans-***3**
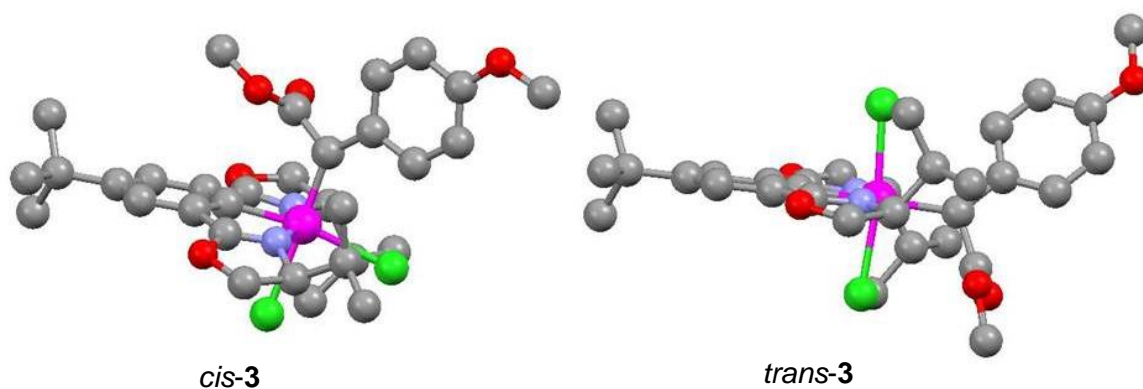
Figure A2.7. Calculated structures of *cis-***3** (left) and *trans-***3** (right) Ir carbene transient species, where blue, grey, red, green, and pink spheres represent N-, C-, O-, Cl- and Ir-atoms, respectively. Hydrogen atoms are omitted for clarity.

The calculated Mayer bond orders of 1.2195 and 1.0066 for *cis-* and *trans-***3**, respectively, reflect the differences in Ir–C$_{carbene}$ bond lengths. These bond orders are slightly higher than the

previously calculated $Rh_2(TPA)_4$ carbene, which has a Rh–$C_{carbene}$ bond order of 0.75.[21] A larger M–$C_{carbene}$ bond order is expected for the Ir carbene than the Rh carbene for two reasons; Ir is a third row transition metal, which typically make stronger metal–ligand bonds than second row transition metals, and the Rh–Rh bond significantly weakens the Rh–$C_{carbene}$ bond.[21]

TD-DFT calculations were performed to help assign the UV-Vis features of **3**. The band at 652 nm was identified as a charge transfer band consisting of contributions from the promotion of an electron from the Ir–Cl π^* molecular orbital (MO) into the Ir–$C_{carbene}$ π^* MO for both the *cis*-**3** (HOMO→LUMO) and *trans*-**3** (HOMO-1→LUMO) isomers (Figure A2.8). The calculated UV-Vis features of either isomer are consistent with the experiemental data, which doesn't allow for easy distinction between the two species.
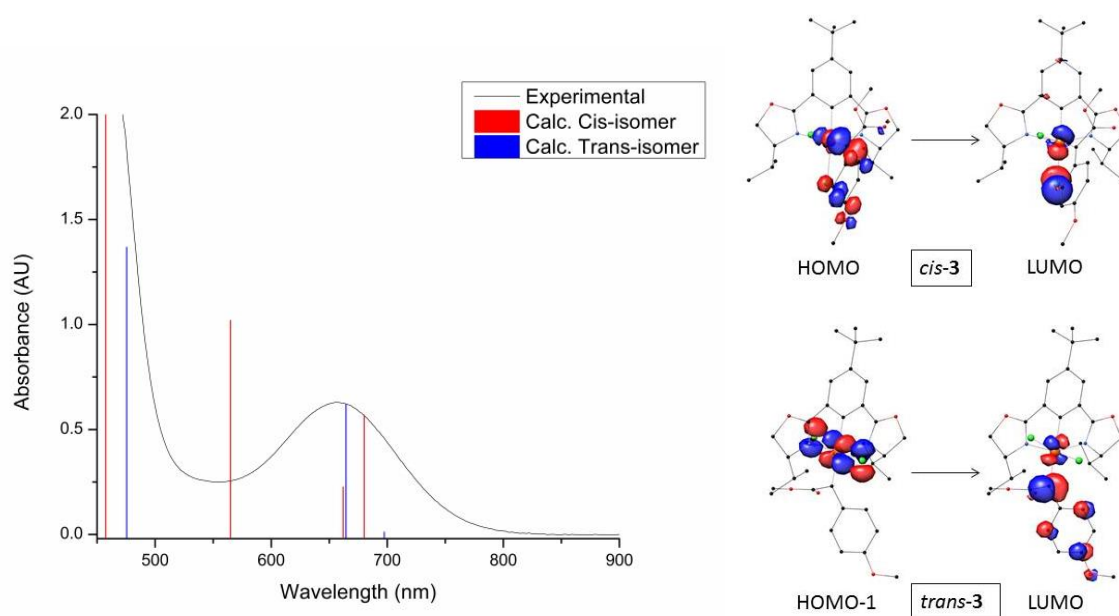
Figure A2.8. UV-Vis spectrum of **3** in DCM under N_2 overlaid with calculated transitions for *cis*- and *trans*-**3** isomers (left). MOs illustrating the major transitions at 680.1 nm and 664.9 nm for the *cis*- and *trans*-isomers, respectively (right).

A2.5 Conclusions

We have successfully observed the presence of two Ir carbene intermediates in C–H functionalization by $^{13}C\{^1H\}$ NMR spectroscopy. Variable temperature NMR spectroscopy suggests these two species are the *cis*- and *trans*-isomers that are possible for the Ir(Phebox)Cl$_2$ complexes, in agreement with computed structures. The Ir carbene species were also observed by UV-Vis spectroscopy, revealing charge transfer bands into the Ir–C$_{carbene}$ $\pi*$ orbital at a similar energy to the reported Rh$_2$(TPA)$_4$ carbene complex. While the two isomers have not been isolated and fully characterized, their observation does support the proposed mechanism for Ir(Phebox) C–H functionalization catalysts.

A2.6 Acknowledgments

A2.7 Supporting Information

Table A2.1. Optimized XYZ coordinates for *cis*-Ir(^{t}Bu-Phebox-^{i}Pr)Cl$_2$ carbene.

Ir	0.003028	-0.002961	-0.013389
C	-1.211787	2.630639	-0.367207
C	-0.004229	1.951545	-0.182622
C	1.216482	2.629337	-0.308812
C	1.221017	4.009046	-0.549640
C	0.008180	4.723080	-0.689978
C	-1.208919	4.010578	-0.617545
H	2.174177	4.526106	-0.652317
H	-2.155695	4.519543	-0.778725
C	-2.298151	1.662270	-0.447683
O	-3.511817	1.970869	-0.889624
N	-2.063789	0.393250	-0.230001
C	2.311408	1.673667	-0.213425
O	3.598057	1.995447	-0.194293
N	2.030523	0.402546	-0.104819
C	0.059407	6.243416	-0.958982

C	-4.240633	0.725187	-1.056176
H	-5.097029	0.747199	-0.372817
H	-4.604918	0.689250	-2.087275
C	4.328936	0.776753	0.123863
H	5.156076	0.689307	-0.586365
H	4.725118	0.892296	1.138478
C	3.280289	-0.366441	0.015849
C	-3.210801	-0.389651	-0.722907
Cl	-0.076798	0.060026	-2.468518
C	0.010782	0.001567	1.949978
C	0.724540	1.185468	2.547100
C	-0.510255	-0.896379	2.964313
O	1.922589	1.235619	2.715955
O	-0.109571	2.191003	2.860028
C	-1.042237	-2.178916	2.669428
C	-0.480360	-0.526327	4.347190
C	0.490647	3.395097	3.352716
C	-1.500561	-3.035068	3.664005
H	-1.026165	-2.518952	1.636740
C	-0.947564	-1.362060	5.341235
H	-0.094544	0.445698	4.642125
H	-0.336297	4.070451	3.583653
H	1.084644	3.194825	4.252037
H	1.140133	3.838345	2.589967
C	-1.463808	-2.635791	5.013280
H	-1.876831	-4.015090	3.381735
H	-0.925753	-1.068163	6.388829
Cl	0.117432	-2.487058	-0.283104
C	0.816664	6.508601	-2.282954
C	0.797351	6.949315	0.204273
C	-1.346463	6.863251	-1.078843
H	-1.935658	6.724802	-0.162957
H	-1.912284	6.438914	-1.917951
H	-1.260575	7.943142	-1.254911
H	0.314740	6.018531	-3.126988
H	1.847585	6.135985	-2.247753
H	0.860398	7.586431	-2.491117
H	1.825366	6.584355	0.319176
H	0.275687	6.787672	1.156905
H	0.848642	8.032171	0.026410
H	-2.867482	-0.882762	-1.644115
C	-3.705261	-1.483220	0.243780
C	-4.171366	-0.940315	1.600753
C	-4.788279	-2.339213	-0.430835

H	-2.829821	-2.125294	0.405705
H	-5.104245	-0.364253	1.518330
H	-3.412682	-0.295508	2.059371
H	-4.366037	-1.766753	2.295697
H	-4.430135	-2.765571	-1.376982
H	-5.697604	-1.757400	-0.643715
H	-5.083918	-3.172960	0.218894
H	3.235248	-0.927302	0.958397
C	3.503445	-1.376546	-1.134350
C	3.591073	-0.720935	-2.518457
C	4.731181	-2.248941	-0.830520
H	2.614806	-2.022316	-1.122386
H	4.449105	-0.037206	-2.606053
H	2.671657	-0.173450	-2.755950
H	3.717120	-1.493222	-3.288450
H	4.638900	-2.752887	0.141403
H	5.663856	-1.664327	-0.820139
H	4.847240	-3.026058	-1.596484
O	-1.886644	-3.384328	6.044013
C	-2.407823	-4.682548	5.812452
H	-1.660462	-5.339011	5.344732
H	-3.306017	-4.649032	5.179388
H	-2.675328	-5.084962	6.793201

Table A2.2. Optimized XYZ coordinates for *trans*-Ir(*t*Bu-Phebox-*i*Pr)Cl₂ carbene.

Ir	0.00020	0.00660	-0.00350
C	-1.20670	2.72210	-0.00540
C	-0.00080	2.02180	-0.00620
C	1.21140	2.71760	-0.01250
C	1.21870	4.11760	-0.01110
C	0.00300	4.84190	-0.01330
C	-1.21270	4.12600	-0.01380
H	2.17000	4.64810	-0.01000
H	-2.16340	4.65290	-0.02080
C	-2.29960	1.76190	-0.02820
O	-3.58770	2.08310	-0.12120
N	-2.02890	0.48340	0.01030
C	2.30340	1.75590	-0.00260
O	3.59320	2.07730	0.05340
N	2.03070	0.47670	-0.02950
C	0.05040	6.38600	-0.01580
C	-4.32150	0.84410	-0.30470
H	-5.16330	0.84470	0.39440

H	-4.70740	0.83740	-1.33090
C	4.33260	0.83840	0.20930
H	5.15610	0.84440	-0.51080
H	4.74400	0.82410	1.22570
C	3.28960	-0.28810	-0.03580
C	-3.28340	-0.28290	-0.04560
Cl	-0.10790	0.13620	-2.40840
C	-0.01270	-2.04430	-0.05480
C	-0.31280	-2.64990	-1.39270
C	0.28290	-3.06260	0.93490
O	0.56770	-3.07700	-2.10410
O	-1.61740	-2.68670	-1.71550
C	-0.17860	-4.40600	0.77460
C	1.04580	-2.78970	2.09980
C	-1.91390	-3.06320	-3.06720
C	0.07620	-5.38450	1.71490
H	-0.77360	-4.66700	-0.09810
C	1.33730	-3.77460	3.03800
H	1.40580	-1.77970	2.26190
H	-3.00390	-3.09420	-3.14190
H	-1.50320	-2.31380	-3.75250
H	-1.48660	-4.04380	-3.30440
C	0.84470	-5.08140	2.86130
H	-0.29400	-6.40100	1.59670
H	1.93800	-3.51740	3.90650
Cl	0.00920	0.18250	2.40300
C	0.79930	6.87770	-1.27810
C	0.79300	6.88110	1.24910
C	-1.35700	7.01390	-0.02010
H	1.82290	6.50640	1.29270
H	0.27940	6.54960	2.16090
H	0.83820	7.97880	1.26350
H	-1.93590	6.72910	0.86790
H	-1.93120	6.72710	-0.91050
H	-1.27400	8.10830	-0.02120
H	0.29060	6.54330	-2.19160
H	1.82960	6.50330	-1.31550
H	0.84420	7.97530	-1.29550
H	-3.22280	-0.96080	-0.90480
C	-3.53180	-1.14430	1.21530
C	-3.66420	-0.32810	2.50730
C	-4.73650	-2.07090	0.99010
H	-2.63700	-1.77470	1.31400
H	-4.53800	0.33950	2.49030

H	-2.76290	0.26700	2.69200
H	-3.79230	-1.00180	3.36470
H	-4.60100	-2.69610	0.09730
H	-5.67200	-1.50490	0.86770
H	-4.87550	-2.74010	1.84870
H	3.27590	-0.98060	0.81640
C	3.50300	-1.12590	-1.31980
C	3.57450	-0.28180	-2.59880
C	4.73690	-2.02760	-1.15700
H	2.62340	-1.77800	-1.40860
H	4.43220	0.40730	-2.59960
H	2.65260	0.29180	-2.74550
H	3.68790	-0.93940	-3.47000
H	4.66010	-2.66390	-0.26440
H	5.66740	-1.44550	-1.07700
H	4.84320	-2.68890	-2.02580
O	1.05530	-6.09750	3.71460
C	1.80760	-5.88750	4.89700
H	1.33790	-5.13430	5.54570
H	2.83770	-5.57680	4.67010
H	1.83090	-6.84710	5.42060

A2.8 References

(1)   Owens, C. P.; Varela-Alvarez, A.; Boyarskikh, V.; Musaev, D. G.; Davies, H. M. L.; Blakey, S. B. *Chem. Sci.* **2013**, *4*, 2590.

(2)   Labinger, J. A.; Bercaw, J. E. *Nature* **2002**, *417*, 507.

(3)   Bergman, R. G., *Nature* **2007**, *446*, 391.

(4)   Davies, H. M. L.; Beckwith, R. E. J. *Chem. Rev.* **2003**, *103*, 2861.

(5)   Davies, H. M. L.; Manning, J. R. *Nature* **2008**, *451*, 417.

(6)   Davies, H. M. L. *Angew. Chem., Int. Ed.* **2006**, *45*, 6422.

(7)   Díaz-Requejo, M. M.; Pérez, P. J. *Chem. Rev.* **2008**, *108*, 3379.

(8)   Godula, K.; Sames, D. *Science* **2006**, *312*, 67.

(9)   Doyle, M. P.; McKervey, M. A.; Ye, T. *Modern Catalytic Methods for Organic Synthesis with Diazo Compounds: From Cyclopropanes to Ylides*. John Wiley & Sons: New York, **1998**.

(10)   Nugent, W. A.; Mayer, J. M. *Metal-Ligand Multiple Bonds*. John Wiley & Sons: New York, **1988**.

(11)   Fischer, E. O. Maasboel, A. *Angew. Chem.* **1964**, *76*, 645.

(12)   Scott, L. T.; DeCicco, G. J. *J. Am. Chem. Soc.* **1974**, *96*, 322.

(13)   Werner, H. *Angew. Chem., Int. Ed.* **2010**, *49*, 4714.

(14)   Herndon, J. W. *Coord. Chem. Rev.* **2011**, *255*, 3.

(15)   Demonceau, A.; Noels, A. F.; Hubert, A. J.; Teyssié, P. *J. Chem. Soc., Chem. Commun.* **1981**, 688.

(16)   Diaz-Requejo, M. M.; Belderrain, T. R.; Nicasio, M. C.; Perez, P. J. *Dalton Trans.* **2006**, 5559.

(17)   Petrukhina, M. A.; Andreini, K. W.; Walji, A. M.; Davies, H. M. L. *Dalton Trans.* **2003**, 4221.

(18)   Demonceau, A.; Noels, A. F.; Teyssié, P.; Hubert, A. J. *J. Mol. Catal.* **1988**, *49*, L13.

(19)   Davies, H. M. L.; Hansen, T. *J. Am. Chem. Soc.* **1997**, *119*, 9075.

(20)   Davies, H. M. L.; Hansen, T.; Churchill, M. R. *J. Am. Chem. Soc.* **2000**, *122*, 3063.

(21)   Kornecki, K. P.; Briones, J. F.; Boyarskikh, V.; Fullilove, F.; Autschbach, J.; Schrote, K. E.; Lancaster, K. M.; Davies, H. M. L.; Berry, J. F. *Sciene* **2013**, *342*, 351.

(22)   Werlé, C.; Goddard, R.; Philipps, P.; Farès, C.; Fürstner, A. *J. Am. Chem. Soc.* **2016**, *138*, 3797.

(23)   Nakamura, E.; Yoshikai, N.; Yamanaka, M. *J. Am. Chem. Soc.* **2002**, *124*, 7181.

(24)   Suematsu, H.; Katsuki, T. *J. Am. Chem. Soc.* **2009**, *131*, 14218.

(25)   Nishiyama, H. *Chem. Soc. Rev.* **2007**, *36*, 1133.

(26)   Nishiyama, H.; Ito, J. *Chem. Commun.* **2010**, *46*, 203.

(27)   Ito, J.; Nishiyama, H. *Synlett* **2012**, *2012*, 509.

(28)   Neese, F. *ORCA- an ab initio, Density Functional and Semiempirical program package*, Univeristy of Bonn: Bonn, **2006**.

(29)   Becke, A. D. *J. Chem. Phys.* **1993**, *98*, 5648.

(30)   Lee, C.; Yang, W.; Parr, R. G. *Phys. Rev. B* **1988**, *37*, 785.

(31)   Vosko, S. H.; Wilk, L.; Nusair, M. *Can. J. Phys.* **1980**, *58*, 1200.

(32).   Stephens, P. J. Devlin, F. J.; Chabalowski, C. F.; Frisch, M. J. *J. Phys. Chem.* **1994**, *98*, 11623.

(33)   Pantazis, D. A.; Chen, X.; Landis, C. R.; Neese, F. *J. Chem. Theory Comput.* **2008**, *4*, 908.

(34)   Pantazis, D. A.; Neese, F. *J. Chem. Theory Comput.* **2009**, *5*, 2229.

(35)   Wullen, C. V. *J. Chem. Phys.* **1998**, *109*, 392.

(36)   Eichkorn, K.; Treutler, O.; Öhm, H.; Häser, M.; Ahlrichs, R. *Chem. Phys. Lett.* **1995**, *240*, 283.

(37)   Eichkorn, K.; Weigend, F.; Treutler, O.; Ahlrichs, R. *Theor. Chem. Acc.* **1997**, *97*, 119.

(38)   Zhou, J. X., X.; Hu, W.; Briones, J. F.; Davies, H. M. L. *Org. Syn.* **2011**, *88*.

(39)   Campos, J.; Peloso, R.; Brookhart, M.; Carmona, E. *Organometallics* **2013**, *32*, 3423.

(40)   Li, Y.; Huang, J.; Zhou, Z.; Che, C. *J. Am. Chem. Soc.* **2001**, *123*, 4843.

(41)   Woo, L. K.; Smith, D. A. *Organometallics* **1992**, *11*, 2344.

(42)   Park, S.; Sakata, N.; Nishiyama, H. *Chem. Eur. J.* **1996**, *2*, 303.

(43)   Straub, B. F.; Hofmann, P. *Angew. Chem., Int. Ed.* **2001**, *40*, 1288.

(44)   Sreenivasulu, M.; Arun Kumar, K.; Sateesh Reddy, K.; Siva Kumar, K.; Rajender Kumar, P.; Chandrasekhar, K. B.; Pal, M. *Tetrahedron Lett.* **2011**, *52*, 727.

(45)   Mindiola, D. J.; Scott, J. *Nat. Chem.* **2011**, *3*, 15.

(46)   Anding, B. J.; Brgoch, J.; Miller, G. J.; Woo, L. K. *Organometallics* **2012**, *31*, 5586.

Appendix 3

Synthesis and Characterization of the Quadruply Bonded

Dirhenium Diazide Complex Re$_2$(DPhF)$_4$(N$_3$)$_2$

Sunderland, T. L. and Berry, J. F.

Department of Chemistry, University of Wisconsin–Madison, 1101 University Avenue, Madison,

WI 53706, United States

A3.1 Abstract

The dirhenium diazide complex, $Re_2(DPhF)_4(N_3)_2$ (**1**), has been synthesized by a salt metathesis reaction of $Re_2(DPhF)_4Cl_2$ with NaN_3. The solution phase ^{1}H NMR spectrum of **1** suggests that the compound has D_{4h} symmetry. Complex **1** crystallizes in the orthorhombic space group *Pbca* and lies on an inversion center within the unit cell. The Re–Re bond distance is 2.2773(1) Å and the Re–N_{ax} distance is 2.133(2) Å. The axial azide ligands exhibit N–N bond activation, suggested by the reduced IR stretching frequencies of 2075 and 2065 cm^{-1}.

A3.2 Introduction

Recently, transition metal nitrido complexes formed from transition metal azide complexes have been of interest for their ability to act as N-atom transfer reagents.[1-3] Our group has recently studied the formation, structure and reactivity of several metal–metal multiply bonded azide complexes and subsequent nitrido species.[4-11] Isolation and study of the metal–metal bonded nitrido species by conventional methods has proven difficult due to their highly reactive nature. We hypothesize that a terminal nitrido species bound to a third row transition metal will be more stable and amenable to study.[12] We report here preliminary work toward a dirhenium nitrido compound: the synthesis and characterization of a dirhenium diazide complex.

A3.3 Experimental Section

A3.3.1 Materials and Methods

All reactions were carried out using oven dried glassware under a dry N_2 atmosphere using Schlenk techniques and glovebox methods. Tetrahydrofuran (THF) was purified using a Vacuum Atmospheres solvent purification system. $Re_2(DPhF)_4Cl_2$ was prepared according to literature procedures.[13] Ethanol (EtOH), dichloromethane (DCM), hexane, dichloromethane-*d* (CD_2Cl_2) and sodium azide (NaN_3) were purchased from Sigma-Aldrich and used without further purification. ^{1}H NMR spectra were recorded on a Bruker Avance-400 MHz spectrometer. ^{1}H NMR

shifts were referenced to residual proteo solvent. [1]H splitting patterns were designated as singlet (s) and multiplet (m). Elemental analysis was carried out by Midwest Microlab, LLC, Indianapolis, IN. IR spectra were taken on a Bruker Tensor 27 FTIR spectrometer using an attenuated total reflectance (ATR) adapter. Mass spectra were obtained at the Paul Bender Chemical Instrumentation Center of the Chemistry Department of the University of Wisconsin–Madison using a Bruker REFLEX™ II MALDI-MS.

A3.3.2 Crystallography

Crystallographic data were measured at the Molecular Structure Laboratory of the Chemistry Department of the University of Wisconsin–Madison. Crystals were selected under oil under ambient conditions and attached to the tip of a MiTeGen MicroMount©. Each crystal was mounted in a stream of cold nitrogen at 100(1) K and centered in the X-ray beam using a video camera. The crystal evaluation and data collection were performed on a Bruker Quazar SMART APEX-II diffractometer with Mo Kα (λ = 0.71073 Å) radiation. The data were collected using a routine to survey an entire sphere of reciprocal space and indexed by the SMART program.[14] The structure was solved *via* direct methods and refined by iterative cycles of least-squares refinement on F^2 followed by difference Fourier synthesis.[15, 16] All H-atoms were included in the final structure factor calculation at idealized positions and allowed to ride on the neighboring atoms with relative isotropic displacement coefficients. Crystals of **1** suitable for structural determination were obtained by slow diffusion of hexane into a dichloromethane solution of **1**. The crystal chosen for diffraction proved to be a twin with a 1.3% minor second component. The crystal was solved using TWINABS.[17]

Re$_2$(DPhF)$_4$(N$_3$)$_2$ **(1)** Solid Re$_2$(DPhF)$_4$Cl$_2$ (88.6 mg, 0.0788 mmol) and NaN$_3$ (100 mg, 1.54 mmol) were combined in a 25 mL Schlenk flask and suspended in 25 mL of THF. The orange/yellow suspension was stirred for 1 d, during which the solution became darker orange. The THF was removed *in vacuo,* and the solid was suspended in EtOH (in air), filtered through a

medium porosity glass frit and washed with EtOH (3 x 20 mL). The resulting orange/red solid was dried under vacuum, dissolved in DCM and layered with hexane to crystallize over the course of several days. Yield: 60.0 mg, 61.4%. Anal. Calcd $Re_2C_{52}H_{44}N_{14} \cdot CH_2Cl_2$: C 48.1, H 3.5, N 14.8. Found: C 48.3, H 3.5, N 14.9. MALDI-TOF-MS (positive ion): m/z 1195.4 ($[M-N_3]^+$). ^1H NMR (CD_2Cl_2, 400 MHz, ppm): δ 8.51 (s, 4H), 7.20 - 7.14 (m, 24H), 6.59 - 6.52 (m, 16H). IR (ATR, cm^{-1}): 2075 (s), 2065 (s), 1585 (w), 1584 (w), 1534 (s), 1488 (s), 1376 (s), 1329 (s), 1262 (m), 1215 (s), 1208 (s), 1164 (w), 1156 (m), 1095 (m), 1080 (m), 1028 (m), 960 (m), 938 (m), 913 (w), 863 (w), 801 (m), 788 (m), 769 (s), 760 (s), 700 (s).

A3.4 Results and Discussion

A3.4.1 Synthesis and Characterization

Compound **1** is readily prepared by performing a salt metathesis reaction on the corresponding dichloride complex with an excess of sodium azide in THF. The ^1H NMR spectrum of **1** in CD_2Cl_2 is consistent with D_{4h} symmetry, displaying signals for only one of the eight mono-substituted phenyl rings in the aryl region as well as the methine proton signal at 8.51 ppm, significantly deshielded due to the magnetic anisotropy of the metal–metal quadruple bond.[13, 18] A key diagnostic feature of transition metal azide complexes is the IR stretching frequency of the bound azide. The bound azide ligands in **1** can be considered activated compared to free azide, as suggested by the reduced azide stretching frequencies of 2075 and 2065 cm^{-1} (free azide = 2115 cm^{-1}). The amount of azide activation is comparable to $M_2(form)_4$ azide complexes of either Os_2 ($\nu(N_3)$ = 2045 cm^{-1})[8] or Ru_2 ($\nu(N_3)$ = 2058 cm^{-1}),[19] the latter of which has shown the ability to perform intramolecular aryl C–H bond insertion from a highly reactive Ru_2 nitrido species generated by thermolysis of the corresponding azide complex.[9] The amount of azide activation also compares well with other Re azide complexes of $Re_2(DMAA)_4(N_3)_2$ (DMAA = 2',6'-dimethylacetanilide ($\nu(N_3)$ = 2064, 2042 cm^{-1})),[20] $ReN(N_3)(Me_2PhP)_3(Et_2tcb)$

(ν(N$_3$) = 2048 cm^{-1}),[21] *trans*-(Re(N$_3$)(N$_2$)(dppe)$_2$ (ν(N$_3$) = 2060 cm^{-1}),[22] and two Re cluster compounds, [Re$_6$Se$_8$(PEt$_3$)$_5$(N$_3$)]BF$_4$ and *cis*-[Re$_6$Se8(PEt$_3$)$_4$(N$_3$)$_2$] (ν(N$_3$) = 2048 and 2045 cm^{-1}, respectively).[23]

A3.4.2 Molecular Structure

The asymmetric unit of the orthorhombic *Pbca* crystal of **1** contains one half molecule of **1**, which lies on an inversion center within the unit cell, the molecular structure and tables of selected geometric parameters and crystallographic data are shown in Figure A3.1 and Tables A3.1 and A3.2, respectively. The molecule is isostructural to the related Re$_2$(form)$_4$Cl$_2$ complexes,[13] with a typical four-fold paddlewheel geometry about the Re–Re axis. The Re-atom lies in an octahedral environment coordinated by four N-atoms equatorially in a square plane, and axially by both a Re-atom and the terminal N-atom from the azide ligand. The Re–Re bond distance is 2.2773(1) Å, which is closely related to several other Re$_2$(form)$_4$Cl$_2$ complexes having Re–Re distances between 2.273 - 2.284 Å.[13]
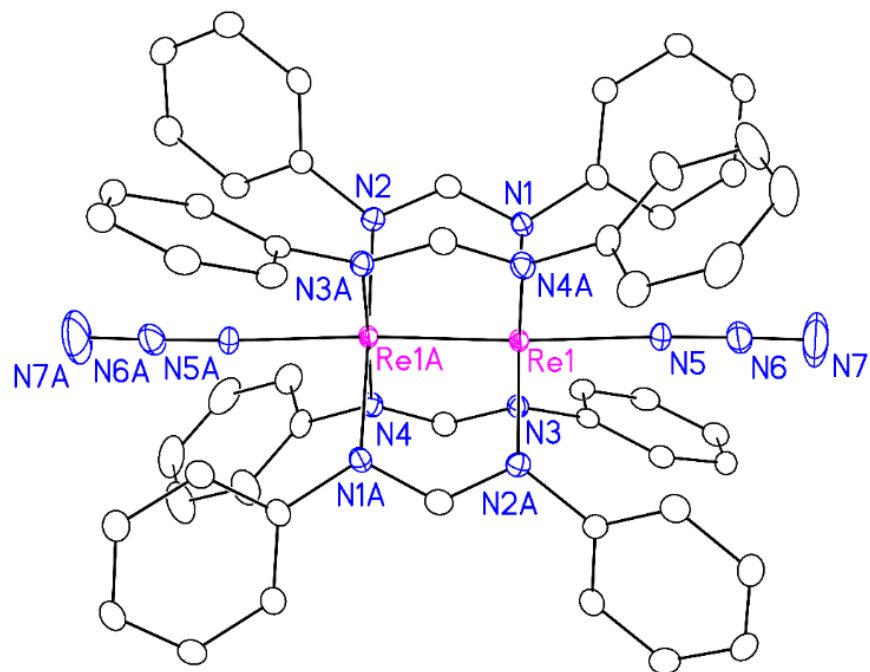
Figure A3.1. Molecular structure of **1** with thermal ellipsoids drawn at the 50% probability level.

Hydrogen atoms have been removed for clarity.

Table A3.1. Selected geometric parameters for **1** (Å, °).

Re1—Re1A	2.2773 (1)	Re1—N5	2.133 (2)
Re1—N1	2.102 (2)	N5—N6	1.177 (3)
Re1—N2A	2.092 (2)	N6—N7	1.142 (3)
Re1—N3	2.078 (2)		
Re1—N4A	2.106 (2)		
N1—Re1—Re1A	91.19 (5)	N3—Re1—N1	89.47 (7)
N1—Re1—N4A	89.94 (7)	N3—Re1—N2A	89.19 (6)
N1—Re1—N5	89.07 (7)	N3—Re1—N4A	178.84 (7)
N2A—Re1—Re1A	89.88 (5)	N3—Re1—N5	94.20 (6)
N2A—Re1—N1	178.31 (6)	N4A—Re1—Re1A	88.80 (5)
N2A—Re1—N4A	91.38 (7)	N4A—Re1—N5	84.78 (7)
N2A—Re1—N5	90.01 (7)	N5—Re1—Re1A	173.58 (5)
N3—Re1—Re1A	92.21 (5)	N6—N5—Re1	177.1 (2)

Table A3.2. Crystallographic data for **1** at 100 K.

Identification code	**1**
Empirical formula	$Re_2 C_{52} H_{44} N_{14}$
Formula weight	1237.41
Temperature	100(1) K
Wavelength	0.71073 Å
Crystal system	Orthorhombic
Space group	*Pbca*
Unit cell dimensions	a = 12.7180(3) Å
	b = 15.6221(4) Å
	c = 23.7857(6) Å
	$\alpha = 90°$
	$\beta = 90°$
	$\gamma = 90°$
Volume	4725.8(2) Å^3
Z	4
Density (calculated)	1.739 g/cm^3
Crystal size	0.181 x 0.114 x 0.076 mm^3
Data / restraints / parameters	4834/ 0 / 307
Goodness-of-fit on F^2	1.050
Final R[a,b] indices [$I>2\sigma(I)$]	$R_1 = 0.0147$, $wR_2 = 0.0324$
R indices (all data)	$R_1 = 0.0174$, $wR_2 = 0.0331$

[a]$R_1 = \Sigma||F_0| - |F_c||/\Sigma|F_0|$

[b]$wR_2 = |[\Sigma[w(F_0^2 - F_c^2)^2] / \Sigma[w(F_0^2)^2]]1/2$, $w = 1/\sigma^2 (F_0^2) + (aP)^2 + bP$, where $P = [max(0$ or $F_0^2) + 2(F_c^2)]/3$.

The short Re–Re distance is consistent with a metal–metal quadruple bond; the small torsion angle about the Re–Re axis (~1°) indicates the presence of δ bonding between the Re-atoms, as well. The Re–N_{ax} distance of 2.133(2) Å is also closely related to other metal–metal bonded formamidinate complexes of Os_2 (2.195(9) and 2.12(2) Å)[8] and Ru_2 (2.076(7) Å)[19] with axial azide ligands. The Re–N–N angle in **1** is 177.2(2)°, similar to the related Os_2 and Ru_2

formamidinate azide complexes with Os–N–N and Ru–N–N angles of 175° and 180°, respectfully. This near linear angle is attributed to the sterically bulky phenyl rings of the equatorial formamidinate ligands protruding out over the metal axial sites. The geometric parameters are similar to other reported Re–N$_3$ complexes; Re$_2$(DMAA)$_4$(N$_3$)$_2$ (DMAA = 2',6'-dimethylacetanilide (Re–Re and Re–N$_3$ = 2.2477(3) and 2.158(5) Å)),[20] ReN(N$_3$)(Me$_2$PhP)$_3$(Et$_2$tcb) (Re–N$_3$ = 2.323(9) Å),[21] [Re$_6$Se$_8$(PEt$_3$)$_5$(N$_3$)]BF$_4$ and *cis*-[Re$_6$Se8(PEt$_3$)$_4$(N$_3$)$_2$] (Re–N$_3$ = 2.1121(8) and 2.113(7) Å, respectively).[23]

A3.5 Conclusions

Compound **1** shows N–N bond activation of the terminal azide ligand similar to other M$_2$(form)$_4$ and Re azide complexes, suggested by the reduced IR stretching frequency of the M–azide compared to free azide. This complex should be able to undergo either thermolysis or photolysis to generate either a mono- or di-nitrido species. The nitrido species should be more stable and amenable to study than Ru$_2$(form)$_4$N, a complex known to undergo intramolecular aryl C–H bond insertion, due to the movement from a second to third row transition metal.

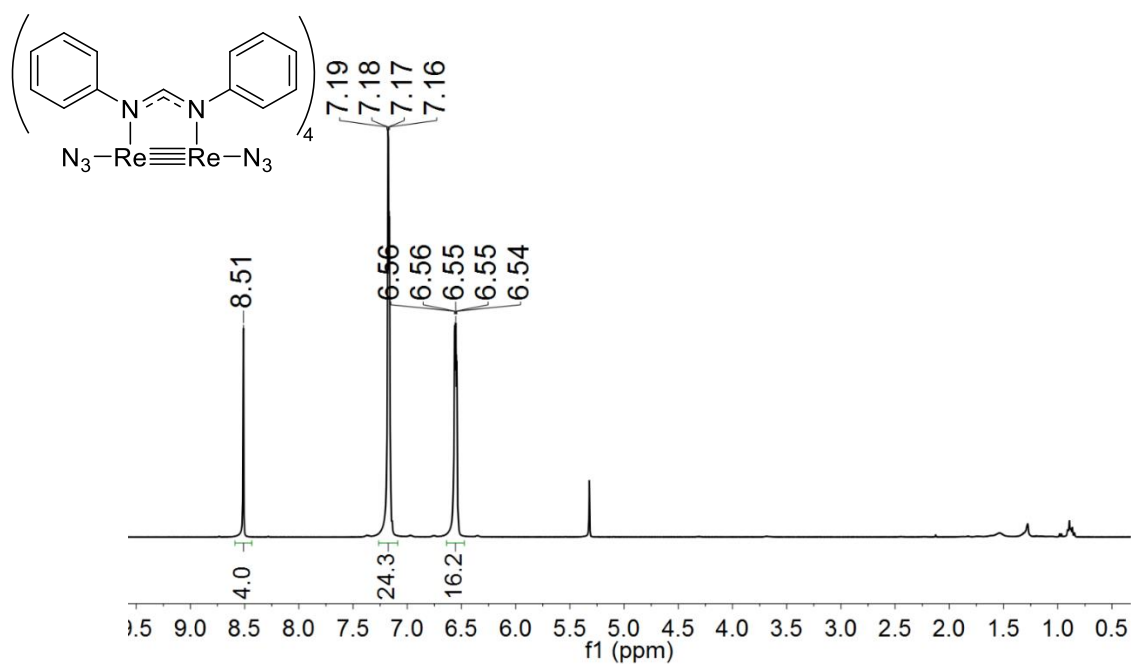## A3.6 Acknowledgments

A3.7 Supporting Information

Figure A3.2. ^{1}H NMR spectrum of **1** in CD$_2$Cl$_2$ at room temperature.

Table A3.3. Selected geometric parameters for **1** (Å).

Re1—Re1A	2.2773 (1)	C4—C5	1.388 (3)
Re1—N1	2.102 (2)	C5—C6	1.383 (3)
Re1—N2A	2.092 (2)	C6—C7	1.392 (3)
Re1—N3	2.078 (2)	C8—C9	1.390 (3)
Re1—N4A	2.106 (2)	C8—C13	1.390 (3)
Re1—N5	2.133 (2)	C9—C10	1.387 (3)
N1—C1	1.327 (3)	C10—C11	1.384 (3)
N1—C2	1.439 (3)	C11—C12	1.385 (3)
N2—Re1A	2.092 (2)	C12—C13	1.389 (3)
N2—C1	1.321 (3)	C15—C16	1.392 (3)
N2—C8	1.446 (3)	C15—C20	1.396 (3)
N3—C14	1.329 (3)	C16—C17	1.386 (3)
N3—C15	1.434 (3)	C17—C18	1.392 (3)
N4—Re1A	2.106 (2)	C18—C19	1.382 (3)
N4—C14	1.322 (3)	C19—C20	1.389 (3)
N4—C21	1.446 (3)	C21—C22	1.391 (3)
N5—N6	1.177 (3)	C21—C26	1.381 (3)
N6—N7	1.142 (3)	C22—C23	1.391 (3)
C2—C3	1.395 (3)	C23—C24	1.381 (4)
C2—C7	1.386 (3)	C24—C25	1.375 (4)
C3—C4	1.385 (3)	C25—C26	1.390 (3)

Table A3.4. Selected geometric parameters for **1** (º).

N1—Re1—Re1A	91.19 (5)	C7—C2—C3	119.0 (2)
N1—Re1—N4A	89.94 (7)	C4—C3—C2	120.1 (2)
N1—Re1—N5	89.07 (7)	C3—C4—C5	120.7 (2)
N2A—Re1—Re1A	89.88 (5)	C6—C5—C4	119.2 (2)
N2A—Re1—N1	178.31 (6)	C5—C6—C7	120.4 (2)
N2A—Re1—N4A	91.38 (7)	C2—C7—C6	120.5 (2)
N2A—Re1—N5	90.01 (7)	C9—C8—N2	118.8 (2)
N3—Re1—Re1A	92.21 (5)	C9—C8—C13	119.9 (2)
N3—Re1—N1	89.47 (7)	C13—C8—N2	121.3 (2)
N3—Re1—N2A	89.19 (6)	C10—C9—C8	120.1 (2)
N3—Re1—N4A	178.84 (7)	C11—C10—C9	120.2 (2)
N3—Re1—N5	94.20 (6)	C10—C11—C12	119.5 (2)
N4A—Re1—Re1A	88.80 (5)	C11—C12—C13	120.8 (2)
N4A—Re1—N5	84.78 (7)	C12—C13—C8	119.4 (2)
N5—Re1—Re1A	173.58 (5)	N4—C14—N3	121.5 (2)
C1—N1—Re1	117.4 (1)	C16—C15—N3	121.1 (2)
C1—N1—C2	115.5 (2)	C16—C15—C20	119.6 (2)
C2—N1—Re1	126.4 (1)	C20—C15—N3	119.2 (2)
C1—N2—Re1A	119.4 (1)	C17—C16—C15	119.8 (2)
C1—N2—C8	114.5 (2)	C16—C17—C18	120.7 (2)
C8—N2—Re1A	124.7 (1)	C19—C18—C17	119.4 (2)
C14—N3—Re1	117.7 (1)	C18—C19—C20	120.5 (2)
C14—N3—C15	115.5 (2)	C19—C20—C15	120.0 (2)
C15—N3—Re1	125.7 (1)	C22—C21—N4	119.6 (2)
C14—N4—Re1A	119.8 (1)	C26—C21—N4	120.7 (2)
C14—N4—C21	114.6 (2)	C26—C21—C22	119.7 (2)
C21—N4—Re1A	125.4 (1)	C21—C22—C23	119.8 (2)
N6—N5—Re1	177.2 (2)	C24—C23—C22	120.5 (2)
N7—N6—N5	176.8 (3)	C25—C24—C23	119.2 (2)
N2—C1—N1	122.1 (2)	C24—C25—C26	121.0 (2)
C3—C2—N1	121.0 (2)	C21—C26—C25	119.7 (2)
C7—C2—N1	119.9 (2)		

A3.8 References

(1)   Eikey, R. A.; Abu-Omar, M. M. *Coord. Chem. Rev.* **2003**, *243*, 83.

(2)   Thomson, R. K.; Cantat, T.; Scott, B. L.; Morris, D. E.; Batista, E. R.; Kiplinger, J. L., *Nat Chem* **2010**, *2*, 723.

(3)   Sieh, D.; Schoffel, J.; Burger, P. *Dalton Trans.* **2011**, *40*, 9512.

(4)   Long, A. K. M.; Timmer, G. H.; Pap, J. S.; Snyder, J. L.; Yu, R. P.; Berry, J. F. *J. Am. Chem. Soc.* **2011**, *133*, 13138.

(5)   Pap, J. S.; Snyder, J. L.; Piccoli, P. M. B.; Berry, J. F. *Inorg. Chem.* **2009**, *48*, 9846.

(6).   Pap, J. S.; DeBeer, S.; Berry, J. F. *Angew. Chem., Int. Ed.* **2008**, *47*, 10102.

(7)   Berry, J. F. *Comm. Inorg. Chem.* **2009**, *30*, 28.

(8)   Piccoli, P. M. B.; Berry, J. F. *J. Clust. Sci.* **2010**, *21*, 351.

(9)   Long, A. K. M.; Yu, R. P.; Timmer, G. H.; Berry, J. F. *J. Am. Chem. Soc.* **2010**, *132*, 12228.

(10)   Turov, Y.; Berry, J. F. *Dalton Trans.* **2012**, *41*, 8153.

(11)   Corcos, A. R.; Long, A. K. M.; Guzei, I. A.; Berry, J. F. *Eur. J. Inorg. Chem.* **2013**, *2013*, 3808.

(12)   Nugent, W. A.; Mayer, J. M. *Metal-Ligand Multiple Bonds*. Wiley: New York, **1988**.

(13)   Eglin, J. L.; Lin, C.; Ren, T.; Smith, L.; Staples, R. J.; Wipf, D. O. *Eur. J. Inorg. Chem.* **1999**, *1999*, 2095.

(14)   Bruker-AXS, *SMART* Program*,* Madison, Wisconsin, USA, **2009**.

(15)   Sheldrick, G. *Acta Cryst. A* **2008**, *64*, 112.

(16)   Dolomanov, O. V.; Bourhis, L. J.; Gildea, R. J.; Howard, J. A. K.; Puschmann, H. *J. Appl. Crystallogr.* **2009**, *42*, 339.

(17)   Sheldrick, G. M. *TWINABS*, Georg-August-Universitaet Goettingen: Goettingen, Germany, **2012**.

(18)   Sunderland, T. L.; Berry, J. F. *Chem. - Eur. J.* **2016**, *Submitted.*

(19)   Chen, W.; De Silva, V.; Lin, C.; Abellard, J.; Marcus, D. M.; Ren, T. *J. Clust. Sci.* **2005**, *16*, 151.

(20)   Lydon, D. P.; Spalding, T. R.; Gallagher, J. F. *Polyhedron* **2003**, *22*, 1281.

(21)   Ritter, S.; Abram, U. *Inorg. Chim. Acta* **1994**, *215*, 159.

(22)   Wang, Y.; Fraústo Da Silva, J. J. R.; Pombeiro, A. J. L.; Pellinghelli, M. A.; Tiripicchio, A. *J. Organomet. Chem.* **1993**, *454*, 211.

(23)   Knott, S. A.; Templeton, J. N.; Durham, J. L.; Howard, A. M.; McDonald, R.; Szczepura, L. F. *Dalton Trans.* **2013**, *42*, 8132.